



2809644669



REFERENCE ONLY

UNIVERSITY OF LONDON THESIS

Degree PHD Year 2007 Name of Author SPRINGELL, Ross Stuart

COPYRIGHT

This is a thesis accepted for a Higher Degree of the University of London. It is an unpublished typescript and the copyright is held by the author. All persons consulting this thesis must read and abide by the Copyright Declaration below.

COPYRIGHT DECLARATION

I recognise that the copyright of the above-described thesis rests with the author and that no quotation from it or information derived from it may be published without the prior written consent of the author.

LOANS

Theses may not be lent to individuals, but the Senate House Library may lend a copy to approved libraries within the United Kingdom, for consultation solely on the premises of those libraries. Application should be made to: Inter-Library Loans, Senate House Library, Senate House, Malet Street, London WC1E 7HU.

REPRODUCTION

University of London theses may not be reproduced without explicit written permission from the Senate House Library. Enquiries should be addressed to the Theses Section of the Library. Regulations concerning reproduction vary according to the date of acceptance of the thesis and are listed below as guidelines.

- A. Before 1962. Permission granted only upon the prior written consent of the author. (The Senate House Library will provide addresses where possible).
B. 1962-1974. In many cases the author has agreed to permit copying upon completion of a Copyright Declaration.
C. 1975-1988. Most theses may be copied upon completion of a Copyright Declaration.
D. 1989 onwards. Most theses may be copied.

This thesis comes within category D.

Checked box

This copy has been deposited in the Library of UCL

Unchecked box

This copy has been deposited in the Senate House Library, Senate House, Malet Street, London WC1E 7HU.



# Growth and Characterisation of Uranium Multilayers

Ross Springell

A Thesis presented for the degree of  
Doctor of Philosophy

Condensed Matter and Materials Physics  
Department of Physics and Astronomy  
University College London  
England

January 2007

UMI Number: U592421

All rights reserved

INFORMATION TO ALL USERS

The quality of this reproduction is dependent upon the quality of the copy submitted.

In the unlikely event that the author did not send a complete manuscript and there are missing pages, these will be noted. Also, if material had to be removed, a note will indicate the deletion.



UMI U592421

Published by ProQuest LLC 2013. Copyright in the Dissertation held by the Author.  
Microform Edition © ProQuest LLC.

All rights reserved. This work is protected against  
unauthorized copying under Title 17, United States Code.



ProQuest LLC  
789 East Eisenhower Parkway  
P.O. Box 1346  
Ann Arbor, MI 48106-1346

*Dedicated to*

Kate

# Growth and Characterisation of Uranium Multilayers

Ross Springell

Submitted for the degree of Doctor of Philosophy

January 2007

## Abstract

This thesis investigates the extents of the 5f-3d and 5f-4f electronic interactions in U/Fe, U/Co and U/Gd thin films, where electronic hybridisation effects are expected to influence the magnetism of the U 5f states. The samples were prepared by DC magnetron sputtering and included niobium buffer and capping layers to instigate crystalline growth and prevent oxidation of the multilayer stack. Layer thicknesses were varied between 5Å and 90Å with up to 30 bilayer repeats. The majority of the samples were grown at room temperature, but selected compositions were grown at elevated substrate temperatures. Many well-defined Bragg peaks were evident in the X-ray reflectivity spectra of multilayers of all three systems, indicating a low impurity contamination and a well-reproduced bilayer structure. High-angle X-ray diffraction spectra of the transition metal multilayers revealed poorly crystalline, oriented transition metal layers with a non-crystalline component of Fe and Co of  $\sim 17\text{\AA}$ . U/Gd X-ray diffraction spectra displayed intensities up to two orders of magnitude greater than those observed for U/Fe or U/Co samples of similar composition and contained satellite peaks, indicating some degree of coherency between the two species. An intense peak was observed, arising from a crystalline uranium component at a position close to that expected for an exotic hcp U phase, oriented in the [001] direction. Bulk magnetisation measurements revealed magnetically 'dead' Fe and Co layers of  $\sim 15\text{\AA}$  and magnetic moments tending towards the bulk values of  $2.2\mu_B$  and  $1.7\mu_B$  for thick Fe and Co layers respectively. A study of the bulk magnetic properties of the U/Gd system did not indicate the presence of any signif-

---

icant 'dead' layer, but reported a saturation magnetic moment for thick Gd layers of  $\sim 4.5\mu_B$ , considerably reduced from the bulk value of  $7.63\mu_B$ . Calculations of the magnetic anisotropy for U/Gd samples revealed a possible transition from the gadolinium moments aligned within the plane of the film to samples displaying perpendicular magnetic anisotropy (PMA), at a gadolinium layer thickness of  $\sim 5\text{\AA}$ . This transition could be achieved for thicker Gd layers if the thickness of the U layers were increased. A finite-size scaling effect was observed in a gadolinium layer thickness dependent study of the Curie temperature, indicating a transition from three to two dimensional behaviour for very thin Gd layers. Polarised neutron reflectivity spectra were taken in the specular geometry at magnetic saturation, and were simulated with separate, reduced moment and bulk moment ferromagnetic layers for U/Fe and U/Co samples and a simple bilayer structure for U/Gd samples. This simultaneous measurement of both the physical composition and bulk magnetisation measurements supported results obtained by X-ray reflectivity and magnetometry. The hybridisation of the electronic states in U/Fe and U/Gd resulted in an induced polarisation, detected using element selective techniques. X-ray magnetic circular dichroism measurements at the U  $M_{IV}$  and  $M_V$  edges were used to investigate the spin and orbital components of the uranium magnetic moment and a total magnetic moment on the U site of  $\sim 0.1\mu_B$  for the case of U/Fe multilayers,  $\sim 0.01\mu_B$  in U/Gd samples and a signal only barely detectable above the statistical noise in the U/Co system were revealed. A uranium layer thickness dependent study of the magnetic moment values was used to indirectly deduce the profile of uranium magnetisation within the layers. X-ray resonant magnetic reflectivity measurements provided a depth dependent measure of the induced U 5f moment for selected U/Fe samples, which indicated a more complicated interfacial structure than that deduced by X-ray and neutron reflectivity techniques and showed that the majority of the U 5f moment was located at the interface region.

# Declaration

The work in this thesis is based on research carried out at the Department of Physics and Astronomy, University College London, England. No part of this thesis has been submitted elsewhere for any other degree or qualification and it is all my own work unless referenced to the contrary in the text.

**Copyright © 2007 by Ross Springell.**

“The copyright of this thesis rests with the author. No quotations from it should be published without the author’s prior written consent and information derived from it should be acknowledged”.

# Acknowledgements

During the course of the PhD I have had the opportunity to work on a myriad of different skills; some will be useful during the course of my career and others will not. I have had a great time nevertheless, and I have been fortunate enough to meet and work with a lot of people I like and respect. I will try to thank as many of these as possible, but I apologize in advance for any omissions.

My first and most grateful thanks are to my supervisor Stan Zochowski who has given me reassurance and invaluable advice for which I am utterly grateful.

Most directly involved with the thesis, are those who are part of the uranium multilayers team. Over the past three years this group has become pretty expansive and includes the great and the good across a multitude of disciplines within condensed matter physics. I have had the pleasure to work with and discuss (sometimes debate) with (in alphabetical order) Angela Beesley, Lawrence Bouchenoire, Simon Brown, Gerry Lander, Sean Langridge, Andrei Rogalev, Bill Stirling, Mike Thomas, Roger Ward, Mike Wells, Fabrice Wilhelm and Stuart Wilkins. Also deserving of a nod are Paul Thompson (of the XMaS beamline), Tim Charlton and Rob Dalglish (CRISP) who have helped me pass some of the long hours on X-ray and neutron experiments.

For me, the PhD process has not just concerned the project, but a host of other commitments at work and at home. I have had the pleasure to demonstrate in the third year physics labs under the guidance of Neal Skipper, Chris Bull, Bernard Bristol and Martin Palmer. I have enjoyed working with Stan to help encourage prospective students to come and study at UCL and worked with Stan, Arthur Lovell and Keith McKewen, marking scripts for 1st and 2nd year courses.

I have also managed to get to grips with the Guardian cryptic crossword during

the course of the PhD, thanks to many coffee breaks spent with the inhabitants of F10a and F10b. These include Mark (Ellerby), Cecilia (Gejke), Tom (Headen), Chris (Howard), Arthur (Lovell), Emily (Milner), Neal (Skipper), Hayley (Spiers), Helen (Walker) and Tom (Weller). These people have made the last three years really good fun and it has been a pleasure to come to work.

My final thank you is to my family and friends, but especially Kate, who has had to endure a fairly stressed out Ross for the last few months, while I have been trying to finish.

# Contents

|   |            |
|---|------------|
| <b>Abstract</b>                             | <b>iii</b> |
| <b>Declaration</b>                          | <b>v</b>   |
| <b>Acknowledgements</b>                     | <b>vi</b>  |
| <b>1 Introduction</b>                       | <b>1</b>   |
| 1.1 Thesis Outline . . . . .                | 3          |
| <b>2 Background</b>                         | <b>4</b>   |
| 2.1 Multilayers . . . . .                   | 4          |
| 2.2 Transition Metal Ferromagnets . . . . . | 6          |
| 2.2.1 Iron . . . . .                        | 7          |
| 2.2.2 Cobalt . . . . .                      | 8          |
| 2.3 Rare-earth Metals . . . . .             | 8          |
| 2.3.1 RKKY Interaction . . . . .            | 9          |
| 2.3.2 Gadolinium . . . . .                  | 10         |
| 2.4 Actinides . . . . .                     | 11         |
| 2.4.1 Uranium . . . . .                     | 12         |
| 2.4.2 Electronic Properties . . . . .       | 13         |
| 2.4.3 Binary Alloys . . . . .               | 16         |
| 2.4.4 Uranium Compounds . . . . .           | 17         |
| <b>3 Fabrication</b>                        | <b>19</b>  |
| 3.1 DC Magnetron Sputtering . . . . .       | 19         |
| 3.2 Experimental Set-up . . . . .           | 24         |

---

|          |  |            |
|----------|--|------------|
| 3.3      | Sample Composition . . . . .                 | 26         |
| 3.3.1    | Uranium/Iron . . . . .                       | 28         |
| 3.3.2    | Uranium/Cobalt . . . . .                     | 29         |
| 3.3.3    | Uranium/Gadolinium . . . . .                 | 30         |
| <b>4</b> | <b>Structural Characterisation</b>           | <b>33</b>  |
| 4.1      | X-rays . . . . .                             | 33         |
| 4.1.1    | X-ray Sources . . . . .                      | 34         |
| 4.1.2    | X-ray Scattering . . . . .                   | 35         |
| 4.1.3    | Photoelectric Absorption . . . . .           | 43         |
| 4.2      | X-ray Reflectivity . . . . .                 | 44         |
| 4.2.1    | Experimental Method . . . . .                | 52         |
| 4.2.2    | Results . . . . .                            | 55         |
| 4.2.3    | Uranium/Iron . . . . .                       | 55         |
| 4.2.4    | Uranium/Cobalt . . . . .                     | 59         |
| 4.2.5    | Uranium/Gadolinium . . . . .                 | 62         |
| 4.2.6    | Summary Analysis . . . . .                   | 67         |
| 4.3      | X-ray Diffraction . . . . .                  | 69         |
| 4.3.1    | X-ray Diffraction from Multilayers . . . . . | 73         |
| 4.3.2    | Experimental Method . . . . .                | 78         |
| 4.3.3    | Results . . . . .                            | 80         |
| 4.3.4    | Uranium/Iron . . . . .                       | 80         |
| 4.3.5    | Uranium/Cobalt . . . . .                     | 84         |
| 4.3.6    | Uranium/Gadolinium . . . . .                 | 88         |
| 4.3.7    | Summary Analysis . . . . .                   | 100        |
| <b>5</b> | <b>Magnetic Characterisation</b>             | <b>104</b> |
| 5.1      | Clarification of Terms . . . . .             | 104        |
| 5.2      | Magnetic Materials . . . . .                 | 106        |
| 5.3      | Hysteresis . . . . .                         | 110        |
| 5.4      | Domains . . . . .                            | 111        |
| 5.5      | Anisotropy . . . . .                         | 112        |

---

|          |  |            |
|----------|--|------------|
| 5.5.1    | Magneto-crystalline Anisotropy . . . . .                       | 112        |
| 5.5.2    | Demagnetising Field . . . . .                                  | 113        |
| 5.6      | SQUID Magnetometry . . . . .                                   | 114        |
| 5.7      | Experimental Method . . . . .                                  | 115        |
| 5.8      | Results . . . . .  | 116        |
| 5.8.1    | Uranium/Iron . . . . .   | 117        |
| 5.8.2    | Uranium/Cobalt . . . . .                                       | 121        |
| 5.8.3    | Uranium/Gadolinium - Field Dependence . . . . .                | 124        |
| 5.8.4    | Uranium/Gadolinium - Temperature Dependence . . . . .          | 136        |
| 5.9      | Summary Analysis . . . . .                                     | 140        |
| 5.10     | Neutrons . . . . .   | 142        |
| 5.10.1   | Neutron Scattering . . . . .                                   | 144        |
| 5.11     | Polarised Neutron Reflectivity . . . . .                       | 145        |
| 5.11.1   | Experimental Method . . . . .                                  | 150        |
| 5.11.2   | Results . . . . .  | 151        |
| 5.11.3   | Uranium/Iron . . . . .   | 151        |
| 5.11.4   | Uranium/Cobalt . . . . .                                       | 157        |
| 5.11.5   | Uranium/Gadolinium . . . . .                                   | 162        |
| 5.11.6   | Summary Analysis . . . . .                                     | 167        |
| <b>6</b> | <b>Element Specific Characterisation</b>                       | <b>170</b> |
| 6.1      | X-ray Magnetic Circular Dichroism . . . . .                    | 171        |
| 6.1.1    | Experimental Method . . . . .                                  | 176        |
| 6.1.2    | U/Fe - Fe K edge . . . . .                                     | 180        |
| 6.1.3    | U/Fe - U M <sub>IV</sub> and M <sub>V</sub> edges . . . . .    | 183        |
| 6.1.4    | U/Co - U M <sub>IV</sub> edge . . . . .                        | 192        |
| 6.1.5    | U/Gd - Gd L <sub>II</sub> and L <sub>III</sub> edges . . . . . | 195        |
| 6.1.6    | U/Gd - U M <sub>IV</sub> and M <sub>V</sub> edges . . . . .    | 197        |
| 6.1.7    | Summary Analysis . . . . .                                     | 202        |
| 6.2      | X-ray Magnetic Scattering . . . . .                            | 203        |
| 6.3      | X-ray Resonant Magnetic Scattering . . . . .                   | 205        |
| 6.4      | X-ray Resonant Magnetic Reflectivity . . . . .                 | 208        |

|   |            |
|---|------------|
| <b>Contents</b>   | <b>xi</b>  |
| 6.4.1 Experimental Method . . . . .   | 211        |
| 6.4.2 Results - SN71 [U <sub>9</sub> /Fe <sub>34</sub> ] <sub>30</sub> . . . . .  | 213        |
| 6.4.3 Results - SN74 [U <sub>32</sub> /Fe <sub>27</sub> ] <sub>30</sub> . . . . . | 221        |
| <b>7 Conclusions</b>  | <b>224</b> |
| 7.1 Articles - Planned and Published . . . . .                                    | 231        |
| <b>Bibliography</b>   | <b>232</b> |

# List of Figures

|     |   |    |
|-----|---|----|
| 2.1 | Body centred cubic structure of $\alpha$ -Fe with $a = b = c = 2.866\text{\AA}$ . . . . .   | 7  |
| 2.2 | Hexagonal close-packed cobalt structure with $a = b = 2.507\text{\AA}$ and $c = 4.070\text{\AA}$ . . . . .  | 8  |
| 2.3 | Hexagonal close-packed gadolinium structure with $a = b = 3.631\text{\AA}$ and $c = 5.777\text{\AA}$ . . . . .  | 11 |
| 2.4 | Orthorhombic $\alpha$ -uranium structure with $a = 2.854\text{\AA}$ , $b = 5.870\text{\AA}$ and $c = 4.955\text{\AA}$ . . . . .   | 12 |
| 2.5 | Phase diagram of the uranium, iron binary alloy system. . . . .   | 16 |
| 3.1 | Schematic diagram of the sputtering process, including the magnetron plasma confinement. . . . .  | 20 |
| 3.2 | Two common geometries of the DC planar magnetron, used to confine the plasma of glow discharges close to the target material. . . . .   | 21 |
| 3.3 | The likely crystal growth as a function of substrate temperature and argon gas pressure for sputtered metals [1]. . . . .   | 23 |
| 3.4 | The photographs (a), (b) and (c) show the sputtering apparatus at the Clarendon Laboratory; the insertion rod, the loading chamber and the main sputter chamber respectively. A stable plasma can be seen through the window to the main chamber. . . . . | 25 |
| 3.5 | RHEED patterns observed from buffer and substrate. . . . .  | 26 |
| 4.1 | Representation of the quantum mechanical description of an elastic scattering event. . . . .  | 37 |

---

|      |  |    |
|------|--|----|
| 4.2  | Coordinate system used to represent the electromagnetic field radiated from an oscillating electronic charge distribution under the influence of an incident plane wave. . . . .   | 39 |
| 4.3  | Radiated field from an oscillating electron in the field of an incident plane wave with the observation point, X (a) in the plane of the incident wave polarisation and (b) in the plane perpendicular to the incident wave polarisation. . . . .  | 41 |
| 4.4  | Description of the elastic scattering of an X-ray photon from an atom and the definition of the wavevector transfer, $\mathbf{Q}$ . . . . .  | 42 |
| 4.5  | The photoelectric absorption process, the incident photon causes an electron to be ejected into the continuum and an electron in an outer shell fills the hole, emitting a photon of a characteristic energy. In this case the $K\alpha$ fluorescence is shown. . . . .  | 44 |
| 4.6  | Reflection and transmittance of an incident X-ray from an infinitely thick layer allows the derivation of Snell's law and the Fresnel equations if the incident wave and its derivative are equivalent at the interface. . . . .   | 46 |
| 4.7  | The reflected intensity from an infinitely thick layer shows the total external reflection below the critical angle and a $q^{-4}$ dependence above it. . . . .  | 47 |
| 4.8  | Keissig fringes from an iron layer of finite thickness on a sapphire substrate. . . . .  | 48 |
| 4.9  | Simulated reflectivity spectra from an ideal U/Fe multilayer (black solid line), showing the extinction of every third Bragg peak, since $t_U : t_{Fe} = 2 : 1$ . The effect of decreasing the bilayer thickness (red dashed line) and the addition of a roughness factor (blue dotted line) can also be observed. Curves have been displaced for clarity. . . . . | 50 |
| 4.10 | X-ray reflectivity spectra taken in the specular geometry, using a Cu- $K\alpha$ source from a U/Fe series of samples grown on sapphire substrates with niobium buffers and capping layers. . . . .  | 56 |

|   |    |
|---|----|
| 4.11 X-ray reflected intensity as a function of the wavevector momentum transfer for U/Fe sample SN77 [U <sub>10.3</sub> /Fe <sub>10</sub> ] <sub>30</sub> . . . . .  | 57 |
| 4.12 Graphs of the X-ray reflected intensity versus the wavevector momentum transfer taken in the specular geometry, $\lambda = 1.54\text{\AA}$ , for the U/Co series of samples. . . . .   | 60 |
| 4.13 Graphs of the X-ray reflected intensity versus the wavevector momentum transfer taken in the specular geometry, using X-rays with a wavelength of $1.54\text{\AA}$ for the U/Co series of samples. . . . .   | 61 |
| 4.14 U/Gd X-ray reflectivity spectra. . . . .   | 62 |
| 4.15 The X-ray reflected intensity as a function of wavevector momentum transfer for the second series of U/Gd multilayer samples. Scans were carried out in the specular geometry using a source wavelength of $1.54\text{\AA}$ . . . . .  | 64 |
| 4.16 Graphs of the X-ray reflectivity from the third series of U/Gd samples. All results were taken in the specular direction, using a Cu-K $\alpha$ source. . . . .  | 66 |
| 4.17 Illustration of Bragg's law in the case of a 2D square lattice. . . . .  | 69 |
| 4.18 A 2D illustration of the Ewald sphere, the Ewald circle is used to visualise diffraction events in reciprocal space. The figure shows the fulfilment of the Laue condition (coincidence of the Ewald circle and reciprocal lattice point) so that a diffraction peak is observed if the detector is placed in the direction of $\mathbf{k}'$ . . . . . | 72 |
| 4.19 A comparison of the diffraction peaks observed for an ideal crystal and a sample comprised of a number of crystallites of finite size . . . . .  | 75 |
| 4.20 Example of an hcp-U/Gd multilayer diffraction pattern as the bilayer repeat distance, $t_B$ is increased. It is possible to resolve the hcp-U (002) and Gd (002) peaks when values of $t_{Gd}$ and $t_U$ are large. . . . .  | 77 |
| 4.21 Lattice plane construction of a crystalline layer within a superlattice. . . . .   | 79 |
| 4.22 Comparison of the X-ray diffraction patterns close to the sapphire $11\bar{2}0$ peak, for U/Fe samples listed in table 3.3. . . . .  | 81 |
| 4.23 X-ray diffraction spectra of the iron component from the U/Fe series of multilayers for selected samples together with fitted curves produced by the SUPREX diffraction program. . . . .   | 82 |

|      |  |     |
|------|--|-----|
| 4.24 | Comparison of the X-ray diffraction patterns close to the sapphire $11\bar{2}0$ peak, for U/Co samples listed in table 3.4. . . . .  | 84  |
| 4.25 | X-ray diffraction spectra of the cobalt component from the U/Co series of multilayers for selected samples together with fitted curves produced by the SUPREX diffraction program. . . . .   | 86  |
| 4.26 | Comparison of the X-ray diffraction patterns close to the sapphire $11\bar{2}0$ peak, for U/Gd samples listed in table 3.5. . . . .  | 88  |
| 4.27 | X-ray diffraction spectra of the 1st U/Gd series of multilayers with fitted curves simulated by the SUPREX diffraction program. . . . .  | 90  |
| 4.28 | Comparison of the X-ray diffraction patterns close to the sapphire $11\bar{2}0$ peak, for U/Gd samples listed in table 3.6. . . . .  | 93  |
| 4.29 | X-ray diffraction spectra of the 2nd U/Gd series of multilayers with fitted curves simulated by the SUPREX diffraction program. . . . .  | 94  |
| 4.30 | Comparison of the X-ray diffraction patterns close to the sapphire $11\bar{2}0$ peak, for U/Gd samples listed in table 3.7. . . . .  | 97  |
| 4.31 | X-ray diffraction from U/Gd samples . . . . .  | 98  |
| 4.32 | Comparison of the cell parameter $a$ , vertical coherence length and particle size for U/Fe samples grown on glass and those grown on sapphire. . . . .  | 101 |
| 4.33 | Variations in the lattice spacings of uranium and gadolinium as a function of $t_{\text{Gd}}$ (full points) and $t_{\text{U}}$ (open squares). Values for the bulk and thick Gd film gadolinium lattice parameter are labeled. . . . | 102 |
| 5.1  | Diagram to show the responses of the magnetic induction and hence the magnetisation to an applied magnetic field for a diamagnet, paramagnet and ferromagnet respectively. . . . .   | 106 |
| 5.2  | Diagram showing the effect of an applied magnetic field on the population of spin up and spin down bands in a Pauli paramagnet. . . .  | 109 |
| 5.3  | Schematic of the relevant parameters, used to describe an hysteresis loop, the saturation magnetisation, $M_{\text{S}}$ , the coercive field, $H_{\text{C}}$ and the remnant magnetisation, $M_{\text{r}}$ . . . . .                 | 111 |

- 
- 5.4 Example of an hysteresis loop that includes a contribution from a diamagnetic substrate and the method used to correct for this, used to reveal the contribution solely from the ferromagnetic sample. . . . 116
- 5.5 Magnetisation as a function of the applied magnetic field, displaying hysteresis for selected U/Fe samples. . . . . 117
- 5.6 (a) Absolute saturation magnetisation, normalised to sample area and number of bilayer repeats. (b) Relative saturation magnetisation values as a function of  $t_{\text{Fe}}$ , insert shows the expected value of  $M_{\text{S}}$  for films with thick Fe layers. . . . . 119
- 5.7 Magnetisation as a function of the applied magnetic field, displaying hysteresis for selected U/Co samples. . . . . 121
- 5.8 (a) Absolute saturation magnetisation, normalised to sample area and number of bilayer repeats. (b) Relative saturation magnetisation values as a function of  $t_{\text{Co}}$ , insert shows the expected value of  $M_{\text{S}}$  for films with thick Co layers. . . . . 122
- 5.9 Magnetisation as a function of the applied magnetic field, displaying hysteresis for series 1, U/Gd samples. The magnetic field has been applied both parallel (black curve) and perpendicular (red curve) to the plane of the film. . . . . 124
- 5.10 Magnetisation as a function of the applied magnetic field, displaying hysteresis for series 2, U/Gd samples. . . . . 125
- 5.11 Magnetisation as a function of the applied magnetic field, displaying hysteresis for series 3, U/Gd samples. The magnetic field has been applied both parallel (black curve) and perpendicular (red curve) to the plane of the film. . . . . 127
- 5.12 The magnetisation as a function of the applied magnetic field for sample SN139 - U-Gd alloy ( $\sim 5\%U$ ). The red curve denotes the response to a field applied perpendicular to the plane of the film and the black curve, a field applied parallel. . . . . 129

- 5.13 (a) Absolute saturation magnetisation, normalised to sample area and number of bilayer repeats. (b) Relative saturation magnetisation values as a function of  $t_{\text{Gd}}$ , insert shows the expected value of  $M_{\text{S}}$  for films with thick Gd layers. Magnetisation values are given for samples with a similar uranium layer thickness. . . . . 130
- 5.14 The variation of the saturation magnetisation as a function of the uranium layer thickness for constant  $t_{\text{Gd}} \sim 20\text{\AA}$ . The exponential decay trend line is shown as a guide to the eye. . . . . 132
- 5.15 The dependence of the coercive field upon the gadolinium layer thickness for two values of constant  $t_{\text{U}}$  (a),  $\sim 20\text{\AA}$ , and (b),  $\sim 10\text{\AA}$ , with the applied field in the plane of the film. . . . . 133
- 5.16 The dependence of the coercive field upon the uranium layer thickness for constant  $t_{\text{Gd}} \sim 20\text{\AA}$  with the magnetic field applied in the plane of the film. . . . . 134
- 5.17 Graph of  $t_{\text{Gd}}k_{\text{eff}}$  vs  $t_{\text{Gd}}$  in order to determine the relative volume and surface contributions to the effective anisotropy of the multilayers. The blue arrow shows the effect of increasing uranium layer thickness on the effective anisotropy. . . . . 136
- 5.18 The temperature dependent magnetisation for a number of magnetic field values measured for sample SN64 -  $[\text{U}_{26}/\text{Gd}_{76}]_{20}$ . . . . . 137
- 5.19 Figures illustrating the finite size scaling effect of reduced layer thickness on the ferromagnetic transition temperature. . . . . 138
- 5.20 Schematic diagram showing the spallation process used to produce the neutron flux at the ISIS time-of-flight source at the Rutherford Appleton Laboratories. . . . . 143
- 5.21 Orientation of the sample magnetisation,  $\mu$ , with respect to the applied field,  $\mathbf{H}$ . . . . . 146
- 5.22 Layout of the CRISP neutron reflectometer at the ISIS neutron spallation source, showing set-up for polarised neutron reflectivity without polarisation analysis in the specular geometry. Dashed lines show the neutron path through the apparatus to the detector. . . . . 149

|      |   |     |
|------|---|-----|
| 5.23 | The polarised neutron reflectivity data measured in the specular geometry at 300K and 4.4kOe simulated by the xPOLLY program for sample SN71 – [U <sub>9</sub> /Fe <sub>34</sub> ] <sub>30</sub> . . . . .  | 152 |
| 5.24 | The polarised neutron reflectivity data measured in the specular geometry at 300K and 4.4kOe simulated by the xPOLLY program for sample SN74 – [U <sub>32</sub> /Fe <sub>27</sub> ] <sub>30</sub> . . . . .                                       | 152 |
| 5.25 | The polarised neutron reflectivity data measured in the specular geometry at 300K and 4.4kOe simulated by the xPOLLY program for sample SN75 – [U <sub>35.2</sub> /Fe <sub>27</sub> ] <sub>30</sub> . . . . .                                     | 153 |
| 5.26 | Comparison of the saturation magnetisation values ( $\mu_B/\text{Fe}$ ) as determined by SQUID magnetometry and PNR, averaged over the entire Fe layer, as a function of the iron layer thickness. . . . .  | 156 |
| 5.27 | The polarised neutron reflectivity data measured in the specular geometry at 300K and 4.4kOe simulated by the xPOLLY program for sample SN116 – [Co <sub>42.5</sub> /U <sub>19</sub> ] <sub>20</sub> . . . . .                                    | 157 |
| 5.28 | The polarised neutron reflectivity data measured in the specular geometry at 300K and 4.4kOe simulated by the xPOLLY program for sample SN117 – [U <sub>9</sub> /Co <sub>51</sub> ] <sub>15</sub> . . . . .                                       | 158 |
| 5.29 | The polarised neutron reflectivity data measured in the specular geometry at 300K and 4.4kOe simulated by the xPOLLY program for sample SN118 – [U <sub>10</sub> /Co <sub>34.5</sub> ] <sub>20</sub> . . . . .                                    | 158 |
| 5.30 | Comparison of the saturation magnetisation values ( $\mu_B/\text{Co}$ ) as determined by SQUID magnetometry and PNR, averaged over the entire Co layer, as a function of the cobalt layer thickness. . . . .                                      | 160 |
| 5.31 | The polarised neutron reflectivity data measured in the specular geometry at 10K/300K in an applied magnetic field of 4.4kOe, simulated using the xPOLLY program for sample SN63 – [U <sub>26</sub> /Gd <sub>33</sub> ] <sub>20</sub> . . . . .   | 163 |
| 5.32 | The polarised neutron reflectivity data measured in the specular geometry at 10K/300K in an applied magnetic field of 4.4kOe, simulated using the xPOLLY program for sample SN67 – [U <sub>63.5</sub> /Gd <sub>20</sub> ] <sub>20</sub> . . . . . | 164 |

|      |  |     |
|------|--|-----|
| 5.33 | The polarised neutron reflectivity data measured in the specular geometry at 10K/300K in an applied magnetic field of 4.4kOe, simulated using the xPOLLY program for sample SN65 – [U <sub>26</sub> /Gd <sub>76</sub> ] <sub>20</sub> . . .      | 165 |
| 5.34 | The polarised neutron reflectivity data measured in the specular geometry at 10K/300K in an applied magnetic field of 4.4kOe, simulated using the xPOLLY program for sample SN124 – [U <sub>10.6</sub> /Gd <sub>24.8</sub> ] <sub>20</sub> . . . | 165 |
| 5.35 | Comparison of the magnetic moment values per Gd atom, determined by bulk magnetisation measurements and polarised neutron reflectometry in a saturation field, as a function of $t_{\text{Gd}}$ (a) and $t_{\text{U}}$ (b). . .                  | 167 |
| 6.1  | In the spin-dependent photoabsorption process a circularly polarised photon excites an electron from the core level, which gains a spin-polarisation. The photoelectron is then captured into a vacancy in the valence band. . . . .             | 173 |
| 6.2  | Schematic layout of the ID12 beamline. . . . .   | 177 |
| 6.3  | Example of the self absorption corrections for two example U/Fe samples. The correction clearly becomes more significant for thick uranium layers. . . . .   | 179 |
| 6.4  | XANES and XMCD signals for three U/Fe samples of varying structural composition across the Fe K edge. . . . .  | 181 |
| 6.5  | XANES and XMCD signals for three U/Fe samples of varying structural composition across the Fe K edge. . . . .  | 183 |
| 6.6  | Comparison between the observed XANES and XMCD signals for a [U <sub>26</sub> /Fe <sub>29</sub> ] <sub>30</sub> multilayer and a UFe <sub>2</sub> single crystal. . . . .  | 185 |
| 6.7  | XANES and XMCD signals for a selection of U/Fe multilayers, with varying $t_{\text{U}}$ and constant $t_{\text{Fe}}$ . . . . .   | 186 |
| 6.8  | Hysteresis loops measured for samples SN71 and SN72 ([U <sub>34</sub> /Fe <sub>9</sub> ] <sub>30</sub> and [U <sub>23.2</sub> /Fe <sub>17</sub> ] <sub>10</sub> ), compared with one obtained for sample SN71, using SQUID magnetometry. . . . . | 187 |
| 6.9  | Profiles of the induced uranium magnetic moment, determined by the evolution of the total induced magnetic moment, as calculated using the XMCD sum rules. Slices are 4Å. . . . .  | 190 |

|      |   |     |
|------|---|-----|
| 6.10 | XANES and XMCD spectra at the U $M_{IV}$ edge for U/Co sample SN116, comprising thick Co layers and thin U layers in order to achieve a maximal observed XMCD signal. . . . .   | 192 |
| 6.11 | XANES and XMCD signals for U/Gd samples SN65 and SN66. . . .  | 195 |
| 6.12 | XANES and XMCD signals for U/Gd sample SN138 and U-Gd alloy, SN139. . . . .   | 196 |
| 6.13 | XANES and XMCD signals at the U $M_{IV}$ and $M_V$ edges, normalised to the white line and corrected for the respective branching ration, but not including SAC. The left panels compare spectra for a series of U/Gd multilayers with varied U layer thicknesses, but constant $t_{Gd}$ , the right panels show a clearer comparison of the spectra observed for a multilayer and that of a U-Gd alloy sample. . . . . | 198 |
| 6.14 | Profiles of the induced U 5f magnetic moment, determined by a comparison of the total U moments for the series of U/Gd samples in table 6.4, considering a $5f^{2.5}$ configuration. Slices are $2.5\text{\AA}$ . . . . .   | 201 |
| 6.15 | Schematic diagram, describing the scattering geometry and the linear and orthogonal components of the polarisation vectors. . . . .   | 207 |
| 6.16 | . . . . .   | 209 |
| 6.17 | Four example energies of the 17-energy mesh describing the X-ray resonant charge reflectivity and the asymmetry, showing the first four Bragg peaks for sample SN71 $[U_9/Fe_{34}]_{30}$ . . . . .  | 214 |
| 6.18 | Asymmetry as a function of $q$ in the vicinity of the first four Bragg peaks, showing results from several different structural and magnetic models. . . . .  | 216 |
| 6.19 | The asymmetry at the first four Bragg peaks as a function of energy across the U $M_{IV}$ edge, showing results from several different structural and magnetic models. . . . .  | 217 |
| 6.20 | Profiles of the induced uranium magnetic moment, for the case of a simple bilayer structure and one containing alloyed interfaces. An idealised profile similar to that proposed by Laref et al. [2] is shown for comparison. . . . .   | 218 |

---

|      |  |     |
|------|--|-----|
| 6.21 | Density profile of the uranium present in sample SN71 from the fitted simulation to the X-ray resonant charge reflectivity data and the magnetic profile determined from the simulation of the asymmetry data. . . . . | 219 |
| 6.22 | Four example energies of the 17-energy mesh describing the X-ray resonant charge reflectivity (upper panels) and the asymmetry (lower panels). . . . .   | 221 |
| 6.23 | The asymmetry at the first four Bragg peaks as a function of energy across the U $M_{IV}$ edge. The fitted simulation of an alloyed interfacial model is shown in red. . . . .   | 222 |
| 6.24 | The profile of the induced U 5f moment determined from the fitted simulation of the asymmetry data, modelling the structure with alloyed interface regions. . . . .  | 223 |

# List of Tables

|     |  |    |
|-----|--|----|
| 2.1 | Shown above are the common classifications for multilayers according to the crystalline structure and orientation of respective layers . . . . .   | 5  |
| 3.1 | The table above provides a summary of important physical properties [3] for the elements and compounds concerned in all of the multilayer systems described within this thesis. Ar/Mr represents the relative atomic/molecular mass. . . . . | 27 |
| 3.2 | The table above provides a summary of the most common bulk structures of the elements used in our multilayer systems . . . . .   | 28 |
| 3.3 | This table provides a summary description of the nominal sample compositions for the U/Fe series of samples considered within this thesis. Thicknesses are quoted in Å. . . . .  | 29 |
| 3.4 | The nominal growth of the U/Co series of samples provides a basis to study thickness and temperature dependent effects on the quality, structure and magnetic response of the multilayers. . . . .   | 30 |
| 3.5 | This table represents the initial U/Gd series, used primarily to investigate the dependence of the multilayer properties on the relative thickness of the individual layers. . . . .   | 31 |
| 3.6 | This U/Gd series looks more closely at thin U and Gd layers, whether quality rare-earth/actinide multilayers can be grown with thin layers and the effect on the gadolinium Curie temperature. . . . .                                       | 31 |

- 3.7 This U/Gd series of samples was grown to look at changes in the magnetic coupling mechanism of the gadolinium layers as the thickness of the uranium spacer layer is varied and to profile any magnetisation within the U layers. . . . . 32
- 4.1 This table summarises the thicknesses,  $t$  ( $\text{\AA} \pm 2\text{\AA}$ ) and roughness values  $\sigma$  ( $\text{\AA} \pm 1\text{\AA}$ ) for the U/Fe series of samples, describing iron layers comprised of three components,  $t_{\text{Fe}}$  permitting.  $\sigma_{\text{Fe}}$  is the roughness of the top of the iron layer and  $\rho_{\text{U}}$  is the average density of the uranium layer  $\times 10^{28}\text{U/m}^3$ . . . . . 57
- 4.2 This table summarises the thicknesses,  $t$  ( $\text{\AA} \pm 2\text{\AA}$ ) and roughness values  $\sigma$  ( $\text{\AA} \pm 1\text{\AA}$ ) for the U/Co series of samples, describing cobalt layers comprised of two components,  $t_{\text{Co}}$  permitting.  $\sigma_{\text{Co}}$  is the roughness of the top of the cobalt layer and  $\rho_{\text{U}}$  is the average density of the uranium layer  $\times 10^{28}\text{U/m}^3$ . . . . . 59
- 4.3 This table summarises the thicknesses,  $t$  ( $\text{\AA} \pm 2\text{\AA}$ ) and roughness values  $\sigma$  ( $\text{\AA} \pm 1\text{\AA}$ ) for the U/Gd series of samples.  $\rho_{\text{U}}$  and  $\rho_{\text{Gd}}$  are the average density of the uranium and gadolinium layers  $\times 10^{28}\text{U/m}^3$  respectively. . . . . 63
- 4.4 This table summarises the thicknesses,  $t$  ( $\text{\AA} \pm 2\text{\AA}$ ) and roughness values  $\sigma$  ( $\text{\AA} \pm 1\text{\AA}$ ) for the U/Gd series of samples.  $\rho_{\text{U}}$  and  $\rho_{\text{Gd}}$  are the average density of the uranium and gadolinium layers  $\times 10^{28}\text{U/m}^3$  respectively. . . . . 65
- 4.5 This table summarises the thicknesses,  $t$  ( $\text{\AA} \pm 2\text{\AA}$ ) and roughness values  $\sigma$  ( $\text{\AA} \pm 1\text{\AA}$ ) for the U/Gd series of samples.  $\rho_{\text{U}}$  and  $\rho_{\text{Gd}}$  are the average density of the uranium and gadolinium layers  $\times 10^{28}\text{U/m}^3$  respectively. . . . . 67
- 4.6 This table summarises the different structural properties of multilayer thin films that can be investigated, using X-ray diffraction ( $t$  is the mean crystallite size). It should be noted that the thickness and composition of the layers can be probed for all sample types. . . . . 74

---

|      |   |     |
|------|---|-----|
| 4.7  | This table summarises the properties attributed to describe the crystal structure of the iron layers determined from fitted simulations to the experimental data. ( $\Delta d$ given in Å) . . . . .                          | 83  |
| 4.8  | This table summarises the properties attributed to describe the crystal structure of the cobalt layers determined from fitted simulations to the experimental data. ( $\Delta d$ given in Å) . . . . .                        | 85  |
| 4.9  | This table summarises the properties attributed to describe the crystal structure of both the uranium and gadolinium layers for U/Gd series 1, modelled as a near coherent superstructure. ( $\Delta d$ given in Å) . . . . . | 92  |
| 4.10 | This table summarises the properties attributed to describe the crystal structure of both the uranium and gadolinium layers for U/Gd series 2, modelled as a near coherent superlattice. ( $\Delta d$ given in Å) . . . . .   | 95  |
| 4.11 | This table summarises the properties attributed to describe the crystal structure of both the uranium and gadolinium layers for U/Gd series 3. ( $\Delta d$ given in Å) . . . . .   | 99  |
| 4.12 | This table summarises the uranium and gadolinium lattice parameters, determined by direct calculation from X-ray diffraction spectra for selected U/Gd samples. . . . .   | 100 |
| 5.1  | This table shows the units of magnetic quantities relevant to experimental methods used in this thesis, using both the CGS and SI conventions. . . . .  | 105 |
| 5.2  | The tabulated values above are those commonly accepted within the literature for the magnetic moments per atom and Curie temperatures for the elements in their bulk metallic form. . . . .                                   | 110 |
| 5.3  | Summary of the properties obtained from the parametrisation of the U/Fe hysteresis loops. . . . .   | 118 |
| 5.4  | Summary of the properties obtained from the parametrisation of the U/Co hysteresis loops. . . . .   | 122 |
| 5.5  | Summary of the absolute saturation magnetisation (normalised per unit area and to the number of bilayer repeats) and $M_s$ ( $\mu_B/\text{Gd}$ ), for all U/Gd samples measured. . . . .                                      | 126 |

|      |   |     |
|------|---|-----|
| 5.6  | Summary of the properties obtained from the parametrisation of the U/Gd hysteresis loops. Blanks have been left for those samples, which have not been measured with the field applied perpendicularly to the plane of the film. . . . .                              | 128 |
| 5.7  | Effective anisotropy values calculated for a selection of U/Gd multilayers. Those with constant U thickness of $\sim 25\text{\AA}$ have been used to deduce the respective surface and volume contributions. . . . .  | 135 |
| 5.8  | Summary of the input parameters used to simulate the polarised neutron reflectivity data, fitted using the xPOLLY [4] program. Table includes the asymmetric, three component iron layer model with values for the respective densities and magnetic moments. . . . . | 154 |
| 5.9  | Comparison of the averaged densities and magnetic moment values as determined from PNR, with those obtained using SQUID magnetometry and X-ray reflectivity techniques. . . . .   | 155 |
| 5.10 | Summary of the input parameters used to simulate the polarised neutron reflectivity data, fitted using the xPOLLY [4] program. Table includes values for the respective densities and magnetic moments for a two component cobalt layer system. . . . .               | 159 |
| 5.11 | Comparison of the averaged densities and magnetic moment values as determined from PNR, with those obtained using SQUID magnetometry and X-ray reflectivity techniques. . . . .   | 160 |
| 5.12 | Summary of the input parameters used to simulate the polarised neutron reflectivity data, fitted using the xPOLLY [4] program. Table includes values for the respective densities and magnetic moments. . .   | 166 |
| 5.13 | Comparison of the averaged densities and magnetic moment values as determined from PNR, with those obtained using SQUID magnetometry and X-ray reflectivity techniques. . . . .   | 167 |
| 6.1  | X-ray spectroscopic notation used to describe elemental energy levels.  | 171 |
| 6.2  | Electric dipole transitions for resonant energies, investigated during the course of this thesis. . . . .   | 176 |

- 
- 6.3 Induced U 5f orbital, spin and total magnetic moments, determined by XMCD for a selection of U/Fe multilayer samples. Results are shown, with and without the inclusion of the  $\langle T_z \rangle$  term for U 5f<sup>2</sup> and 5f<sup>3</sup> configurations. The measurements were made at 5K in an applied field of 10kOe, large enough to magnetically saturate the U moments. 188
- 6.4 Induced U 5f orbital, spin and total magnetic moments, determined by XMCD for a selection of U/Gd multilayer samples. Results are shown, with and without the inclusion of the  $\langle T_z \rangle$  term for U 5f<sup>2</sup> and 5f<sup>3</sup> configurations. The measurements were made at 5K in an applied field of 1T, large enough to magnetically saturate the U moments. . . 200

# Chapter 1

## Introduction

The growth and characterisation of uranium multilayers describes the general contents of this thesis, but the main purpose and drive of the following investigations has been to unravel the magnetic phenomena exhibited within these systems. The following introduction provides a brief insight into the common themes encountered within the vast and quickly developing field of thin film magnetism.

The general concepts behind studies into multilayer research involve low dimensionality, tuneability and interface interactions. The properties of a material can differ greatly from the bulk when reduced in size into the nanometre regime and varying the structural composition can be used to directly manipulate the electronic and magnetic behaviour of the respective elements. The interaction of these elements at the interfacial boundaries provides the mechanism for a whole range of interesting phenomena. Perpendicular magnetic anisotropy (PMA) [5] has been observed in Tb/Fe systems where the competing magnetic anisotropy terms lead to an alignment of the easy axis magnetisation perpendicular to the plane of the film. Giant magneto-resistance (GMR) [6] in Fe/Cr superlattices, caused by the antiferromagnetic alignment of the Fe layers produces large decreases in the resistance for relatively small applied magnetic fields. This alignment is manifest from the exchange coupling interaction, which has also been observed in a number of other systems [7]. These interaction properties have generated a great deal of interest in element specific magnetic characterisation, probing the hybridisation of electronic states of the constituent elements [8] and investigating induced polarisation effects [9].

A large proportion of these systems involve the combination of transition metal ferromagnets with other transition metals or metals from the rare-earth (lanthanide) series. Our intention has been to place the actinide element, uranium, in a magnetic environment and to systematically study the properties that such a system might exhibit. In order to grasp some possible outcomes of this endeavour it is necessary to look at similar systems.

Ce/Fe multilayers investigate the magnetic interaction of the 4f cerium electrons with the itinerant 3d band of iron [10]. This interaction produces some interesting magnetic results; an induced moment was found in the cerium layers, using X-ray magnetic circular dichroism (XMCD) [11] and PMA was observed for certain compositions [12]. These effects were predicted to be even more extreme with the inclusion of uranium instead of cerium, since the large orbital moment of uranium and its coupling to the lattice produces some of the largest known anisotropy in magnetic materials [13].

The UAs/Co system was investigated in the early 1990s by a group at the IBM Yorktown Heights Laboratories [14] and an induced moment was observed on the uranium site, using magneto-optic measurements [15]. The uranium magnetisation was not observable in polarised neutron reflectivity experiments, since the size of the magnetic splitting from the cobalt layers was too large for the smaller uranium moment to be distinguished [16]. X-ray magnetic circular dichroism measurements [17] were then employed to confirm the results obtained by Fumagalli et al.

The interests of this study lie in the use of uranium in multilayers with a view to manipulating the large orbital moment and spatial extent of the 5f electrons to provide unique magnetic interactions. In this vein, a program of research has been started, by first looking at U/Fe multilayers and carrying out a full structural and magnetic characterisation on a series of samples [18, 19]. This investigation continues the study of the U/Fe system. Initial bulk measurements on U/Co have been reported previously [20], but further characterisation of this system and a comprehensive study of the U/Gd system should provide a means to compare and contrast the electronic interactions of the uranium in each of these environments.

## 1.1 Thesis Outline

The thesis plan can be described in terms of several main objectives; to make and characterise actinide multilayers with well defined interfaces, to use X-ray and neutron scattering techniques to understand the electronic and magnetic properties, to investigate trends across the transition metal ferromagnets and to compare their behaviour with that of the 5f-4f U/Gd system [21].

The main drive of this project is to understand the fundamental interaction of the 5f uranium electrons in proximity to 3d and 4f ferromagnetic elements, so it is important to use techniques that are able to selectively probe the uranium layers within these systems. X-ray magnetic circular dichroism (XMCD) and X-ray magnetic resonant reflectivity (XRMR) can be used to directly investigate the magnetism of the uranium atoms, by tuning to absorption edges that probe the uranium electrons responsible for any observed magnetism. Both of these methods have previously been employed on the U/Fe system; the XRMR technique first uncovered an induced uranium magnetic moment [22], which was then studied systematically using XMCD [23]. The XMCD technique provides numerical values for the spin and orbital components of the total magnetic moment and can be used to give a magnetisation profile within the uranium layers indirectly, by comparison across a series of samples of varying layer thicknesses. XRMR can be used to directly measure the magnetisation profile [24].

An understanding of the magnetism within the uranium layers gives an indication as to the nature and extent of the hybridisation between the 5f uranium electrons and the 3d bands of the transition metals, iron and cobalt, or the 4f gadolinium electrons. This project not only sheds light on the electronic behaviour of uranium, but on the differences between respective transition metal ferromagnets and differences between 3d-5f and 4f-5f systems.

# Chapter 2

## Background

### 2.1 Multilayers

The term 'multilayers' encompasses an enormous range of different materials with various structures and a plethora of new, intriguing properties. The possibility of placing numerous elements in close proximity to one another and studying their electronic interactions, as both the structures and elemental properties are modified from the bulk, has opened up an entirely new field within condensed matter physics. This novel branch of nanotechnology began in the early 1980s and opened the ability to probe the fundamental nature of materials and manipulate electronic and magnetic properties in a very precise manner.

The quality, often determined by the sharpness of the interfaces and the smoothness of the layers, relies heavily on the method and conditions employed for the growth of the films. Common classifications for multilayers found in the literature can be summarised as in table 2.1. The variations in structure are not solely the product of the growth environment, but are also a consequence of the registry between close packed planes of atoms of the respective materials.

The motivation behind the majority of research into multilayer systems stems from the exhibition of properties significantly different from those observed in the bulk. Modifications to the bulk properties are caused by changes to the structure of the layers as a consequence of the low dimensionality, growth properties and strains at the interfaces. The modified structure can then have new static configurations

| Structure Type           | Definition  |
|--------------------------|---|
| Perfect epitaxial        | Single crystal in perfect registry with the single crystal substrate  |
| Nearly perfect epitaxial | Slight imperfections in crystal registry and in crystal substrate   |
| Textured epitaxial       | Layer consists of mosaic blocks that are in close registry to the substrate   |
| Textured polycrystalline | Distribution of crystalline grain sizes that have a random in-plane orientation with a preferred orientation out-of-plane |
| Perfect polycrystalline  | Crystallites of similar size and shape with a perfectly random orientation  |
| Amorphous                | No long range order   |

Table 2.1: Shown above are the common classifications for multilayers according to the crystalline structure and orientation of respective layers

and dynamic modes, which introduces band gaps in the dispersion relations of the fundamental excitations. Interface effects also make a large contribution to the electronic interactions, since the multilayer system provides a macroscopic sample comprised predominantly of interfacial regions. It is then possible for the electrons of one material to affect, or in some cases hybridise with those of the neighbouring layer, via either direct or indirect exchange mechanisms.

The physics of thin films incorporates a wide range of phenomena, but the majority of investment is in the study of superconductivity, semiconductor technologies and magnetic behaviour. This thesis is concerned only with the properties of magnetic multilayers. The low dimensional, layered structure allows for a variation in the magnitude and orientation of magnetic moments, which can be tailored by choosing certain structural parameters. In certain cases it is possible to have entirely different exchange constants, such that multilayers composed of alternating magnetic elements can result in an antiferromagnetic alignment of magnetic moments, seen on the surface of Gd [25] films and in Gd/Fe systems [26]. It is also possible to

affect the orientation and magnitude of the spin moments; reduced values of the magnetic moment have been seen in Gd/V [27] and Gd/Cr [28] systems, although the full moment has been observed in Gd/Fe [29] multilayers; it is not clear as to the mechanism for the Gd moment modification. It is also possible for some systems to exhibit PMA, where anisotropy fields are strong enough to orient the moments out of the plane of the film [30]. One of the most commonly used technological examples of multilayers benefits from the interaction of magnetic materials through non-magnetic, metallic spacer layers via long-range, indirect exchange coupling to give antiferromagnetically coupled repeat units with a period equivalent to double the chemical bilayer repeat distance, such as those found in Gd/Y systems [31]. This leads to the existence of high and low resistance states effectuated by small applied magnetic fields, resulting in the giant magnetoresistance (GMR) phenomenon. The largest of these affects has been observed in Fe/Cr [6] and Co/Cu [32] thin films, which are commonly used in magnetic read heads in hard disk drives.

This investigation is concerned with the electronic and magnetic interactions observable in multilayer systems, which include a magnetic component and a non-magnetic, metallic spacer layer, specifically the actinide element, uranium. The itinerant ferromagnets iron and cobalt, and the localised, rare-earth, ferromagnet, gadolinium will be used as the magnetic component.

## 2.2 Transition Metal Ferromagnets

The transition metals occupy the region of the periodic table in between the group IIA and IIIB elements. The first period of these elements has the  $[\text{Ar}]3d^n4s^2$  configuration and contains the ferromagnetic elements iron, cobalt and nickel. The magnetic electrons in this case are those in the partially filled, outer 3d band where the magnetic moments are a consequence of the unpaired electrons. Since these electrons are the furthest removed from the nucleus, they are relatively free to move through the solid and are not well described in a localised, atomic-like picture, but in an itinerant electronic framework [33].

The band theory of ferromagnetism was first proposed by Stoner [34] and Slater

[35]. This treatment allows the existence of a non-integral, net magnetic moment per atom by including an exchange energy that removes the degeneracy of the spin-up and spin-down half bands, a framework that is described in more detail in Chapter 5. The itinerancy of these band electrons stems from the overlap of the d orbitals and the strong s-d hybridisation between the 3d electrons and the s-p states of the conduction band [36]. In the context of magnetic multilayers, this delocalised electronic behaviour is evidenced in the hybridisation of the conduction band of the transition metal ferromagnet and the electronic states of the non-magnetic spacer layer. This direct exchange mechanism causes a polarisation of the spacer layer.

### 2.2.1 Iron

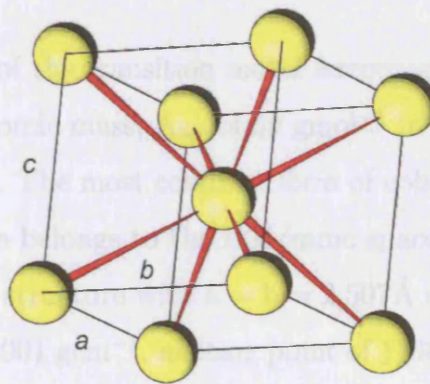


Figure 2.1: Body centred cubic structure of  $\alpha$ -Fe with  $a = b = c = 2.866\text{\AA}$ .

Iron is the first of the transition metal ferromagnets and has atomic number,  $Z = 26$ , a relative atomic mass,  $A_{\text{Mr}}$  of  $56 \text{ g mol}^{-1}$  in the bulk and an electronic configuration,  $[\text{Ar}]3d^64s^2$ . The most common form of iron found at ambient room temperature and pressure is  $\alpha$ -Fe, which belongs to the  $\text{Im-3m}$  space group and has a body centred cubic (bcc) crystal structure with  $a = b = c = 2.866\text{\AA}$ , figure 2.1. Iron has a density of  $7.874 \text{ g cm}^{-3}$ , melting point of  $1811\text{K}$ , an electrical resistivity of  $9.7 \times 10^{-8}\Omega\text{m}$  and an atomic radius of  $140\text{pm}$ .

In its alpha form, iron has a magnetic moment of  $\sim 2.2\mu_{\text{B}}/\text{Fe}$  and an ordering temperature,  $T_{\text{C}}$ , of  $1043\text{K}$  (Curie temperature).

### 2.2.2 Cobalt

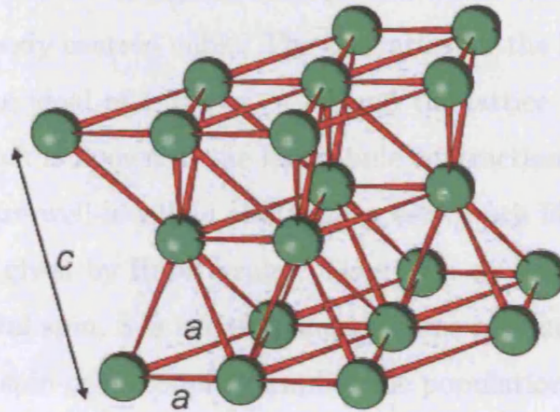


Figure 2.2: Hexagonal close-packed cobalt structure with  $a = b = 2.507\text{\AA}$  and  $c = 4.070\text{\AA}$ .

Cobalt is the second of the transition metal ferromagnets and has atomic number,  $Z = 27$ , a relative atomic mass,  $A_{\text{Mr}}$  of  $59\text{ gmol}^{-1}$  in the bulk and an electronic configuration,  $[\text{Ar}]3d^74s^2$ . The most common form of cobalt found at ambient room temperature and pressure belongs to the  $P63/mmc$  space group and has an hexagonal close-packed crystal structure with  $a = b = 2.507\text{\AA}$  and  $c = 4.070\text{\AA}$ , figure 2.2. Cobalt has a density of  $8.901\text{ gcm}^{-3}$ , melting point of  $1768\text{K}$ , an electrical resistivity of  $6 \times 10^{-8}\Omega\text{m}$  and an atomic radius of  $135\text{pm}$ .

In its hcp form, cobalt has a magnetic moment of  $\sim 1.8\mu_{\text{B}}/\text{Co}$  and a  $T_{\text{C}}$  of  $1388\text{K}$ .

## 2.3 Rare-earth Metals

The rare-earth or lanthanide metals are the period of elements which describe the filling of the 4f electron shell from lanthanum to lutetium. They are the first elements in the periodic table that have occupied 4f electron shells. The number of outer valence electrons remains unchanged (excluding Ytterbium) as the 4f electron shell is filled, resulting in very similar chemical properties across the period, although the magnetic characteristics can vary enormously. The majority of the heavy lanthanide elements, from Gd to Lu display the hexagonal close-packed crystal structure, while

the lighter rare-earth elements display a more varied range of crystal structures. La, Pr, Nd and Pm are double hexagonal close-packed, Ce is face-centred cubic, Sm is rhombic and Eu is body centred cubic. The  $c/a$  ratios for the hcp heavy rare-earths are reduced from the ideal of 1.633 by  $\sim 3\%$  and the lattice parameters reduce as the 4f shell fills, which is known as the lanthanide contraction.

The f electrons are well-localised and behave very much like those of a free ion, with a ground state given by Hund's rules. Thus for a specific electronic configuration the maximal total spin,  $S$  is adopted and then the maximum value of  $L$  for the given  $S$ . The strong spin-orbit coupling implies the population of the lowest lying  $J$  multiplet at 298K so that  $J = L \pm S$  for a more/less than half filled 4f electron shell.

The majority of the lanthanide elements exhibit crystal field effects, which consider the electric field produced at the 4f electrons due to changes in the local environment around a single ion. However, since gadolinium is a pure S state ion its charge cloud is completely spherical and yields no multipole moments.

The observed magnetisation is a consequence of the open-shell 4f electrons yet there is almost no direct overlap of the 4f wavefunctions. The large number of unusual magnetic structures exhibited by the rare-earth metals indicates that the interaction is a long-range, oscillatory, indirect one. This exchange is well-described by the Ruderman-Kittel-Kasuya-Yosida (RKKY) interaction, which includes the coupling of nuclear spins by the hyperfine contact interaction and the indirect coupling between electronic localised states through s-d s-f exchange with the conduction electrons.

### 2.3.1 RKKY Interaction

In this model, a magnetic moment located on a lattice site  $\mathbf{R}_n$ , interacts with the spin moments of the surrounding conduction electrons via an exchange interaction, creating a polarisation. This spin polarisation is then sensed by a second magnetic moment at a site  $\mathbf{R}'_n$ , which is also interacting with the conduction electrons. The resultant interaction energy of these two interacting moments is the RKKY interaction, which can take the form of an oscillatory exchange coupling, assuming a negligible spin-orbit interaction in the conduction band.

$$E_{RKKY} = -2J(\mathbf{R})\mathbf{S}_n \cdot \mathbf{S}'_n \quad (2.1)$$

where  $\mathbf{S}_n$  and  $\mathbf{S}'_n$  are the spins of the interacting magnetic moments and  $\mathbf{R} = \mathbf{R}_n - \mathbf{R}'_n$ .  $J(\mathbf{R})$  is related to the band structure of the metal and is dependent to a large extent on the Fermi surface.

$$J(\mathbf{R}) = \frac{1}{V^2} \sum_{\mathbf{k}} \sum_{\mathbf{k}'} |I(\mathbf{k}', \mathbf{k})|^2 \frac{f_{\mathbf{k}} - f_{\mathbf{k}'}}{E_{\mathbf{k}} - E_{\mathbf{k}'}} e^{i(\mathbf{k}' - \mathbf{k}) \cdot \mathbf{R}} \quad (2.2)$$

$V$  is the volume and the scattering elements,  $I(\mathbf{k}', \mathbf{k})$  are taken between electron states with wave vectors  $\mathbf{k}$  and  $\mathbf{k}'$  and energies  $E$  and  $E'$  for electron wavefunctions  $e^{i\mathbf{k} \cdot \mathbf{R}}$  and  $e^{i\mathbf{k}' \cdot \mathbf{R}}$ , where  $f_{\mathbf{k}}$  and  $f_{\mathbf{k}'}$  are the thermal occupation factors. However, this expression does not include a summation over multiple bands. A more complete treatment is given by Roth et al. [37].

A large body of experimental and theoretical evidence exists to support the RKKY mechanism of exchange coupling in rare-earth metals and it has been assumed that a similar magnetic coupling will be seen in rare-earth multilayers. In the multilayer geometry, the RKKY interaction couples atomic planes of parallel spins belonging to different layers of the magnetic metal. The total exchange coupling acting on a magnetic moment at a lattice site  $\mathbf{R}_n$  is then the sum over basal planes of the RKKY exchange coupling  $J_l(\mathbf{R}_n)$ , generated at the lattice point  $\mathbf{R}_n$  by an atomic layer  $l$ , of spins.

### 2.3.2 Gadolinium

Gadolinium is at the centre of the lanthanide period of metals and consequently, has an exactly half-filled 4f electron shell. It has a proton number,  $Z = 64$ , a relative atomic mass,  $A_{Mr}$  of  $157 \text{ gmol}^{-1}$  in the bulk and an electronic configuration,  $[\text{Xe}]4f^7 5d6s^2$ . The most common form of gadolinium found at ambient room temperature and pressure belongs to the P63/mmc space group and has an hexagonal close-packed (hcp) crystal structure with  $a = b = 3.631 \text{ \AA}$  and  $c = 5.777 \text{ \AA}$ , figure 2.3. Gadolinium has a density of  $7.901 \text{ gcm}^{-3}$ , melting point of  $1585 \text{ K}$ , an electrical resistivity of  $130 \times 10^{-8} \Omega\text{m}$  and an atomic radius of  $180 \text{ pm}$ .

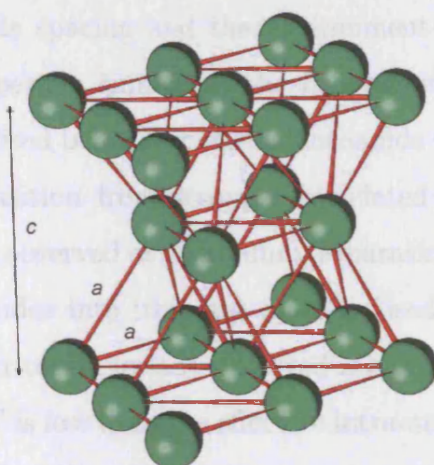


Figure 2.3: Hexagonal close-packed gadolinium structure with  $a = b = 3.631\text{\AA}$  and  $c = 5.777\text{\AA}$ .

Gadolinium has a magnetic moment of  $\sim 7.6\mu_{\text{B}}/\text{Gd}$  and a  $T_{\text{C}}$  of 292K [38]. Since there is no orbital contribution to the total moment, the theoretically expected value ought to be  $\sim 7\mu_{\text{B}}/\text{Gd}$ , considering only the 7 unpaired spins in the 4f electron shell. However, the experimentally observed saturation moment contains a contribution of  $\sim 0.6\mu_{\text{B}}/\text{Gd}$  from a polarisation of the conduction electrons. In the bulk, the easy magnetisation axis is parallel to the c-axis down to 232K, below this temperature the moments begin to cant away from the c-axis to a maximum canting angle of  $65^\circ$  at 180K and then reduce to  $32^\circ$  at lower temperatures.

## 2.4 Actinides

The actinide metals occupy the period of elements at the bottom of the periodic table from actinium to nobelium. These materials display a wide range of unique physical and chemical properties, mainly as a consequence of the unusual properties of their 5f electrons. Actinides are the rarest group of elements that exist within the periodic table, such that only thorium, actinium and uranium occur naturally within the Earth's crust.

The physics and chemistry of the actinides differ from the lanthanides due to the extended nature of the 5f wavefunctions. Depending on the specific actinide

element, the interactinide spacing and the environment within a compound, it is possible to observe properties similar to the itinerancy of transition metals and those similar to the localised behaviour of the lanthanide elements. Traveling across the period, a Mott transition from strongly correlated electronic interactions to weak correlations can be observed at plutonium, separating the electronic behaviour of light and heavy actinides into itinerant and localised respectively. In a Mott-Hubbard approach, the criterion for any observed magnetic ordering is simply if the 5f electron bandwidth,  $W$  is less than the effective intra-atomic Coulomb correlation,  $U_{\text{eff}}$ . For the light actinides,  $W > U_{\text{eff}}$  so that any magnetic ordering is forbidden.

### 2.4.1 Uranium

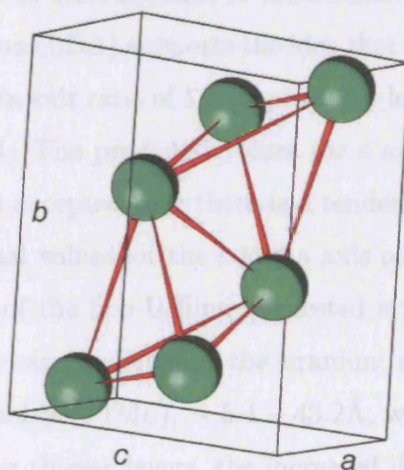


Figure 2.4: Orthorhombic  $\alpha$ -uranium structure with  $a = 2.854\text{\AA}$ ,  $b = 5.870\text{\AA}$  and  $c = 4.955\text{\AA}$ .

Uranium is one of the light actinide metals and has a proton number,  $Z = 92$ , a relative atomic mass,  $A_{\text{Mr}}$  of  $238 \text{ gmol}^{-1}$  in the bulk and an electronic configuration,  $[\text{Rn}]5f^36d7s^2$ . The most common form of uranium found at ambient room temperature and pressure belongs to the  $\text{Cmcm}$  space group and has an orthorhombic crystal structure with  $a = 2.854\text{\AA}$ ,  $b = 5.870\text{\AA}$  and  $c = 4.955\text{\AA}$ , figure 2.4. Uranium has a density of  $19.050 \text{ gcm}^{-3}$ , melting point of  $1405\text{K}$ , an electrical resistivity of  $28 \times 10^{-8} \Omega\text{m}$  and an atomic radius of  $\sim 140\text{pm}$  in its metallic state.

The crystal structure of uranium undergoes three crystallographic transitions as the temperature is elevated. The structure takes on the orthorhombic  $\alpha$  form from low temperatures up to 961K where a tetragonal  $\beta$  phase is reached. At 1049K the uranium structure undergoes another transition to a bcc  $\gamma$ -U phase. This sequence of structures is only present in the bulk form, but it is possible to access unusual conditions when investigating the crystallinity of materials towards a two dimensional form and under pressures exerted by the proximity of other crystal structures. In the case of uranium, a hexagonal close-packed structure has been reported [39]. The uranium was grown on top of a bcc, tungsten (110 oriented) substrate and STM images described a hexagonal arrangement of atoms with a U-U distance of  $a = 3.5 \pm 0.5\text{\AA}$ , although a previous report by Molodtsov et al. [40] suggested a U-U distance of  $3.2\text{\AA} \pm 0.5\text{\AA}$ . A theoretical model [39], employing the local density approximation (LDA) supports the idea that an hcp-U crystal structure can be stabilised with a  $c/a$  axis ratio of 1.8, appreciably larger than the hard sphere, hcp model value of 1.633. The predicted values for  $c$  and  $a$  are  $5.35\text{\AA}$  and  $2.97\text{\AA}$  respectively, however it is accepted that there is a tendency for the LDA treatment to over-bind and the actual values for the  $c$  and  $a$  axis parameters may be larger.

The reported growth of the hcp-U film, suggested a Stranski-Krastanov island growth, caused by lattice strains between the uranium and tungsten respectively, of between 2 and 16 monolayers (ML),  $\sim 5.4 - 43.2\text{\AA}$ , with a variation in density, size and island height. For thicker layers, the increased density of islands produces a closed film, but with a stacking that is prone to dislocations. These dislocations then promote the possible adsorption of oxygen and water contaminants.

### 2.4.2 Electronic Properties

In order to understand the electronic interactions, which might take place in uranium/transition metal or uranium/rare-earth systems it is important to grasp current theories that attempt to describe the nature of the uranium electrons. The electronic configuration can be represented  $[\text{Rn}]5f^36d^17s^2$ , describing a strongly bound radon core with electrons occupying more extended 5f, 6d and 7s shells. These more spatially extended electrons are responsible for the majority of the properties exhib-

ited by the uranium metal and are integral in forming bonds in uranium compounds. It is these electrons that will provide the basis for any interactions that may take place at a multilayer interface.

Theories have been proposed, which attempt to explain the extent of the actinide outer shell electrons. Since the descriptions vary, depending on the actinide element in question, those most relevant to uranium will be covered. Most of the major accepted theories fall into two categories: localised electron theories and itinerant ones. However, descriptions including features from both of these camps have also been proposed as intermediate electron theories.

### Localised Electron Model

The crystal field model is the most common theoretical treatment of electrons, which are well localised around their ions. In our case, a well localised 5f electron shell surrounding a uranium ion. This theory proposes that the intra-atomic potential is perturbed by an electrostatic potential formed from neighbouring ions and conduction electrons. Crystal field theory (CFT) only holds true if certain assumptions are made about the nature of the electronic interactions. Electrons in unfilled shells feel an electrostatic potential, which is provided by all of the charged particles within the crystal, but contributions from those localised on the ion in question are neglected. Electronic correlations between neighbouring ions are also neglected, implying that the potential will give rise to bound states that will produce sharp well-defined energy levels, which are narrow and atomic-like.

In metallic compounds of uranium and in the metal itself the 6d and 7s electrons form conduction bands of itinerant electrons. In this case, the large spatial extent of the 6d and 7s levels allow electron wavefunctions of neighbouring atoms to overlap, spreading the energy levels into bands of energy widths that increase with decreasing atomic separation. However, the f electron levels have a smaller spatial extent and can remain very atomic-like; especially true in the case of the rare earth, lanthanide elements. In order for the CFT to be valid, the energy gap between the 5f electron level and the bottom of the conduction band must be large compared to energies of the order of thermal fluctuations,  $E = k_B T$ . In the presence of these thermal energies

if the 5f electrons were sufficiently close to the conduction band in energy the CFT would not be able to determine the electronic configuration of a given magnetic ion.

The crystal field model has been shown to work extremely well for lanthanide elements and compounds, because the 4f electron levels are narrow and sit well below the electronic bands, but for the actinide elements this is not always the case.

There is both experimental and theoretical evidence that shows that this model cannot be applied to the light actinide elements (Th, U, Np, Pu). The itinerant nature of the 5f electrons of uranium and their proximity in energy to the 6d and 7s bands conflicts with the most important assumptions of the CFT.

### **Itinerant Electron Model**

In an itinerant view of electronic interactions the electron energy levels form broad bands. In the band model, electrons experience an average potential due to both the atomic nuclei and each other, neglecting any intra-atomic Coulomb correlations. The band model produces eigenstates, which are independent and single-particle, in direct opposition to the CFT, which results in states that are highly correlated, localised and many-particle.

The 6d and 7s actinide electrons can be treated in the band model due to the large overlap of the d and s orbitals on neighbouring atoms, but the nature of the 5f actinide electrons may be more accurately described by an intermediate model, neither entirely band-like nor entirely atomic-like.

For uranium and the remainder of the lighter actinide elements experimental evidence for an absence of any local magnetic moment would suggest that the 5f electrons are indeed itinerant and can be described as band-like. The spatial extent of relevant orbitals and the nearest neighbour atomic distances in these metals lead to an overlap of f orbitals between neighbouring atoms and to a hybridisation of the f and d orbitals. Theoretical band calculations by Freeman and Koelling [41] based on the relativistic augmented plane wave (RAPW) method, which include the spin-orbit coupling and other relativistic terms find that the uranium 5f band is  $\sim 1\text{eV}$  broad and is strongly hybridised with the 6d band, whereas the heavier actinides have extremely narrow bands with no evidence of hybridisation.

### 2.4.3 Binary Alloys

The energies involved in the sputtering process can lead to the formation of alloys, which may result in a range of observed compounds and properties. In this section, the binary alloy phase diagrams for the U-Fe, U-Co and U-Gd systems have been summarised.

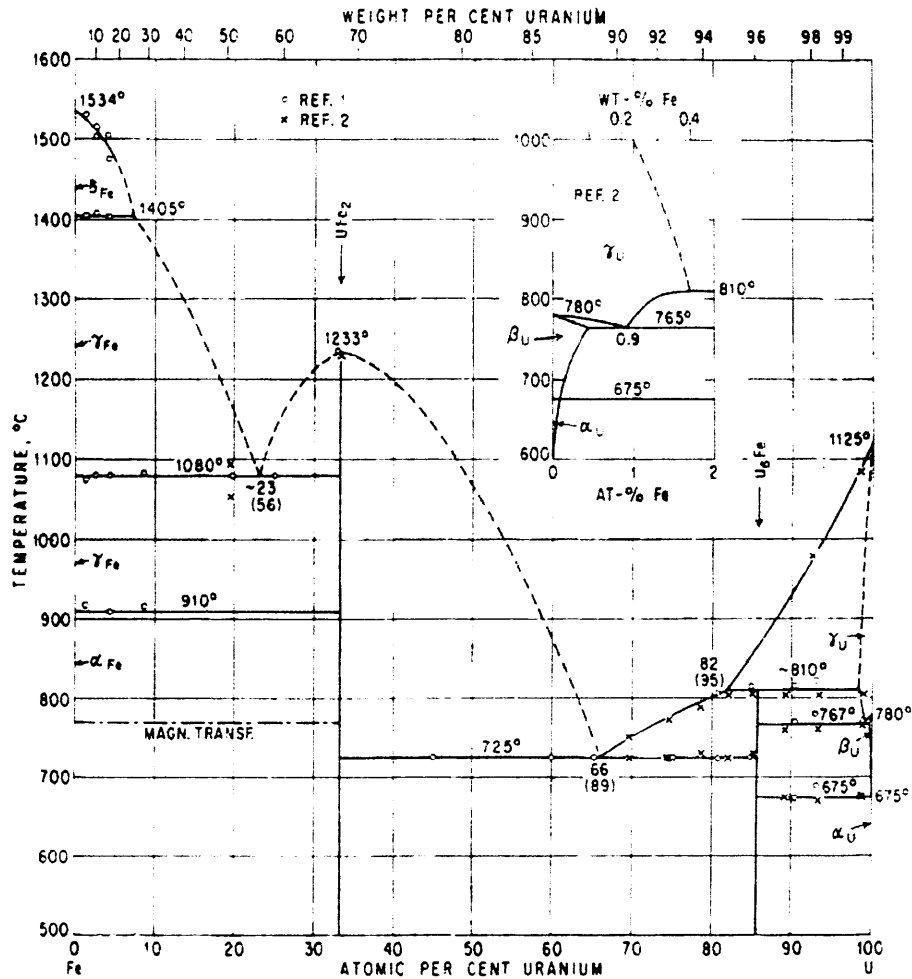


Figure 2.5: Phase diagram of the uranium, iron binary alloy system.

This system is characterised by the formation of two uranium compounds [42],  $\text{UFe}_2$  and  $\text{U}_6\text{Fe}$  at  $\sim 33\text{at.}\%$  and  $\sim 86\text{at.}\%$  U respectively. The maximal solubility of Fe in  $\gamma\text{-U}$  is reported as 1.5-2.0 at. % Fe with the eutectoid lying just below 1.0 at. % Fe. The solubility of Fe in  $\beta\text{-U}$  is 0.42 at. % Fe at 1038K, reducing to 0.06 % at 923K. The Fe solubility in  $\alpha\text{-U}$  is even lower with values approaching 0.005 at. % Fe.

The U-Co phase diagram closely resembles that of U-Fe [42] and shows the formation of three intermediate phases;  $\text{UCo}_2$  at  $\sim 33\text{at.}\% \text{Co}$ ,  $\text{UCo}$  at  $50 \text{ at. } \% \text{Co}$  and  $\text{U}_6\text{Co}$  at  $\sim 86\text{at.}\% \text{Co}$ .

There exists very little data on the phase diagram of the U-Gd system, but it is known that uranium and gadolinium are immiscible in the liquid state and that the solid solubility of Gd in  $\alpha\text{-U}$  is  $< 0.08 \text{ at. } \%$  [42].

It is possible to draw some comparisons between the electronic behaviour of the uranium compounds and the likely interactions at the interfacial region.

#### 2.4.4 Uranium Compounds

In the series of compounds between U and transition metals the best-known series is that of the Laves phase  $\text{UX}_2$  ( $\text{X} = \text{Fe}, \text{Co}, \text{Ni}$ ). Of these,  $\text{UFe}_2$  is ferromagnetic with moments on both the U and Fe sites [43] and a  $T_C$  of 165K; the moment on the Fe site is  $0.6\mu_B$ , but the U moment is very small since the spin and orbital components are of almost equivalent magnitude and directed opposite to one another.  $\text{UCo}_2$  is paramagnetic and  $\text{UNi}_2$  is a ferromagnet but with moments only on the U sites. This sequence of polarisation of the individual atoms was qualitatively explained by L. Severin et al. [44] in terms of band-structure calculations and the position of the transition-metal d band with respect to the Fermi surface,  $E_F$ . In the  $\text{UFe}_2$  system, there is a strong hybridisation, causing a mixing of 3d-5f states at the Fermi level. The larger Stoner integral of the iron then leads to a magnetisation dominated by the iron atoms. For  $\text{UCo}_2$  the 3d band is lower in energy, leading to a decrease in hybridisation and a reduced density of states in between the 3d and 5f bands. The extra electron in cobalt then places the Fermi level in this region so that  $\text{UCo}_2$  is paramagnetic. In  $\text{UNi}_2$  the separation in energy between 3d and 5f bands is increased still further and there is a reduction in 3d-5f hybridisation. The extra nickel electron moves the Fermi level into the region dominated by the 5f band, leading to a magnetic ordering in  $\text{UNi}_2$  dominated by the uranium electrons.

Although X-ray diffraction spectra and X-ray absorption near edge spectroscopy data have indicated that the presence of these binary compounds in our multilayers is unlikely, the hybridisation at the U/T interface may well be driven by the same

---

underlying physics. In the  $UT_2$  structure the inter-atomic distance between the U and T atoms is short, about  $3\text{\AA}$ , thus allowing direct overlap between the 3d and 5f states. This U-T distance is replicated at the multilayer interface.

# Chapter 3

## Fabrication

When planning an extensive program of experimental research it is important to consider certain implications with regards to sample growth. For the purpose of this project, a large number of samples were needed to study systematic, thickness dependent properties. The targets are metallic and need to be relatively easy to transfer so that several different systems can be studied. The DC magnetron sputtering technique is the most commonly adopted process for this type of investigation.

### 3.1 DC Magnetron Sputtering

In a basic description of the sputtering process, gaseous ions are bombarded against a target material, forming a glow discharge. Particles from the target then deposit onto a substrate, see figure 3.1. However, although this is the predominant process there are a large number of other events that can occur at the target surface, which can affect the growth of the films. *Secondary electron emission* results from the high negative potential of the sputtering target, which accelerates electrons away from the target, further ionising the neutral gaseous atoms and helping to sustain the glow discharge. At the same time, these secondary electrons also retain a substantial amount of energy, even after thermalising collisions in the gas, and this energy is dissipated at the substrate in the form of heat [45]. *Secondary ion emission* deals with the generation of both positive and negative ions at the target surface, but during the DC sputtering process, the large negative potential prevents the

escape of any positive ions formed and virtually no negative ions are produced in the case of inert gas bombardment of pure metal targets. *Reflection of incident particles* describes the neutralisation and subsequent reflection of bombarding ions toward the substrate. *Desorption of gases* can contaminate the sputtered film. Either adsorbed, chemisorbed or occluded gases are released from the target during sputtering. This effect can be overcome to some extent by sputter-cleaning the target prior to sample fabrication. *Ion implantation* occurs when the bombarding particles embed themselves in the target, becoming neutralised and trapped [46]. It is clear that there are many experimental considerations to take into account in order to optimise this process.

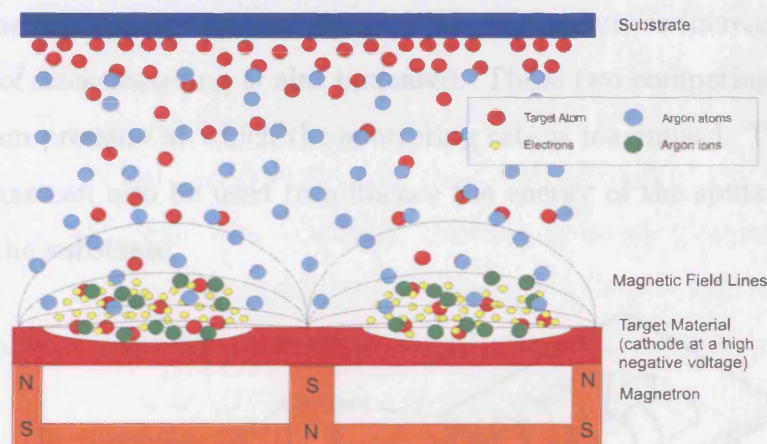


Figure 3.1: Schematic diagram of the sputtering process, including the magnetron plasma confinement.

The main growth chamber is kept under UHV conditions  $\sim 10^{-10}$  mbar to prevent sample contamination by residual gases. A gas of argon atoms at low pressure is fed into the main chamber.  $\text{Ar}^+$  ions are then formed by natural cosmic radiation, which are accelerated towards a cathode of target material at a negative potential of several hundred volts, supplied by a high-impedance dc power supply. During the bombardment process secondary electrons are produced, causing further ionisation of the gas, resulting in a self-sustaining dc glow discharge. A break through voltage provides a measure of the experimental parameters required to set up a glow discharge, primarily the conductivity of the gas and the electrode-substrate distance.

The number of atoms(molecules) per second per  $\text{cm}^2$  that are sputtered onto a substrate is known as the sputtering rate. Townes [47] gave one of the first calculations of the sputtering rate,  $j$ .

$$j = \frac{\pi j_0 \lambda}{2Sd} \quad (3.1)$$

In this case,  $j_0$  is the ejection rate from the target,  $\lambda$  is the mean free path of the sputtered atoms,  $S$  is the fraction of atoms that stick to the substrate and  $d$  is the distance from the cathode to the substrate surface.

The relationship between the power and the sputtering rate is a linear one, while there is a more complicated dependence on the gas pressure. The discharge current and hence the sputtering rate increases as the gas pressure is increased. However, the amount of backscattering is also increased. These two competing effects result in an optimum pressure at which the sputtering rate is maximised. The pressure of the sputter gas can also be used to influence the energy of the sputtered material, incident on the substrate.

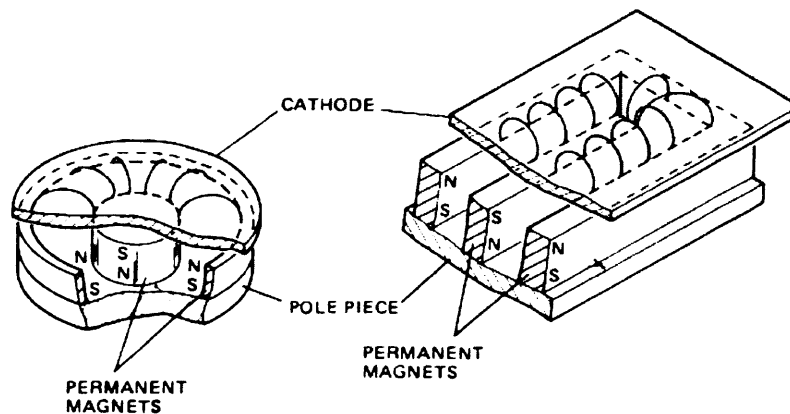


Figure 3.2: Two common geometries of the DC planar magnetron, used to confine the plasma of glow discharges close to the target material.

The rate and uniformity of the sputter deposition can be improved by confining the plasma of the dc glow discharge. The most common method for the confinement of the plasma is the use of permanent magnets below the cathode target, figure 3.2, which increases the rate of ionisation by secondary electrons. The electrons are trapped over the surface of the target in circular paths called cycloids, giving a

longer dwell time, causing a higher ionisation probability. This process is known as magnetron sputtering and can decrease the required ignition pressures for a stable plasma, by up to two orders of magnitude.

There are some disadvantages to this type of sputtering; the use of lower pressures to create the plasma means that there are fewer collisions between the gaseous atoms and the sputtered target material. The larger kinetic energy carried by the target material can cause re-sputtering of material from the substrate and embedding of one species into another.

A non-conducting target would lead to a charging of the surface from the bombardment of positive argon ions. The charged surface would shield the electric field and the ion current would extinguish, i.e. only conducting materials can be used in DC sputtering.

Contemplating the physical action of the sputtering process highlights that the sequence of events is not simply limited to the bombardment of the target and the adhering of target material to a substrate, although these are integral components. Once the target material has stuck to the substrate it is possible for further material to bombard and eject atoms from this newly formed layer or embed itself under the surface of the layer. The energies that these sputtered atoms/molecules possess allow a certain amount of diffusion to occur; this can be an advantage for crystalline self-assembly, but can also lead to diffusion between atomic species and interfacial disruption. The quality of multilayers is often ascribed by low values of layer roughness and interdiffusion.

There are two parameters that can be easily independently varied to control the diffusion between layers within a sample. The gas pressure and the substrate temperature can both be varied, affecting the kinetic energy of the incident target material and the energy available for crystalline assembly and interdiffusion respectively. The roughness of the layers, which is usually described as the root mean squared value of the variation in height of the top of the layer, can be affected by both of the variables described above, but is predominantly dependent on the choice of substrate and seed layer, and the lattice match between the different component elements. It is possible to grow high quality multilayers with well-defined interfaces,

by optimising all of the factors mentioned above.

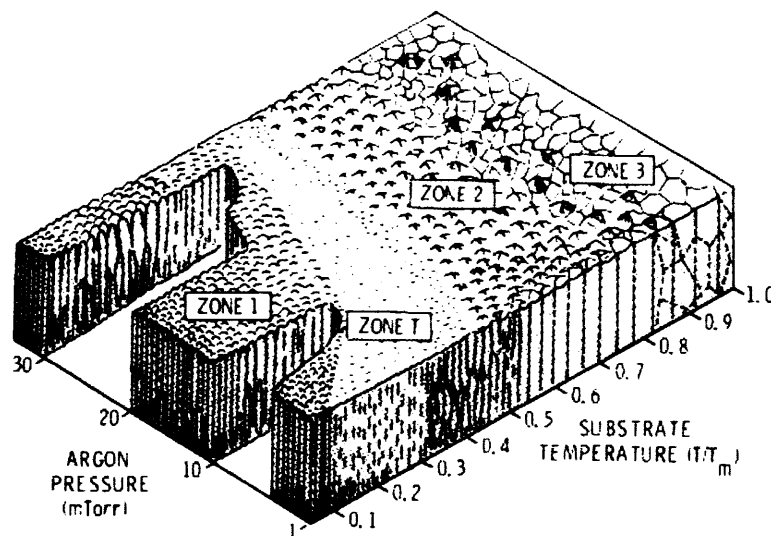


Figure 3.3: The likely crystal growth as a function of substrate temperature and argon gas pressure for sputtered metals [1].

A microstructural investigation of the crystal growth of sputter deposited materials has been carried out by Thornton [1], which gives a structure zone model for the affects of substrate temperature and gas pressure on the growth dynamics 3.3. This zonal description includes 4 regions of crystalline growth; zone 1 ( $T/T_m < 0.3$ ) represents a columnar structure with voided growth boundaries, where  $T_m$  is the melting point of the respective elements, zone 2 ( $0.3 < T/T_m < 0.5$ ) gives a growth of columnar grains with grain boundaries that increase in width as the temperature is increased. A transition zone (zone T in figure 3.3) exists between these first two zones that describes a region of poorly defined fibrous grains. The final high temperature region, zone 3 consists of equiaxed grains that increase in size as the temperature is elevated. In our case, for the majority of the samples which were sputtered at 300K,  $T/T_m$  lies in the range 0.17-0.21 in an argon pressure of  $5 \times 10^{-3}$ mbar or 3.76 mTorr, i.e the majority of the samples lie in the zone 1 region of microstructural growth.

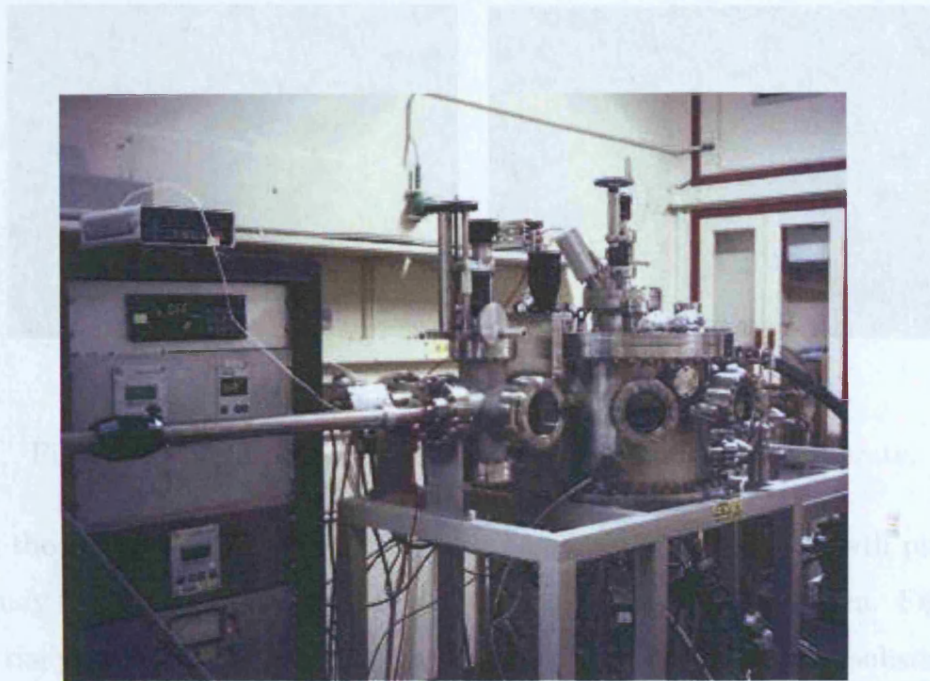
## 3.2 Experimental Set-up

The main components of the sputtering apparatus are shown figure 3.4 (a-c). This system is situated at the Clarendon Laboratory, Oxford, under the supervision of Dr. Roger Ward. The entire system is designed to be UHV compatible and the main chamber can reach working pressures of  $\sim 10^{-10}$  mbar. A vacuum gate separates the loading chamber from the main chamber to allow removal and replacement of samples, while simultaneously keeping vacuum in the main chamber.

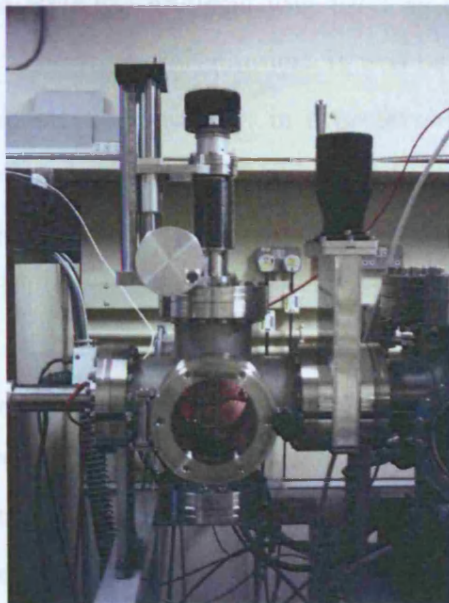
When loading samples, the vacuum gate is closed and the pump to the loading chamber is turned off. Nitrogen is fed into the chamber to inhibit the influx of any air or water molecules so that substrates can be loaded and unloaded. The substrates are fixed tightly onto metal discs with a rebate designed to accommodate the precise sample sizes. Once the loading chamber has been pumped back to vacuum the vacuum gate is opened and the insertion rod is used to manipulate the sample disc into position in the main chamber. A cradle is raised to take the sample disc and set at a height of  $\sim 10$ cm above the sputtering guns. There are three guns in the sputtering chamber to allow for a buffer and cap to be added to the two-component, multilayer system. The vacuum gate is closed before the argon gas is fed in at a pressure of  $5 \times 10^{-3}$  mbar. The guns are then ignited, by applying negative potentials of several hundred volts to the targets, which produces a self-sustaining glow discharge, confined by a planar magnetron. Shutters above the guns are controlled electronically, using a purpose-made Labview program to grow selected samples. This is achieved by simply applying a selected shutter sequence, with layer thicknesses chosen by calculating opening times from calibrated sputtering rates.

Before growing any series of samples the targets were checked for signs of wear caused by non-uniform sputtering; an unwanted side-effect of using a confined plasma. The targets were then sputter-cleaned to remove any surface gas deposits or impurities.

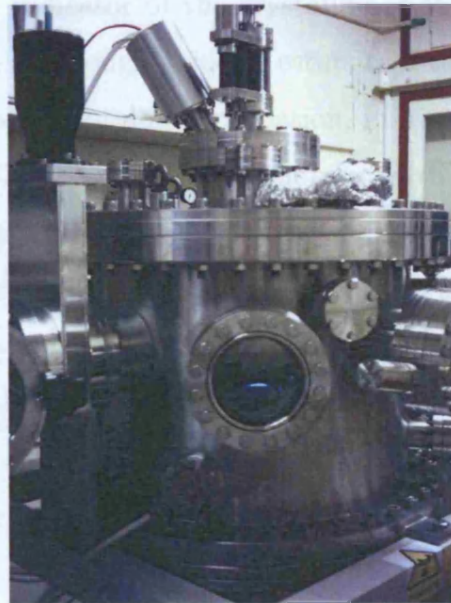
A reflection high energy electron diffraction (RHEED) apparatus proved to be a useful addition to the sputter system, since it was possible to monitor the crystallinity through the multilayer stack in-situ. Although this could not be observed



(a) insertion rod



(b) loading chamber



(c) main chamber

Figure 3.4: The photographs (a), (b) and (c) show the sputtering apparatus at the Clarendon Laboratory; the insertion rod, the loading chamber and the main sputter chamber respectively. A stable plasma can be seen through the window to the main chamber.

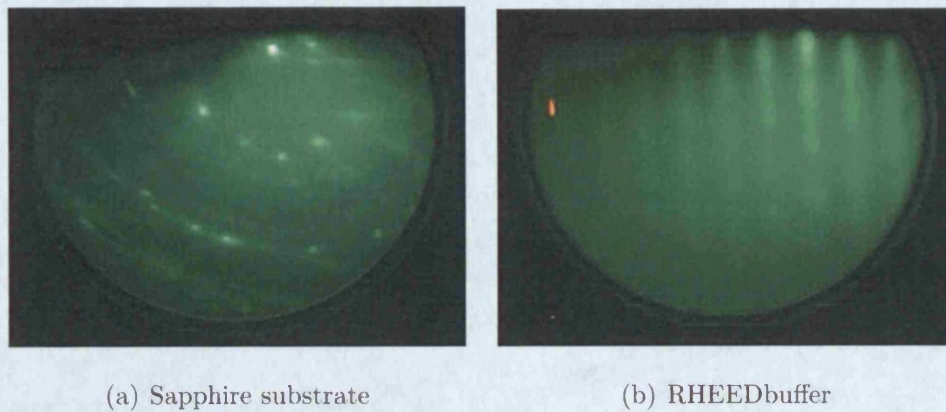


Figure 3.5: RHEED patterns observed from buffer and substrate.

during the actual sputter process it is still possible to pause the growth procedure and study the crystallinity of the surface of the last layer to be grown. Figure 3.5 shows the patterns observed from the surface of the epitaxial  $\text{Al}_2\text{O}_3$  substrate and the niobium buffer layer.

The RHEED analysis was used as an indicator of the crystalline growth only and in a very general manner. It was used as a rough guide to estimate if the metal was deposited epitaxially, in a preferred polycrystalline orientation, in a randomly oriented polycrystalline fashion or if the layer showed amorphous growth. These inferences could be made by rotating the sample stage and watching and changes in the RHEED pattern. If there is no pattern at all then it is likely that the layer has grown with a near amorphous structure, the presence of diffraction rings denotes the onset of polycrystalline growth and diffraction spots/streaks show a degree of preferred crystallographic orientation. As the growth becomes epitaxial the streaks (diffraction truncation rods) become more defined and move relative to the sample rotation.

### 3.3 Sample Composition

All of the samples considered in this study were grown on sapphire substrates. Sapphire is the compound  $\text{Al}_2\text{O}_3$ , and in this case is grown epitaxially in the  $[110]$  direction. The substrates are  $12\text{mm} \times 4.5\text{mm}$ , 1mm thick, highly polished and atomically flat. A niobium buffer layer of  $\sim 50\text{\AA}$  was used to seed the crystalline

growth of the bilayers. The usual preferred orientation of close-packed crystal structures is along the direction of the closest packed plane, which in the case of niobium, a body centred cubic structure (bcc), is the (110) plane. A study of epitaxial Nb films grown on a-plane sapphire in the [110] direction has been carried out by Hellwig et al. [48], which concentrates on the oxidation rates and processes for thin films of niobium. This study highlights the effect of increased temperature and atmospheric conditions, but states that at room temperature the oxide layer is stable and passivating, creating a protective layer of  $\sim 20\text{\AA}$  that does not expand by any significant margin over periods as long as one year.

| Material                       | Ar/Mr<br>(g/mol) | Density<br>(kg/m <sup>3</sup> ) | N<br>(atoms/m <sup>3</sup> $\times 10^{28}$ ) | melting point<br>(K) |
|--------------------------------|------------------|---------------------------------|---|----------------------|
| Nb <sub>2</sub> O <sub>5</sub> | 265.81           | 4600                            | 1.04  | 1460                 |
| Nb                             | 92.9             | 8570                            | 5.55  | 2750                 |
| U                              | 238.02           | 19050                           | 4.82  | 1405                 |
| Fe                             | 55.85            | 7874                            | 8.49  | 1811                 |
| Co                             | 58.93            | 8900                            | 9.09  | 1768                 |
| Ni                             | 58.69            | 8908                            | 9.14  | 1728                 |
| Gd                             | 157.25           | 7901                            | 3.02  | 1585                 |
| Al <sub>2</sub> O <sub>3</sub> | 101.96           | 4000                            | 2.36  | 2054                 |

Table 3.1: The table above provides a summary of important physical properties [3] for the elements and compounds concerned in all of the multilayer systems described within this thesis. Ar/Mr represents the relative atomic/molecular mass.

Initially, it is useful to tabulate the relevant properties of the elements and compounds concerned in the production of these multilayer samples and in order to understand the possible crystal structures and preferred crystallographic growth directions that might occur in thin film multilayer systems it is useful to recollect the observed structures in the bulk elements, tables 3.1, 3.2.

Tables 3.3, 3.4, 3.5, 3.6 and 3.7 contain lists of all of the samples considered in the experiments described in this work. The bilayers consist of varying thicknesses of the respective elements and a range of repeats. Each sample has been capped by

| Element | Z  | Common Structure | Space Group   |
|---------|----|------------------|---------------|
| Nb      | 41 | bcc              | Im-3m (229)   |
| U       | 92 | Ortho-rhombic    | Cmcm (63)     |
| Fe      | 26 | bcc              | Im-3m (229)   |
| Co      | 27 | hcp              | P63/mmc (194) |
| Ni      | 28 | fcc              | Fm3m (225)    |
| Gd      | 64 | hcp              | P63/mmc (194) |

Table 3.2: The table above provides a summary of the most common bulk structures of the elements used in our multilayer systems

a  $\sim 50\text{\AA}$  layer of niobium to prevent oxidation of the multilayer stack and a similar niobium buffer layer. The buffer is grown directly on the substrate, acting as a seed to improve the crystallinity of the multilayer stack, by intermediating the lattice mismatch of the sapphire and the multilayer.

In order to grow samples with layer thicknesses close to the nominal values listed in the following tables it was first necessary to calibrate the deposition rates of the sputter guns. Each target was sputtered for 500s onto a sapphire substrate, including a Nb buffer and cap. The thickness,  $t$  was determined by simulating the observed X-ray reflectivity, giving a deposition rate  $t/500$ , measured in  $\text{\AA}/s$ .

### 3.3.1 Uranium/Iron

This series of uranium/iron samples was fabricated as a continuation of the measurements carried out in an earlier study [18, 19] in order to further investigate the induced moment seen on the uranium atoms, using X-ray resonant magnetic reflectivity (XRMR) [22]. These samples differed from those studied previously, since they were grown on atomically flat, epitaxial, highly polished sapphire substrates as opposed to simple glass substrates. Modifications to the sputtering system included the use of a third sputter gun to allow the fabrication of multilayers with buffer and capping layers. The purpose of these improvements were primarily to reduce the layer roughnesses and improve the interfacial quality.

This series of samples was used to confirm the structural and magnetic charac-

| Sample Number | Nominal Description                                |
|---------------|--|
| SN71          | [U <sub>10</sub> /Fe <sub>30</sub> ] <sub>30</sub> |
| SN72          | [U <sub>30</sub> /Fe <sub>15</sub> ] <sub>10</sub> |
| SN73          | [U <sub>30</sub> /Fe <sub>15</sub> ] <sub>10</sub> |
| SN74          | [U <sub>30</sub> /Fe <sub>30</sub> ] <sub>30</sub> |
| SN75          | [U <sub>30</sub> /Fe <sub>30</sub> ] <sub>30</sub> |
| SN76          | [U <sub>30</sub> /Fe <sub>60</sub> ] <sub>20</sub> |
| SN77          | [U <sub>10</sub> /Fe <sub>10</sub> ] <sub>30</sub> |

Table 3.3: This table provides a summary description of the nominal sample compositions for the U/Fe series of samples considered within this thesis. Thicknesses are quoted in Å.

terisation results uncovered in earlier investigations and to further study the extent of the 5f-3d electronic hybridisation, by probing the uranium polarisation, discussed in Chapter 6. X-ray magnetic circular dichroism (XMCD) was used to give magnitudes of the uranium spin and orbital magnetic moments. The profile of the uranium magnetisation was inferred by a systematic layer thickness dependent investigation, using a combination of measurements carried out on previous U/Fe samples [49] and results from this new series. These samples were also used to make simulations of the uranium magnetisation profile from XRMR data. The distribution of the magnetisation within the iron layers was also investigated with these samples, using the polarised neutron reflectivity (PNR) technique.

### 3.3.2 Uranium/Cobalt

The uranium cobalt series of samples was grown with a range of systematics. For a constant number of bilayer repeats, the uranium layer thickness,  $t_U$  was varied for constant cobalt thickness,  $t_{Co}$  and vice versa. This allowed for a detailed structural and magnetic investigation. Selected samples were grown at elevated temperatures in order to observe any effects this may have on the structural and bulk magnetic properties.

A similar range of techniques was used to study the U/Co series of samples as

| Sample Number      | Nominal Description                   |
|--------------------|---------------------------------------|
| SN108              | $[\text{Co}_{30}/\text{U}_{30}]_{20}$ |
| SN109              | $[\text{Co}_{30}/\text{U}_{20}]_{20}$ |
| SN111              | $[\text{Co}_{30}/\text{U}_{10}]_{20}$ |
| SN112              | $[\text{Co}_{20}/\text{U}_{20}]_{20}$ |
| SN113              | $[\text{Co}_{20}/\text{U}_{15}]_{20}$ |
| SN114              | $[\text{Co}_{20}/\text{U}_{10}]_{20}$ |
| SN115              | $[\text{Co}_{10}/\text{U}_{10}]_{30}$ |
| SN116              | $[\text{Co}_{50}/\text{U}_{20}]_{20}$ |
| SN117 <sup>1</sup> | $[\text{Co}_{60}/\text{U}_{10}]_{15}$ |
| SN118 <sup>2</sup> | $[\text{U}_{10}/\text{Co}_{40}]_{20}$ |

Table 3.4: The nominal growth of the U/Co series of samples provides a basis to study thickness and temperature dependent effects on the quality, structure and magnetic response of the multilayers.

was used for the U/Fe series before. Both the magnetisation distribution within the Co layers and the 5f-3d hybridisation were probed for this system, using a combination of X-ray and neutron techniques. This system then provides a direct comparison between the extent of electronic interactions between the uranium and similar itinerant ferromagnets.

### 3.3.3 Uranium/Gadolinium

The initial series of uranium/gadolinium multilayers was grown to study the layer thickness dependence of the crystalline structure and the bulk magnetic properties. Due to the low gadolinium Curie temperature ( $\sim 292\text{K}$ ) relative to those of the 3d band ferromagnets, it was possible to investigate both the field and temperature

---

<sup>1</sup>The niobium buffer was grown at an elevated temperature of 1075K to promote epitaxial growth and the multilayer was sputtered at a temperature of 503K to encourage crystalline structure of the individual layers.

<sup>2</sup>This multilayer was grown at a temperature of  $\sim 500\text{K}$  on a niobium buffer layer of  $\sim 100\text{\AA}$ , which was sputtered at a temperature of 1075K

| Sample Number | Nominal Description                                |
|---------------|--|
| SN62          | Gd <sub>500</sub>                                  |
| SN63          | [U <sub>20</sub> /Gd <sub>30</sub> ] <sub>20</sub> |
| SN64          | [U <sub>20</sub> /Gd <sub>50</sub> ] <sub>20</sub> |
| SN65          | [U <sub>20</sub> /Gd <sub>70</sub> ] <sub>20</sub> |
| SN66          | [U <sub>30</sub> /Gd <sub>20</sub> ] <sub>20</sub> |
| SN67          | [U <sub>50</sub> /Gd <sub>20</sub> ] <sub>20</sub> |
| SN68          | [U <sub>70</sub> /Gd <sub>20</sub> ] <sub>20</sub> |

Table 3.5: This table represents the initial U/Gd series, used primarily to investigate the dependence of the multilayer properties on the relative thickness of the individual layers.

dependence of the magnetisation upon respective layer thickness.

| Sample Number      | Nominal Description                                |
|--------------------|--|
| SN119              | [Gd <sub>30</sub> /U <sub>20</sub> ] <sub>30</sub> |
| SN120              | [Gd <sub>60</sub> /U <sub>30</sub> ] <sub>20</sub> |
| SN121              | [Gd <sub>30</sub> /U <sub>10</sub> ] <sub>30</sub> |
| SN122              | [U <sub>10</sub> /Gd <sub>10</sub> ] <sub>30</sub> |
| SN123              | [U <sub>10</sub> /Gd <sub>20</sub> ] <sub>20</sub> |
| SN124 <sup>3</sup> | [U <sub>10</sub> /Gd <sub>20</sub> ] <sub>20</sub> |

Table 3.6: This U/Gd series looks more closely at thin U and Gd layers, whether quality rare-earth/actinide multilayers can be grown with thin layers and the effect on the gadolinium Curie temperature.

The SN119-124 series of U/Gd samples, table 3.6, was grown in order to look more closely at the structural and magnetic characteristics of very thin gadolinium layers, and of the difference in observed properties from multilayers grown at elevated temperatures (direct comparison between SN123 and SN124) and different sputtering powers.

<sup>3</sup>sample SN124 was grown at a temperature of  $\sim 600K$  - RHEED pattern showed a greater degree of epitaxy obtainable at an elevated temperature

| Sample Number | Nominal Description                                |
|---------------|--|
| SN134         | [U <sub>10</sub> /Gd <sub>15</sub> ] <sub>30</sub> |
| SN135         | [U <sub>15</sub> /Gd <sub>15</sub> ] <sub>30</sub> |
| SN136         | [U <sub>20</sub> /Gd <sub>15</sub> ] <sub>30</sub> |
| SN137         | [U <sub>30</sub> /Gd <sub>15</sub> ] <sub>30</sub> |
| SN138         | [U <sub>5</sub> /Gd <sub>15</sub> ] <sub>30</sub>  |
| SN139         | UGd alloy $\sim 1000\text{\AA} \sim 5\%U$          |

Table 3.7: This U/Gd series of samples was grown to look at changes in the magnetic coupling mechanism of the gadolinium layers as the thickness of the uranium spacer layer is varied and to profile any magnetisation within the U layers.

Since the XMCD signal from the uranium is small for the case of U/Gd multilayers, and the detection is in fluorescence yield it was necessary to grow films with very thin uranium layers. This series of U/Gd samples was fabricated with that in mind, so that a magnetisation profile of the induced uranium polarisation could be calculated from a layer thickness dependent study of the spin and orbital magnetic moments observed in the U layers. This series of samples also included the growth of an uranium-gadolinium alloy, made by co-sputtering the respective elements, which consisted of  $\sim 5\%$  uranium in a matrix of gadolinium atoms. This sample was grown to compare the induced uranium moment observed in this environment with that observed in U/Gd multilayers.

# Chapter 4

## Structural Characterisation

The main drive of this work is to investigate the nature of the electronic interactions between the uranium and the ferromagnetic layers, but in order to make sense of any of the measurements that can be used to probe this interaction it is important to have reasonable confidence in the structures of the samples that have been grown. There are generally two characteristic length scales of importance when considering the structural characterisation of multilayer thin films, these include the physical composition of the samples; layer thicknesses, roughness and interdiffusion (10 – 1000Å), and the crystalline structure within the layers (1 – 5Å). X-rays are the most common probe of these distances and have ideal wavelengths and penetration depths to study these systems.

### 4.1 X-rays

Since their discovery by William Roentgen in 1895, X-rays have become one of the most widely used probes in the investigation of the atomic structure of materials. X-rays have a range of wavelengths belonging to the broad spectrum of electromagnetic radiation, which have electric and magnetic fields perpendicular to their directions of motion and to each other. They are produced by the acceleration of electrons, most commonly in metal targets for laboratory sources, but also in vacuum at synchrotrons, required for the production of much brighter beams that can be tuned to provide X-rays with specific energies.

### 4.1.1 X-ray Sources

The two most common laboratory sources of X-rays are the X-ray tube and the rotating anode source. The former was developed by Coolidge in 1912 and uses the acceleration of electrons towards a water cooled metal anode as its source. X-ray radiation of this type has two main components; Bremsstrahlung radiation, which has a broad energy range and is caused by the deceleration of electrons as they reach the metal anode, and discrete fluorescent lines of radiation, caused by the excitation and subsequent relaxation of electrons within the inner electron shells of the metal atoms. The intensity of tube sources is then limited to the efficiency with which one can cool the metal anode and the incident X-ray energy is fixed so that the optimal experimental wavelength cannot be chosen at will. The rotating anode source is simply an adaptation of the simple tube, which allows the heat from the metal anode to be dissipated much more efficiently to give a higher intensity source.

For experiments which require tuneable energies, particular polarisation conditions and a large amount of incident flux the synchrotron is the most common modern source. Typically, synchrotron radiation is produced in storage rings, where electrons travel at relativistic speeds, moving through a series of straight and curved sections. The curved sections are comprised of bending magnets, which force the electrons to describe circular paths, generating X-rays. In the horizontal plane the radiation is linearly polarised, but by viewing the emitted radiation out of the orbit plane it is possible to produce circularly polarised X-rays of both left and right-handed helicities, depending on whether the X-rays are viewed above or below the orbit plane.

Technological advances have allowed the production of X-ray beams in a much more efficient way than just by using the circular arc of a bending magnet. It is also possible to insert devices into the straight sections of the storage ring that cause the electrons to execute oscillations in the horizontal plane, producing intense X-ray sources. These devices are often divided into two classes, wigglers and undulators: wigglers use an array of magnets to push the electrons through a series of circular arcs. The intensity is then the sum of the intensities from each wiggler. Undulators however, cause the electrons to execute small amplitude oscillations, resulting in

an intensity that is the square of the sum of the radiated wave amplitudes. One particular variation, the helical undulator, causes the electrons to travel in a helical path, which viewed by an observer becomes a circular polarisation.

The interaction of X-rays with matter is specifically attributed to their interaction with the electron density of a material. The typical wavelengths of the order  $\sim 1\text{\AA}$  make them a convenient probe to study the nature of materials on an atomic scale. The two main processes responsible for the interactions of X-rays are absorption and scattering.

### 4.1.2 X-ray Scattering

When X-ray photons interact with a large number of atoms, the scattering manifests itself in terms of refraction and reflection in a similar way to the nature of light scattering in materials of different refractive indices. Materials also have specific refractive indices concerning their interaction with X-rays, but deviate negatively from unity of order  $10^{-5}$ . To understand the phenomena we observe experimentally from the scattering of X-rays from bulk samples it is first necessary to grasp the way that an X-ray interacts with a single electron.

#### Scattering from an Electron

In a classical treatment, the electric field of the X-ray exerts a force on the charge of the electron, which in turn exerts a reactionary force, accelerating the scattered wave. In order to correctly describe this interaction it is necessary to form a quantum mechanical treatment, where the incident photon has energy proportional to its angular frequency  $\hbar\omega$  and a momentum  $\hbar k$ . This treatment allows for the inelastic scattering of electrons via an energy transfer mediated by a difference in frequency between the incident and scattered photons, which is known as Compton scattering. However, in most scattering events used to characterise the properties of materials and for the techniques considered in this report, the process is elastic. X-ray frequencies are  $10^{19}$  Hz and four orders of magnitude greater than the eigen frequency of a bound electron, which allows elastic scattering to be treated classically to first order, although a quantum mechanical account is still valid.

A measure of the elastic scattering process can be understood as the efficiency of the scattering from the particles in the sample and can be represented as the differential cross-section.

$$\left(\frac{d\sigma}{d\Omega}\right) = \frac{I\Delta\Omega}{I_0N\Delta\Omega} \quad (4.1)$$

$$\left(\frac{d\sigma}{d\Omega}\right) = \frac{I}{\Phi_0N\Delta\Omega} \quad (4.2)$$

The two situations represented here describe the experimental conditions; firstly, that the cross-sectional area of the incident beam is smaller than the sample and secondly, that the beam area is larger than the sample size. The first case is a ratio of the X-ray photons scattered per second,  $I$  (intensity) subtending a solid angle  $\Delta\Omega$ , to the intensity of the beam  $I_0$  incident on a sample of  $N$  scattering elements per unit area seen along the beam direction, subtending a solid angle  $\Delta\Omega$ . The second is a ratio of the X-ray photons scattered per second,  $I$  to the flux,  $\Phi_0$  of the incident beam subtending a solid angle  $\Delta\Omega$ . The differential cross-section is important since it is a quantity that can be derived theoretically and measured experimentally.

### ***Quantum Mechanical Description***

The scattering process can be described using time-dependent perturbation theory in a quantum mechanical treatment [50] [51] [52] that characterises the interaction between sample and incident X-rays with an Hamiltonian  $H_I$ , producing transitions between initial and final combined states of the sample and X-ray field,  $|i\rangle$  and  $|f\rangle$ . For the case of elastic scattering it is necessary to include a delta function  $\delta(\varepsilon_f - \varepsilon_i)$  and to integrate over  $\varepsilon_f$ .

$$W = \frac{2\pi}{\hbar} \int \langle f|H_I|i\rangle^2 \rho(\varepsilon_f) \delta(\varepsilon_f - \varepsilon_i) d(\varepsilon_f) \quad (4.3)$$

In this instance  $W$  is the number of transitions per second between initial and final states and  $\rho(\varepsilon_f)$  is the density of states.

In an elastic scattering event, conservation of energy dictates that  $\varepsilon_i = \varepsilon_f$ . By enforcing periodic boundary conditions to the X-ray wavefunctions and with a volume,  $V$  for the total system the density of states can be calculated.

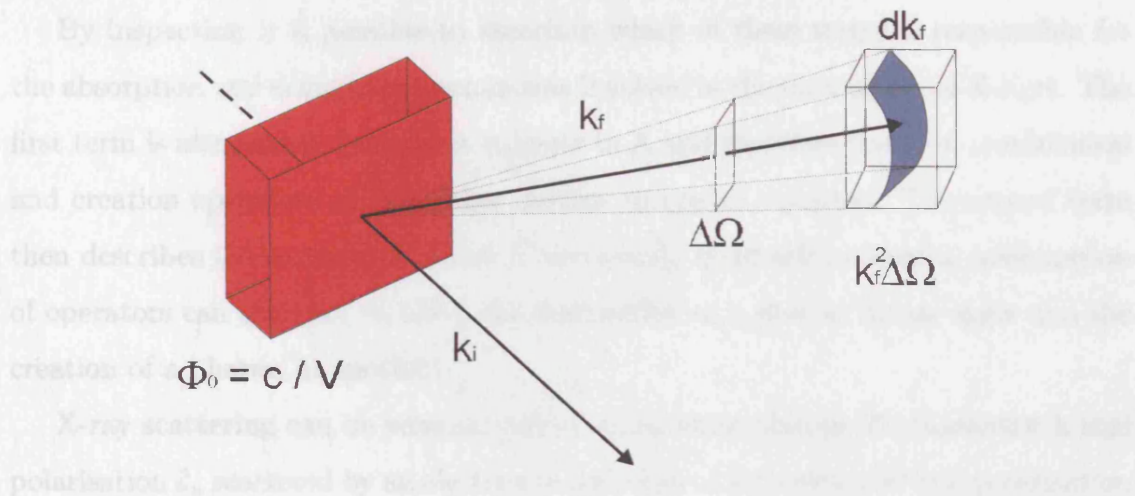


Figure 4.1: Representation of the quantum mechanical description of an elastic scattering event.

$$\rho(\varepsilon_f) = \frac{V}{8\pi^3} \frac{dk_f}{d\varepsilon_f} \quad (4.4)$$

Looking at Figure 4.1 the differential volume element can be replaced by the term  $k_f^2 dk_f \Delta\Omega$ . Since  $\varepsilon_f = \hbar k_f c$  and  $\Phi_0 = \frac{c}{V}$ , it is possible to simplify the differential cross-section, where  $W$  the number of transitions per second is equivalent to  $I$ .

$$\left(\frac{d\sigma}{d\Omega}\right) = \frac{W}{\Phi_0 \Delta\Omega} = \left(\frac{V}{2\pi}\right)^2 \frac{1}{\hbar^4 c^4} \int \langle f | H_I | i \rangle^2 \varepsilon_f^2 \delta(\varepsilon_f - \varepsilon_i) d(\varepsilon_f) \quad (4.5)$$

A quantum mechanical treatment of the sample and the electromagnetic field is necessary to fully describe the absorption or scattering of an X-ray, which relies on specifying both the non-interacting ( $H_0$ ) and perturbing ( $H_I$ ) Hamiltonians. The total Hamiltonian  $H = H_0 + H_I$  and  $H_0 = H_e + H_{rad}$ , where  $H_e = \frac{p^2}{2m}$ . The total Hamiltonian can be written as,

$$H = \frac{(\mathbf{p} + e\mathbf{A})^2}{2m} + H_{rad} \quad (4.6)$$

So expanding the first term gives,

$$H_I = \frac{e\mathbf{A} \cdot \mathbf{p}}{m} + \frac{e^2 A^2}{2m} \quad (4.7)$$

By inspection it is possible to ascertain which of these terms is responsible for the absorption and scattering mechanisms involved in the interaction of X-rays. The first term is absorption, because it is linear in  $A$  and therefore linear in annihilation and creation operators so can either destroy or create a photon. The second term then describes the scattering, which is necessarily quadratic so that a combination of operators can then act to allow the destruction of a photon in one state and the creation of a photon in another.

X-ray scattering can be summarised as an incident photon of wavevector  $\mathbf{k}$  and polarisation  $\hat{\epsilon}_u$  scattered by an electron to a photon of wavevector  $\mathbf{k}'$  and polarisation  $\hat{\epsilon}_v$ . When the situation is elastic, energy is conserved so that  $\hbar\omega = \hbar\omega'$  and the electron occupies its ground state  $|p\rangle$ . The interacting Hamiltonian term in the differential cross section can then be determined by evaluating the matrix element of the scattering term in equation (4.5).

$$\langle i|H_I|f\rangle = \frac{e^2}{2m\epsilon_0 V} \frac{[\hat{\epsilon}_u \cdot \hat{\epsilon}_v]}{(\omega\omega')^{1/2}} \langle p|e^{i(\omega-\omega')t} e^{i(\mathbf{k}-\mathbf{k}')\mathbf{r}}|p\rangle \quad (4.8)$$

Since the X-ray energy in the final state  $\epsilon_f \equiv \hbar\omega'$ , the differential cross-section can be rewritten in terms of the angular velocity, which via the substitution of the matrix element evaluated for the initial and final states of the scattered photon provides the Thomson scattering cross-section.

$$\left(\frac{d\sigma}{d\Omega}\right) = \left(\frac{e^2}{4\pi\epsilon_0 mc^2}\right)^2 [\hat{\epsilon}_u \cdot \hat{\epsilon}_v]^2 |f(\mathbf{Q})|^2 \quad (4.9)$$

The first term is the square of the Thomson scattering length,  $r_0$ , the second term is the polarisation,  $P$  and the final term is the squared modulus of the form factor, where  $f(\mathbf{Q}) = \langle p|e^{i\mathbf{Q}\cdot\mathbf{r}}|p\rangle$ . It is possible to derive an equivalent result for the Thomson scattering cross-section from a classical standpoint.

### ***Classical Description***

In a classical description of X-ray scattering the electric field,  $\mathbf{E}_{\text{in}}$  of an incident plane wave causes an electronic charge distribution to oscillate, radiating a wave in all directions, which is then evaluated at a position  $X$ , a distance  $R$  and at an

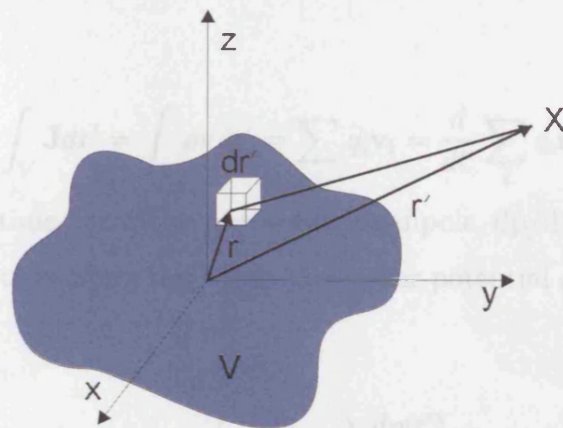


Figure 4.2: Coordinate system used to represent the electromagnetic field radiated from an oscillating electronic charge distribution under the influence of an incident plane wave.

angle  $\theta$  from the electron, see Figure 4.2. This can be simplified by making certain assumptions; the distance  $r$  must be larger than the spatial extent of the charge distribution and the wavelength of the radiation, while the charge distribution is treated as being formed by free electrons.

$$\mathbf{E} = -\nabla\Phi - \frac{\partial\mathbf{A}}{\partial t} \quad (4.10)$$

$$\mathbf{B} = \nabla \times \mathbf{A} \quad (4.11)$$

$\mathbf{E}$  and  $\mathbf{B}$  represent the electric and magnetic fields respectively. Since the X-ray is a transverse electromagnetic wave then these terms are perpendicular to one another and to the direction of propagation. The vector potential  $\mathbf{A}$  is given by,

$$\mathbf{A}(\mathbf{r}, t) = \frac{1}{4\pi\epsilon_0 c^2} \int_V \frac{\mathbf{J}(\mathbf{r}', t - \frac{|\mathbf{r}-\mathbf{r}'|}{c})}{|\mathbf{r}-\mathbf{r}'|} d\mathbf{r}' \quad (4.12)$$

Assuming  $\mathbf{r} \gg \mathbf{r}'$  then,

$$\mathbf{A}(\mathbf{r}, t) \approx \frac{1}{4\pi\epsilon_0 c^2 r} \int_V \mathbf{J}(\mathbf{r}', t - \frac{r}{c}) d\mathbf{r}' \quad (4.13)$$

For a distribution of discrete charges  $q_i$  the integral can be replaced by a sum, where the current density  $\mathbf{J} = \rho\mathbf{v}$ , the product of the charge density and the velocity

respectively.

$$\int_V \mathbf{J} d\mathbf{r}' = \int_V \rho \mathbf{v} d\mathbf{r}' = \sum_i q_i \mathbf{v}_i = \frac{d}{dt'} \sum_i q_i \mathbf{r}'_i \quad (4.14)$$

This term is the time derivative of the electric dipole,  $dp/dt$ . By linearly polarising the incident photons along the z-axis the vector potential can then be rewritten for a single dipole,

$$A_z = \left( \frac{1}{4\pi\epsilon_0 c^2 r} \right) \frac{dp(t')}{dt} \quad (4.15)$$

Using equation (4.11), in the far field limit,

$$\mathbf{B} = \left( \frac{1}{4\pi\epsilon_0 c^2} \right) \frac{1}{cr} \frac{d^2 \mathbf{p}(t')}{dt^2} \times \hat{\mathbf{r}} \quad (4.16)$$

Evaluating the cross product in equation (4.16) and noting that the electric field is perpendicular to both the magnetic field and to the unit vector,  $\hat{\mathbf{r}}$ , it is possible to extract an expression for the electric field at an observation angle,  $\phi$ . The second derivative of the electric dipole moment can also be defined in terms of the incident electric field to give the ratio of radiated and incident electric fields.

$$E(t) = - \left( \frac{1}{4\pi\epsilon_0 c^2} \right) \frac{1}{r} \frac{d^2 p(t')}{dt^2} \cos \phi \quad (4.17)$$

$$\frac{E(t)}{E_{in}(t)} = - \left( \frac{e^2}{4\pi\epsilon_0 mc^2} \right) \left( \frac{e^{ikr}}{r} \right) \cos \phi \quad (4.18)$$

The first term is the Thomson scattering length,  $r_0$ , and the  $\cos \phi$  term is central to the origin of the polarisation factor in X-ray scattering. The negative sign leading the ratio of the incident and radiated electric fields indicates the  $\pi$  phase-shift between the incident and scattered photons.

$$\left( \frac{d\sigma}{d\Omega} \right) = r_0^2 P \quad (4.19)$$

In a synchrotron the electrons orbit in a horizontal plane, which means that the X-ray photons are linearly polarised in this same plane so the polarisation factor takes different forms depending on which scattering geometry is used. In a horizontal

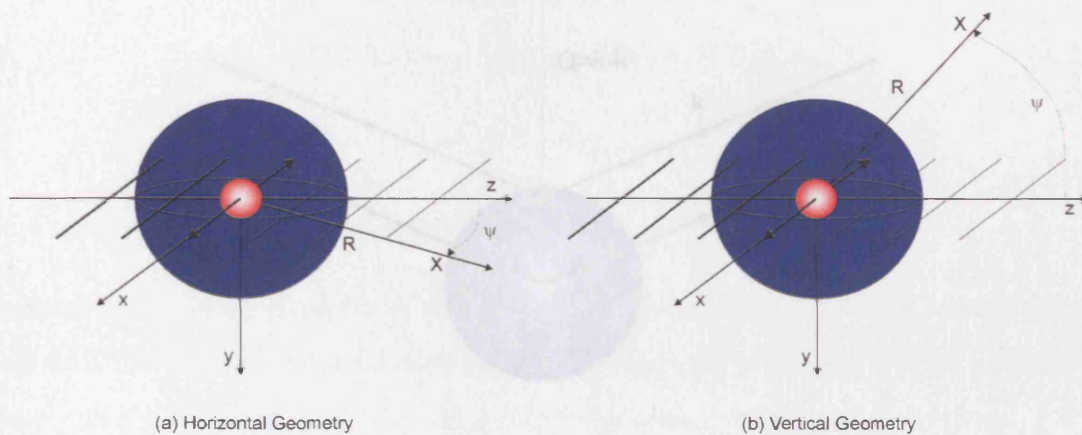


Figure 4.3: Description of the elastic scattering of an X-ray photon from an atom

Figure 4.3: Radiated field from an oscillating electron in the field of an incident plane wave with the observation point, X (a) in the plane of the incident wave polarisation and (b) in the plane perpendicular to the incident wave polarisation.

scattering geometry  $P = \cos^2 \psi$  Figure 4.3(a) and in the vertical geometry  $P = 1$  Figure 4.3(b), so that the full acceleration is observed at all scattering angles. At an unpolarised source  $P = \frac{1}{2}(1 + \cos^2 \psi)$ .

### Scattering from an Atom

So far we have only dealt with the interaction of X-rays with an electron, but in order to understand the observed results from bulk samples it is necessary to extend the approach to treat the scattering from an atom and then to a collection of atoms, which can take the form of a molecule or a crystal.

The quantum mechanical description of the X-ray photon momentum still allows for the transfer of momentum even in an elastic scattering event, leading to the definition of the wavevector transfer,  $\mathbf{Q}$ .

$$\hbar\mathbf{Q} = \hbar\mathbf{k} - \hbar\mathbf{k}' \quad (4.20)$$

In this case  $|\mathbf{k}| = |\mathbf{k}'|$  and on inspection of Figure 4.4  $|\mathbf{Q}| = 2|\mathbf{k}|\sin\theta$ .

It is possible to extend the classical approach adopted earlier to an atom of  $Z$  electrons, by describing the charge distribution by an electron density,  $\rho(\mathbf{r})$ . The

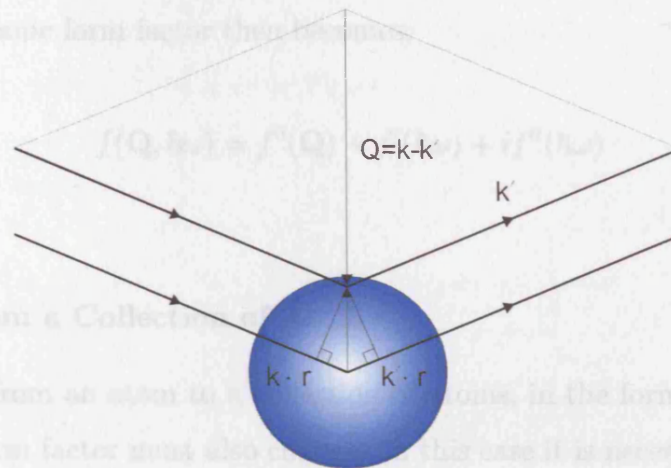


Figure 4.4: Description of the elastic scattering of an X-ray photon from an atom and the definition of the wavevector transfer,  $\mathbf{Q}$ .

total scattering length for an atom is the product of the Thomson scattering and the atomic form factor  $f^0(\mathbf{Q})$ , which is the Fourier transform of the electron density distribution.

$$f^0(\mathbf{Q}) = \int p(\mathbf{r})e^{i\mathbf{Q}\cdot\mathbf{r}}d\mathbf{r} \quad (4.21)$$

As the momentum transfer tends to zero the atomic form factor tends to  $Z$ , because the scattering from volume elements  $d\mathbf{r}$  is in phase. However, the scattering drifts further and further out of phase the greater the momentum transfer becomes. In most experiments involving the use of X-ray scattering the energies involved are in the relative vicinity of the discrete electronic energy levels within the atom and so it is necessary to include quantum mechanical considerations to completely describe the atomic form factor.

X-ray photons have typical energies close to the binding energy of the innermost electrons, which are part of the tightly bound K shell. As the X-ray photon energy is reduced, the scattering length of the atom decreases and this is accounted for by the inclusion of an  $f'$  term in the form factor. However, an additional  $if''$  term is also added to include the energy dependent phase response, which is related to the absorption. These new terms are commonly known as the (anomalous) dispersion corrections and have very little  $\mathbf{Q}$  dependence, but vary with changing photon

energy. The atomic form factor then becomes,

$$f(\mathbf{Q}, \hbar\omega) = f^0(\mathbf{Q}) + f'(\hbar\omega) + if''(\hbar\omega) \quad (4.22)$$

### Scattering from a Collection of Atoms

In progressing from an atom to a collection of atoms, in the form of a molecule or unit cell, the form factor must also change. In this case it is necessary to label each atom  $j$  at a position  $\mathbf{r}_j$  and take the sum of the atomic form factors to give,

$$F(\mathbf{Q}) = \sum_{\mathbf{r}_j} f_j(\mathbf{Q}) e^{i\mathbf{Q}\cdot\mathbf{r}_j} \quad (4.23)$$

This factor is then further modified when considering a crystalline material where a unit cell of atoms is repeated periodically in space to form a lattice. This modification results in the inclusion of a lattice sum,

$$F(\mathbf{Q}) = \sum_{\mathbf{r}_j} f_j(\mathbf{Q}) e^{i\mathbf{Q}\cdot\mathbf{r}_j} \sum_{\mathbf{R}_n} e^{i\mathbf{Q}\cdot\mathbf{R}_n} \quad (4.24)$$

$\mathbf{R}_n$  are the lattice vectors and  $\mathbf{r}_j$  become the positions of the atoms with respect to the lattice position.

### 4.1.3 Photoelectric Absorption

When an atom absorbs an X-ray photon, an electron is ejected to leave the atom ionised. This can be quantified by an absorption coefficient  $\mu$ , where the intensity of the X-ray beam at a depth  $z$ , can be represented as,

$$I(z) = I_0 e^{-\mu z} \quad (4.25)$$

The absorption coefficient can then be determined experimentally from the ratio of intensities of the X-ray beam with and without a sample.  $\mu$  can then be defined as the product of the absorption cross-section  $\sigma_a$  and the atomic number density  $\rho_a$ . The hole left by the ejected electron is then filled by an electron in one of the outer

shells, which releases a photon of characteristic energy to give a fluorescence signal. This two-stage process can be seen in figure 4.5

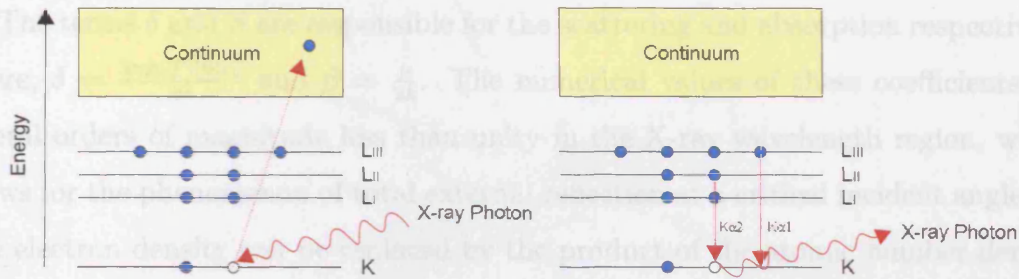


Figure 4.5: The photoelectric absorption process, the incident photon causes an electron to be ejected into the continuum and an electron in an outer shell fills the hole, emitting a photon of a characteristic energy. In this case the  $K\alpha$  fluorescence is shown.

## 4.2 X-ray Reflectivity

The physical and chemical structures of the multilayers are a product of the growth parameters selected in the sputtering process. Two-component systems are generally described by the thickness, roughness and density of the individual layers, which provides a spatial variation in electron density in the z-direction. X-ray reflectivity is the ideal technique to probe the electron density profile across the distances commonly found in multilayer systems. Reflectivity in the specular direction, where the angle of incidence is equal to the angle of reflection, gives information perpendicular to the sample surface. Off-specular or diffuse scattering, gives information about the structure in the plane of the sample surface. These measurements are commonly called transverse scans or rocking curves, where the detector is held fixed and the sample is rotated.

### Specular Reflectivity

Since X-rays are electromagnetic radiation it is possible to observe analogous effects to those observed with the scattering of light at the interfaces of different media, which result in an index of refraction,  $n$ .

$$n = 1 - \delta + i\beta \quad (4.26)$$

The terms  $\delta$  and  $\beta$  are responsible for the scattering and absorption respectively, where,  $\delta = \frac{2\pi\rho_a f^0(0)r_0}{k^2}$  and  $\beta = \frac{\mu}{2k}$ . The numerical values of these coefficients are several orders of magnitude less than unity in the X-ray wavelength region, which allows for the phenomenon of total external reflection at a critical incident angle,  $\theta_c$ . The electron density can be replaced by the product of the atomic number density and the atomic scattering factor, where the anomalous dispersion corrections are included to account for the scattering and absorption of the X-ray photons.

$$n = 1 - \frac{2\pi\rho_a r_0}{k^2} (f^0(0) + f' + if'') \quad (4.27)$$

The reflectivity can be treated first for a layer of infinite thickness, then for a finite single layer and eventually for a multilayer sample with rough interfaces.

### Reflection from an Infinitely Thick Slab

To begin with it's necessary to clarify the nomenclature used to note the amplitudes and wavevectors. The incident, reflected and transmitted amplitudes are  $a_I$ ,  $a_R$  and  $a_T$  and the respective wavevectors are  $\mathbf{k}_I$ ,  $\mathbf{k}_R$  and  $\mathbf{k}_T$ . In analogy to Snell's law and the Fresnel equation for light, the equivalent can be seen for X-rays.

In this instance Snell's law is  $\cos\theta = n \cos\theta'$ , which can be derived from simplifying the components of  $\mathbf{k}$  parallel and perpendicular to the interface. The critical angle,  $\theta_c$  can be found by setting the reflected angle to zero, which gives  $\theta_c = \sqrt{2\delta}$ . In a small angle approximation to Snell's law and substituting for the refractive index,

$$\theta^2 = \theta'^2 + \theta_c^2 - 2i\beta \quad (4.28)$$

The Fresnel equations can be obtained from the perpendicular projection of the wavevector and the boundary conditions to give the amplitude reflectivity,  $r$  and the amplitude transmittivity,  $t$ , which are the ratios of the reflected and transmitted amplitudes to the incident amplitude respectively.

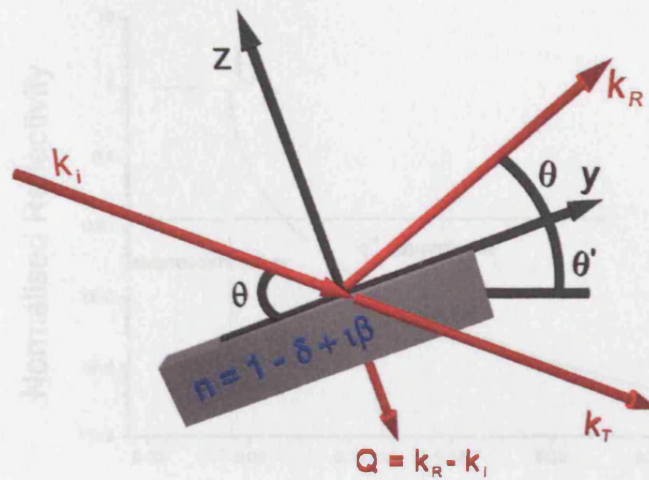


Figure 4.6: Reflection and transmittance of an incident X-ray from an infinitely thick layer allows the derivation of Snell's law and the Fresnel equations if the incident wave and its derivative are equivalent at the interface.

$$r = \frac{\alpha_R}{\alpha_I} = \frac{\theta - \theta'}{\theta + \theta'} \quad (4.29)$$

$$t = \frac{2\theta}{\theta + \theta'} \quad (4.30)$$

The reflected and transmitted intensities  $R$  and  $T$  are equivalent to the square of  $r$  and  $t$ .

It is more useful to consider these definitions in terms of the wavevector transfers, normalised to the wavevector transfer at the critical angle. As  $\theta$  is small  $Q$  becomes equivalent to  $2k\theta$  and in the same way  $Q_c = 2k\theta_c$  so that,

$$\frac{Q}{Q_c} \approx \frac{2k\theta}{2k\theta_c} = \frac{\theta}{\theta_c} \quad (4.31)$$

This ratio can then be defined as the dimensionless quantity  $q$  and  $q'$  can be defined similarly. The quantities  $r$  and  $t$  can be rewritten in terms of  $q$  and  $q'$ .

$$r(q) = \frac{q - q'}{q + q'} = \frac{q^2 - q'^2}{(q + q')^2} \quad (4.32)$$

$$t(q) = \frac{2q}{q + q'} \quad (4.33)$$

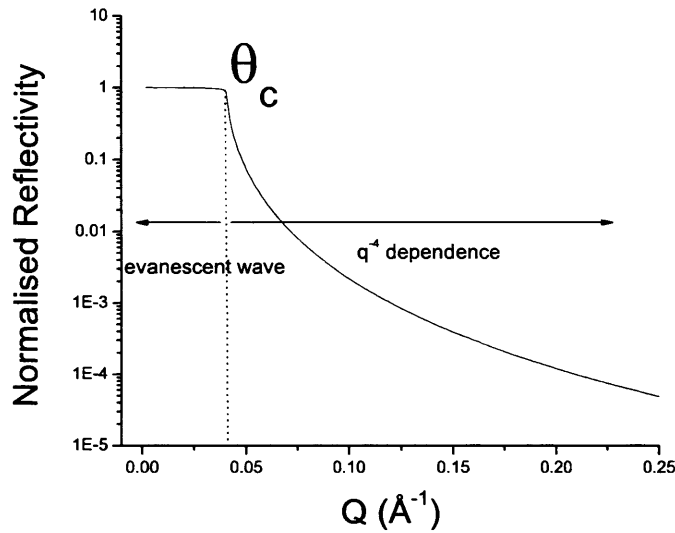


Figure 4.7: The reflected intensity from an infinitely thick layer shows the total external reflection below the critical angle and a  $q^{-4}$  dependence above it.

Rewriting equation (4.28),

$$q^2 = q'^2 + 1 - 2i \left( \frac{2k}{Q_c^2} \right) \mu \quad (4.34)$$

The reflectivity,  $R$  takes the shape of Figure 4.7.

Considering equation (4.33) and taking the limits  $\theta \gg \theta_c$ ,  $\theta \ll \theta_c$  and  $\theta = \theta_c$  the distinctive shape of the curve can be explained in each of these regions. At angles greater than the critical angle, the incident and reflected waves are in phase. In this case  $q$  becomes large and  $r(q)$  varies as  $q^{-2}$  and so beyond the critical edge the reflected intensity  $R$ , decreases with a  $q^{-4}$  dependence with approximately 100 % transmission. Below the critical angle, the incident and reflected waves are out of phase. In this regime, the transmitted wave is known as an evanescent wave, since it has a penetration depth of  $\approx 1/Q_c$ , independent of angle, and the incident wave is totally externally reflected. At the critical angle, the penetration depth increases sharply, the incident and reflected waves move in phase with each other and the intensity of the evanescent wave increases to its maximal value.

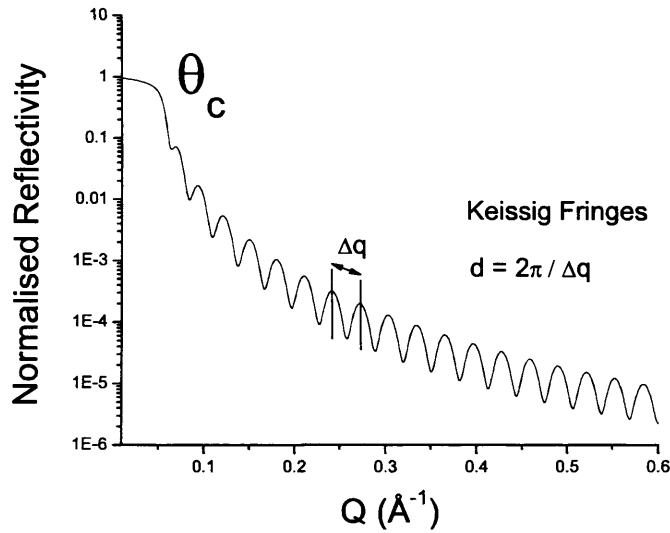


Figure 4.8: Keissig fringes from an iron layer of finite thickness on a sapphire substrate.

### Reflection from a Layer of Finite Thickness

For a layer of finite thickness deposited on an infinitely thick substrate the incident X-rays experience three media; the air, the layer and the substrate, which can be labeled 0, 1 and 2 respectively. This instance then allows for an infinite sum of reflections between the top and bottom interfaces of the finite layer. The description of the amplitude reflectivity then includes a term,  $r_{01}$ , corresponding to external reflection from the top surface of the layer, a prefactor,  $t_{01}t_{10}r_{12}p^2$ , which is the transmission through the layer in both directions and the reflection from the bottom surface, including a phase factor  $p = e^{iQd}$  and an infinite sum of reflections.

$$r = r_{01} + t_{01}t_{10}r_{12}p^2 \sum_{n=0}^{\infty} (r_{10}r_{12}p^2)^n \quad (4.35)$$

This equation can be simplified since  $\sum_{n=0}^{\infty} x^n = \frac{1}{1-x}$  to give,

$$r = r_{01} + \frac{t_{01}t_{10}r_{12}p^2}{1 - r_{10}r_{12}p^2} \quad (4.36)$$

Using the Fresnel equations stated earlier it is possible to make substitutions, such that  $r_{01} = -r_{10}$  and  $r_{01}^2 + t_{01}t_{10} = 1$ , which leaves,

$$r = \frac{r_{01} + r_{12}p^2}{1 + r_{10}r_{12}p^2} \quad (4.37)$$

Plotting the reflected intensity  $R$  versus the wavevector transfer  $Q(\text{\AA}^{-1})$  in figure 4.8 shows a periodic oscillation overlaid onto the reflectivity seen for an infinite block. These oscillations are known as Keissig fringes and are directly related to the thickness of the layer,  $d(\text{\AA}) = 2\pi/L$  where  $L$  is the period of the fringes measured in  $\text{\AA}^{-1}$ .

### Reflection from a Multilayer

There are a number of approaches that one can use to evaluate the reflected intensity from multilayered systems as a function of wavevector transfer. General methods extend the derived reflectivity from a single layer to include multiple reflections and refraction effects. However, one can make the assumptions that these effects are very small at angles sufficiently larger than the critical angle. This is the kinematical regime and yields similar results to the scattering of light from a diffraction grating. A large drawback of this approximation is its failure to correctly generate the reflected intensity in the vicinity of the critical edge.

Parratt in 1954 developed an exact recursive method [53], which included refraction and multiple scattering for a stack of  $N$  layers on top of an infinitely thick substrate. This method was then modified further by Nevot and Croce [54] to include a term that could describe the roughness of the layers.

Traditionally, the layers are numbered from the surface towards the substrate. The refractive index can be written  $n_j = 1 - \delta_j + i\beta_j$  for each layer,  $j$  of thickness  $d_j$  and the wavevector transfer becomes  $Q_j = 2\mathbf{k}_j \sin\theta_j = 2k_{z,j}$  where,

$$k_{z,j}^2 = (n_j \mathbf{k})^2 - k_{x,j}^2 \quad (4.38)$$

The wavevector component in the  $x$  direction is constant throughout the multilayer stack so  $k_{x,j}$  is then  $k_x$ . The wavevector transfer for each layer is then,

$$Q_j = \sqrt{Q^2 - 8k^2\delta_j + i8k^2\beta_j} \quad (4.39)$$

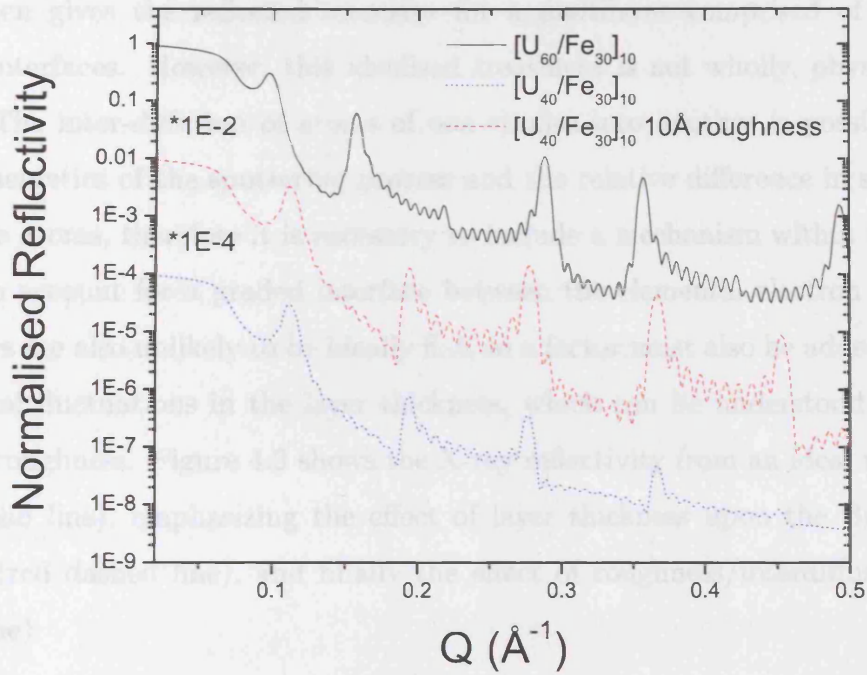


Figure 4.9: Simulated reflectivity spectra from an ideal U/Fe multilayer (black solid line), showing the extinction of every third Bragg peak, since  $t_U : t_{Fe} = 2 : 1$ . The effect of decreasing the bilayer thickness (red dashed line) and the addition of a roughness factor (blue dotted line) can also be observed. Curves have been displaced for clarity.

The reflectivity from each interface can be derived from the Fresnel relations to give,

$$r'_{j,j+1} = \frac{Q_j - Q_{j+1}}{Q_j + Q_{j+1}} \quad (4.40)$$

This relationship does not include multiple reflections; it can be used to calculate the reflectivity from the substrate and the bottom of layer  $N$ , denoted by  $r'_{N,\infty}$ . The prime symbol is used to indicate that the reflectivity does not include multiple reflections. The reflectivity for any interface above the substrate can then be summarised by using equation (4.37) for a single layer, where  $p_j^2 = e^{id_j Q_j}$ .

$$r_{N-x,N-x+1} = \frac{r'_{N-x,N-x+1} + r_{N-x+1,N-x+2} p_{N-x+1}^2}{1 + r'_{N-x,N-x+1} r_{N-x+1,N-x+2} p_{N-x+1}^2} \quad (4.41)$$

This formula can be used recursively from the bottom of the stack to the top,

which then gives the reflected intensity for a multilayer comprised of perfectly smooth interfaces. However, this idealised treatment is not wholly, physically accurate. The inter-diffusion of atoms of one species into another is possible based on the energetics of the sputtering process and the relative difference in size of the respective atoms, therefore it is necessary to include a mechanism within the calculations to account for a graded interface between the elemental electron densities. The layers are also unlikely to be ideally flat, so a factor must also be added to allow for vertical fluctuations in the layer thickness, which can be understood as an interfacial roughness. Figure 4.9 shows the X-ray reflectivity from an ideal multilayer (black solid line), emphasizing the effect of layer thickness upon the Bragg peak position (red dashed line), and finally the effect of roughness/interdiffusion (blue dotted line).

### Reflection from a Multilayer with Non-ideal Interfaces

The reflectivity from a multilayer with diffuse interfaces is simply the product of the intensity from an ideal multilayer,  $R_I(\mathbf{Q})$  and a factor describing a graduated change in electron density across the interface. To model this gradual change it is possible to sum the contributions of infinitesimally thin layers, allowing for any changes in phase and including a function describing the density profile,  $f(z)$ . Remembering that the reflected intensity is the square of the amplitude then,

$$R(\mathbf{Q}) = R_I(\mathbf{Q}) \left| \int_0^\infty \left( \frac{df(z)}{dz} e^{i\mathbf{Q}z} dz \right) \right|^2 \quad (4.42)$$

The modulus squared term representing the nature of the interfacial region is the Fourier transform of the electron density gradient. This term allows for numerous different analytical functions to describe the electron density profile across the interface, which can be modeled by an error function. The derivative of this function is a Gaussian and the Fourier transform of a Gaussian is another Gaussian, which leaves,

$$R(\mathbf{Q}) = R_I(\mathbf{Q}) e^{-\mathbf{Q}^2 \sigma^2} \quad (4.43)$$

The  $\sigma$  term represents the thickness of the interfacial region.

The roughness of individual layers can also be included in calculations of the reflected intensity, by modeling the effects of variations in the height of the layers. Assuming the heights at different positions are uncorrelated it is possible to understand the roughness by varying the index of refraction; a method proposed by Nevot and Croce [54] and adapted by others [55–59], combined with Parratt’s recursive method for the calculation of the reflected intensity.

$$n_j(z) = n_j + (n_{j+1} - n_j)F(z, \sigma_j) \quad (4.44)$$

The Fourier transform,

$$F(z, \sigma_j) = \frac{1}{\sigma_j \sqrt{2\pi}} \int_{-\infty}^z e^{(-z^2/2\sigma_j^2)} dz \quad (4.45)$$

The reflected intensity is then the product of the reflectivity from an ideal multilayer and a factor describing the uncorrelated roughness. In this case,

$$R(\mathbf{Q}) = R_I(\mathbf{Q})e^{-\mathbf{Q}_z^2 \sigma^2} \quad (4.46)$$

This formula is identical to equation (4.43), describing a diffuse interface. In this instance  $\sigma_j$  is the root mean square (rms) roughness. The equivalence of these two representations highlights the difficulty in distinguishing between interfacial diffusion and roughness effects, using this treatment of the specular reflectivity.

### 4.2.1 Experimental Method

X-ray reflectivity scans were carried out on a Philips diffractometer at the Clarendon Laboratory, Oxford. This diffractometer was optimised for low-angle diffraction measurements. A copper anode tube source provided Cu K $\alpha$  X-rays of wavelength 1.54Å, selected by a germanium monochromator and attenuated by a nickel foil to avoid detector saturation and reduce Cu K $\beta$  background. The samples were mounted onto copper stubs using vacuum grease and the height was aligned by hand. Alignment scans were then carried out at fixed detector angle to determine any offset angle in  $\theta$ .

The scans were taken in a specular geometry with the scattering vector normal to the sample surface. The X-ray source remained in a fixed position with the sample and detector able to rotate in a vertical plane about a fixed position at the centre of the sample. In this case measurements were taken with the reflected angle,  $2\theta$  twice the incident angle,  $\theta$ . The samples were mounted on brass stubs, using vacuum grease. The height of the samples were adjusted to be in the centre of rotation of the scattering geometry and alignment scans of the sample angle,  $\theta$  were carried out to account for any angular offsets.

The data were fitted to simulations of the reflected intensity, based on a matrix method of interferometry that reduces to Parratt's recursive method in the case of X-rays, described in the calculations earlier. The simulations and fitting routines are part of the xPOLLY program, written by Sean Langridge at ISIS [4]. The reflectivity is simulated by a set of input parameters, which describe the physical nature of the multilayers. The parameters include the anomalous scattering factors of the respective materials at the energy of the incident photons, the density ( $\text{atoms}/\text{\AA}^3$ ), the layer thickness ( $\text{\AA}$ ) and the rms roughness ( $\text{\AA}$ ). All of these values can be varied, although in reality the scattering factors are kept constant and the structural parameters are varied. The starting points for the structural models begin with an oxidised capping layer, a cap, repeated bilayer, buffer and substrate. Complexity can then be introduced by stratifying the bilayer to account for regions of reduced density at the interfaces, where strain caused by lattice mismatches between relevant species can produce defects affecting the crystal structure of the layers.

The parameters are kept within realistic physical ranges, but varied to give the closest possible match between simulation and experimental data. Two fitting routines are available with xPOLLY, simplex and simulated annealing; the first is an adaptation of the steepest gradient method of minimisation, which is relatively easy on computer power, whereas the simulated annealing method involves the exploration of a much larger area of parameter space to avoid local minima, which requires a great deal more effort computationally. These minimisations give values of chi squared for the specular reflectivity as a measure of how well the theoretical curves match the experimental data. It is then possible to achieve some consistency

across a series of samples by using a combination of information from the fitted structural parameters and the growth conditions.

Later measurements to investigate the polarised neutron reflectivity have also been used to adjust the structural parameters of the multilayers used in the fitting of the X-ray data, based on their sensitivity to the distribution of magnetic moment, which is largely dependent on the structure of the magnetic layers.

The niobium capping layer was chosen to provide a protective screen, preventing oxidation of the multilayer stack. The oxidation characteristics of niobium thin films has been well described [48] and a film of niobium was grown to characterise the thickness of the oxide layer. It was found that over a period of 24hrs the niobium oxidised to a depth of  $\sim 20\text{\AA}$  and this thickness did not substantially increase over a one year period. This result was then used to characterise the capping layer contribution to the reflected intensity. Since X-ray reflectivity is a surface sensitive technique and the niobium oxide is at the very surface, although it comprises a relatively small portion of the multilayer sample, it is still detectable in most of the reflectivity scans performed. The contribution from the oxide and capping layer can be seen as a broad modulation of the Bragg peaks and Keissig fringes of the multilayer reflectivity.

### 4.2.2 Results

The results are presented for the specular reflectivity of U/Fe, U/Co and U/Gd systems respectively. The normalised reflected intensity is plotted against the wavevector momentum transfer,  $Q$  ( $\text{\AA}^{-1}$ ) normal to the sample surface, where  $2\theta$  is the scattering angle,  $Q = 2k \sin \theta$  and the wavevector  $k = \frac{2\pi}{\lambda}$ . This scattering geometry probes the reflected intensity as a function of depth, where the X-rays are sensitive to the electron density profile.

This technique provides an excellent measure of the bilayer thickness, but is limited in its sensitivity to the relative thicknesses of individual layers. Good fits to the data could be produced by simulations that varied in individual layer thickness by several angstroms. For this reason, the reflectivity was not treated as a stand-alone result; consistency was maintained by consideration of the growth parameters and results from other techniques.

Experimental curves, including error bars for each sample are plotted together with the fitted, simulated reflectivity. The results are grouped into as-grown series and the growth conditions are described in detail. Tables of the simulated parameters have been used to summarise the physical properties of the multilayers. The roughness values used in the xPOLLY program describe the top surface of the layer below, but those listed in the summary tables represent the roughness of the layer to which they are ascribed.

### 4.2.3 Uranium/Iron

Following previous work [18, 19], and evidenced by techniques described later in this text, the iron layers were stratified into three components. Bulk magnetisation measurements have shown a reduced moment (see Chapter 5), relating to a 'dead' magnetic layer, possibly a U/Fe alloy at the interface and an amorphous section of iron with a reduced moment. It is clear from the polarised neutron reflectivity, Chapter 5, that the magnetisation profile is best fit with an asymmetric moment distribution within the iron layers. Table 4.1 summarises the thickness and roughness parameters for the U/Fe series of samples discussed in chapter 3.

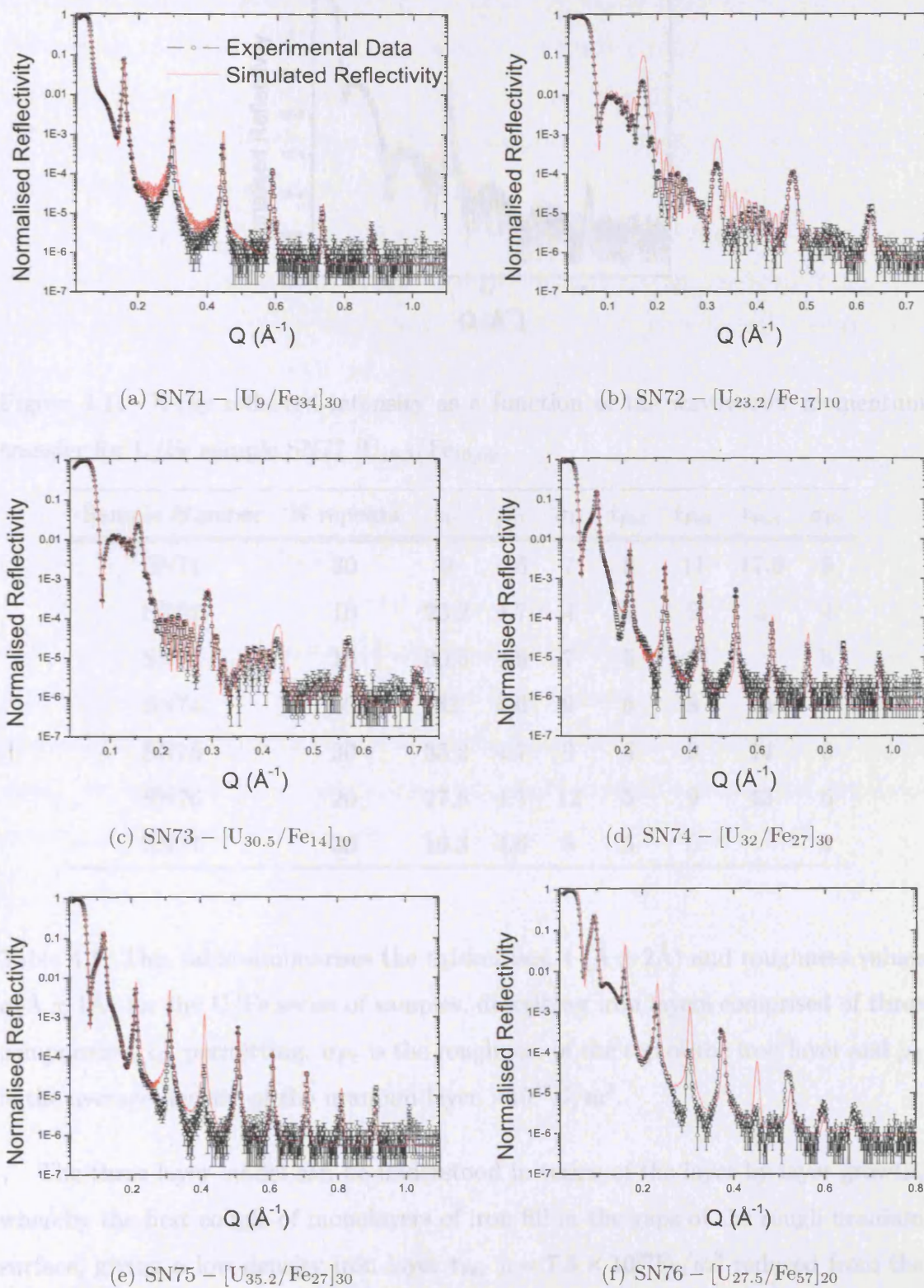


Figure 4.10: X-ray reflectivity spectra taken in the specular geometry, using a  $\text{Cu-K}\alpha$  source from a U/Fe series of samples grown on sapphire substrates with niobium buffers and capping layers.

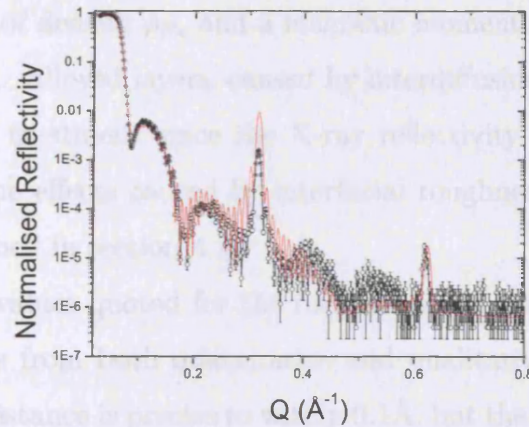


Figure 4.11: X-ray reflected intensity as a function of the wavevector momentum transfer for U/Fe sample SN77 [U<sub>10.3</sub>/Fe<sub>10</sub>]<sub>30</sub>

| Sample Number | N repeats | $t_U$ | $\rho_U$ | $\sigma_U$ | $t_{Fe1}$ | $t_{Fe2}$ | $t_{Fe3}$ | $\sigma_{Fe}$ |
|---------------|-----------|-------|----------|------------|-----------|-----------|-----------|---------------|
| SN71          | 30        | 9     | 4.5      | 7          | 5         | 11        | 17.9      | 5             |
| SN72          | 10        | 23.2  | 4.7      | 4          | 5         | 9         | 3         | 4             |
| SN73          | 10        | 30.5  | 4.6      | 7          | 5         | 9         |           | 3             |
| SN74          | 30        | 32    | 4.6      | 9          | 5         | 8         | 14        | 3             |
| SN75          | 30        | 35.2  | 4.7      | 9          | 4         | 9         | 14        | 6             |
| SN76          | 20        | 27.5  | 4.7      | 12         | 5         | 9         | 43        | 6             |
| SN77          | 30        | 10.3  | 4.6      | 8          | 5         | 5         |           | 4             |

Table 4.1: This table summarises the thicknesses,  $t$  ( $\text{\AA} \pm 2\text{\AA}$ ) and roughness values  $\sigma$  ( $\text{\AA} \pm 1\text{\AA}$ ) for the U/Fe series of samples, describing iron layers comprised of three components,  $t_{Fe}$  permitting.  $\sigma_{Fe}$  is the roughness of the top of the iron layer and  $\rho_U$  is the average density of the uranium layer  $\times 10^{28}\text{U}/\text{m}^3$ .

The three layer model can be understood in terms of the layer by layer growth, whereby the first couple of monolayers of iron fill in the gaps of the rough uranium surface, giving a low density iron layer  $t_{Fe1}$   $\rho = 7.5 \times 10^{28}\text{Fe}/\text{m}^3$  reduced from the bulk value  $\rho_{Fe} = 8.4 \times 10^{28}\text{Fe}/\text{m}^3$ , the next monolayers begin to arrange themselves in a crystalline structure, but are still essentially amorphous with a reduced density of  $8 \times 10^{28}\text{Fe}/\text{m}^3$  and a reduced magnetisation. The topmost iron layer forms a

crystalline structure of density  $\rho_{Fe}$  and a magnetic moment per atom equivalent to that seen in the bulk. Alloyed layers, caused by interdiffusion at the interfaces were not included in this treatment since the X-ray reflectivity is not sensitive to the difference between the effects caused by interfacial roughness and those caused by interdiffusion, described in section 4.2.

The uncertainty values quoted for the roughness and thickness of the iron and uranium layers arises from both quantitative and qualitative considerations. The total bilayer repeat distance is precise to within  $0.1\text{\AA}$ , but the reflected intensity only begins to lose coherence with the experimental data when the respective thickness are changed by  $\sim 2\text{\AA}$ . Restrictions were also fixed on the individual layer thickness due to the sputtering times and known calibrations. The roughness values greatly affect the Bragg peak intensities and changes greater than  $\sim 1\text{\AA}$  can drastically alter the fall-off in reflected intensity.

The U/Fe samples analysed previous to this work using X-ray reflectivity [18] were grown on glass substrates and did not include either a buffer or a capping layer to prevent oxidation. The series considered here has reduced the complexity of the surface layers to give greater detail about the reflected intensity from the multilayer stack. For samples of similar thickness the single crystal, optically flat, sapphire substrates have reduced the respective roughness of the individual layers.

### 4.2.4 Uranium/Cobalt

The uranium/cobalt samples were fit by separating the cobalt layers into two components; one reduced density component  $\sim 15\text{\AA}$  and the remainder of the layer forms a crystalline component of bulk Co density,  $\rho_{\text{Co}} = 9 \times 10^{28}\text{Co}/\text{m}^3$ . This structural profile was determined from polarised neutron reflectivity and bulk magnetisation measurements. Interdiffusion effects were not considered due to the equivalence of roughness and diffusion effects manifest in the reflected intensity.

The following table summarises the thicknesses of the individual layer components and the roughnesses of the uranium and topmost cobalt layers.

| Sample Number | N repeats | $t_{\text{U}}$ | $\rho_{\text{U}}$ | $\sigma_{\text{U}}$ | $t_{\text{Co}1}$ | $t_{\text{Co}2}$ | $\sigma_{\text{Co}}$ |
|---------------|-----------|----------------|-------------------|---------------------|------------------|------------------|----------------------|
| SN108         | 20        | 27.5           | 4.8               | 4.8                 | 14.5             | 13               | 7                    |
| SN109         | 20        | 19             | 4.6               | 4                   | 14.6             | 13               | 8                    |
| SN111         | 20        | 9              | 4.2               | 3.5                 | 14               | 12               | 10                   |
| SN112         | 20        | 19             | 4.6               | 11                  | 15               | 4.2              | 11                   |
| SN113         | 20        | 13.7           | 4.5               | 9                   | 15               | 4.7              | 14                   |
| SN114         | 20        | 8.8            | 4.4               | 10                  | 13               | 5                | 10                   |
| SN115         | 30        | 9              | 4.3               | 7                   | 10.1             |                  | 8                    |
| SN116         | 20        | 19             | 4.6               | 6                   | 14               | 28.5             | 10                   |
| SN117         | 15        | 9              | 4.6               | 12                  | 14               | 37               | 5                    |
| SN118         | 20        | 10             | 4.6               | 3                   | 13               | 21.5             | 8                    |

Table 4.2: This table summarises the thicknesses,  $t$  ( $\text{\AA} \pm 2\text{\AA}$ ) and roughness values  $\sigma$  ( $\text{\AA} \pm 1\text{\AA}$ ) for the U/Co series of samples, describing cobalt layers comprised of two components,  $t_{\text{Co}}$  permitting.  $\sigma_{\text{Co}}$  is the roughness of the top of the cobalt layer and  $\rho_{\text{U}}$  is the average density of the uranium layer  $\times 10^{28}\text{U}/\text{m}^3$ .

The majority of the features observed in the reflected intensity have been reproduced by the simulation, including the extinction of even order Bragg peaks in the case of samples SN108 and SN112 in figure 4.12 where  $t_{\text{U}}$  and  $t_{\text{Co}}$  are almost equal. Greater deviations were apparent between the simulated and experimental

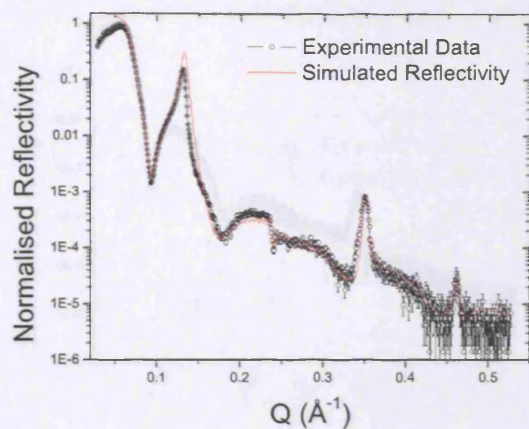
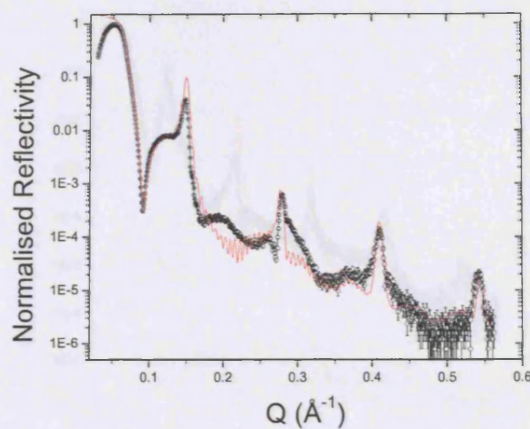
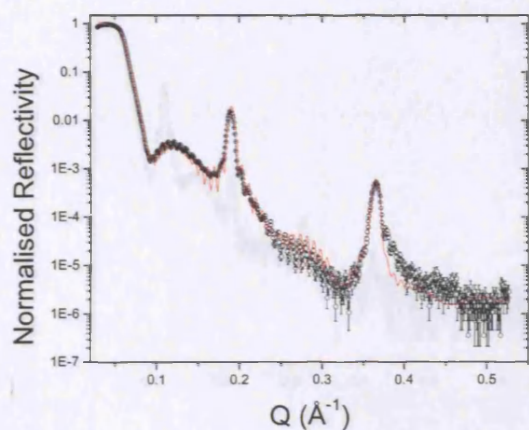
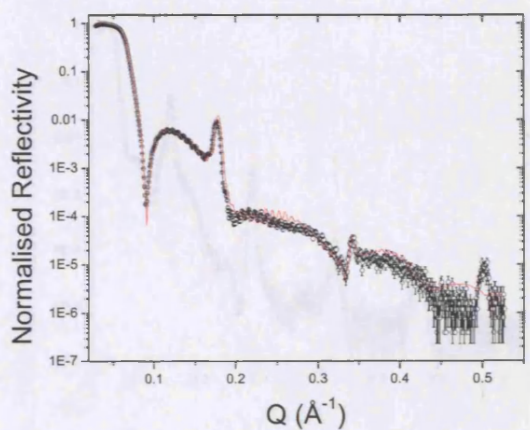
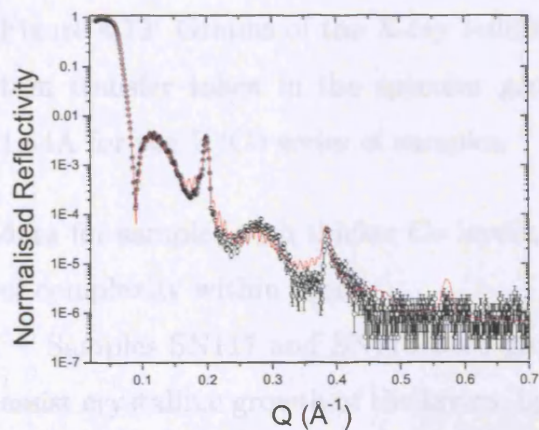
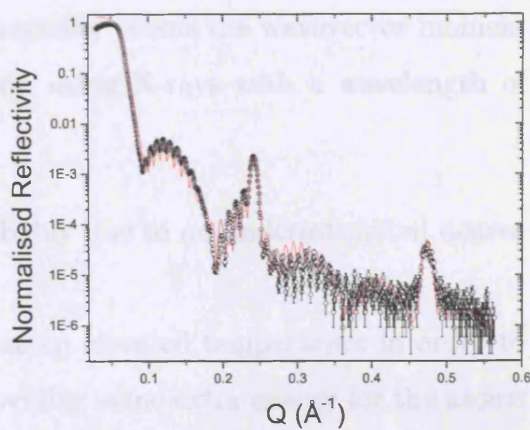
(a) SN108 -  $[Co_{27.5}/U_{27.5}]_{20}$ (b) SN109 -  $[Co_{25.6}/U_{21}]_{20}$ (c) SN111 -  $[Co_{26}/U_9]_{20}$ (d) SN112 -  $[Co_{18.8}/U_{19}]_{20}$ (e) SN113 -  $[Co_{19.7}/U_{13.7}]_{20}$ (f) SN114 -  $[Co_{18}/U_{8.8}]_{20}$ 

Figure 4.12: Graphs of the X-ray reflected intensity versus the wavevector momentum transfer taken in the specular geometry,  $\lambda = 1.54\text{\AA}$ , for the U/Co series of samples.

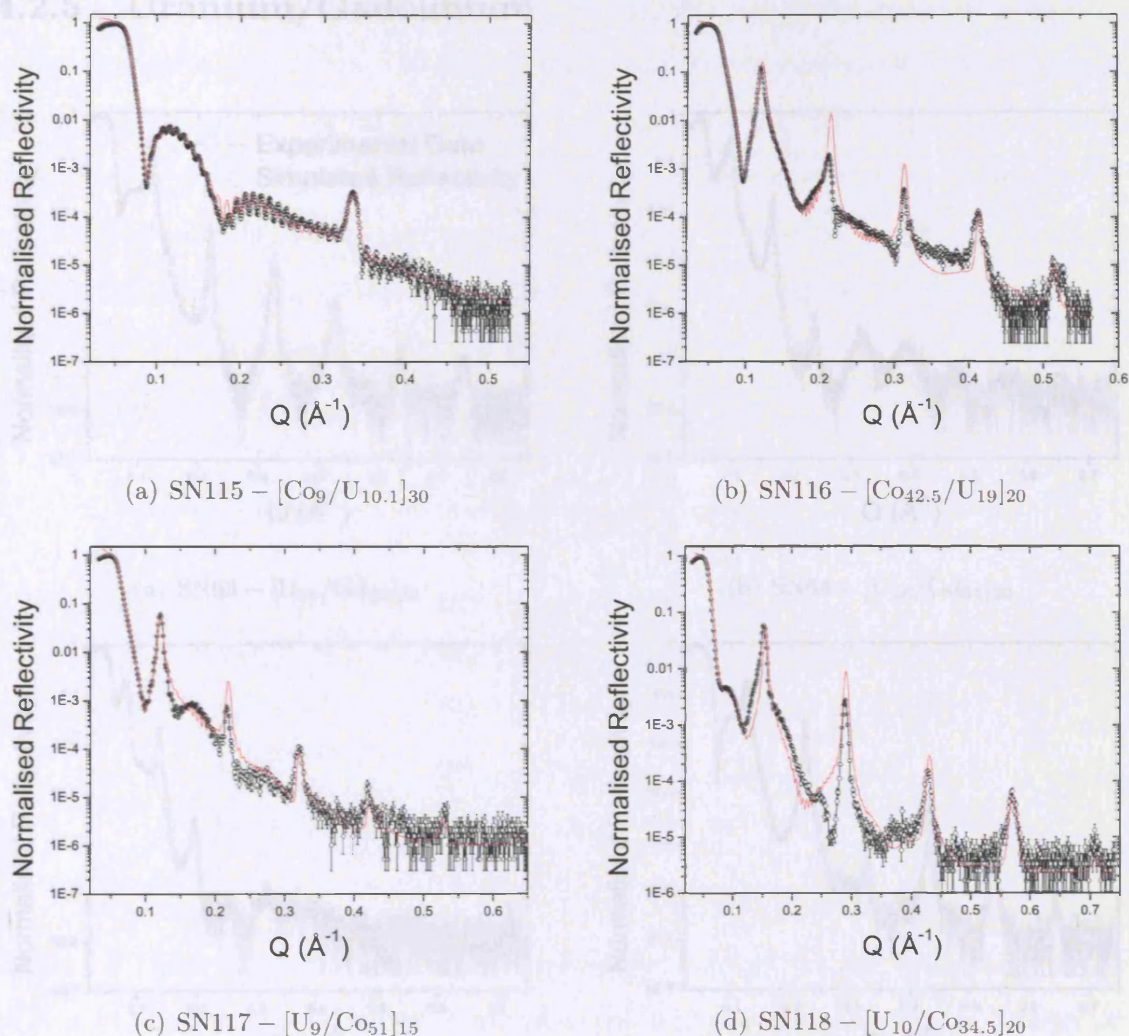


Figure 4.13: Graphs of the X-ray reflected intensity versus the wavevector momentum transfer taken in the specular geometry, using X-rays with a wavelength of  $1.54\text{\AA}$  for the U/Co series of samples.

data for samples with thicker Co layers, probably due to an underestimated degree of complexity within them.

Samples SN117 and SN118 were grown at an elevated temperature in order to assist crystalline growth of the layers, by providing some extra energy for the atoms to manoeuvre once they adhere to the substrate. Although this may also provide a mechanism for a greater amount of diffusion at the interface, in this case the former is more likely, since the roughness values for the heated samples are lower than those for other samples of like thickness, i.e, compare SN116 and SN118.

## 4.2.5 Uranium/Gadolinium

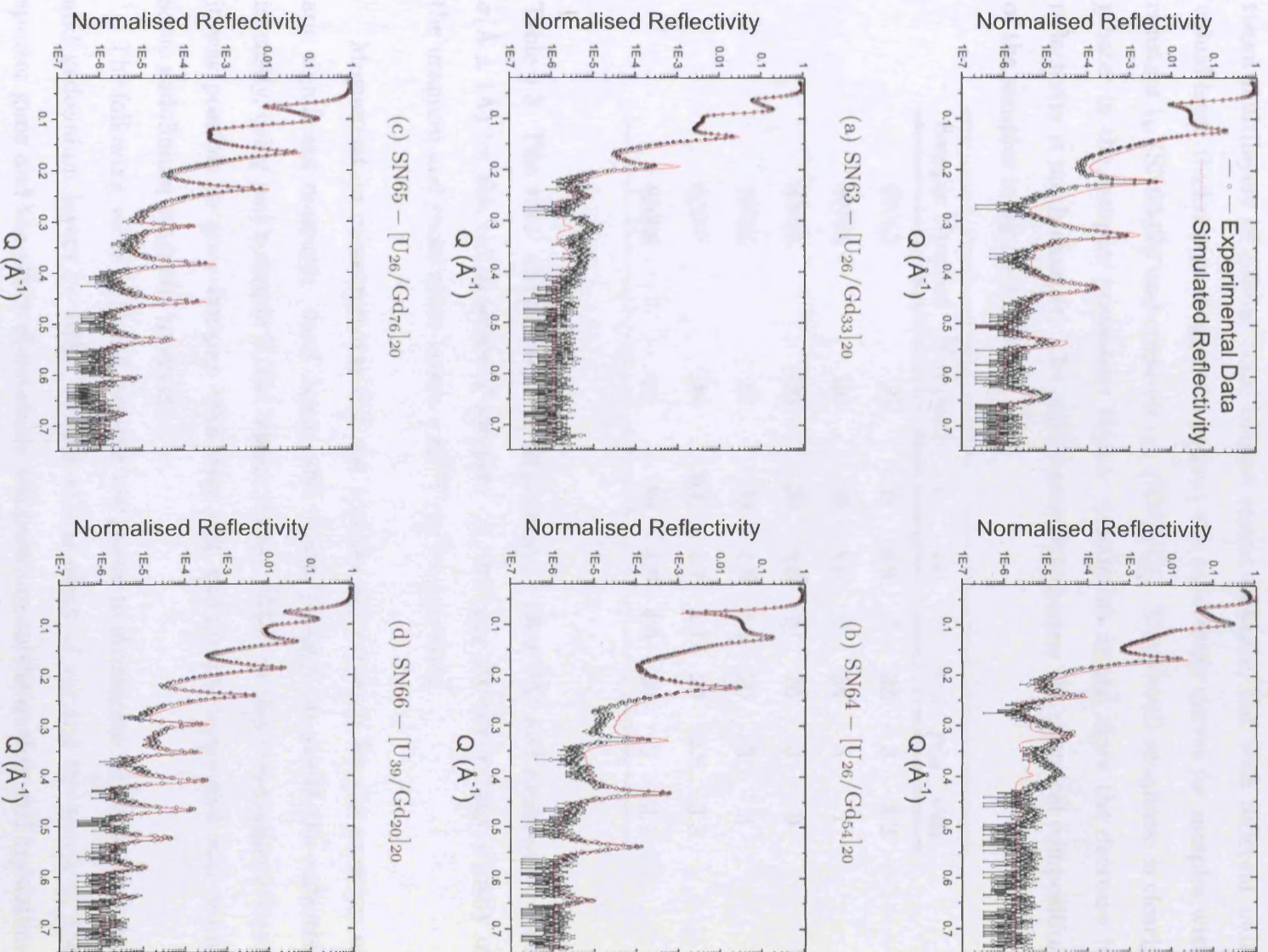


Figure 4.14: U/Gd X-ray reflectivity spectra.

This initial series of uranium gadolinium samples was grown to investigate uranium and gadolinium layer thickness effects. There are noticeable differences between multilayers of similar total bilayer repeat distance, but with different individual layer thicknesses. Figure 4.14 shows the reflectivity curves for samples with constant  $t_U$  (SN63-65) and constant  $t_{Gd}$  (SN66-68). The overall roughness is clearly greater in the samples possessing thicker gadolinium layers, since the decrease in reflectivity is much sharper. The table below summarises the chemical composition of the samples in figure 4.14.

| Sample Number | N repeats | $t_U$ | $\rho_U$ | $\sigma_U$ | $t_{Gd}$ | $\rho_{Gd}$ | $\sigma_{Gd}$ |
|---------------|-----------|-------|----------|------------|----------|-------------|---------------|
| SN63          | 20        | 26    | 4.6      | 7          | 33       | 3           | 3.2           |
| SN64          | 20        | 26    | 4.6      | 8          | 54       | 3           | 7             |
| SN65          | 20        | 26    | 4.6      | 10         | 76       | 3           | 9             |
| SN66          | 20        | 39    | 4.8      | 4.5        | 20       | 3           | 3             |
| SN67          | 20        | 63.5  | 4.7      | 4.1        | 20       | 2.8         | 3.3           |
| SN68          | 20        | 89    | 4.8      | 4.5        | 20       | 3           | 3.1           |

Table 4.3: This table summarises the thicknesses,  $t$  ( $\text{\AA} \pm 2\text{\AA}$ ) and roughness values  $\sigma$  ( $\text{\AA} \pm 1\text{\AA}$ ) for the U/Gd series of samples.  $\rho_U$  and  $\rho_{Gd}$  are the average density of the uranium and gadolinium layers  $\times 10^{28} \text{U/m}^3$  respectively.

Magnetisation measurements did not provide any evidence for the presence of any significant magnetic 'dead' layer, and it was possible to model the reflected intensity, using just a simple U/Gd bilayer repeat. Without this non-magnetic layer it was possible to grow samples with very thin gadolinium layers and still retain some gadolinium magnetic moment.

The following series of U/Gd samples was grown to investigate very thin uranium and gadolinium layers ( $\sim 10\text{\AA}$ ), to look at the effect of varying the power to the sputter guns and the effect of substrate temperature on the quality and crystalline nature of the multilayers, see figure 4.15. Samples SN119-121 were grown with a Gd sputtering power of 50W (normally 25W) and sample SN124 was grown with identical growth parameters to SN123, but at an elevated substrate temperature of

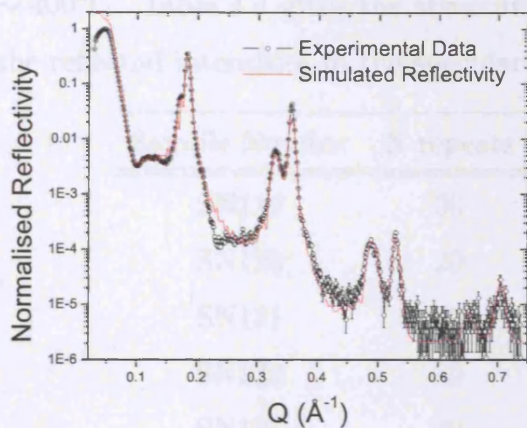
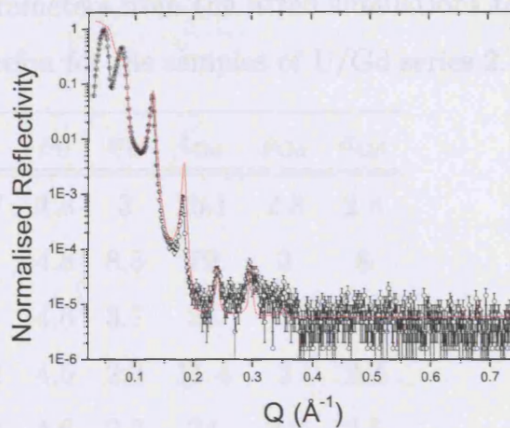
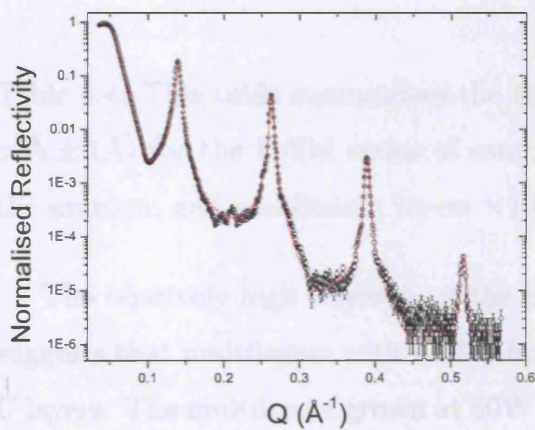
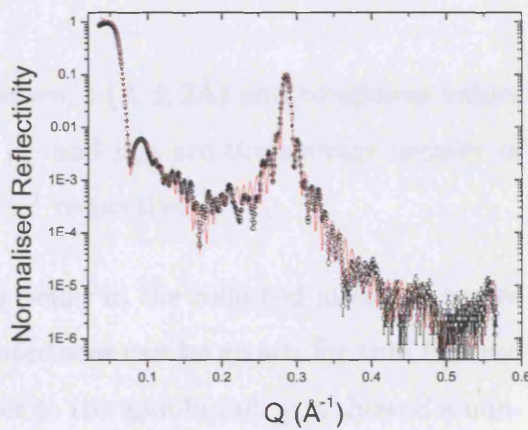
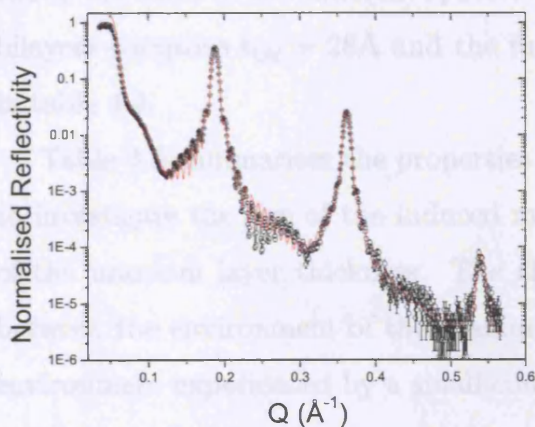
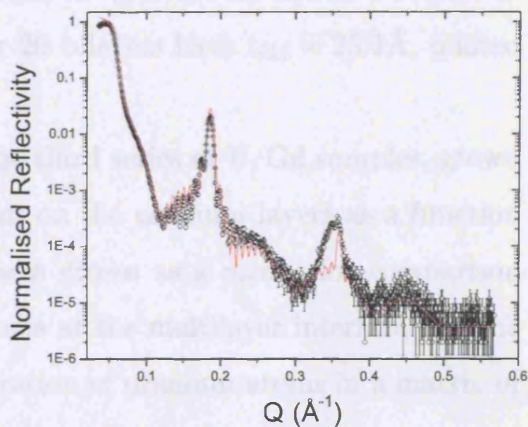
(a) SN119 – [U<sub>10.8</sub>/Gd<sub>25.1</sub>]<sub>30</sub>(b) SN120 – [U<sub>29</sub>/Gd<sub>79</sub>]<sub>20</sub>(c) SN121 – [U<sub>11</sub>/Gd<sub>38</sub>]<sub>30</sub>(d) SN122 – [U<sub>11.1</sub>/Gd<sub>11.4</sub>]<sub>30</sub>(e) SN123 – [U<sub>11.1</sub>/Gd<sub>24</sub>]<sub>20</sub>(f) SN124 – [U<sub>10.6</sub>/Gd<sub>24.8</sub>]<sub>20</sub>

Figure 4.15: The X-ray reflected intensity as a function of wavevector momentum transfer for the second series of U/Gd multilayer samples. Scans were carried out in the specular geometry using a source wavelength of 1.54Å.

$\sim 400^\circ\text{C}$ . Table 4.4 gives the structural parameters from the fitted simulations to the reflected intensities in the specular direction for the samples of U/Gd series 2.

| Sample Number | N repeats | $t_U$ | $\rho_U$ | $\sigma_U$ | $t_{Gd}$ | $\rho_{Gd}$ | $\sigma_{Gd}$ |
|---------------|-----------|-------|----------|------------|----------|-------------|---------------|
| SN119         | 30        | 10.7  | 4.8      | 3          | 25.1     | 2.8         | 2.8           |
| SN120         | 20        | 29    | 4.8      | 8.5        | 79       | 3           | 8             |
| SN121         | 30        | 11    | 4.6      | 3.7        | 38       | 3           | 3.4           |
| SN122         | 30        | 11.1  | 4.5      | 2.3        | 11.4     | 3           | 2.4           |
| SN123         | 20        | 11.1  | 4.6      | 2.5        | 24       | 2.8         | 2.5           |
| SN124         | 20        | 10.6  | 4.2      | 12         | 24.8     | 3           | 6             |

Table 4.4: This table summarises the thicknesses,  $t$  ( $\text{\AA} \pm 2\text{\AA}$ ) and roughness values  $\sigma$  ( $\text{\AA} \pm 1\text{\AA}$ ) for the U/Gd series of samples.  $\rho_U$  and  $\rho_{Gd}$  are the average density of the uranium and gadolinium layers  $\times 10^{28}\text{U}/\text{m}^3$  respectively.

The relatively high intensity of the Bragg peaks in the reflected intensity curves suggests that multilayers with well-defined interfaces can be grown for thin Gd and U layers. The multilayers grown at 50W power to the gadolinium gun showed a non-linear relationship between the power and the material sputtered. Sample SN119 shows the effect of two different sputter times for the gadolinium layers. The first 10 bilayers comprise  $t_{Gd} = 28\text{\AA}$  and the further 20 bilayers have  $t_{Gd} = 25.1\text{\AA}$ , quoted in table 4.4.

Table 4.5 summarises the properties of the third series of U/Gd samples, grown to investigate the size of the induced moment on the uranium layers as a function of the uranium layer thickness. The alloy was grown as a means for comparison between the environment of the uranium atoms at the multilayer interface and the environment experienced by a small concentration of uranium atoms in a matrix of gadolinium.

The X-ray reflectivity profiles of this series of samples indicated a similar interfacial quality to previous U/Gd samples. The values of the individual layer thicknesses obtained from the reflectivity simulations were within  $2\text{\AA}$  of the nominal values. The alloy sample SN139 proposed in section 3 was grown with the gadolinium sputtering

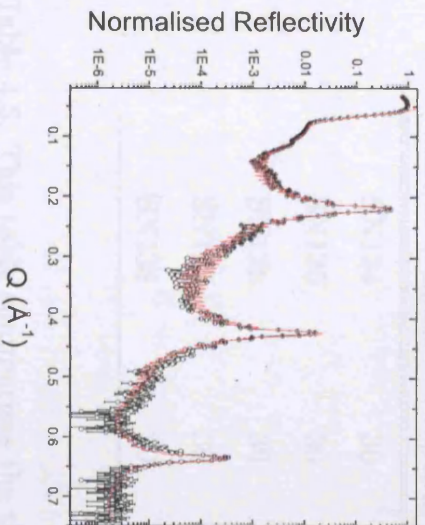
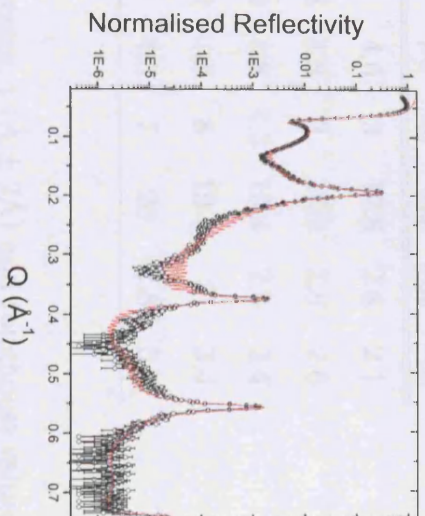
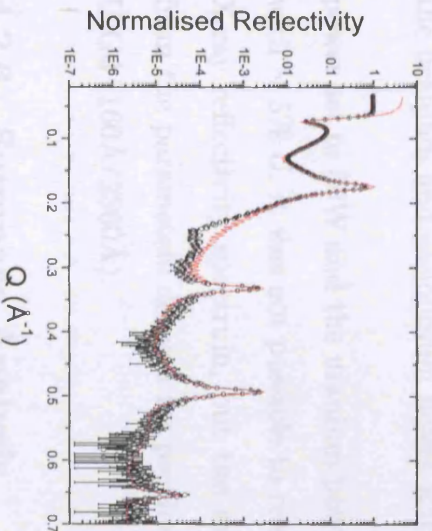
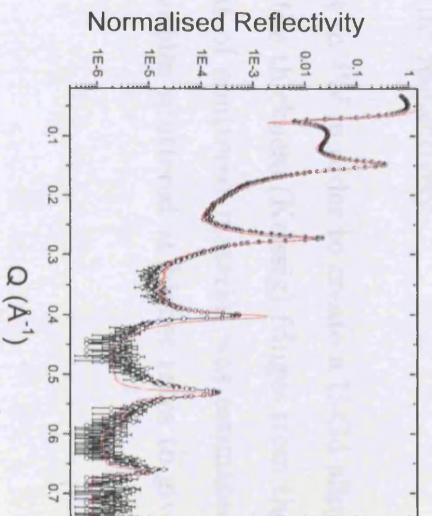
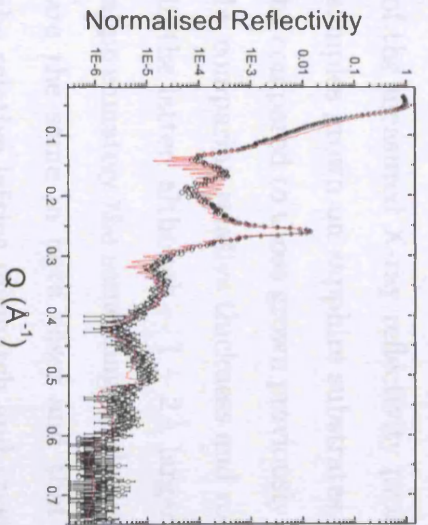
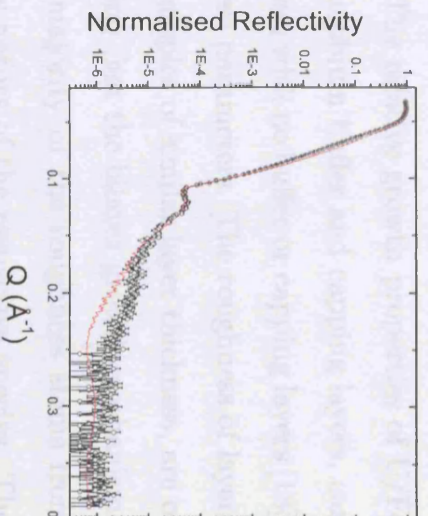
(a) SN134 – [U<sub>10</sub>/Gd<sub>19,8</sub>]<sub>30</sub>(b) SN135 – [U<sub>15,8</sub>/Gd<sub>18,2</sub>]<sub>30</sub>(c) SN136 – [U<sub>19,2</sub>/Gd<sub>19,4</sub>]<sub>30</sub>(d) SN137 – [U<sub>28,2</sub>/Gd<sub>19,5</sub>]<sub>30</sub>(e) SN138 – [U<sub>4,8</sub>/Gd<sub>20</sub>]<sub>30</sub>(f) SN139 – U<sub>3,5%</sub>Gd<sub>2410</sub>

Figure 4.16: Graphs of the X-ray reflectivity from the third series of U/Gd samples. All results were taken in the specular direction, using a Cu-K $\alpha$  source.

| Sample Number | N repeats | $t_U$ | $\rho_U$ | $\sigma_U$ | $t_{Gd}$ | $\rho_{Gd}$ | $\sigma_{Gd}$ |
|---------------|-----------|-------|----------|------------|----------|-------------|---------------|
| SN134         | 30        | 10    | 4.6      | 3          | 19.8     | 2.8         | 2.1           |
| SN135         | 30        | 15.8  | 4.8      | 3          | 18.2     | 2.8         | 2.6           |
| SN136         | 30        | 19.2  | 4.8      | 4.3        | 19.4     | 2.8         | 3.4           |
| SN137         | 30        | 28.2  | 4.8      | 8          | 19.5     | 3           | 3.4           |
| SN138         | 30        | 4.8   | 4.3      | 7          | 20       | 2.8         | 5.5           |

Table 4.5: This table summarises the thicknesses,  $t$  ( $\text{\AA} \pm 2\text{\AA}$ ) and roughness values  $\sigma$  ( $\text{\AA} \pm 1\text{\AA}$ ) for the U/Gd series of samples.  $\rho_U$  and  $\rho_{Gd}$  are the average density of the uranium and gadolinium layers  $\times 10^{28} \text{U/m}^3$  respectively.

power set to 50W and the uranium power set to 4W in order to create a U-Gd alloy with  $\sim 5\%$  U. It was not possible to resolve the thickness (Keissig) fringes from the X-ray reflectivity spectrum, but the amount of sputtered material was estimated from the parameters derived for previous samples sputtered at higher rates to give U-Gd ( $160\text{\AA}/2500\text{\AA}$ ).

#### 4.2.6 Summary Analysis

The general good quality of multilayer samples in all cases is supported by the form of the measured X-ray reflectivity profiles. The relative growth properties of U/Fe samples grown on sapphire substrates with niobium buffer and capping layers, can be compared to those grown previously on glass with no buffer or capping layers [18], by comparing relative thickness and roughness parameters. The roughness of layers in the latter, although  $\sim 1 - 2\text{\AA}$  larger for samples of similar layer thickness, are of approximately the same magnitude, indicating that the bilayer growth mechanisms are the same in both cases and that the majority of the roughness stems from the relative lattice mismatch and crystalline nature of the respective species. The slightly reduced roughness can be observed as an effect of the smooth substrate surface and low roughness value of the niobium buffer layer.

The structure used to model the U/Fe bilayer system is the same in both studies;

by separating the iron layer into three strata of different density. One low density, amorphous, non-magnetic layer of  $\sim 5\text{\AA}$ , a possible consequence of an interdiffused U-Fe alloy region. The next layer is  $\sim 10\text{\AA}$  of amorphous iron that has a magnetisation reduced from that in the bulk, and the remainder of the iron layer is modeled with full density and magnetisation attributed to that observed in bulk crystalline bcc iron. This model is supported by results obtained in polarised neutron reflectivity (see Chapter 5), Mossbauer [18] [19] and SQUID magnetometry measurements (see Chapter 5) and can be understood as a model of the growth of layers with a large mismatch in lattice spacings,  $\sim 20\%$ . It should be noted at this point that it would also be possible to model the three separate iron components in a two layer model of full and reduced moment, bulk and reduced density respectively.

The U/Co system yielded much the same bulk properties as those observed for the U/Fe series of samples. A magnetic 'dead' layer was revealed by a  $t_{\text{Co}}$  dependence of the saturation magnetisation, which was further supported by PNR results requiring the inclusion of a dramatically reduced magnetic moment, reduced density component of the cobalt layers in order to reproduce the observed reflectivity profiles. The lattice mismatch in this case is  $\sim 30\%$  along the a-axis and  $\sim 15\%$  along the b-axis, leading to a similarly incoherent growth observed in the U/Fe series.

All three uranium/gadolinium series of samples were modelled with a simple bilayer structure, since magnetisation measurements had not revealed the presence of any substantial 'dead' layer, requiring a stratified density gadolinium layer. For thick uranium layers a large number of Bragg peaks were observed over a wide Q range, characterised by a low rms roughness. For an equivalent bilayer thickness, but with thick gadolinium layers, the roughness was much larger possibly caused by a more columnar crystal growth, resulting in a step-like roughness profile. The large difference between the X-ray reflectivity in these two cases was not apparent for similar situations in the U/Fe and U/Co systems.

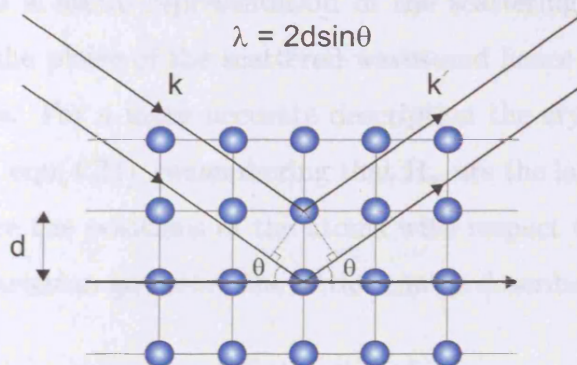


Figure 4.17: Illustration of Bragg's law in the case of a 2D square lattice.

### 4.3 X-ray Diffraction

The previous sections have dealt with the use of X-rays to probe the physical composition of the multilayers on length scales  $\sim 10 \rightarrow 1000 \text{ \AA}$ , including measurements perpendicular to and within the plane of the sample. It is also important however, to be able to determine the crystal structure and orientation of the respective layers and various properties of the crystallites that have formed. A study of this type gives insight into the growth mechanisms and interfacial structure of the multilayer samples. X-ray diffraction is the most commonly used and readily available tool for the investigation of these properties. In the case of experiments considered in this thesis the diffracting volume was small and the scattering was weak. This implies that the Born approximation of the X-ray-sample interaction is valid and that the kinematical approximation of X-ray diffraction holds, where multiple scattering effects can be ignored.

The basic understanding of X-ray diffraction stems directly from the X-ray scattering theory discussed earlier, principally from the scattering of X-rays from a collection of atoms arranged in a periodic lattice, eqn.(4.24).

It is first possible to generate a simple understanding of the scattering mechanism from crystal planes using Bragg's law, Figure 4.17

$$n\lambda = 2d \sin \theta \quad (4.47)$$

Although this is a useful representation of the scattering mechanism it lacks information about the phase of the scattered waves and hence cannot calculate the diffracted intensities. For a more accurate description the crystal structure factor must be considered, eqn(4.24), remembering that  $\mathbf{R}_n$  are the lattice vectors defining the lattice and  $\mathbf{r}_j$  are the positions of the atoms with respect to a lattice site. In a three dimensional cartesian geometry the lattice can be described by a set of vectors,

$$\mathbf{R}_n = n_1\mathbf{a}_1 + n_2\mathbf{a}_2 + n_3\mathbf{a}_3 \quad (4.48)$$

In this case  $\mathbf{a}_1$ ,  $\mathbf{a}_2$  and  $\mathbf{a}_3$  are the lattice basis vectors and  $n_1$ ,  $n_2$ ,  $n_3$  are integers. All known crystal structures can be described by 32 point groups and 230 possible symmetry groups, considering the combination of all of the possible symmetries of the basis with those of the lattice.

On describing the diffraction of X-rays from a crystal lattice, the scattered intensities are a consequence of atoms lying in common planes. Miller indices (h,k,l) can be used to describe the scattering planes of a crystal, such that  $\frac{a_1}{h}$ ,  $\frac{a_2}{k}$  and  $\frac{a_3}{l}$  define the intercepts of the plane on the  $\mathbf{a}_1$ ,  $\mathbf{a}_2$  and  $\mathbf{a}_3$  axes.

The lattice sum contained within eqn(4.24) implies that when the phases of the scattered waves are a multiple of  $2\pi$  the condition below is satisfied, at all other phases the sum is  $\sim$ unity.

$$\mathbf{Q} \cdot \mathbf{R}_n = 2\pi n \quad (4.49)$$

It is possible to solve this equation by generating a set of lattice vectors in reciprocal (wavevector) space ( $\mathbf{b}_1$ ,  $\mathbf{b}_2$ ,  $\mathbf{b}_3$ ) where,

$$\mathbf{b}_1 = \frac{\mathbf{a}_2 \times \mathbf{a}_3}{\mathbf{a}_1 \cdot \mathbf{a}_2 \times \mathbf{a}_3}, \mathbf{b}_2 = \frac{\mathbf{a}_3 \times \mathbf{a}_1}{\mathbf{a}_1 \cdot \mathbf{a}_2 \times \mathbf{a}_3}, \mathbf{b}_3 = \frac{\mathbf{a}_1 \times \mathbf{a}_2}{\mathbf{a}_1 \cdot \mathbf{a}_2 \times \mathbf{a}_3} \quad (4.50)$$

$$\mathbf{a}_i \cdot \mathbf{b}_j = 2\pi\delta_{ij} \quad (4.51)$$

The delta function  $\delta_{ij}$  is defined such that  $\delta_{ij} = 1$  if  $i = j$  and  $\delta_{ij} = 0$  if  $i \neq j$ .

The reciprocal lattice,  $\mathbf{G}$  can then be described by a set of basis vectors and integers in a similar manner to the lattice in real space.

$$\mathbf{G} = h\mathbf{b}_1 + k\mathbf{b}_2 + l\mathbf{b}_3 \quad (4.52)$$

$$\mathbf{G} \cdot \mathbf{R}_n = 2\pi(hn_1 + kn_2 + ln_3) \quad (4.53)$$

This scalar product of the real and reciprocal lattices shows that for the condition of constructive interference from a crystal  $\mathbf{Q}$  must coincide with a reciprocal lattice vector. This situation is known as the Laue condition, which can be expressed mathematically as,

$$\sum_{\mathbf{R}_n} e^{i\mathbf{Q} \cdot \mathbf{R}_n} = Nv_c^* \delta(\mathbf{Q} - \mathbf{G}) \quad (4.54)$$

where  $N$  is the number of unit cells and  $v_c^*$  is the unit cell volume in reciprocal space. For a lattice in real space with separation  $d$ , the corresponding separation in reciprocal space is given by  $\frac{2\pi}{d}$ . Since  $\mathbf{G} = \mathbf{Q}$  and  $Q = 2k \sin \theta$  then  $n\lambda = 2d \sin \theta$  and we have an equivalence to Bragg's law eqn(4.47) by invoking the Laue condition of diffraction.

Diffraction events that satisfy this condition can be visualised in reciprocal space by constructing an Ewald sphere of reciprocal lattice points. A two-dimensional representation, known as an Ewald circle is shown in Figure 4.18. This figure shows a reciprocal lattice with an incident X-ray beam originating at  $A$  and terminating at the origin,  $O$ . The incident beam is labelled  $\mathbf{k}$  and the diffracted beam  $\mathbf{k}'$ . A circle is then drawn of radius  $\mathbf{k}$ , centred at  $A$  and passing through the origin. Any lattice points which fall on the circle then satisfy the Laue condition and provide a diffracted intensity.

In order to obtain information about the scattered intensity though, the differential scattering cross-section must be considered.

$$\left( \frac{d\sigma}{d\Omega} \right) = r_0^2 P |F^{uc}(Q)|^2 Nv_c^* \delta(\mathbf{Q} - \mathbf{G}) \quad (4.55)$$

In this case  $F^{uc}(Q)$  is the unit cell structure factor,

$$F^{uc} = \sum_{n=1}^N f_n(Q) e^{2\pi i(hu_n + kv_n + lw_n)} \quad (4.56)$$

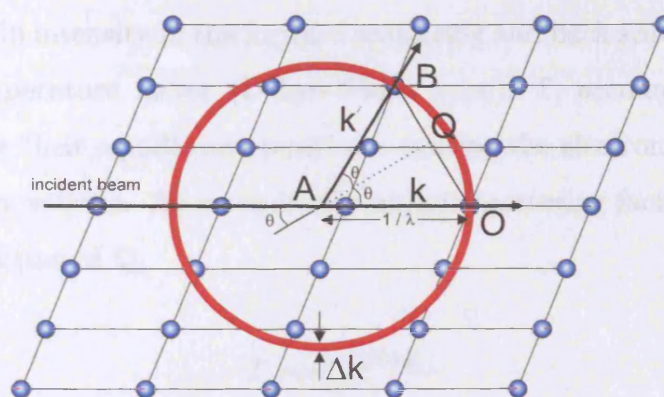


Figure 4.18: A 2D illustration of the Ewald sphere, the Ewald circle is used to visualise diffraction events in reciprocal space. The figure shows the fulfilment of the Laue condition (coincidence of the Ewald circle and reciprocal lattice point) so that a diffraction peak is observed if the detector is placed in the direction of  $\mathbf{k}'$

This form factor describes a unit cell in which the coordinates of the atom are  $u$ ,  $v$ , and  $w$ .  $f_n(Q)$  is the Fourier transform of the electron density, giving the atomic form factor of the  $n$ th atom. There are however, several multiplicative factors which affect the intensity of the diffracted beam:

A) The polarisation factor,  $p$ , arises because the electron does not scatter along its direction of vibration, but radiates in other directions with an intensity proportional to  $\sin^2 \alpha$  where  $\alpha$  is the angle between the scattered photon and the oscillation direction of the electron. So, for an unpolarised incident beam the polarisation factor is,

$$p = \frac{1 + \cos^2 2\theta}{2} \quad (4.57)$$

B) The Lorentz factor,  $L$  is a geometrical factor that corrects the intensity for different rates at which the reciprocal lattice points intersect the Ewald sphere.  $L$  depends on the measurement technique used, but for  $\theta - 2\theta$  and  $\omega - 2\theta$  scans,

$$L = \frac{1}{\sin 2\theta} \quad (4.58)$$

The polarisation and Lorentz factors are often described together as the Lorentz-polarisation factor, which results in a decrease in intensity at intermediate angles

and an increase in intensity in the forward scattering and back scattering geometries.

C) The temperature factor (Debye-Waller type),  $T$ , accounts for the atomic vibrations about their equilibrium positions, causing the electron density to spread out over a larger volume. As a result, the atomic scattering factor decreases more rapidly as a function of  $Q$ .

$$T = e^{-\frac{1}{2}Q^2\langle u_{Q,n}^2 \rangle} \quad (4.59)$$

where  $\langle u^2 \rangle$  is the mean square displacement of the atomic vibration.

D) The multiplicity factor considers the isotropic distribution of crystallite orientations, where there will be several sets of hkl-planes with different orientations in a crystal, but with the same  $d$  and  $F^2(Q)$  values.

E) The absorption factor,  $A$  considers the angle-dependent absorption within a sample and is dependent on the type of sample. For a multilayer thin film,

$$A = 1 - e\left(-\frac{2\mu\tau}{\sin\theta}\right) \quad (4.60)$$

where  $\mu$  is the absorption coefficient and  $\tau$  is the total film thickness.

### 4.3.1 X-ray Diffraction from Multilayers

So far, we have dealt with diffraction arising from ideally imperfect, infinitely large crystals free of any strain effects. From observations of the in-situ RHEED patterns of the multilayers it is likely that due to the lattice mismatch between the substrate, buffer (Nb) and multilayer and the mismatch between the constituent layers themselves, the samples considered here will be principally comprised of polycrystalline layers with a preferred orientation and a range of crystallite sizes, see table 2.1. Table 4.6 summarises all of the possible information that can be gleaned, using X-ray diffraction on a variety of multilayer types.

The systems under investigation in this thesis tend towards a textured polycrystalline layer structure. X-ray diffraction patterns of these samples should reveal corroborating evidence for the composition and thickness of the respective layers determined from the X-ray reflectivity measurements and indicate the crystallite

| Structure Type           | Relaxation | Distortion | t | Orientation | Defects |
|--------------------------|------------|------------|---|-------------|---------|
| Perfect epitaxy          |            |            |   | ×           |         |
| Nearly perfect epitaxial |            |            |   | ×           | ×       |
| Textured epitaxial       | ×          | ×          | × | ×           | ×       |
| Textured polycrystalline |            | ×          | × | ×           |         |
| Perfect polycrystalline  |            | ×          | × |             |         |
| Amorphous                |            |            |   |             |         |

Table 4.6: This table summarises the different structural properties of multilayer thin films that can be investigated, using X-ray diffraction (t is the mean crystallite size). It should be noted that the thickness and composition of the layers can be probed for all sample types.

sizes and preferred orientation.

The powder diffraction method is commonly used to determine the physical properties of polycrystalline materials. In this instance the sample angle,  $\theta$  and the detector angle,  $2\theta$  are variable and the incident X-ray wavelength,  $\lambda$  is fixed. For an infinitely thick crystallite, the diffracted beam would only occur at the exact position of the Bragg angle with an intensity of infinitesimal width. As the crystallites become smaller the diffraction peaks become wider see Figure 4.19 below.

Using this treatment of the X-ray diffraction it is possible to show a relationship between the mean crystallite size, t and the width of the diffraction peak, B, where  $B \approx \frac{1}{2}(2\theta_1 - 2\theta_2) = \theta_1 - \theta_2$ . The mean size of the crystallite can be understood as the product of the distance between scattering planes, d and the number of scattering planes, m. Using Bragg's law,  $2t \sin \theta_1 = (m + 1)\lambda$  and  $2t \sin \theta_2 = (m - 1)\lambda$ , which when subtracted gives,

$$2t \cos \left( \frac{\theta_1 + \theta_2}{2} \right) \sin \left( \frac{\theta_1 - \theta_2}{2} \right) = \lambda \quad (4.61)$$

Since  $\theta_1 + \theta_2 \approx 2\theta_B$  and from the small angle approximation,  $\sin \left( \frac{\theta_1 - \theta_2}{2} \right) \approx \left( \frac{\theta_1 - \theta_2}{2} \right)$  it is possible to define the crystallite size in terms of the wavelength of incident radiation,  $\lambda$ , the Bragg angle  $\theta_B$ , the range of angles at half maximum intensity B (rads) and a numerical constant,  $K = 0.9394$  known as the Scherrer constant [60].

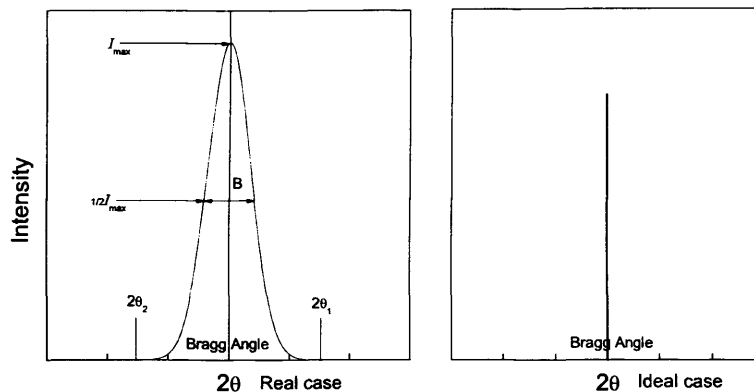


Figure 4.19: A comparison of the diffraction peaks observed for an ideal crystal and a sample comprised of a number of crystallites of finite size

The formula is known as the Scherrer formula,

$$t = \frac{K\lambda}{B \cos \theta_B} \quad (4.62)$$

Previous results on U/Fe systems [18] modelled the X-ray diffraction as resultant from an amorphous/crystalline bilayer composition. In this instance a peak was observed at the Fe bcc (110) position and a broad hump was present at the  $\alpha$  – U ortho-rhombic (110) position, allowing a simulation of the diffraction profile by considering the iron layers to be polycrystalline in a preferred orientation and the uranium layers as amorphous. The incoherent growth of these samples is mainly due to the lattice mismatch between the close-packed planes of the iron and uranium layers  $\sim 25\%$ .

Summaries of the X-ray diffraction from series of samples considered within this thesis can be seen in figures 4.22, 4.24, 4.26, 4.28 and 4.30. U/Fe and U/Co systems exhibit characteristics of amorphous/crystalline structures, whereas the diffraction from U/Gd samples resembles that of a coherent multilayer or superlattice structure, where the difference between the respective lattice parameters are  $< 5\%$ .

Schuller in 1980 was the first to report the sequential deposition of ultrathin layers of dissimilar metals and the subsequent diffraction profiles [61]. The diffracted intensity was given by,

$$I \propto \frac{1 + \cos^2 2\theta}{\sin \theta \sin 2\theta} \left| \sum_{j=1}^n e^{-W_A(\sin \theta/\lambda)^2} f_A(\theta) \sigma_A e^{iQx_j} + \sum_{j=1}^m e^{-W_B(\sin \theta/\lambda)^2} f_B(\theta) \sigma_B e^{iQx_j} \right|^2 \quad (4.63)$$

The prefactor includes the polarisation, Lorentz and geometric terms. The scattering functions are labelled  $f_A$  and  $f_B$  for elements A and B, comprising a superlattice structure.  $\sigma_A$  and  $\sigma_B$  represent the atomic plane densities for the planes of preferred orientation of the growth direction.  $x_j$  is the position of the  $j$ th atomic plane,  $n/m$  are the number of planes of element A/B in a layer and  $W_A$  and  $W_B$  are the Debye/Waller coefficients of the respective elements.

Clemens showed that by including variations in layer thicknesses, distinctive trends could be seen in the X-ray diffraction for coherent structures. For very thin samples, a broad peak was observed, overlapping the region where the peaks from the individual elements would be expected. Satellites were seen either side of this peak, relating to the bilayer repeat distance. For samples with thicker layers it was possible to begin to resolve the peaks from the each of the elements; the evolution of the diffraction pattern can be seen in figure 4.20.

The X-ray diffraction measurements of all of the systems described in the body of this thesis were simulated by the SUPREX refinement program written by Schuller, Fullerton, Vanderstraeten and Bruynseraede [62], using a kinematic diffraction model. This software is based on the original premises for high angle diffraction from superlattices set out by Schuller [61] and includes modifications to account for layer thickness fluctuations [63] and cumulative disorder [64] effects. The layer thickness fluctuations that can exist in amorphous/crystalline (U/Fe and U/Co) and crystalline/crystalline (U/Gd) superlattices behave very differently, which has implications for the observed diffraction patterns for these structures. The layer thickness fluctuations in the latter are discrete, since the crystalline coherency confines the fluctuations in layer thickness to multiples of the plane spacing of either of the constituent materials. Amorphous/crystalline superlattices can have continuous fluctuations that can be modelled as a gaussian distribution that causes loss of resolution of superlattice lines.

The theoretical treatment described by Sevenhans [64] is used to model the

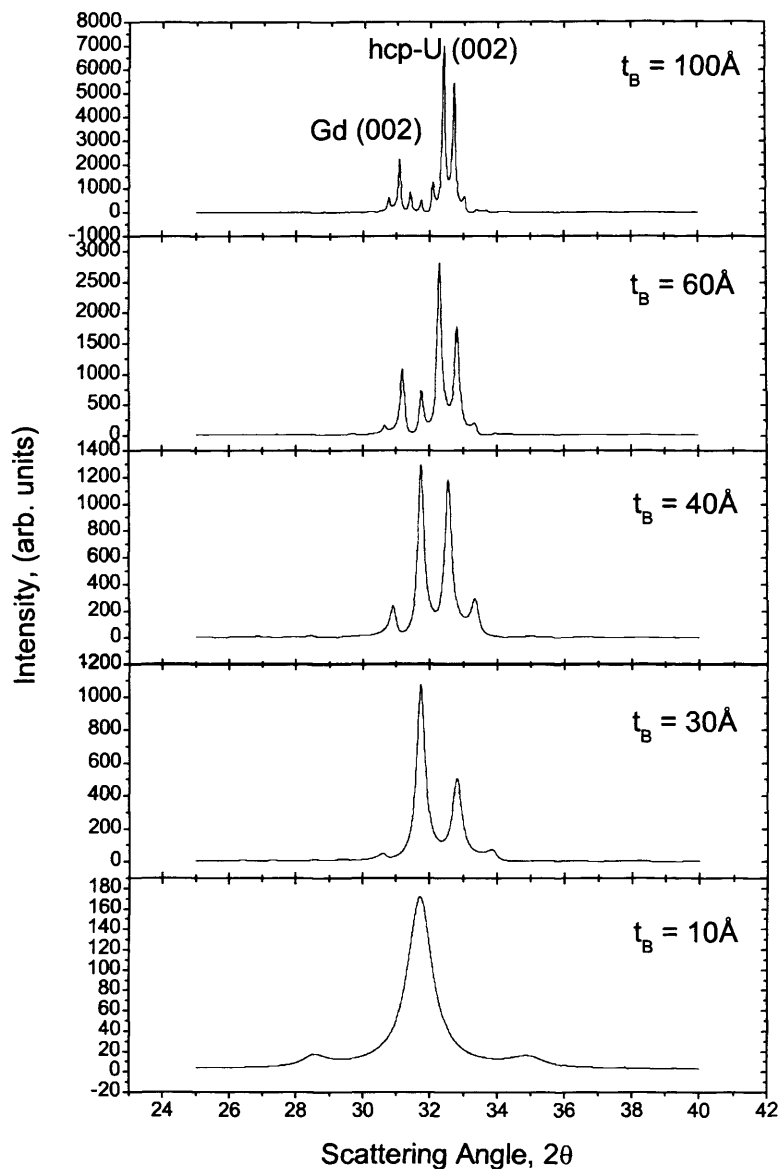


Figure 4.20: Example of an hcp-U/Gd multilayer diffraction pattern as the bilayer repeat distance,  $t_B$  is increased. It is possible to resolve the hcp-U (002) and Gd (002) peaks when values of  $t_{Gd}$  and  $t_U$  are large.

diffraction from amorphous/crystalline systems, such as the U/Fe and U/Co series, which assumes the amorphous layer, in this case uranium, to have a constant scattering density. The scattering amplitude is then given by,

$$A(Q) = \sum_{n=0}^{N-1} e^{iQnd} f(Q) \left\{ 1 + e^{iQ(a_1+Nd)} + e^{iQ(a_1+a_2+2Nd)} + \dots + e^{iQ[\sum_{j=1}^{M-1} a_j + (M-1)Nd]} \right\} \quad (4.64)$$

where the multilayer comprises  $M$  bilayers of  $N$  crystalline layers with scattering power  $f(Q)$  and interlayer spacing  $d$ . Each bilayer includes an amorphous layer of low scattering power and thickness  $a_j$ . Complexity is added to the model by including random fluctuations of the amorphous layer thickness, where the average value is denoted  $\bar{a}$  and including lateral thickness variations along the plane of the film, described in the reflection of X-rays as the roughness.

The diffraction profile can be altered by non-cumulative disorder, considering only the variation in average position of one layer, by surface roughness and by the finite-crystallite size coherence length, but the factor attributed as having the greatest effect on the diffracted intensity from multilayers is that of cumulative disorder, where the exponent of the  $R$ th term in equation (4.64) is replaced by,

$$R\bar{a} + RNd + \sum_{j=1}^R \Delta a_j \quad (4.65)$$

where the average position of the  $R$ th layer,  $R\bar{a}+RNd$  is changed by the sum of the changes in average position of previous layers. This factor affects both the relative intensities and linewidths of the diffraction peaks. Assuming a gaussian distribution for the variation of  $\bar{a}$  with a width  $c^{-1}$  the intensity becomes,

$$I(Q) = f^2(Q) \frac{\sin^2(NQd/2)}{\sin^2(Qd/2)} \left[ M + 2 \sum_{j=1}^{M-1} (M-j) e^{(-Q^2j/4c^2) \cos[Qj(Nd+\bar{a})]} \right] \quad (4.66)$$

### 4.3.2 Experimental Method

The X-ray diffraction measurements described in the following sections were carried out at UCL on a Philips X'pert powder diffractometer in an asymmetric, specular geometry, where the incident X-ray beam was provided from a fixed Cu  $K\alpha$  tube source; the incident angle was varied by manipulating the sample angle  $\theta$  and detector/scattering angle  $2\theta$ . Summaries of the X-ray diffraction patterns can be seen

in figures 4.22, 4.24, 4.26, 4.28 and 4.30 for U/Fe, U/Co and three series of U/Gd samples respectively.

The diffraction curves were fitted to simulations of the chemical composition and crystal structure within the layers, using the SUPREX refinement program mentioned in the previous section. The input parameters require a description of the scattering power,

$$f(q) = \eta e^{-W(q/4\pi)^2} (f_0(q) + \Delta f' + i\Delta f'') \quad (4.67)$$

where the Debye-Waller coefficients,  $W$ , the in-plane atomic densities,  $\eta$ , the atomic scattering power,  $f_0(q)$  (as a function of  $q$ ) and the anomalous dispersion corrections,  $\Delta f'$  and  $\Delta f''$  provide the input.

It is then possible to choose between a crystalline/crystalline (type 0) or amorphous/crystalline (type 1) structural model, which include variables that describe the crystalline structure of the layers and that can be varied to improve the fit of the simulation. Figure 4.21 shows a representation of the way that a crystalline layer is constructed in this simulation for an element, A.

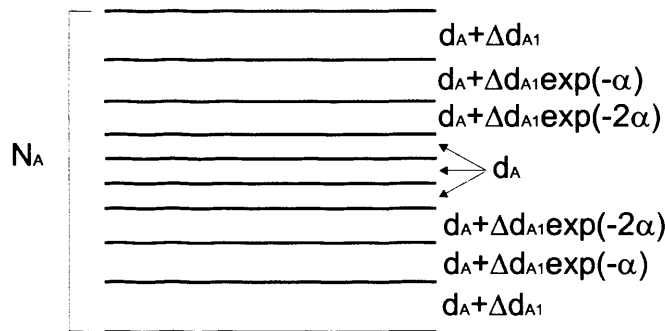


Figure 4.21: Lattice plane construction of a crystalline layer within a superlattice.

$N_A$  is the number of lattice planes within a layer and  $d_A$  is the distance between adjacent planes, with the strain described by variations in the distance between planes,  $\Delta d$ , which decays to  $d_A$  by an exponential factor  $\alpha$ . It is also possible to input properties describing the substrate and buffer layer into the simulation. For type 0 superlattices, which in our case includes the U/Gd series of samples, the fitted variables include the cumulative disorder,  $c$ ,  $d_{Gd}$ ,  $d_U$ ,  $\Delta d_{Gd1}$ ,  $\Delta d_{Gd2}$ ,  $\Delta d_{U1}$ ,

and  $\Delta d_{U_2}$ . For type 1 superlattices, U/Fe and U/Co systems, the uranium layer was modelled as amorphous, thus the atomic in-plane density was replaced by the atomic volume density and the fitted variables were simply  $c$ ,  $d_{Fe/Co}$  and  $\Delta d_{Fe/Co}$ . Due to the incoherence of these superlattices it was possible to determine the mean crystallite size from the simulation or by using the Scherrer equation. The vertical coherence length,  $\xi$ , could also be determined, since  $\xi = 2\pi/\Delta Q$ , where  $\Delta Q$  is the range in  $Q$  of the full-width, half-maximum of the crystalline peak.

The simulation program uses a Marquadt algorithm type fitting routine to give values of  $\chi^2$  and it is possible to choose the number of iterations of the fit and the tolerance at which the fitting routine will stop.

### 4.3.3 Results

The results are presented for the X-ray diffraction in an asymmetric  $\theta - 2\theta$  geometry for U/Fe, U/Co and U/Gd systems respectively. The normalised diffracted intensity is plotted against the scattering angle,  $2\theta$  for the summaries of each of the series of samples in order to qualitatively compare structural variations of the properties across the series. The fitted simulations of individual samples are plotted with the intensity in arbitrary units versus the wave-vector momentum transfer,  $Q$  ( $\text{\AA}^{-1}$ ).

This technique gives information about the chemical composition of the multilayers and the crystalline structure within the layers, including cumulative disorder, lattice strains and parameters that can describe the size of the crystallites in the case of polycrystalline materials. Experimental curves, including error bars for each sample are plotted together with the fitted, simulated X-ray diffraction profiles in the region of interest. An example of the fit over a wider range of  $Q$  is also given for one sample from each system.

### 4.3.4 Uranium/Iron

Figure 4.22 shows a summary of the X-ray diffraction patterns taken for the U/Fe series of samples. The intense peak at  $38^\circ$  in  $2\theta$  is due to the epitaxial sapphire substrate and the fringes that appear on the low angle side of the substrate peak are a

consequence of the  $\sim 50\text{\AA}$  thick niobium buffer layer. The closely packed  $\alpha$ -uranium (110), (021) and (002) peaks that were observed previously in the U/Fe multilayer system [18] sit at  $34.92^\circ$   $35.53^\circ$   $36.23^\circ$  for the Cu-K $\alpha$  wavelength. These peaks cannot be seen above the buffer diffraction peaks, whose intensity is a consequence of the crystalline quality of the niobium layer. However, it is possible to see an increase in the background intensity at the  $\alpha$ -uranium peak positions, dependent on the thickness of the uranium layers.

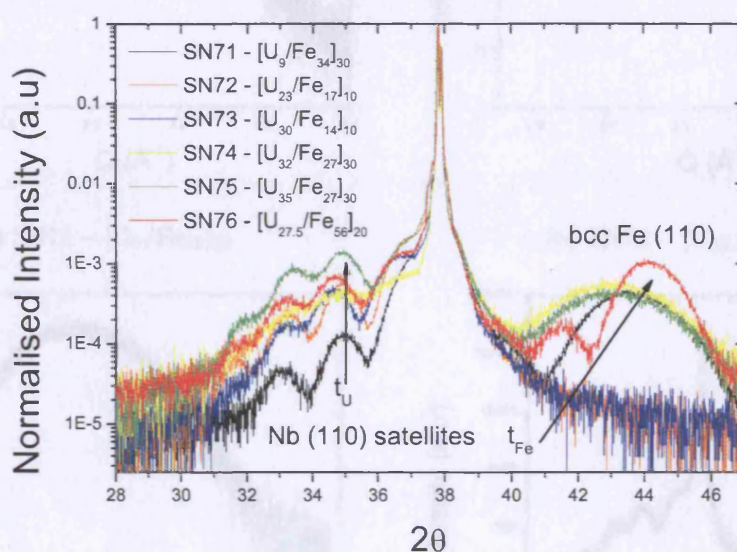


Figure 4.22: Comparison of the X-ray diffraction patterns close to the sapphire  $11\bar{2}0$  peak, for U/Fe samples listed in table 3.3.

The broad hump on the high-angle side of the substrate peak is close to the bulk bcc (110) iron position and there are no peaks at other allowed bcc Fe crystallographic directions, suggesting a preferred orientation in this growth direction. This confirms predictions, considering only the likely growth in the direction of the most closely packed plane as discussed in Chapter 3. The lack of any intensity at all at iron layer thicknesses of  $< 20\text{\AA}$  suggests that this is an approximate value for a crystalline limit, below which the growth would be expected to be amorphous and consequently of a reduced magnetisation. As  $t_{\text{Fe}}$  increases, the width of the hump becomes narrower and the peak intensity increases, its position moving closer to the bulk value for the bcc (110) position. The iron peaks have been simulated and fit to

the measured data to give values for the average lattice spacing in the z-direction, the thickness of the uranium layers (modelled as amorphous layers), values for the mean crystallite size and the vertical coherence length.

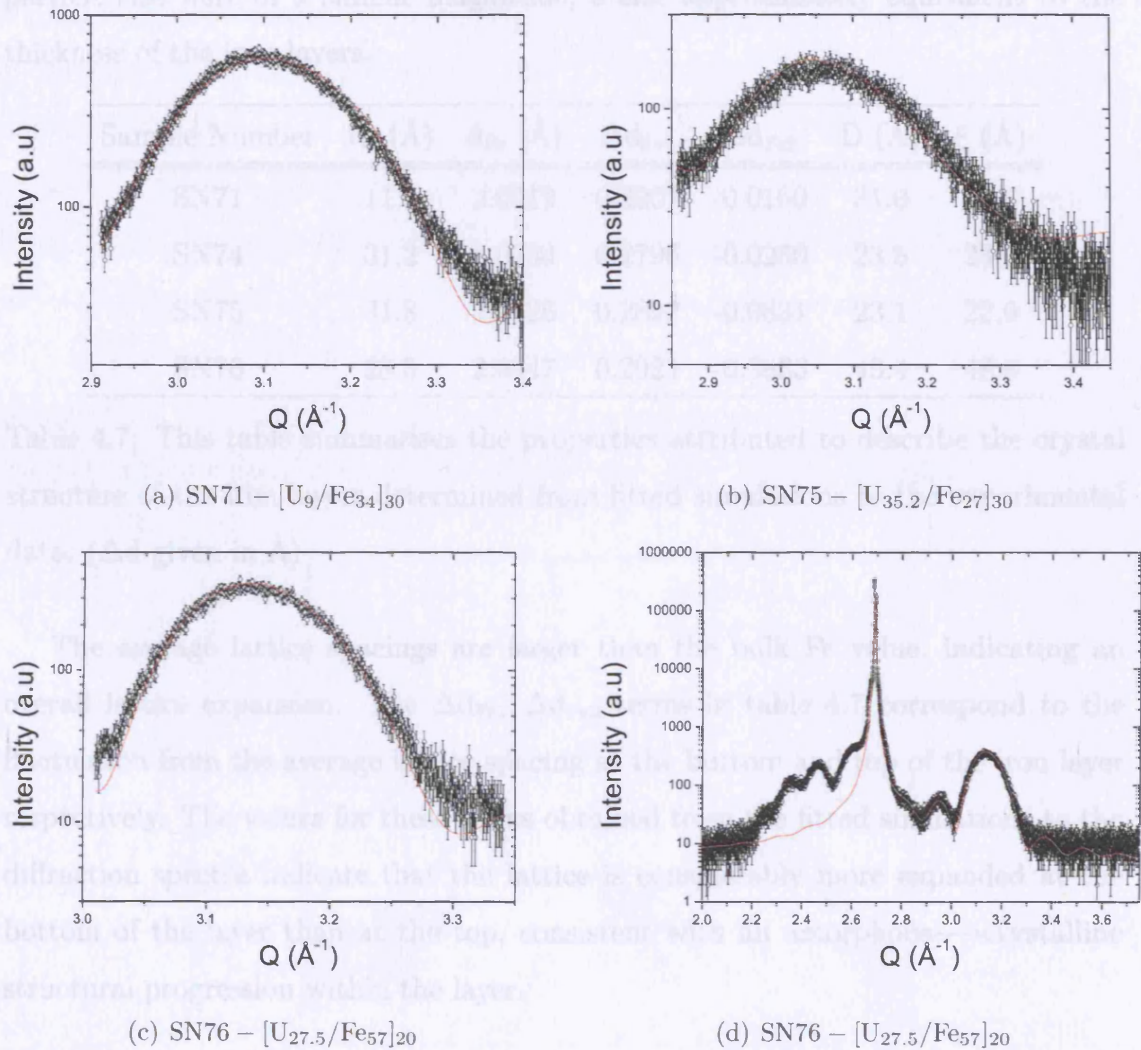


Figure 4.23: X-ray diffraction spectra of the iron component from the U/Fe series of multilayers for selected samples together with fitted curves produced by the SUPREX diffraction program.

Table 4.7 provides a summary of the properties obtained from fitted simulations of the high angle diffraction, examples of which can be seen in figure 4.23. Figure 4.23 (d) shows the entire range of the simulated diffraction pattern for sample SN76, including the intense sapphire substrate peak, but neglecting the niobium buffer contributions. Values of the uranium layer thicknesses are within  $\sim 2\text{\AA}$  of those

found using X-ray reflectivity. As the thickness of the iron layer is increased, the average value of the lattice spacing approaches that of the bulk value for a bcc (110 oriented) crystal,  $d \approx 2.0266 \text{ \AA}$ . Both the vertical coherence length and the average particle size were of a similar magnitude, a size approximately equivalent to the thickness of the iron layers.

| Sample Number | $t_U$ ( $\text{\AA}$ ) | $d_{\text{Fe}}$ ( $\text{\AA}$ ) | $\Delta d_{\text{Fe1}}$ | $\Delta d_{\text{Fe2}}$ | $D$ ( $\text{\AA}$ ) | $\xi$ ( $\text{\AA}$ ) |
|---------------|------------------------|----------------------------------|-------------------------|-------------------------|----------------------|------------------------|
| SN71          | 11.2                   | 2.0519                           | 0.3007                  | -0.0160                 | 31.0                 | 30.6                   |
| SN74          | 31.2                   | 2.0734                           | 0.2796                  | -0.0250                 | 23.5                 | 23.3                   |
| SN75          | 31.8                   | 2.0726                           | 0.2892                  | -0.0831                 | 23.1                 | 22.9                   |
| SN76          | 28.5                   | 2.0447                           | 0.2921                  | -0.5833                 | 49.4                 | 48.8                   |

Table 4.7: This table summarises the properties attributed to describe the crystal structure of the iron layers determined from fitted simulations to the experimental data. ( $\Delta d$  given in  $\text{\AA}$ )

The average lattice spacings are larger than the bulk Fe value, indicating an overall lattice expansion. The  $\Delta d_{\text{Fe1}}, \Delta d_{\text{Fe2}}$  terms in table 4.7 correspond to the fluctuation from the average lattice spacing at the bottom and top of the iron layer respectively. The values for these terms obtained from the fitted simulations to the diffraction spectra indicate that the lattice is considerably more expanded at the bottom of the layer than at the top, consistent with an amorphous  $\rightarrow$  crystalline structural progression within the layer.

### 4.3.5 Uranium/Cobalt

Figure 4.24 shows a summary of the X-ray diffraction patterns taken for several U/Co samples. In this figure it is possible to see the changing period of the niobium fringes on the low angle side of the sapphire substrate peak as the buffer thickness is changed, SN117 has  $\sim 50\text{\AA}$ Nb and SN118,  $\sim 100\text{\AA}$ Nb. It was not possible to see any effect of varying  $t_U$  on the observed diffracted intensity. The diffraction patterns for the U/Co series of samples are remarkably similar in character to those of the U/Fe system, since the position of the hcp (002) cobalt peak lies at almost exactly the same angle as the bcc (110) iron one. The nature of the broad hump on the high angle side of the substrate peak is then influenced by the thickness of the cobalt layers and a similar relationship can be observed between  $t_{Co}$  and the diffracted intensity of the cobalt layers as was seen for the U/Fe series of samples.

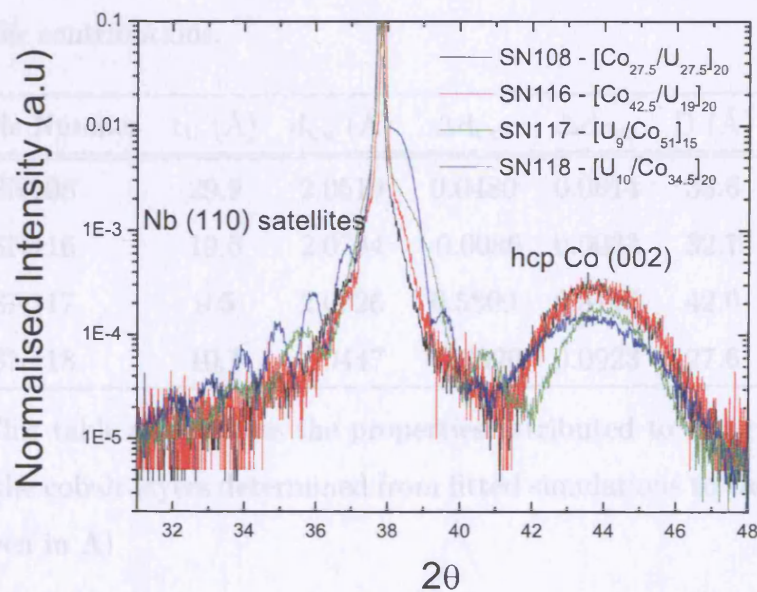


Figure 4.24: Comparison of the X-ray diffraction patterns close to the sapphire  $11\bar{2}0$  peak, for U/Co samples listed in table 3.4.

The observed intensity of the cobalt hcp (002) peak and no other peaks apparent at other allowed hcp Co crystallographic directions, indicates a preferred orientation in this growth direction, which is expected since it is the most closely packed plane within the hcp crystal structure. The absence of a diffraction peak at the

(002) position (not shown in figure 4.24) for samples with  $< 20\text{\AA}$  suggests a similar  $t_{\text{Co}}$ , crystalline limit as was observed for the U/Fe series. The presence of a non-crystalline, amorphous layer is a consequence of the large lattice mismatches (when comparing lattice planes in the preferred orientations of  $[110] \alpha - \text{U}$  and  $[001] \text{hcp cobalt}$ ) at the U-Co interface, and is evidenced in the SQUID magnetometry and PNR results discussed in Chapter 5.

The cobalt peaks were then simulated and fit to the measured data, see figure 4.25, to give values for the average lattice spacing in the z-direction, the thickness of the uranium layers (modelled as amorphous layers), values for the mean crystallite size and the vertical coherence length. Table 4.8 provides a summary of these parameters.

Figure 4.25 (e) shows the entire range of the simulated diffraction pattern for sample SN117, including the intense sapphire substrate peak, but neglecting the niobium buffer contributions.

| Sample Number | $t_{\text{U}}$ ( $\text{\AA}$ ) | $d_{\text{Co}}$ ( $\text{\AA}$ ) | $\Delta d_{\text{Co}1}$ | $\Delta d_{\text{Co}2}$ | $D$ ( $\text{\AA}$ ) | $\xi$ ( $\text{\AA}$ ) |
|---------------|---------------------------------|----------------------------------|-------------------------|-------------------------|----------------------|------------------------|
| SN108         | 29.9                            | 2.0519                           | 0.0480                  | 0.0614                  | 33.6                 | 33.2                   |
| SN116         | 19.5                            | 2.0734                           | -0.0086                 | 0.0033                  | 32.7                 | 32.3                   |
| SN117         | 9.5                             | 2.0726                           | 0.5809                  | 0.3117                  | 42.0                 | 41.4                   |
| SN118         | 10.1                            | 2.0447                           | -0.0090                 | 0.0923                  | 27.6                 | 27.3                   |

Table 4.8: This table summarises the properties attributed to describe the crystal structure of the cobalt layers determined from fitted simulations to the experimental data. ( $\Delta d$  given in  $\text{\AA}$ )

The simulated values of the uranium layer thicknesses derived from the X-ray diffraction data coincide ( $\pm 2\text{\AA}$ ) with those obtained from the X-ray reflectivity measurements summarised in table 4.2. The bulk value for the lattice separation in the cobalt  $[001]$  preferred orientation is  $d \approx 2.034\text{\AA}$  and the fitted values indicate an expanded lattice. However, the same relationship between  $t_{\text{Co}}$  and  $d_{\text{Co}}$  that could be seen between  $t_{\text{Fe}}$  and  $d_{\text{Co}}$  in the U/Fe system is not obvious. There is also no distinct relationship between the expansion of the average lattice spacing at the U/Co and Co/U interfaces. The vertical coherence length and the average particle

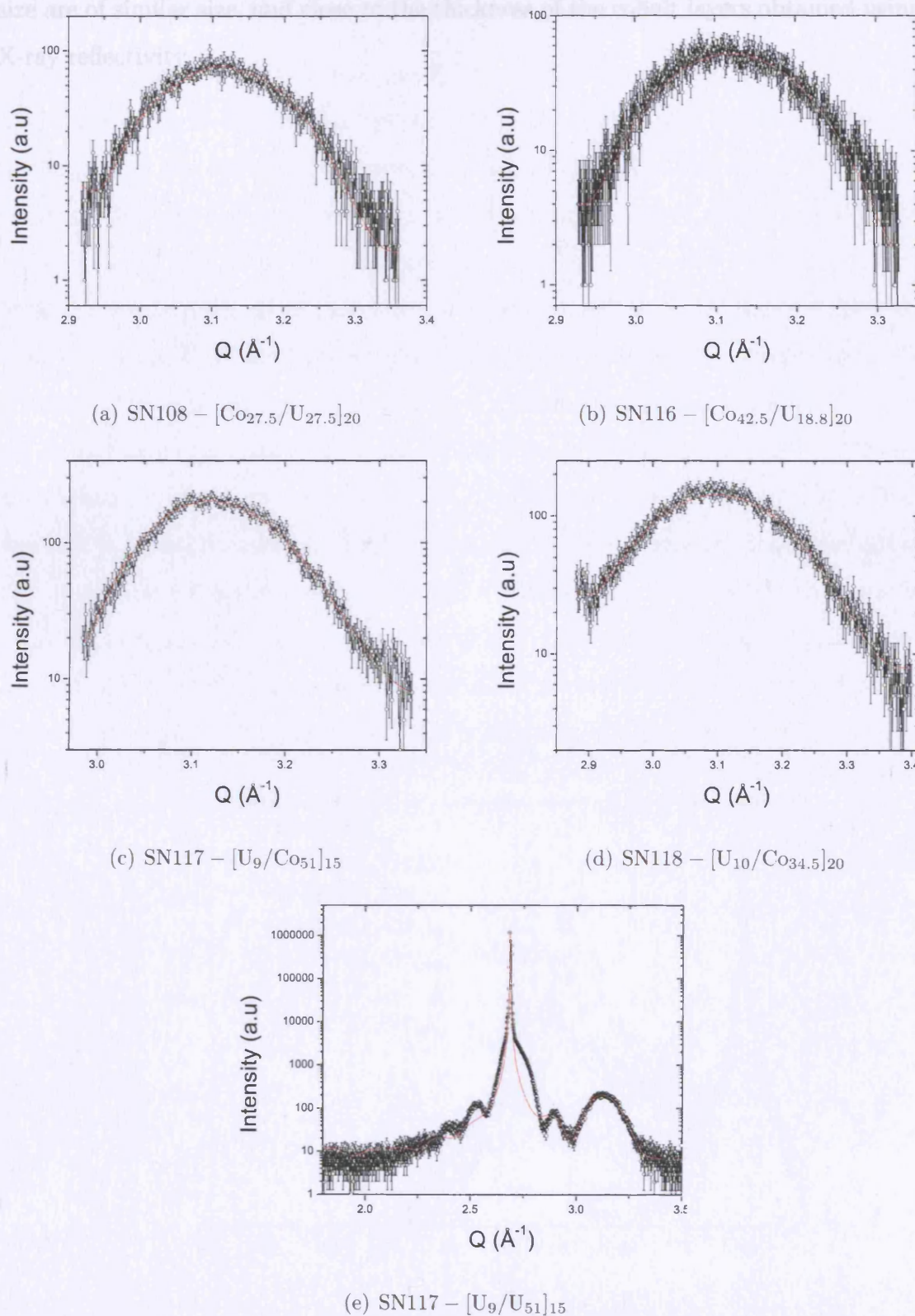


Figure 4.25: X-ray diffraction spectra of the cobalt component from the U/Co series of multilayers for selected samples together with fitted curves produced by the SUPREX diffraction program.

size are of similar size, and close to the thickness of the cobalt layers obtained using X-ray reflectivity.

### 4.3.6 Uranium/Gadolinium

Figure 4.26 shows a summary of the X-ray diffraction patterns taken for the 1st U/Gd series of samples. In this instance there are a number of striking differences in the form of the diffracted intensity between U/transition metal and U/Gd multilayers. The multilayer diffraction peaks sit on the low angle side of the sapphire substrate peak and their intensity reaches values up to one tenth of the intensity of the substrate peak, more than two orders of magnitude larger than the intensity observed in the U/Fe and U/Co systems. Superlattice peaks are observable in the vicinity of the  $2\theta$  positions, corresponding to a plane spacing in the growth direction, which indicates a relatively low structural size mismatch and a good registry between the different crystal structures at the U-Gd interfaces. The diffraction fringes from the highly crystalline niobium buffer layers are not observable in most cases above the multilayer diffraction peaks, although a contribution from the niobium can be observed as a shoulder on the low angle side of the substrate peak. A gadolinium film (SN62) of  $\sim 500\text{\AA}$  was grown to confirm the expected position of the diffraction peaks in the multilayer samples and this is shown in orange in figure 4.26.

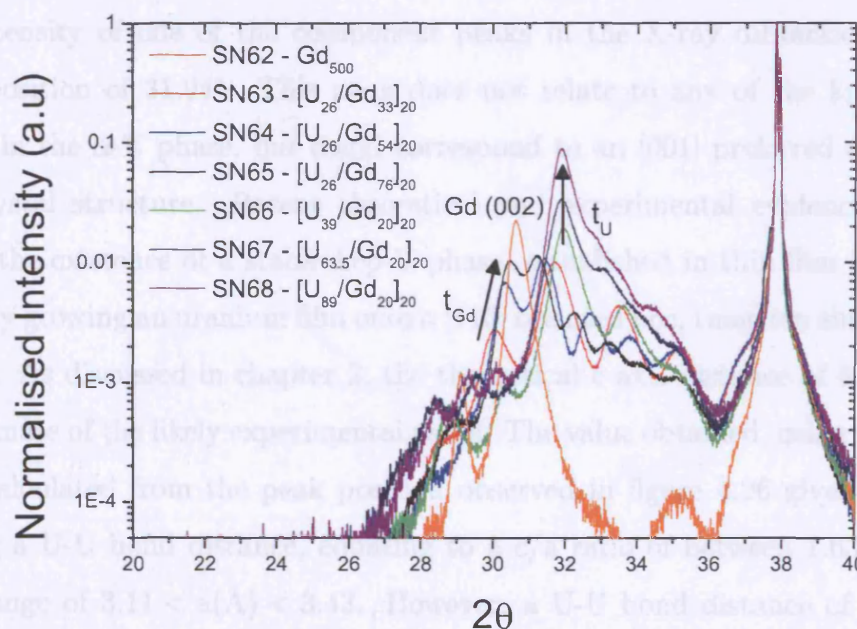


Figure 4.26: Comparison of the X-ray diffraction patterns close to the sapphire  $11\bar{2}0$  peak, for U/Gd samples listed in table 3.5.

This series was grown to investigate the relationship between  $t_{\text{Gd}}$  and  $t_{\text{U}}$  on the structural and magnetic properties of the U/Gd system. The observed diffraction patterns show a peak close to the bulk (002) reflection for the common hexagonal close-packed crystal structure, where  $a = 3.6310\text{\AA}$  and  $c = 5.7770\text{\AA}$ , giving a contraction from the hard sphere model for the  $c/a$  ratio (1.633) to 1.5910. In the case of the single film of gadolinium the (002) peak is centred at a  $2\theta$  value of  $30.58^\circ$ , corresponding to a  $c$ -axis lattice parameter of  $5.84\text{\AA}$ . It is also possible to observe intensity from the niobium buffer at  $\sim 35^\circ$  in  $2\theta$  and a peak at  $\sim 29^\circ$ , corresponding to the hcp (100) reflection. The hcp (100) position in the bulk sits at  $28.34^\circ$ . This shift to higher angle in the thin Gd film suggests a contraction of the lattice along the basal plane of  $\sim 2\%$  towards a value of  $a = 3.55\text{\AA}$  and a  $c/a$  ratio of  $\sim 1.65$ .

Indicated on figure 4.26, as  $t_{\text{Gd}}$  increases, there is a distinct increase in intensity of one of the component peaks in the diffraction patterns, close to the hcp (002) peak observed for the thin Gd film. This increase in intensity is accompanied by a shift in position from the low angle side of the (002) peak towards the thin film value, indicating a lattice expansion for thinner Gd layers.

As the uranium layer thickness,  $t_{\text{U}}$ , is varied there is a clearly visible increase in the intensity of one of the component peaks in the X-ray diffraction spectra, at a  $2\theta$  position of  $31.94^\circ$ . This peak does not relate to any of the known peak positions in the  $\alpha$ -U phase, but could correspond to an [001] preferred orientation hcp-U crystal structure. Recent theoretical and experimental evidence [39] [40] supports the existence of a stable hcp-U phase, established in thin film structures, specifically growing an uranium film onto a [110] oriented bcc, tungsten single crystal substrate. As discussed in chapter 2, the theoretical  $c$  axis distance of  $5.35\text{\AA}$  is an underestimate of the likely experimental value. The value obtained, using the lattice spacing calculated from the peak position observed in figure 4.26 gives  $c = 5.6\text{\AA}$ . Assuming a U-U bond distance, equating to a  $c/a$  ratio of between 1.633 and 1.8 gives a range of  $3.11 < a(\text{\AA}) < 3.43$ . However, a U-U bond distance of  $3.5\text{\AA}$  was observed in STM images of the hcp-U surface, suggesting a possible relaxation of the lattice at the surface, which might be reproduced at the interface of a multilayer thin film.

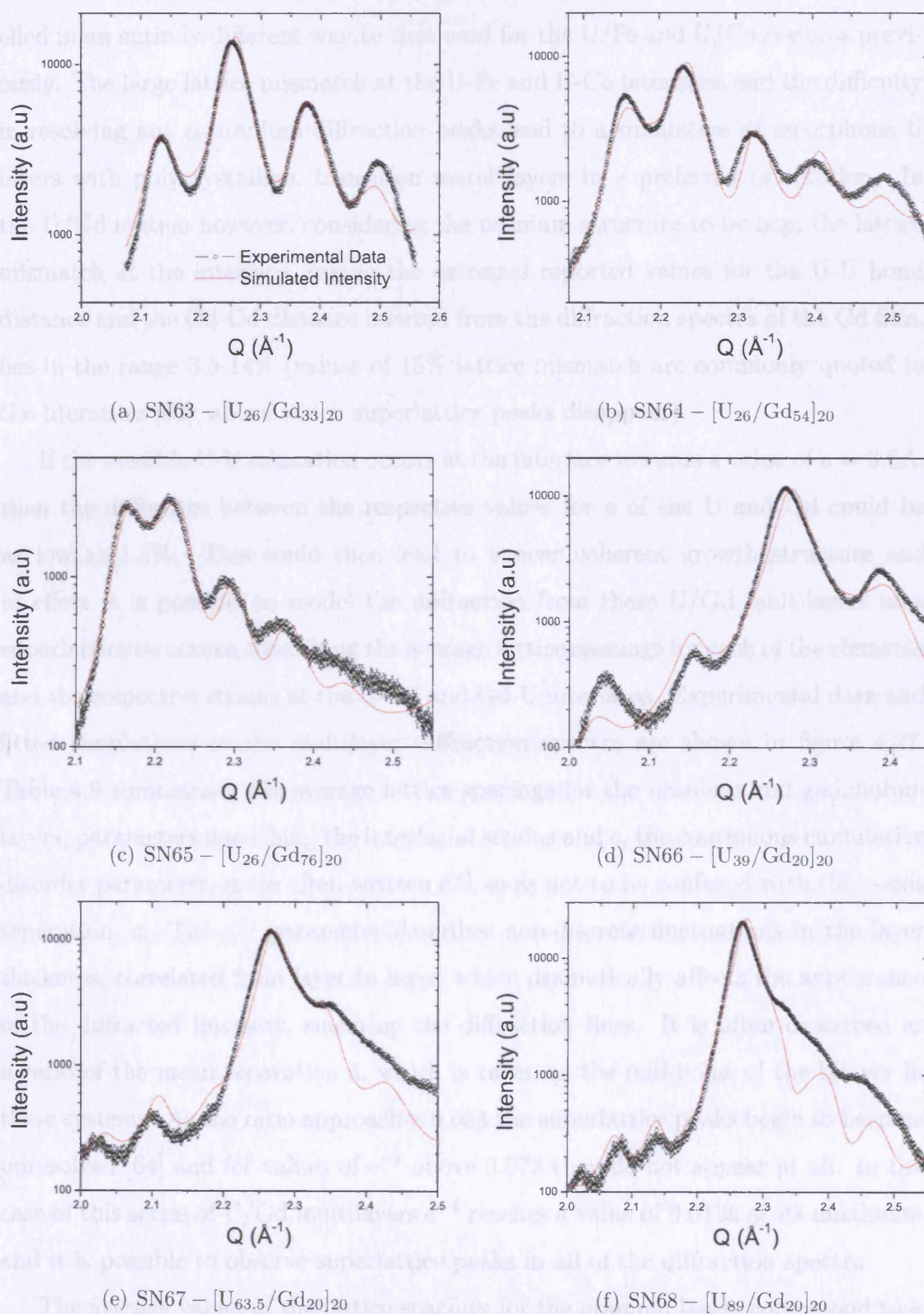


Figure 4.27: X-ray diffraction spectra of the 1st U/Gd series of multilayers with fitted curves simulated by the SUPREX diffraction program.

The simulation of the X-ray diffraction spectra from U/Gd multilayers was modelled in an entirely different way to that used for the U/Fe and U/Co systems previously. The large lattice mismatch at the U-Fe and U-Co interfaces and the difficulty in resolving any  $\alpha$ -uranium diffraction peaks lead to a simulation of amorphous U layers with polycrystalline, transition metal layers in a preferred orientation. In the U/Gd system however, considering the uranium structure to be hcp, the lattice mismatch at the interface, taking the extremal reported values for the U-U bond distance and the Gd-Gd distance inferred from the diffraction spectra of the Gd film, lies in the range 3.5-14% (values of 15% lattice mismatch are commonly quoted in the literature [63], above which superlattice peaks disappear).

If the possible U-U relaxation occurs at the interface towards a value of  $a = 3.5\text{\AA}$ , then the difference between the respective values for  $a$  of the U and Gd could be as low as 1.5%. This could then lead to a near coherent growth structure and in effect it is possible to model the diffraction from these U/Gd multilayers as a superlattice structure, describing the average lattice spacings for each of the elements and the respective strains at the U-Gd and Gd-U interfaces. Experimental data and fitted simulations to the multilayer diffraction spectra are shown in figure 4.27. Table 4.9 summarises the average lattice spacings for the uranium and gadolinium layers, parameters describing the interfacial strains and  $c$ , the continuous cumulative disorder parameter, more often written  $c^{-1}$  so as not to be confused with the  $c$ -axis separation,  $c$ . The  $c^{-1}$  parameter describes non-discrete fluctuations in the layer thickness, correlated from layer to layer, which dramatically affects the appearance of the diffracted intensity, smearing the diffraction lines. It is often described as a ratio of the mean separation  $\bar{a}$ , which is taken as the mid-point of the bilayer in these systems. As the ratio approaches  $0.05\bar{a}$  the superlattice peaks begin to become unresolved [64] and for values of  $c^{-1}$  above  $0.07\bar{a}$  they do not appear at all. In the case of this series of U/Gd multilayers  $c^{-1}$  reaches a value of  $0.013\bar{a}$  at its maximum and it is possible to observe superlattice peaks in all of the diffraction spectra.

The average values of the lattice spacings for the uranium layers correspond to a  $c$ -axis U-U distance of  $5.55 - 5.68\text{\AA}$ , close to that quoted by Berbil-Bautista [39] for hcp-U grown on tungsten. There is no obvious relationship between the respective

| Sample Number | $c^{-1}$ (Å) | $d_U$ (Å) | $d_{Gd}$ (Å) | $\Delta d_{U1}$ | $\Delta d_{U2}$ | $\Delta d_{Gd1}$ | $\Delta d_{Gd2}$ |
|---------------|--------------|-----------|--------------|-----------------|-----------------|------------------|------------------|
| SN63          | 0.3824       | 2.7774    | 3.0354       | -0.0378         | -0.3316         | -0.1962          | -0.1245          |
| SN64          | 0.5572       | 2.7772    | 2.9142       | -0.2916         | -0.0180         | 0.0319           | -0.0320          |
| SN65          | 0.6161       | 2.8390    | 2.9096       | -0.3830         | -0.0854         | 0.0451           | -0.0765          |
| SN66          | 0.3918       | 2.7899    | 2.9432       | -0.2230         | -0.0823         | 0.0424           | -0.0296          |
| SN67          | 0.2793       | 2.8081    | 3.1315       | -0.4343         | -0.1736         | -0.1238          | -0.1289          |
| SN68          | 0.3935       | 2.8054    | 2.9245       | -0.3971         | -0.1358         | -0.1597          | -0.1542          |

Table 4.9: This table summarises the properties attributed to describe the crystal structure of both the uranium and gadolinium layers for U/Gd series 1, modelled as a near coherent superstructure. ( $\Delta d$  given in Å)

layer thicknesses and calculated  $d_U$  values. However, the gadolinium lattice spacing,  $d_{Gd}$  has some dependence on the gadolinium layer thickness, such that it moves closer to the bulk value and the value observed for the Gd thin film at larger thicknesses (SN63-SN65). The average values for the lattice spacings of the gadolinium layers correspond to a c-axis Gd-Gd distance of  $5.82 - 6.26 \text{ \AA}$ , expanded from that observed in the bulk and the Gd thin film sample. There seems to be no obvious trend in the interfacial strains as a function of layer thickness, but the layers can generally be described as contracted from their average lattice spacing values at both U-Gd and Gd-U interfaces, forming a concertina type growth. The cumulative disorder, increases in magnitude as the gadolinium layer thickness increases, but there seems to be no observed  $t_U$  dependence.

Figure 4.28 shows a summary of the X-ray diffraction patterns taken for the 2nd U/Gd series of samples. This series was grown as a study of the effects of temperature, sputtering power and simply to see if it would be possible to grow thin (approaching  $10\text{\AA}$ ) crystalline layers. The thinnest of these films (SN122) had a bilayer thickness of just  $22.5\text{\AA}$  yet an appreciable diffracted intensity was still observable. It is clear that the crystalline limit for this multilayer system exists only for very thin layers.

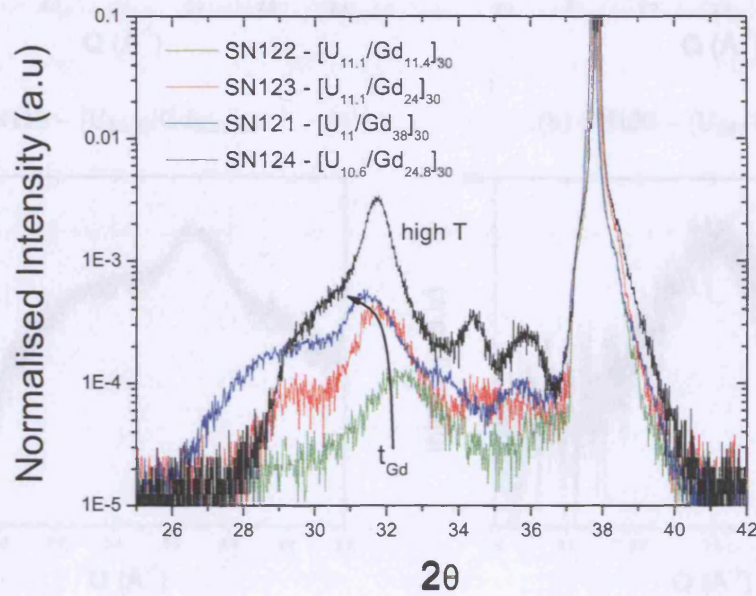


Figure 4.28: Comparison of the X-ray diffraction patterns close to the sapphire  $11\bar{2}0$  peak, for U/Gd samples listed in table 3.6.

All of the samples shown in figure 4.28 consist of thin uranium layers of approximately  $10\text{\AA}$ . The prominent peak in these diffraction spectra sits at the hcp-U peak position observed previously, which shifts to lower angles as the gadolinium layer thickness increases. This indicates that the uranium grows in a more crystalline nature than the gadolinium layers at low values of  $t_U$  and  $t_{Gd}$  respectively, and that as  $t_{Gd}$  increases the average U lattice spacing is increased, possibly as a consequence of the Gd crystallinity. Samples SN123 and SN124 share similar compositions, but were grown at room temperature and an elevated substrate temperature of 600K respectively. The diffracted intensity of the latter shares the same characteristics as that grown at room temperature, but carries an intensity that is more than an

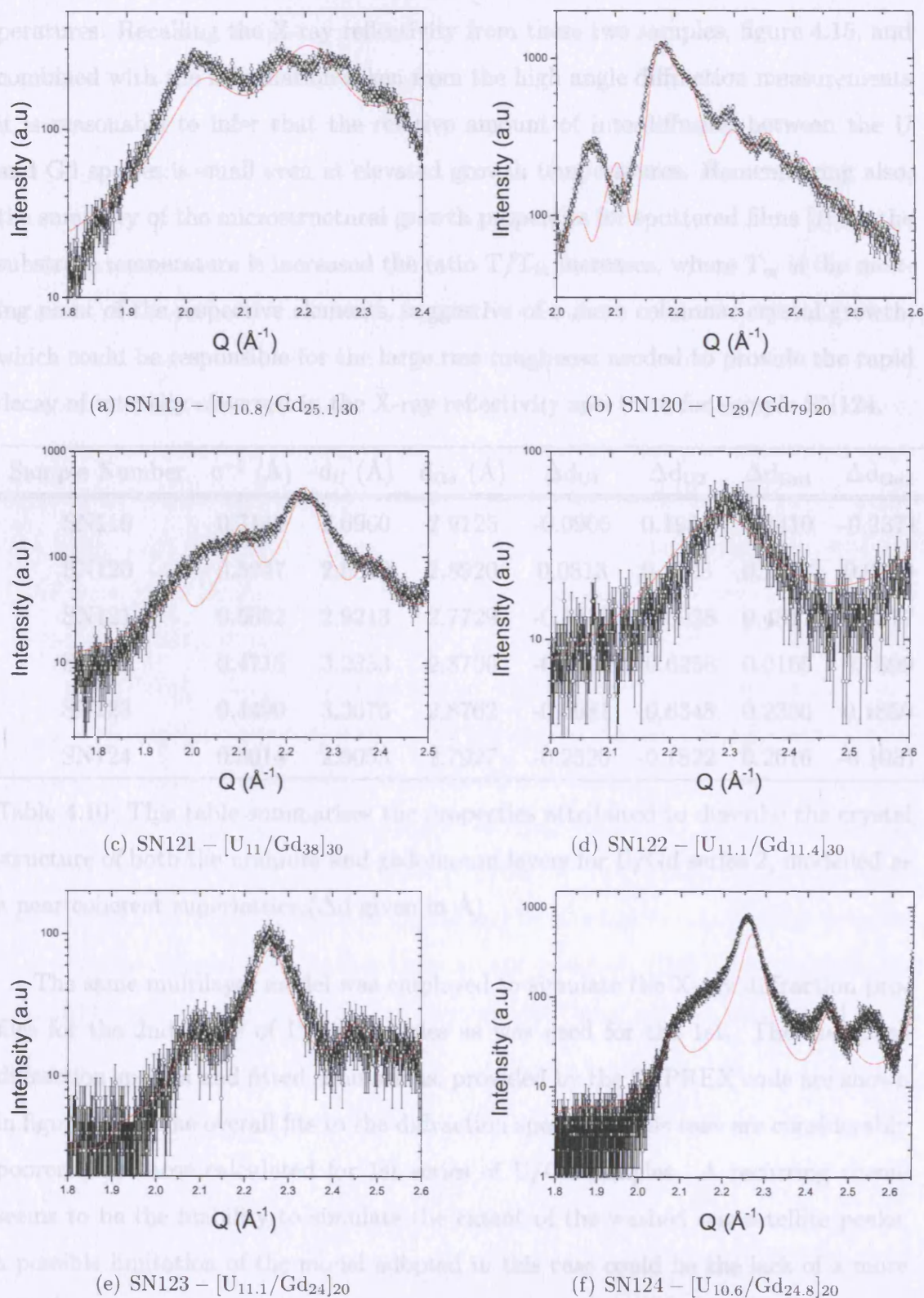


Figure 4.29: X-ray diffraction spectra of the 2nd U/Gd series of multilayers with fitted curves simulated by the SUPREX diffraction program.

order of magnitude greater, indicating a more crystalline assembly at elevated temperatures. Recalling the X-ray reflectivity from these two samples, figure 4.15, and combined with the information taken from the high angle diffraction measurements it is reasonable to infer that the relative amount of interdiffusion between the U and Gd species is small even at elevated growth temperatures. Remembering also, the summary of the microstructural growth properties for sputtered films [1], as the substrate temperature is increased the ratio  $T/T_m$  increases, where  $T_m$  is the melting point of the respective elements, suggestive of a more columnar crystal growth, which could be responsible for the large rms roughness needed to provide the rapid decay of intensity observed in the X-ray reflectivity spectrum for sample SN124.

| Sample Number | $c^{-1}$ (Å) | $d_U$ (Å) | $d_{Gd}$ (Å) | $\Delta d_{U1}$ | $\Delta d_{U2}$ | $\Delta d_{Gd1}$ | $\Delta d_{Gd2}$ |
|---------------|--------------|-----------|--------------|-----------------|-----------------|------------------|------------------|
| SN119         | 0.7148       | 2.6960    | 2.9125       | -0.0905         | 0.1984          | 0.2410           | -0.2371          |
| SN120         | 0.5247       | 2.6349    | 2.8920       | 0.0813          | 0.2225          | 0.2273           | 0.0230           |
| SN121         | 0.5652       | 2.9213    | 2.7729       | -0.1450         | -0.0928         | 0.4317           | 0.0877           |
| SN122         | 0.4715       | 3.2353    | 2.8706       | -0.6410         | -0.6258         | 0.0165           | 0.1599           |
| SN123         | 0.4490       | 3.3670    | 2.8762       | -0.5681         | -0.6348         | 0.2300           | 0.1850           |
| SN124         | 0.3014       | 2.9053    | 2.7927       | -0.2520         | -0.1822         | 0.2616           | -0.1037          |

Table 4.10: This table summarises the properties attributed to describe the crystal structure of both the uranium and gadolinium layers for U/Gd series 2, modelled as a near coherent superlattice. ( $\Delta d$  given in Å)

The same multilayer model was employed to simulate the X-ray diffraction profiles for the 2nd series of U/Gd samples as was used for the 1st. The measured diffraction spectra and fitted simulations, provided by the SUPREX code are shown in figure 4.29. The overall fits to the diffraction spectra in this case are considerably poorer than those calculated for 1st series of U/Gd samples. A recurring theme seems to be the inability to simulate the extent of the washed out satellite peaks; a possible limitation of the model adopted in this case could be the lack of a more complex strain profile at the interfaces or any component of diffusion. The general shapes however, are reproduced, so that the major structural parameters may still be reliable, although the more subtle lattice strains and disorder values may not.

Table 4.10 summarises the relevant properties fit to these diffraction spectra.

The average lattice spacing within the gadolinium layers, ranges between 2.7927 and 2.9125Å giving a *c*-axis distance of  $\sim 5.6 - 5.8\text{Å}$ , although there is no clear relationship between  $t_{\text{Gd}}$  and the size or variation in size of  $d_{\text{Gd}}$ . The uranium layers display a wider range of lattice spacings (2.6349 – 3.3670Å), which have a loose dependence on the thickness of the gadolinium layers.  $d_{\text{U}}$  tends towards the minimum value for Gd layers more than ten monolayers (ML) thick and the more expanded values when  $t_{\text{Gd}} \sim < 10\text{ML}$ . This observed expansion could be a consequence of poorer crystalline structure, where defects such as dislocations, vacancies and diffusion carry a larger relative effect. It seems that sputtering at an elevated temperature (SN124) can improve the crystalline growth, giving a value for  $d_{\text{U}}$  much closer to those achieved by samples with greater U layer thicknesses. There is a similar dependence between the variation in  $d_{\text{U}}$  close to the interface,  $\Delta d_{\text{U}}$ , and the gadolinium layer thickness  $t_{\text{Gd}}$ , which again shows improvements upon increased sputtering power and substrate temperature. In this series of U/Gd samples the cumulative disorder parameter has a greater effect on the observed diffraction spectra, since it reaches values approaching those quoted [64] as causing a smearing of the satellite peaks. These values are evaluated as a function of the position  $\bar{a}$  of the middle of the bilayer and thus have a greater relative effect for thinner samples. In this case  $c^{-1}$  reaches its maximum value (0.042 $\bar{a}$ ) for the thinnest of the U/Gd samples (SN122). At this magnitude it should still be possible to resolve some intensity from satellite diffraction peaks, but these are not observed. This could be due to the relatively small amount of crystalline material, providing a weak intensity signal.

The third series of U/Gd multilayer samples was principally grown to investigate the magnitude of the polarisation within the uranium layers as a function of uranium layer thickness, using X-ray magnetic circular dichroism. These measurements have been explained in detail in Chapter 6 and were taken in fluorescence yield, which results in a significant reabsorption of fluoresced photons. To this end, the gadolinium layer thickness,  $t_{\text{Gd}}$  was held constant, as much as experimental accuracy would allow ( $\pm 2\text{\AA}$ ) and  $t_{\text{U}}$  was varied in steps of  $5\text{\AA}$  from a thickness of  $5\text{\AA}$ . This systematic approach to the multilayer growth also allowed a  $t_{\text{U}}$  dependent study of the high angle diffraction spectra in the thin U layer regime. Figure 4.30 shows a summary of the X-ray diffraction patterns taken for the 3rd U/Gd series of samples.

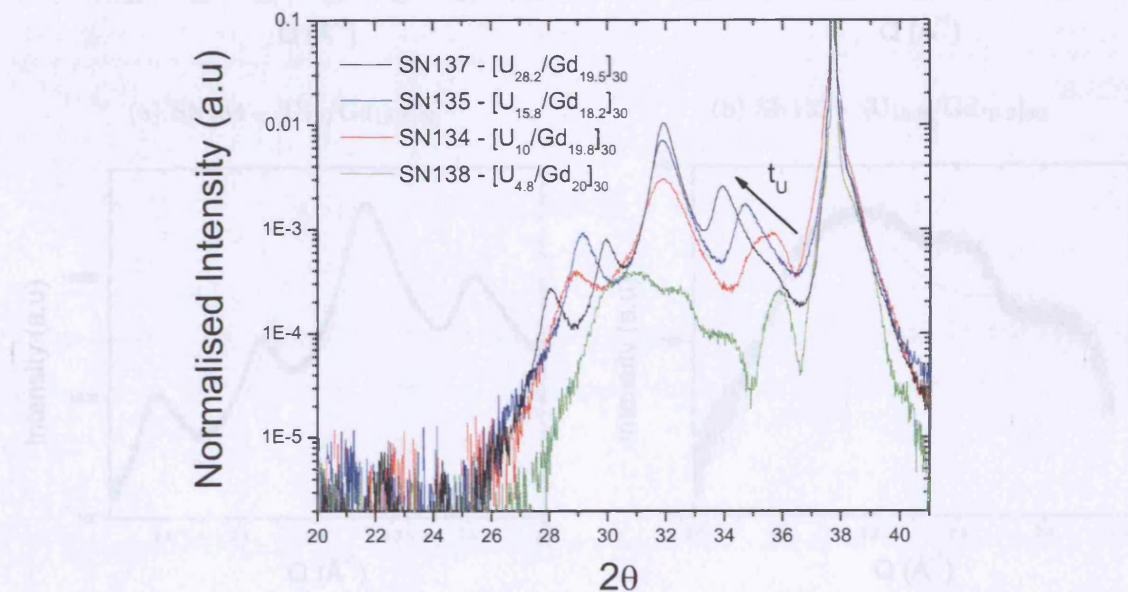


Figure 4.30: Comparison of the X-ray diffraction patterns close to the sapphire  $11\bar{2}0$  peak, for U/Gd samples listed in table 3.7.

The summary figure 4.30 again highlights the greater tendency for the uranium to adopt a crystalline structure than the gadolinium. In this series  $t_{\text{Gd}}$  has an approximately constant value of  $20\text{\AA}$ , but does not provide a distinct contribution to the diffracted intensity until  $t_{\text{U}}$  reaches  $10\text{\AA}$ . Even at a thickness of only  $4.8\text{\AA}$  the signal from the uranium layers is observable in the diffraction spectra. This graph also shows a very clear relationship between bilayer thickness and satellite peak position, in fact it is possible to estimate the bilayer thickness simply from

the distance between the satellite peak positions, using Bragg's law. Simulations to the diffraction spectra were fit to the measured data using the SUPREX software developed at NIST [62] and these are shown in figure 4.31.

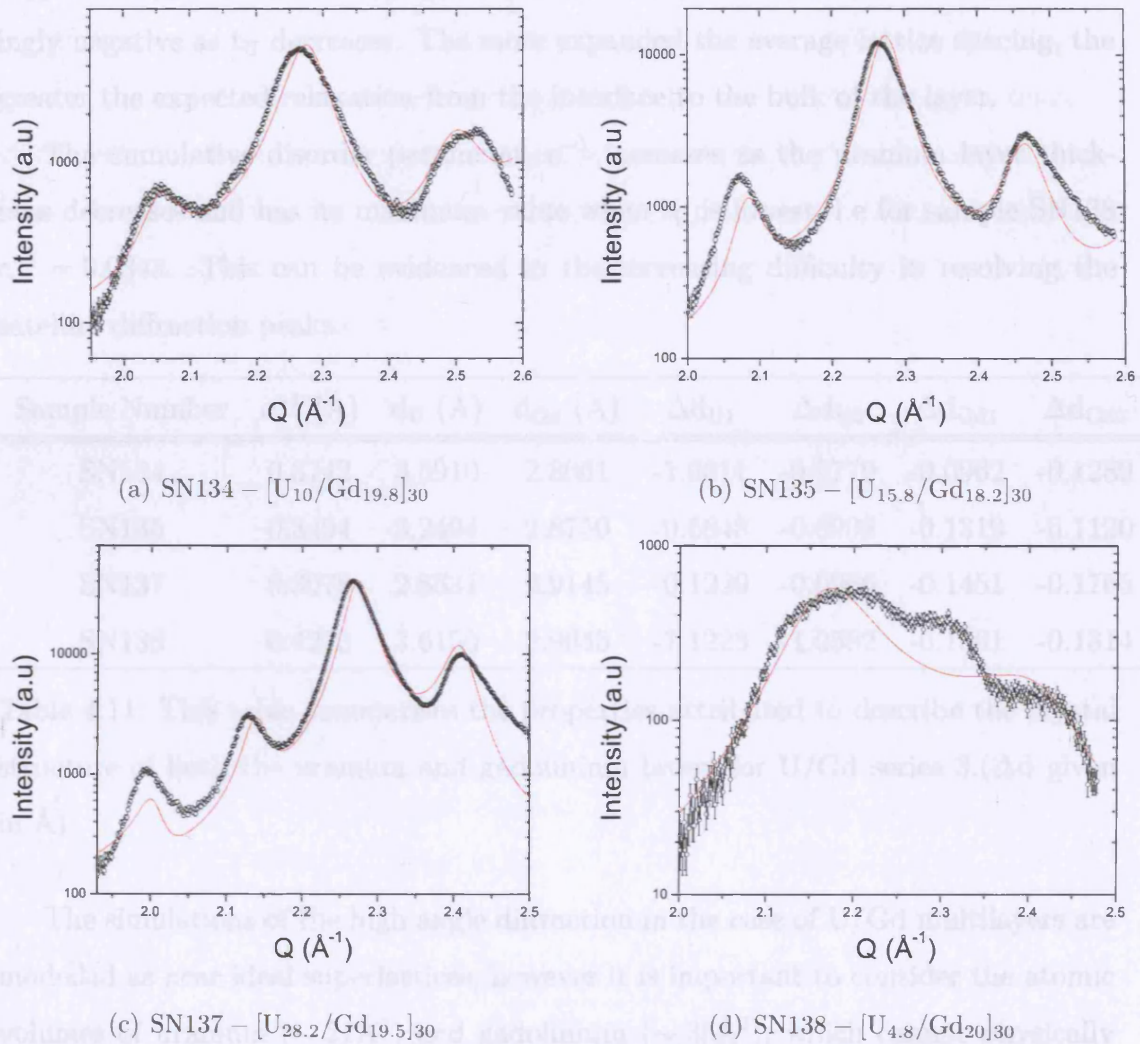


Figure 4.31: X-ray diffraction from U/Gd samples

For this series of U/Gd samples, the fitted simulations provide reasonably close descriptions of the experimental data, although the quality of the fit depreciates with decreasing bilayer thickness. Table 4.11 summarises the relevant properties fit to these diffraction spectra.

The average lattice spacing within the gadolinium layers, ranges between 2.8061 and 2.9645Å giving a c-axis distance of  $\sim 5.6 - 5.9\text{\AA}$  even though  $t_{Gd}$  remains roughly constant.  $d_U$  has a much wider range in values,  $2.8331 < d_U(\text{\AA}) < 3.6150$

as  $t_U$  is varied. Both uranium and gadolinium lattice spacings vary with uranium layer thickness and as  $t_U$  becomes thinner the uranium lattice expands causing a small expansion in the gadolinium layers. The variation in  $d_U$  through the lattice,  $\Delta_{U1}$  and  $\Delta_{U2}$  also show a dependence on the U layer thickness, becoming increasingly negative as  $t_U$  decreases. The more expanded the average lattice spacing, the greater the expected relaxation from the interface to the bulk of the layer.

The cumulative disorder parameter,  $c^{-1}$  increases as the uranium layer thickness decreases and has its maximum value when  $t_U$  is lowest, i.e for sample SN138  $c^{-1} = 0.034\bar{a}$ . This can be evidenced in the increasing difficulty in resolving the satellite diffraction peaks.

| Sample Number | $c^{-1}$ (Å) | $d_U$ (Å) | $d_{Gd}$ (Å) | $\Delta_{U1}$ | $\Delta_{U2}$ | $\Delta_{Gd1}$ | $\Delta_{Gd2}$ |
|---------------|--------------|-----------|--------------|---------------|---------------|----------------|----------------|
| SN134         | 0.3742       | 3.5910    | 2.8061       | -1.0611       | -0.9779       | -0.0962        | -0.1289        |
| SN135         | 0.3494       | 3.2494    | 2.8750       | -0.6648       | -0.6098       | -0.1319        | -0.1120        |
| SN137         | 0.3078       | 2.8331    | 2.9145       | -0.1229       | -0.0966       | -0.1451        | -0.1765        |
| SN138         | 0.4233       | 3.6150    | 2.9645       | -1.1223       | -1.0582       | -0.1661        | -0.1314        |

Table 4.11: This table summarises the properties attributed to describe the crystal structure of both the uranium and gadolinium layers for U/Gd series 3. ( $\Delta d$  given in Å)

The simulations of the high angle diffraction in the case of U/Gd multilayers are modelled as near ideal superlattices, however it is important to consider the atomic volumes of uranium ( $\sim 21\text{Å}^3$ ) and gadolinium ( $\sim 33\text{Å}^3$ ), which cannot physically vary by more than a few percent. This constraint has important implications, concerning the lattice spacings and their extremal values, taking into account expansions and contractions in the  $c$  and  $a$  axes. The large variations in Gd lattice parameter for multilayers with thin U and Gd layers suggest that, rather than indicating real values of the lattice parameter, the simulation program and fitting routine is not able to reliably replicate the diffraction spectra with any likely physical system. An observation of the diffraction spectra from samples with thin Gd layers ( $\leq 20\text{Å}$ ), in figures 4.28 and 4.30, indicates that the majority of the diffracted intensity is due to the crystalline U layers, and that the intensity from diffracting crystal planes of

gadolinium are weak in comparison. It is possible that only a fraction of the 20Å Gd layers are highly crystalline, and that the assumption of a superlattice model, on which to base our simulations, is not accurate.

In order to compare and contrast relative lattice spacings with respect to those of the 500Å gadolinium film, a more simple approach was adopted. The lattice spacings,  $d$  (Å), were calculated by using Bragg's law and determining the position of the peaks, corresponding to the U and Gd components of the diffraction spectra respectively. This was only possible to calculate if peaks from individual elements could be distinguished from one another, i.e. where the thicknesses of the layers were large. Table 4.12 provides a summary of these results.

| Sample | Composition  | $d_{\text{Gd}}$ (Å)<br>$\pm 0.005\text{Å}$ | $d_{\text{U}}$ (Å)<br>$\pm 0.005\text{Å}$ |
|--------|--|--|---|
| SN63   | [U <sub>26</sub> /Gd <sub>33</sub> ] <sub>20</sub>     | 2.974                                      | 2.822                                     |
| SN64   | [U <sub>26</sub> /Gd <sub>33</sub> ] <sub>20</sub>     | 2.940                                      | 2.846                                     |
| SN65   | [U <sub>26</sub> /Gd <sub>33</sub> ] <sub>20</sub>     | 2.935                                      | 2.863                                     |
| SN134  | [U <sub>10</sub> /Gd <sub>19.8</sub> ] <sub>30</sub>   | -  | 2.795                                     |
| SN135  | [U <sub>15.8</sub> /Gd <sub>18.2</sub> ] <sub>30</sub> | -  | 2.797                                     |
| SN137  | [U <sub>28.2</sub> /Gd <sub>19.5</sub> ] <sub>30</sub> | -  | 2.799                                     |
| SN66   | [U <sub>39</sub> /Gd <sub>20</sub> ] <sub>20</sub>     | -  | 2.799                                     |
| SN67   | [U <sub>63.5</sub> /Gd <sub>20</sub> ] <sub>20</sub>   | -  | 2.805                                     |
| SN68   | [U <sub>89</sub> /Gd <sub>20</sub> ] <sub>20</sub>     | -  | 2.805                                     |

Table 4.12: This table summarises the uranium and gadolinium lattice parameters, determined by direct calculation from X-ray diffraction spectra for selected U/Gd samples.

### 4.3.7 Summary Analysis

The U/Fe series of samples considered within this study can be compared directly to results published previously, investigating the differences and similarities in the growth of the two sets of multilayers. Figure 4.32 compares the cell parameter  $a = 2d/\sqrt{2}$  (a), the particle size and the vertical coherence length values (b) taken

from the structural characterisation results published by Beesley et al. [18] with those obtained more recently for the samples grown on sapphire substrates with niobium buffer and capping layers to investigate any differences/similarities. The particle sizes and vertical coherence lengths of both sets of samples (full and open data points respectively) follow the same trend, within experimental errors. The cell parameter however, seems to follow a much steeper exponential trend towards the bulk value in the case of the more recent series of samples than those grown previously, although a similar thickness dependence is observed for both.

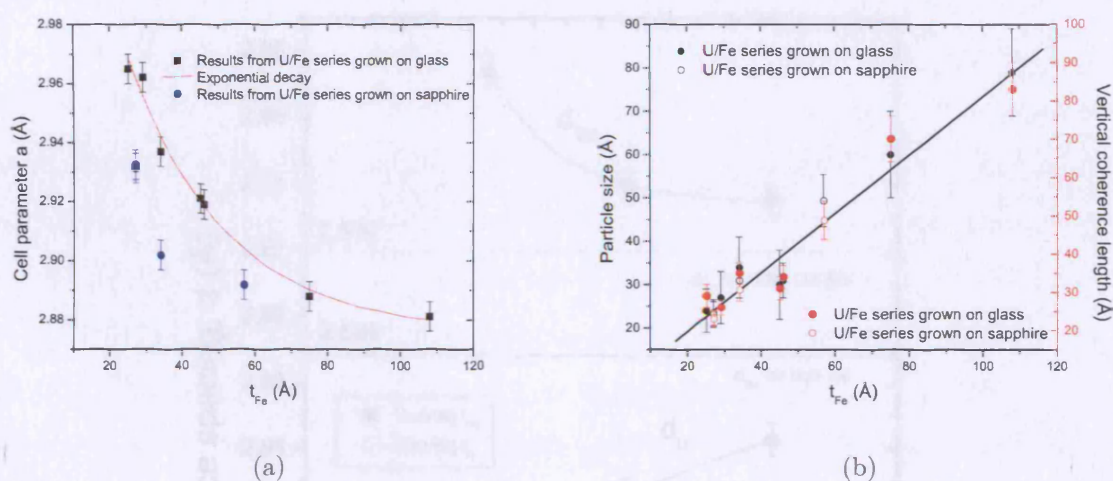


Figure 4.32: Comparison of the cell parameter  $a$ , vertical coherence length and particle size for U/Fe samples grown on glass and those grown on sapphire.

The diffraction spectra observed for U/Fe and U/Co series of samples are very similar in appearance, due to the magnitude of lattice mismatches at the U-Fe ( $\sim 14\%$  in one axis and  $\sim 35\%$  in the other when comparing lattice planes in the preferred orientations of  $[001]$   $\alpha$ -U and  $[110]$  bcc iron) and U-Co interfaces ( $\sim 10\%$  in one axis and  $\sim 25\%$  in the other when comparing lattice planes in the preferred orientations of  $[110]$   $\alpha$ -U and  $[001]$  hcp cobalt) respectively. Both show a preferred orientation, bcc iron in the  $[110]$  direction and hcp cobalt in the  $[001]$ , but any uranium peaks were difficult to resolve due to the intensity from the niobium buffer diffraction fringes. In the U/Co series grown there was not an obvious relationship between  $t_{Co}$  and cell parameter  $a$  (Å).

The U/Gd diffraction spectra are markedly different from those observed for

U/transition metal multilayers investigated thus far. The lattice mismatch in this case could be as low as 4%, taking the cell parameters of Gd and U to be  $a = 3.631\text{\AA}$  and  $a = 3.5\text{\AA}$  [39] respectively, although the in-plane lattice spacing is not known in this case. This results in diffraction spectra, which are high in intensity and contain intensity components from both the U and Gd layers that can be modelled as a near coherent superstructure (superlattice). Figure 4.33 summarises the variations in lattice parameter as a function of U and Gd layer thickness, as determined by direct calculation from the X-ray diffraction spectra, see table 4.12.

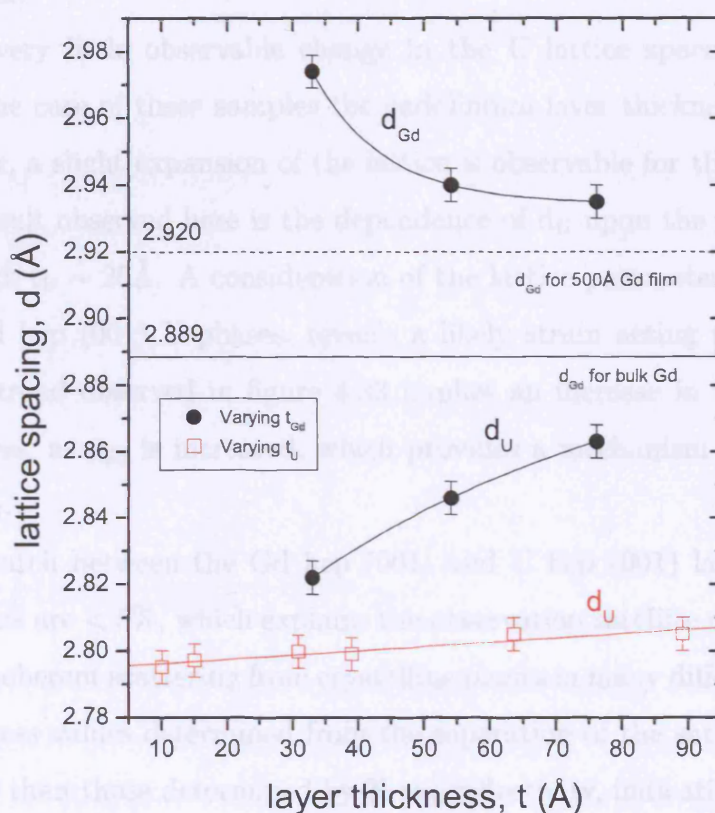


Figure 4.33: Variations in the lattice spacings of uranium and gadolinium as a function of  $t_{Gd}$  (full points) and  $t_U$  (open squares). Values for the bulk and thick Gd film gadolinium lattice parameter are labeled.

When the layers grow coherently in a multilayer it is possible for variations in the layer thickness of one element to affect the strain profile of another, which will be reflected in the lattice spacing values. The variation of both  $d_{Gd}$  and  $d_U$  are shown in figure 4.33 as a function of  $t_{Gd}$ , full points (black) and the dependence

of the uranium lattice parameter upon the U layer thickness is represented by the open squares (red). It was not possible to distinguish the gadolinium diffraction peak positions in the case of varying  $t_U$ , since the gadolinium layers were too thin to give an appreciable diffracted intensity.

As described earlier, the lattice parameter in a sputtered thin film of gadolinium is expanded compared to that of bulk Gd; both of these values are clearly marked in figure 4.33. For multilayers containing thin gadolinium layers the Gd lattice is further expanded, but contracts towards the sputtered thin film value as the layers become thicker.

There is very little observable change in the U lattice spacing,  $d_U$ , as  $t_U$  is varied. For the case of these samples the gadolinium layer thickness is constant at 20Å. However, a slight expansion of the lattice is observable for thick U layers. An interesting result observed here is the dependence of  $d_U$  upon the gadolinium layer thickness, with  $t_U \sim 26\text{Å}$ . A consideration of the lattice parameter sizes of the hcp (001) Gd and hcp (001) U phases, reveals a likely strain acting to expand the U lattice. The trend observed in figure 4.33 implies an increase in the strain acting on the U layers, as  $t_{\text{Gd}}$  is increased, which provides a mechanism for the observed increase in  $d_U$ .

The mismatch between the Gd hcp (001) and U hcp (001) lattice parameters along the c-axis are  $< 5\%$ , which explains the observation satellite diffraction peaks, produced by coherent scattering from crystalline planes in many different layers. The bilayer thickness values determined from the separation of the satellite peaks were several Å less than those determined by X-ray reflectivity, indicating a small interface region of noncrystalline material. A comparison of U/Gd and U/Co systems, suggests that the reason behind such crystalline growth of U layers in the U/Gd system is not simply due to the hexagonal packing arrangement of the gadolinium atoms, since the Co layers also adopt the hcp crystal structure.

# Chapter 5

## Magnetic Characterisation

One of the major purposes of this investigation is to study the magnetic interactions between the ferromagnetic and uranium layers. In order to understand the possible electronic processes and mechanisms it is important to first lay some foundations concerning the origin, effects and observation of magnetisation within different materials. This chapter presents a background to bulk and neutron magnetic measurements and describes results from SQUID magnetometry and polarised neutron reflectivity.

### 5.1 Clarification of Terms

A magnetic field is produced by the motion of electrical charge, either by the orbital motion and spin of electrons within permanent magnets or conventional current in conductors. This field produces an energy gradient within a volume of space that then exerts a force, detectable by a reorientation of electron spins in certain elements and compounds.

The magnetic field strength,  $\mathbf{H}$  is measured in  $\text{Am}^{-1}$  and is generally independent of material properties, determined only by the extent and magnitude of the current generating it. In free space or in a medium, a magnetic field will produce a magnetic flux,  $\Phi$  measured in webers (Wb), which is dependent on both the field strength and the permeability,  $\mu$  of the material. The response of a material to the presence of a magnetic field is known as the magnetic induction,  $\mathbf{B}$ , equivalent to the magnetic

flux density  $\text{Wb/m}^2$ . The magnetic field strength and magnetic induction can be related by the permeability,

$$\mathbf{B} = \mu\mathbf{H} \quad (5.1)$$

The magnetic induction can also be produced by a magnetisation within a material,  $\mathbf{M}$ , which is the magnetic moment,  $\mathbf{m}$  per unit volume of a solid. The magnetic moment is the simplest reducible unit of magnetisation and can be modelled by a circular loop of current, generating a magnetic field. The magnetisation and magnetic induction can be related in free space by the permeability, which then gives a total induction related to the sum of magnetisation and magnetic field components.

$$\mathbf{B} = \mu_0(\mathbf{H} + \mathbf{M}) \quad (5.2)$$

It is important to note at this point that two distinct unit systems are still used to describe magnetic properties in modern experimental and theoretical physics. These unit systems are the CGS (Gaussian) and SI (Sommerfeld) conventions. Table 5.1 below summarises the units of relevant magnetic quantities for both of these conventions.

| Quantity       | SI  | CGS  |
|----------------|---|--|
| Field          | $\text{Am}^{-1}$                              | oersteds, Oe                               |
| Induction      | tesla, T                                      | gauss, G                                   |
| Magnetisation  | $\text{Am}^{-1}$                              | $\text{emu/cm}^3$                          |
| Flux           | weber, Wb                                     | maxwell, Mx                                |
| Moment         | $\text{Am}^2$                                 | emu  |
| Field equation | $\mathbf{B} = \mu_0(\mathbf{H} + \mathbf{M})$ | $\mathbf{B} = \mathbf{H} + 4\pi\mathbf{M}$ |

Table 5.1: This table shows the units of magnetic quantities relevant to experimental methods used in this thesis, using both the CGS and SI conventions.

## 5.2 Magnetic Materials

The classification of magnetic materials is generally based on their permeability,  $\mu$  and susceptibility,  $\chi$ , which is the ratio of the magnetisation and the applied field,  $\frac{M}{H}$ . Materials which have small negative values of susceptibility are called diamagnets and have a magnetic response that acts to oppose the applied field. Those that have a weak parallel alignment to the applied field have small positive values of the susceptibility and are called paramagnets. A major concern of this project is the microscopic interaction of a group of materials that possess large positive values of magnetic susceptibility; these are called ferromagnets and include the transition metal elements iron, cobalt and nickel, and several rare-earth metals. This thesis shall describe and compare the magnetic interactions in U/Fe, U/Co and U/Gd systems in order to understand differences and similarities between the electronic interactions of transition metal, 3d ferromagnets and lanthanide, 4f ferromagnets and to study any effects on the magnetism of uranium.

One way of highlighting the differences between certain types of magnetic materials is to plot the magnetisation versus the applied magnetic field and figure 5.1 shows typical responses of paramagnets, ferromagnets and diamagnets.

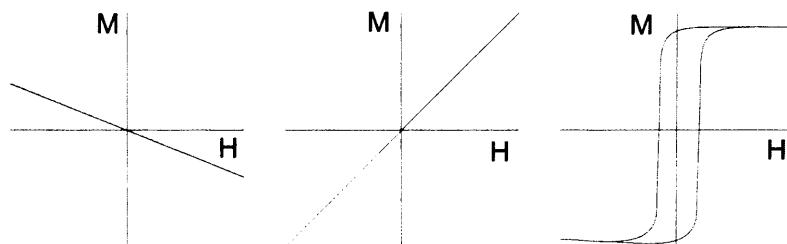


Figure 5.1: Diagram to show the responses of the magnetic induction and hence the magnetisation to an applied magnetic field for a diamagnet, paramagnet and ferromagnet respectively.

The magnetic moments of free atoms have contributions from the spin of their electrons, the associated orbital angular momentum and changes in the orbital moment, induced by applied magnetic fields. The latter of these effects is responsible for the observation of diamagnetism, while the former exhibit paramagnetic proper-

ties. These magnetic materials can be classed in terms of their susceptibility, which in SI units is,

$$\chi = \frac{\mu_0 \mathbf{M}}{\mathbf{B}} \quad (5.3)$$

Following Lenz's law, changing the flux through an electrical circuit or in this case conduction electrons, provides an induced current which acts to oppose the flux change. Hence the magnetic field of the induced current results in an induced magnetic field in opposition to the applied field, giving a diamagnetic susceptibility described by the classical Langevin result or derived from first order perturbation theory,

$$\chi_D = -\frac{\mu_0 N Z e^2}{6m} \langle r^2 \rangle \quad (5.4)$$

where  $\langle r^2 \rangle$  is the mean square distance of the electrons from the nucleus.

In a quantum mechanical treatment, for a paramagnet, the magnetic moment is  $\mu = -g\mu_B \mathbf{J}$  where  $g$  is the Landé  $g$  factor,

$$g = 1 + \frac{J(J+1) + S(S+1) - L(L+1)}{2J(J+1)} \quad (5.5)$$

The values of  $J$ ,  $S$ , and  $L$  are dependent on Hund's rules, which state: 1) the total spin  $S$  takes the maximum value allowed by the Pauli exclusion principle, 2) The total orbital angular momentum  $L$  assumes its maximum value associated with  $S$  inferred by rule 1, 3) the total angular momentum  $J$  is  $|L - S|$  for a less than half-full electron shell,  $|L + S|$  when the electron shell is more than half filled and  $L = 0$ ,  $J = S$  for an exactly half filled shell.

In a magnetic field, the magnetisation for  $N$  atoms per unit volume is given by,

$$M = NgJ\mu_B B_j(x) \quad (5.6)$$

where  $x \equiv gJ\mu_B B/k_B T$  and  $B_j(x)$  is the Brillouin function defined by,

$$B_j(x) = \frac{2J+1}{2J} \coth\left(\frac{(2J+1)x}{2J}\right) - \frac{1}{2J} \coth\left(\frac{x}{2J}\right) \quad (5.7)$$

This treatment leads to a Curie Law susceptibility,

$$\chi_C = \frac{NJ(J+1)g^2\mu_B^2}{3k_B T} = \frac{C}{T} \quad (5.8)$$

where  $C$  is the Curie constant. This form of the paramagnetic susceptibility can be used to describe the paramagnetic response of most metals and metal ions, but in order to describe the paramagnetic susceptibility of conduction electrons it is necessary to include Fermi-Dirac statistics. In this case, only a fraction  $T/T_F$  ( $T_F$  is the Fermi temperature) of the total number of electrons can contribute to the susceptibility, which is then temperature independent,

$$\chi_P = \frac{N\mu_B^2}{k_B T_F} \quad (5.9)$$

Weiss proposed a paramagnetic susceptibility that included a term that accounted for the interaction of magnetic moments via an atomic field that yielded the Curie-Weiss law,

$$\chi = \frac{C}{T - T_C} \quad (5.10)$$

which describes localised, interacting atomic moments. Below the critical, Curie temperature the interaction energy dominates the random fluctuations caused by thermal energies providing a mechanism for the spontaneous alignment of the magnetic moments. Thus, a ferromagnet below  $T_C$  behaves as a paramagnet above it. Just as Weiss added a term to describe the magnetic moment interactions in a classical way it is also possible to include a perturbation in the form of an interaction, or exchange coupling into the quantum mechanical theory of paramagnetism. The magnetisation then includes a term,  $\alpha\mathbf{M}$ , representing the interaction of the moments so that,

$$M = NgJ\mu_B B_j \left[ \frac{gJ\mu_B\mu_0(\mathbf{H} + \alpha\mathbf{M})}{k_B T} \right] \quad (5.11)$$

The magnetism of materials is manifest in their unfilled outer electron shells and so far we have dealt with localised magnetic moments, which although valid for lanthanide metals such as gadolinium where the magnetic 4f electrons are closely bound to the nucleus, it is not feasible to use this model to describe the magnetism

observed in itinerant electron systems, such as the transition metal elements Fe, Co and Ni. In order to describe these electronic systems it is necessary to recall the Pauli susceptibility in equation (5.9).

In this case the electrons are modelled as a gas of free electrons, which occupy bands of spin up and spin down states. Figure 5.2 shows a diagram of these bands and the effect of an applied field.

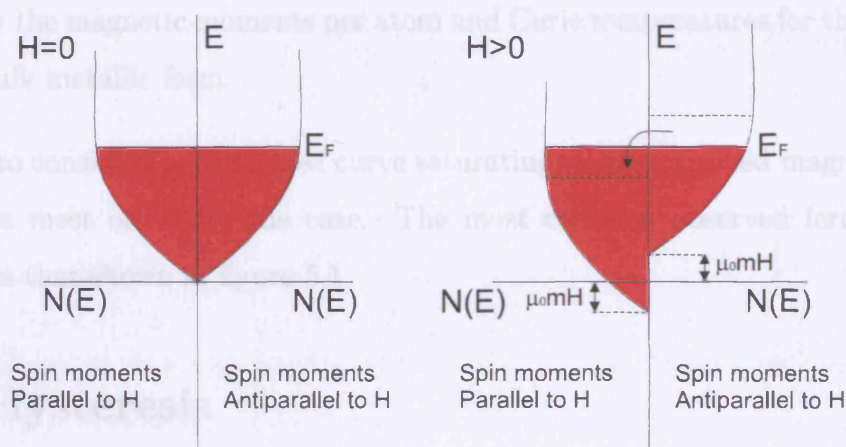


Figure 5.2: Diagram showing the effect of an applied magnetic field on the population of spin up and spin down bands in a Pauli paramagnet.

This theory can be adopted for a ferromagnet by including an exchange coupling between the electrons, first proposed by Stoner [34] and Slater [35]. In a band picture the exchange energy controls the splitting of the spin up and spin down bands. If these bands overlap in energy as in figure 5.2, since the electrons occupy the bands from the lowest energy up, it is possible for the spin down band to become populated before the spin up band is filled. This can then give rise to non-integral values of magnetic moment per atom. In the transition metal ferromagnets Fe, Co and Ni the magnetic properties are due to the 3d band electrons. This band can hold 10 electrons and by allowing the exchange energy to cause the alignment of 5 spin up electrons and the remainder down it is possible to make approximations to the observed moment values. Table 5.2 summarises accepted values for the magnetic moment per atom and Curie temperature for the ferromagnets Fe, Co, Ni and Gd.

As a function of field, below  $T_C$  the magnetisation of ferromagnets would be

| Element    | $m$ ( $\mu_B$ ) | $T_C$ (K) |
|------------|-----------------|-----------|
| Iron       | 2.22            | 1043      |
| Cobalt     | 1.72            | 1388      |
| Nickel     | 0.606           | 627       |
| Gadolinium | 7.63            | 296       |

Table 5.2: The tabulated values above are those commonly accepted within the literature for the magnetic moments per atom and Curie temperatures for the elements in their bulk metallic form.

expected to consist of an S-shaped curve saturating at large applied magnetic fields, but this is most often not the case. The most common observed ferromagnetic response is that shown in figure 5.1.

### 5.3 Hysteresis

The term hysteresis literally means to lag behind and is used to describe the nature of the response of the magnetisation within a ferromagnet to an applied magnetic field. This phenomenon is primarily caused by impurities and structural imperfections, such as dislocations and point defects which result in an energy loss as the field is varied, resulting in an hysteresis loop. Magneto-crystalline anisotropy, where moments prefer to lie along a specific crystallographic axis can also cause energy losses responsible for hysteresis as the moments jump to axes closer to the direction of the applied magnetic field.

The most common method of characterising the magnetic response of ferromagnets to the application of a magnetic field is the parametric characterisation of the observed hysteresis loop. The magnetisation and field values used to describe the shape of the loop have been summarised in figure 5.3.

If the maximum applied field used is large enough to saturate the sample then the resultant loop is termed a saturation hysteresis loop with  $M_S$ , the saturation magnetisation. When the applied field is reduced to zero, the remaining alignment of magnetic moments is termed the remnant magnetisation,  $M_r$ . If the ferromagnet

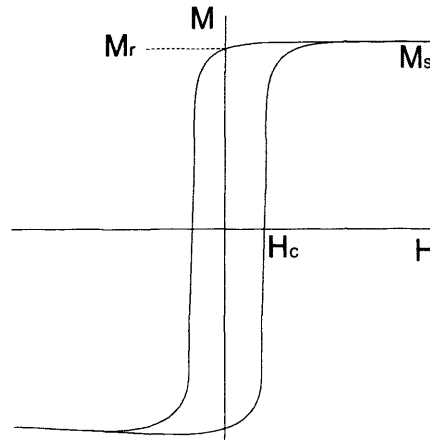


Figure 5.3: Schematic of the relevant parameters, used to describe an hysteresis loop, the saturation magnetisation,  $M_s$ , the coercive field,  $H_C$  and the remnant magnetisation,  $M_r$

is then subjected to a demagnetising field, the field at which the magnetisation reaches zero is coined the coercive field,  $H_C$ . The area of the loop is equivalent to the energy dissipated, or the conversion of energy per unit volume to heat per cycle.

## 5.4 Domains

With the inclusion of exchange coupling within a ferromagnet the existence of localised regions of magnetisation (domains) is necessary to explain why a ferromagnet is not spontaneously aligned. Landau and Lifschitz [65] showed that the separation of the magnetisation into domains reduces the large magneto-static energy associated with a single domain structure, and provided the energy decrease is greater than the energy required to form domain walls then multi-domain structures will occur.

The question then arises as to how the domains behave under the influence of an applied magnetic field. Initially, domains aligned in the direction of the applied field grow at the expense of the domains aligned opposing the field. As the field strength is increased, atomic magnetic moments within unfavourably aligned domains overcome the anisotropy energy and rotate incoherently towards the crystallographic easy axis closest to the field direction. As the field is increased further all of the moments

rotate coherently from the easy axis until they are aligned along the direction of the applied field to produce one single domain.

## 5.5 Anisotropy

Magnetic anisotropy is of considerable importance when investigating the magnetic properties of multilayer thin films, since both the unusual shape and the crystallographic orientation can effect the magnetisation. It is possible in some multilayer systems for the interfacial and surface contributions to the magnetic anisotropy to rotate the easy axis of the magnetisation out of the plane of the film and in some cases, perpendicular magnetic anisotropy (PMA) can be seen.

The magnetic anisotropy energy,  $K$  can be separated into contributions from the volume of the multilayer and the interfaces [66] such that,

$$K = K_V + \frac{2K_S}{t} \quad (5.12)$$

where  $K_V$  is the volume anisotropy,  $K_S$  is the surface anisotropy and  $t$  is the thickness of the magnetic layer.

The two most important sources of magnetic anisotropy in these systems are the dipolar interaction or shape anisotropy, and the spin-orbit interaction. The shape anisotropy can be described by a demagnetising field.

### 5.5.1 Magneto-crystalline Anisotropy

Magneto-crystalline anisotropy is an intrinsic crystal property for atoms that possess both orbital and spin magnetic moments. Coupling between the orbital moments and the lattice can be very strong and it is possible for the spin angular momentum to be coupled to the lattice, due to spin-orbit coupling.

Although the domain growth is not principally concerned with the anisotropy, the incoherent (irreversible) and coherent (reversible) rotations are dependent on the magneto-crystalline anisotropy. The energy associated with domain rotations can be written in terms of the anisotropy energy  $E_a(\theta, \phi)$  and the field energy,  $E_H = -\mu_0 \mathbf{M} \cdot \mathbf{H}$ .

$$E_{tot} = E_a(\theta, \phi) + E_H \quad (5.13)$$

The anisotropy energy for a hexagonal crystal is described as uniaxial where,

$$E_a = K_{u1} \sin^2 \phi \quad (5.14)$$

$K_{u1}$  is the uniaxial anisotropy constant and  $\phi$  is the angle of the magnetisation to the unique axis.

For a cubic crystal,

$$E_a = K_1(\cos^2 \theta_1 \cos^2 \theta_2 + \cos^2 \theta_2 \cos^2 \theta_3 + \cos^2 \theta_3 \cos^2 \theta_1) \quad (5.15)$$

where  $\theta_{1,2,3}$  are the angles between the magnetisation and the three crystal axes.

The effective magnetic anisotropy  $K_{eff}$  can be calculated from the area enclosed within the parallel and perpendicular hysteresis loops or from the hard axis saturation field,  $H_S$  where,

$$H_S = -\frac{2K_{eff}}{M_S} \quad (5.16)$$

### 5.5.2 Demagnetising Field

When a magnetic sample has finite length, magnetic poles develop at the ends of the sample. The magnetic induction inside a sample then points in the opposite direction to the applied field as a consequence of the magnetisation and then results in a field, which acts to oppose the applied field, known as a demagnetising field. The demagnetising field,  $\mathbf{H}_d$  is then related to the magnetisation by a factor,  $N_d$  purely dependent on the geometry of the sample.

$$\mathbf{H}_d = N_d \mathbf{M} \quad (5.17)$$

When the magnetic field is applied along the plane of the sample the shape dependent demagnetising tensor  $N_d$  is equal to 1 for thin films, so that the energy contribution per unit volume [66] can be written,

$$E_d = \frac{\mu_0 M_S^2 \cos^2 \theta}{2} \quad (5.18)$$

where  $M_S$  is the saturation magnetisation, subtending an angle  $\theta$  to the normal of the plane of the thin film. This energy term clearly favours an in-plane alignment of magnetic moments, but only contributes to the volume anisotropy term, since it is independent of the thickness of the film.

## 5.6 SQUID Magnetometry

A Superconducting QUantum Interference Device or SQUID magnetometer consists of two parallel superconducting rings with small, weakly conducting links. These rings are known as Josephson junctions. The insulating links allow flux trapped in the superconducting rings to change by discrete amounts, thus the device is sensitive to changes in flux quanta.

The supercurrent flowing within the rings is,

$$I = I_c \sin(\phi_A - \phi_B) \quad (5.19)$$

equivalent to the product of the critical current,  $I_c$  and the sine of the phase difference between the two sections of the superconducting ring. The flux density in the ring due to the applied field can be represented as,

$$\Phi = \Phi_a + LI = N\Phi_0 \quad (5.20)$$

where  $\Phi_a$  is the flux due to the applied field and  $L$  is the inductance of the ring. This flux density is also equivalent to the number of flux quanta,  $N$  multiplied by the flux quantum,  $\Phi_0 = 2.067 \times 10^{-15}$ . The phase difference,  $\Delta\phi$  is then  $2\pi N - 2\pi(\Phi/\Phi_0)$  so that the flux density becomes,

$$\Phi = \Phi_a - LI_c \sin(2\pi\Phi/\Phi_0) \quad (5.21)$$

A voltage pulse is induced in the coil for each quantum jump when the condition that  $\Delta\phi = \sin(2\pi\Phi/\Phi_0)$  is satisfied. This voltage pulse can then be detected by placing a coil of wire around the superconducting ring.

## 5.7 Experimental Method

The magnetisation measurements were carried out in a Quantum Design MPMS (Magnetic Property Measurement System) at UCL and at the Clarendon Laboratory, Oxford. The system consists of a liquid helium cryostat, able to reach temperatures between 2 and 400K and a superconducting magnet able to provide an applied field up to 7T.

The data were taken using both the DC and the reciprocating sample option (RSO). In the case of DC measurements the sample is moved through the coils in discrete steps, whereas the RSO mechanism uses a servo motor to rapidly oscillate the sample. The sensitivity of these measurements is  $5 \times 10^{-9}$  emu.

The signal from the SQUID is fitted to an ideal dipole moment response, that is based on a cylindrical sample size of 3mm in diameter and 3mm in height. The samples considered here were often several millimetres larger in at least one of the dimensions so a calibration was carried out in order to survey the magnitude of the effect of sample size upon the observed saturation magnetisation.

Measurements were made with the magnetic field applied parallel and perpendicular to the plane of the film. The magnetisation was recorded as a function of field at 10K, well below the Curie temperatures of iron, cobalt and gadolinium. Recalling the dimensions of the samples as-grown ( $12\text{mm} \times 4.5\text{mm} \times Nt_{\text{bilayer}}$ ), the maximum width of the samples that could be mounted and fit into the magnetometer was only 5mm. Thus it was necessary to cut the samples to size, so that measurements of the same sample could be made perpendicular and parallel to the plane of the film. Samples were cut to  $\sim 4\text{mm}$  in length, using a diamond wheel, and the areas calculated, using Vernier's calipers to measure the side lengths. The areas were also approximated by weighing the fragments. Since the multilayer mass is negligible compared to the whole sample, the mass is almost entirely due to the sapphire substrate. The substrate is 1mm thick and the density of sapphire  $\sim 4\text{kgm}^{-3}$  so it is possible to calculate the area of the top surface.

The samples were mounted in plastic straws at the centre of their length ( $\sim 20\text{cm}$ ), which were then attached to the end of the sample rod.

Due to the fact that such a large portion of the sample was comprised of sapphire

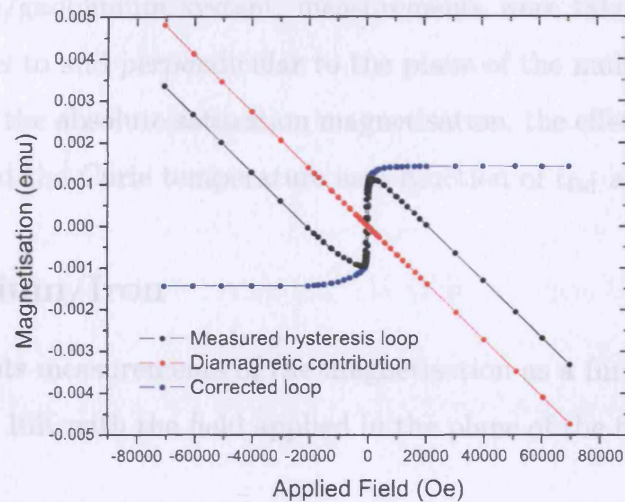


Figure 5.4: Example of an hysteresis loop that includes a contribution from a diamagnetic substrate and the method used to correct for this, used to reveal the contribution solely from the ferromagnetic sample.

and the sample mount was made of plastic, the hysteresis loops recorded included a distinct diamagnetic contribution that could be corrected for, to leave only the response due to the multilayer sample. As described earlier, diamagnets exhibit a negative linear response to an applied field. The ferromagnetic component due to the multilayer samples saturates at relatively low values of the applied field, so at larger field values the diamagnetic signal dominates. A straight line can be fit to this high field signal and the gradient of this line then yields the substrate contribution, which can be subtracted from the measured signal to leave the response due to the sample alone.

## 5.8 Results

SQUID magnetometry measurements probe only magnetisation properties from the bulk of the sample, but it is possible to resolve effects from each of the individual components by investigating layer thickness dependence effects. For U/Fe and U/Co systems, trends in the saturation magnetisation are presented as a function of  $t_{\text{Fe}}$  and  $t_{\text{Co}}$  respectively for the magnetic field applied parallel to the plane of the film.

For the uranium/gadolinium system, measurements were taken with the applied field both parallel to and perpendicular to the plane of the multilayer film. Results are presented for the absolute saturation magnetisation, the effective anisotropy, the coercive field, and the Curie temperature as a function of  $t_{\text{Gd}}$  and  $t_{\text{U}}$ .

### 5.8.1 Uranium/Iron

Figure 5.5 presents measurements of the magnetisation as a function of the applied magnetic field at 10K with the field applied in the plane of the film for several U/Fe samples.

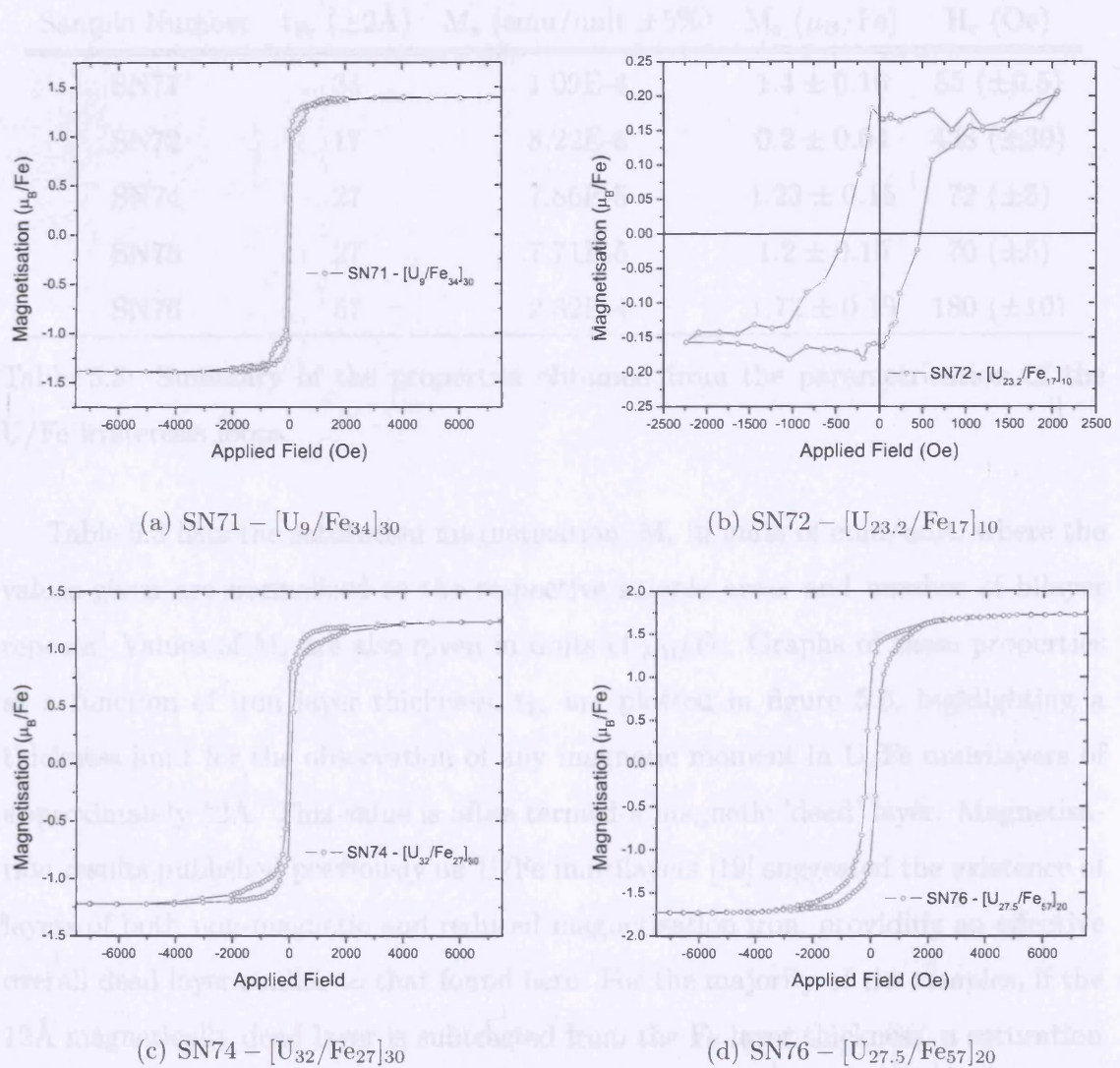


Figure 5.5: Magnetisation as a function of the applied magnetic field, displaying hysteresis for selected U/Fe samples.

The structural details revealed by the X-ray reflectivity and X-ray diffraction investigations reported in the previous chapter showed a strong similarity to the results published previously [18]. The magnetisation measurements for the U/Fe system were then compared with the earlier series [19]. The hysteresis loops were corrected for the diamagnetic contribution from the sapphire substrates and summarised in figure 5.5 for selected samples. The magnetisation has been plotted as a function of the applied field in units of  $\mu_B/\text{Fe}$ , which in bulk bcc iron carries a value of  $2.2\mu_B$ . The properties parametrising the hysteresis loops are summarised in table 5.3.

| Sample Number | $t_{\text{Fe}}$ ( $\pm 2\text{\AA}$ ) | $M_s$ (emu/unit $\pm 5\%$ ) | $M_s$ ( $\mu_B/\text{Fe}$ ) | $H_c$ (Oe)       |
|---------------|---------------------------------------|-----------------------------|-----------------------------|------------------|
| SN71          | 34                                    | 1.09E-4                     | $1.4 \pm 0.16$              | 55 ( $\pm 0.5$ ) |
| SN72          | 17                                    | 8.22E-6                     | $0.2 \pm 0.04$              | 438 ( $\pm 30$ ) |
| SN74          | 27                                    | 7.86E-5                     | $1.23 \pm 0.15$             | 72 ( $\pm 5$ )   |
| SN75          | 27                                    | 7.71E-5                     | $1.2 \pm 0.15$              | 70 ( $\pm 5$ )   |
| SN76          | 57                                    | 2.32E-4                     | $1.72 \pm 0.19$             | 180 ( $\pm 10$ ) |

Table 5.3: Summary of the properties obtained from the parametrisation of the U/Fe hysteresis loops.

Table 5.3 lists the saturation magnetisation,  $M_s$  in units of emu/unit, where the values given are normalised to the respective sample areas and number of bilayer repeats. Values of  $M_s$  are also given in units of  $\mu_B/\text{Fe}$ . Graphs of these properties as a function of iron layer thickness,  $t_{\text{Fe}}$  are plotted in figure 5.6, highlighting a thickness limit for the observation of any magnetic moment in U/Fe multilayers of approximately  $12\text{\AA}$ . This value is often termed a magnetic 'dead' layer. Magnetisation results published previously on U/Fe multilayers [19] suggested the existence of layers of both non-magnetic and reduced magnetisation iron, providing an effective overall dead layer similar to that found here. For the majority of the samples, if the  $12\text{\AA}$  magnetically dead layer is subtracted from the Fe layer thickness, a saturation magnetisation of close to the bulk moment,  $2.2\mu_B/\text{Fe}$ , is found for the remainder of the layer. This layer is also supported by results from the X-ray diffraction that showed a limit for the observation of crystalline iron.

The summary graphs shown in figure 5.6 indicate a similar trend in iron layer thickness as was observed by Beesley et al. [19].

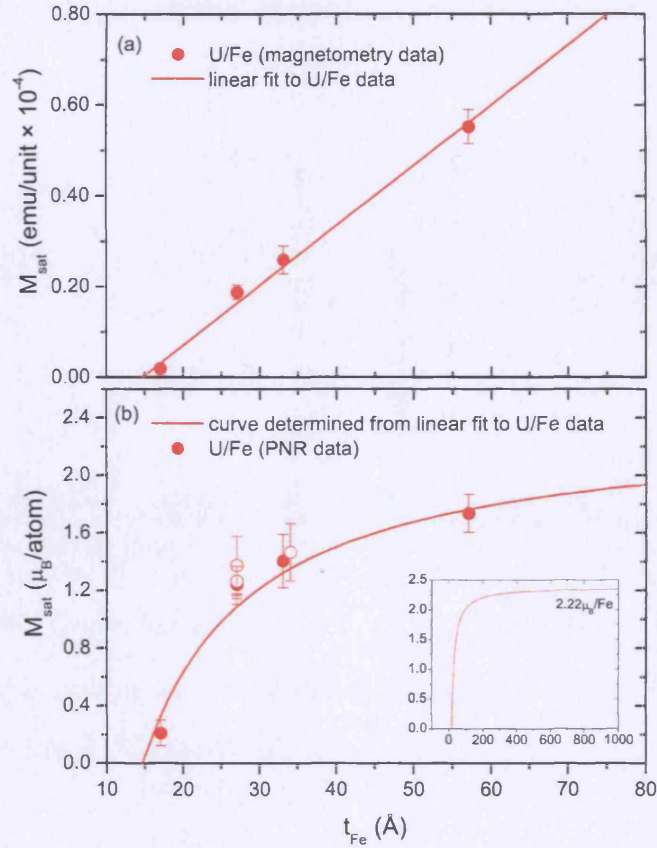


Figure 5.6: (a) Absolute saturation magnetisation, normalised to sample area and number of bilayer repeats. (b) Relative saturation magnetisation values as a function of  $t_{Fe}$ , insert shows the expected value of  $M_S$  for films with thick Fe layers.

Results obtained from the samples grown on glass substrates showed a dependence of the coercive field upon  $t_{Fe}$  that developed with the variation in particle size, suggesting a transition from a single domain to a multidomain magnetic structure. No such trend was observed in this series, possibly as a result of the lower roughness values and lack of conformal roughness, which would lead to a magnetic roughness closely linked to domain formation. The structural and magnetic roughness was studied using polarised neutron reflectivity in the off-specular direction. Results published by Beesley et al. [19] highlight a magnetic roughness indicative of domain sizes of several  $\mu\text{m}$ , calculated from the large amount of diffuse scattered in-

tensity. There was no significant off-specular scattering observable for U/Fe samples considered in this thesis.

### 5.8.2 Uranium/Cobalt

Figure 5.7 presents measurements of the magnetisation as a function of the applied magnetic field at 10K with the field applied in the plane of the film for U/Co samples SN108 and SN112.

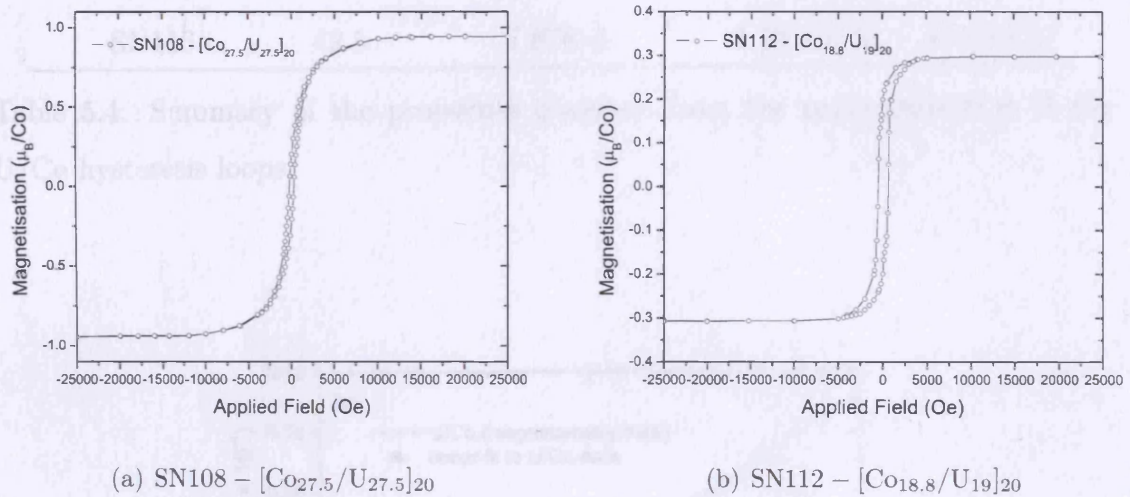


Figure 5.7: Magnetisation as a function of the applied magnetic field, displaying hysteresis for selected U/Co samples.

Table 5.4 lists the saturation magnetisation,  $M_s$  in units of emu/unit, where the values given are normalised to the respective sample areas and number of bilayer repeats. Values of  $M_s$  are also given in units of  $\mu_B/\text{Co}$ . Graphs of these properties as a function of cobalt layer thickness,  $t_{\text{Co}}$  are plotted in figure 5.8, highlighting a thickness limit for the observation of any magnetic moment in U/Co multilayers of approximately  $12\text{\AA}$ . However, neglecting sample SN116 would imply a magnetic dead layer of closer to  $15\text{\AA}$ . Using this latter value to recalculate the magnetic moment of the remaining cobalt component yields a magnetisation saturation of closer to that of bulk hcp cobalt.

Figure 5.8 describes the variation of both the absolute (normalised to the area and number of bilayer repeats) and the relative saturation magnetisation values with  $t_{\text{Co}}$ . The respective trends of these graphs are very similar to those for the U/Fe series and the observation of a magnetically dead layer of a similar magnitude suggests that this is a product of the growth properties of the multilayer. X-ray diffraction spectra

| Sample Number | $t_{\text{Co}}$ (Å) | $M_s$ (emu/unit $\pm 5\%$ ) | $M_s$ ( $\mu_B/\text{Co}$ ) | $H_c$ (Oe)       |
|---------------|---------------------|-----------------------------|-----------------------------|------------------|
| SN108         | 27.5                | $4.38\text{E-}5$            | $0.94 \pm 0.12$             | 252 ( $\pm 15$ ) |
| SN112         | 18.8                | $9.50\text{E-}6$            | $0.30 \pm 0.05$             | 559 ( $\pm 25$ ) |
| SN114         | 18                  | $4.44\text{E-}6$            | $0.19 \pm 0.05$             | 208 ( $\pm 15$ ) |
| SN116         | 42.5                | $7.87\text{E-}5$            | $1.10 \pm 0.23$             | 49 ( $\pm 0.5$ ) |

Table 5.4: Summary of the properties obtained from the parametrisation of the U/Co hysteresis loops.

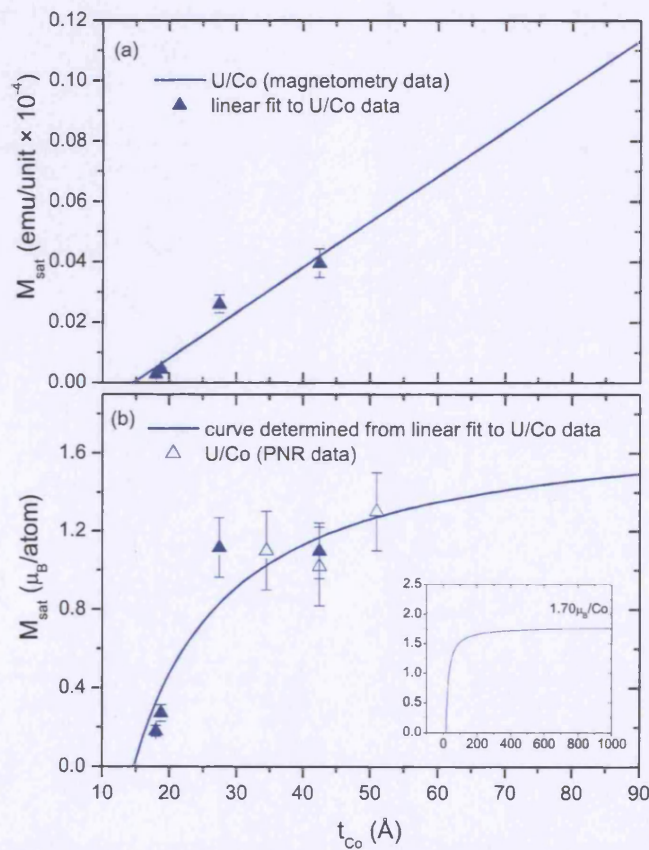


Figure 5.8: (a) Absolute saturation magnetisation, normalised to sample area and number of bilayer repeats. (b) Relative saturation magnetisation values as a function of  $t_{\text{Co}}$ , insert shows the expected value of  $M_S$  for films with thick Co layers.

---

showed similar thickness dependencies in U/Fe and U/Co multilayers and similar limiting layer thicknesses for the onset of crystallinity. Figure 5.8 (b) indicates that the magnetic dead layer is  $\sim 15\text{\AA}$ . This value is slightly larger than that observed in the U/Fe system and could be understood as a larger degree of diffusion and alloying at the U/Co interface, which might be revealed by polarised neutron reflectivity as a means to identify regions of different magnetisation values within the cobalt layers.

### 5.8.3 Uranium/Gadolinium - Field Dependence

A more in-depth study of the magnetisation properties was made for the U/Gd series of multilayers. The samples were cut so that measurements could be made with the applied field parallel to and perpendicular to the plane of the film. This section presents a systematic study of the magnetisation as a function of  $t_{\text{Gd}}$  and  $t_{\text{U}}$ .

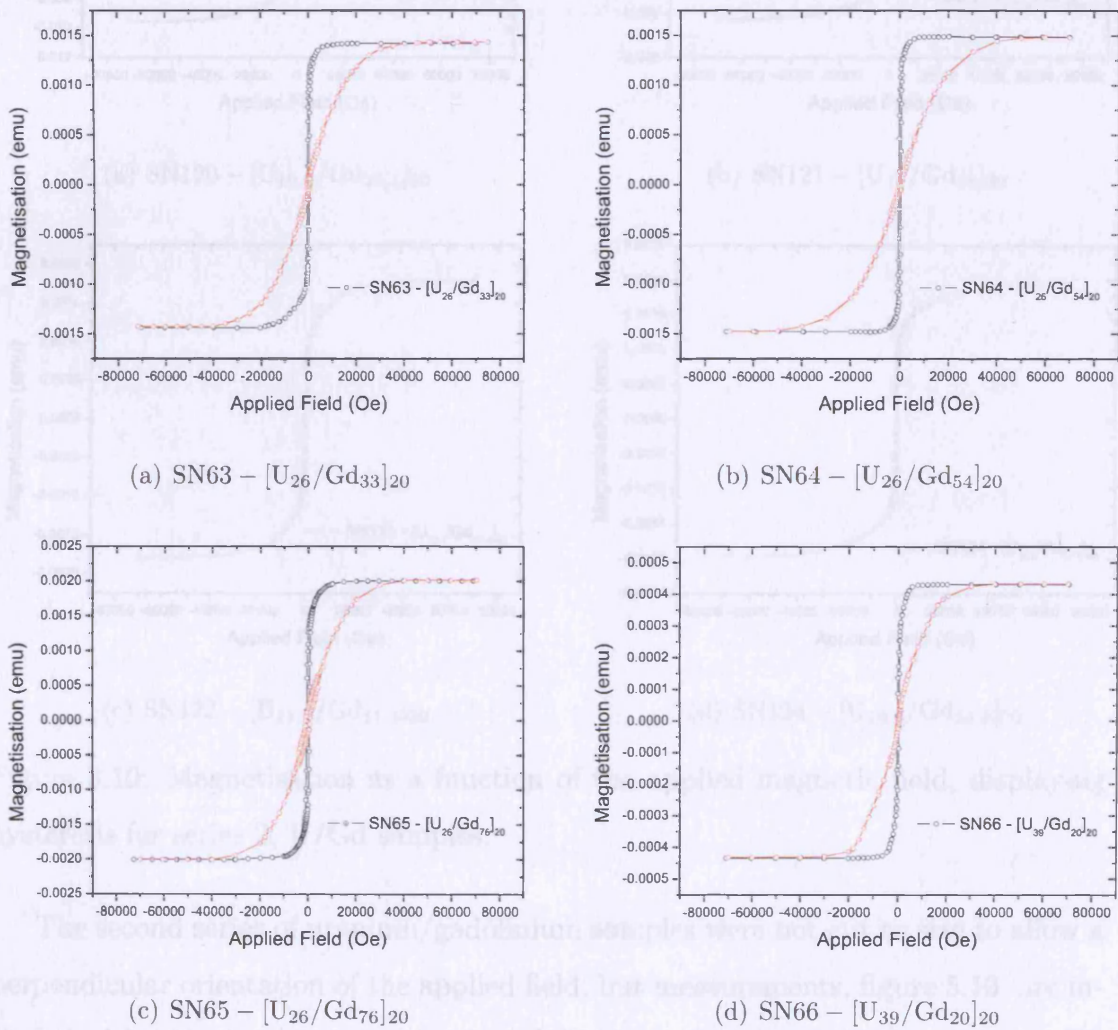


Figure 5.9: Magnetisation as a function of the applied magnetic field, displaying hysteresis for series 1, U/Gd samples. The magnetic field has been applied both parallel (black curve) and perpendicular (red curve) to the plane of the film.

Figure 5.9 shows a summary of the hysteresis loops for several of the U/Gd series 1 samples with the magnetic field applied in the plane (black circles) and

perpendicular to the plane of the film (red circles).

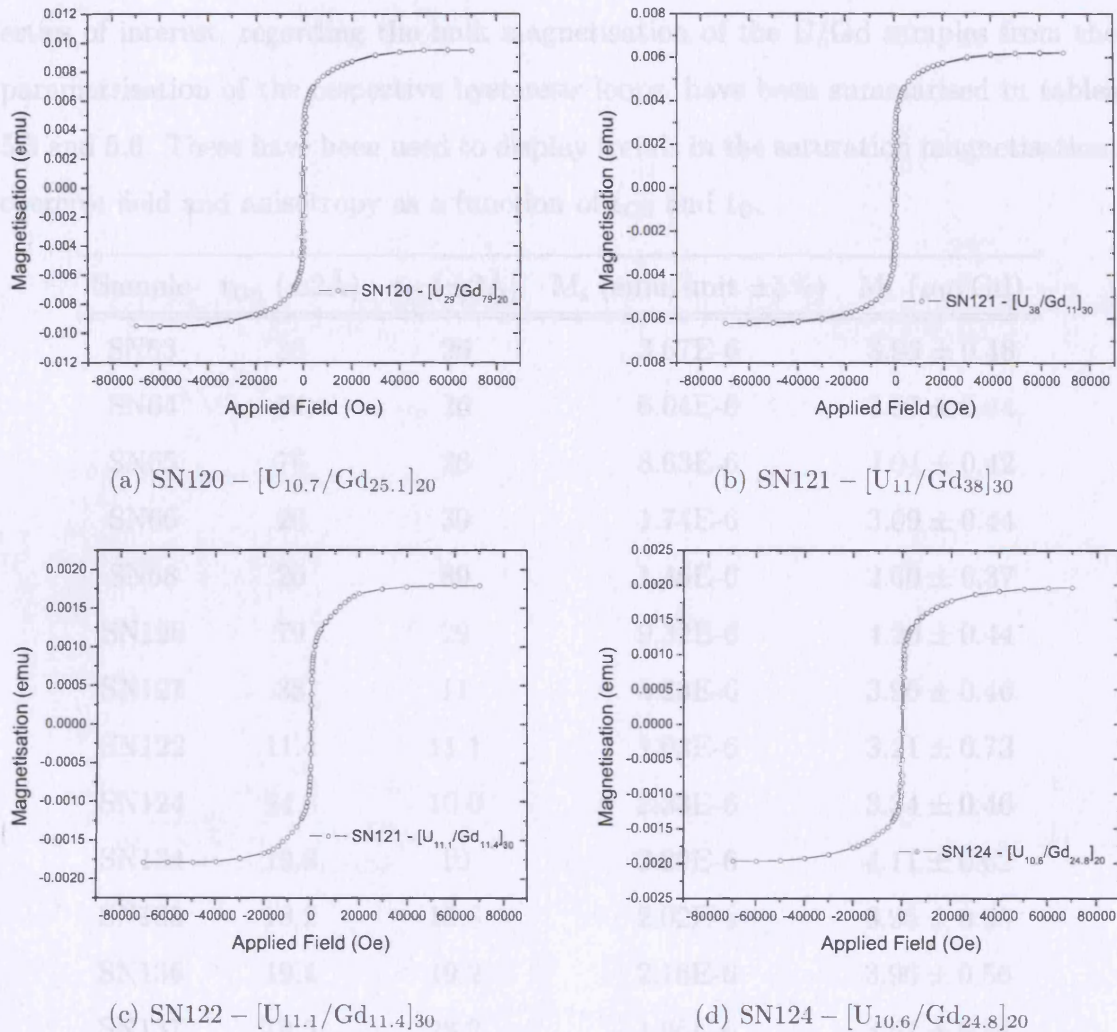


Figure 5.10: Magnetisation as a function of the applied magnetic field, displaying hysteresis for series 2, U/Gd samples.

The second series of uranium/gadolinium samples were not cut to size to allow a perpendicular orientation of the applied field, but measurements, figure 5.10, are included within the in-plane investigation of the saturation magnetisation and coercive field. A correction factor was included where necessary to allow for the discrepancy between the experimental sample length and the ideal sample size, resulting in an underestimate of the measured magnetisation.

Figure 5.11 presents a summary of the magnetisation measurements carried out in-plane and perpendicular to the plane of the film for U/Gd series 3 samples. Properties of interest, regarding the bulk magnetisation of the U/Gd samples from the parametrisation of the respective hysteresis loops, have been summarised in tables 5.5 and 5.6. These have been used to display trends in the saturation magnetisation, coercive field and anisotropy as a function of  $t_{\text{Gd}}$  and  $t_{\text{U}}$ .

| Sample | $t_{\text{Gd}}$ ( $\pm 2\text{\AA}$ ) | $t_{\text{U}}$ ( $\pm 2\text{\AA}$ ) | $M_s$ (emu/unit $\pm 5\%$ ) | $M_s$ ( $\mu_{\text{B}}/\text{Gd}$ ) |
|--------|---------------------------------------|--------------------------------------|-----------------------------|--------------------------------------|
| SN63   | 33                                    | 26                                   | 3.67E-6                     | $3.96 \pm 0.48$                      |
| SN64   | 54                                    | 26                                   | 6.04E-6                     | $3.97 \pm 0.44$                      |
| SN65   | 76                                    | 26                                   | 8.63E-6                     | $4.04 \pm 0.42$                      |
| SN66   | 20                                    | 39                                   | 1.74E-6                     | $3.09 \pm 0.44$                      |
| SN68   | 20                                    | 89                                   | 1.46E-6                     | $2.60 \pm 0.37$                      |
| SN120  | 79                                    | 29                                   | 9.32E-6                     | $4.20 \pm 0.44$                      |
| SN121  | 38                                    | 11                                   | 4.23E-6                     | $3.96 \pm 0.46$                      |
| SN122  | 11.4                                  | 11.1                                 | 1.03E-6                     | $3.21 \pm 0.73$                      |
| SN124  | 24.8                                  | 10.6                                 | 2.33E-6                     | $3.34 \pm 0.46$                      |
| SN134  | 19.8                                  | 10                                   | 2.29E-6                     | $4.11 \pm 0.62$                      |
| SN135  | 18.2                                  | 15.8                                 | 2.02E-6                     | $3.95 \pm 0.56$                      |
| SN136  | 19.4                                  | 19.2                                 | 2.16E-6                     | $3.96 \pm 0.56$                      |
| SN137  | 19.5                                  | 28.2                                 | 1.96E-6                     | $3.57 \pm 0.54$                      |
| SN138  | 20                                    | 4.8                                  | 2.67E-6                     | $4.75 \pm 0.67$                      |

Table 5.5: Summary of the absolute saturation magnetisation (normalised per unit area and to the number of bilayer repeats) and  $M_s$  ( $\mu_{\text{B}}/\text{Gd}$ ), for all U/Gd samples measured.

All of the magnetisation measurements were taken at 10K in applied magnetic fields of 7T to -7T. It is possible to make some comments about the form of the magnetisation from a general qualitative perspective. The hysteresis loops measured with the applied field perpendicular to the plane of the film are sheared compared to those with the field applied parallel. This indicates an effective anisotropy that leads to a preferred orientation of the magnetic moments in the plane of the film. The

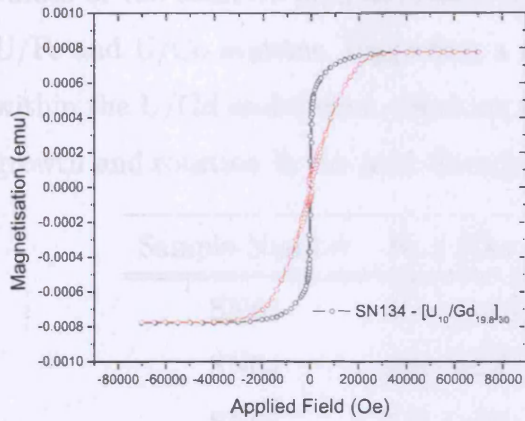
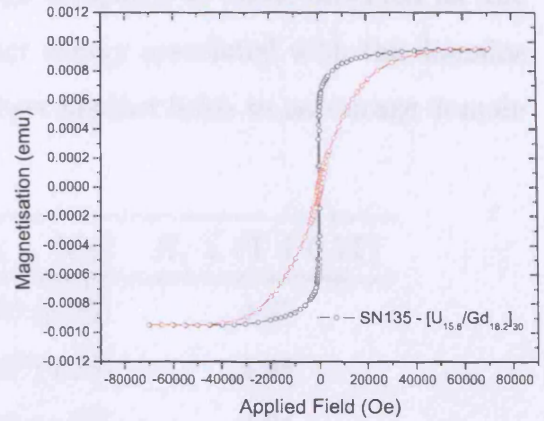
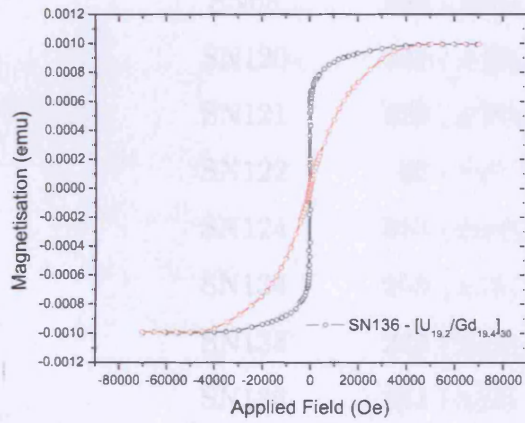
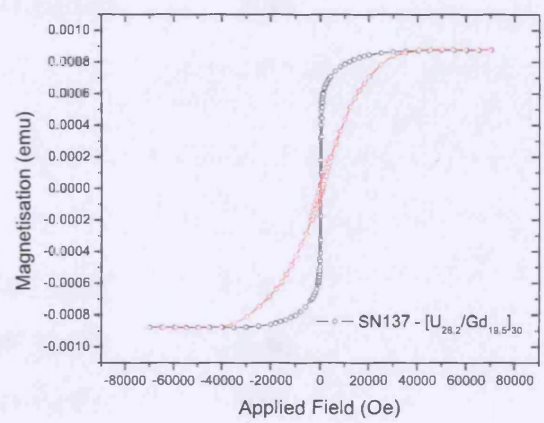
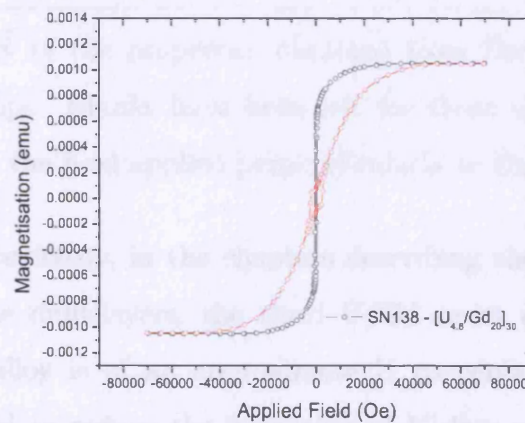
(a) SN134 –  $[U_{10}/Gd_{19.8}]_{30}$ (b) SN135 –  $[U_{15.8}/Gd_{18.2}]_{30}$ (c) SN136 –  $[U_{19.2}/Gd_{19.4}]_{30}$ (d) SN137 –  $[U_{28.2}/Gd_{19.5}]_{30}$ (e) SN138 –  $[U_{4.8}/Gd_{20}]_{30}$ 

Figure 5.11: Magnetisation as a function of the applied magnetic field, displaying hysteresis for series 3, U/Gd samples. The magnetic field has been applied both parallel (black curve) and perpendicular (red curve) to the plane of the film.

values of the coercive field are relatively large compared to those observed for the U/Fe and U/Co systems, suggesting a greater energy associated with the domains within the U/Gd multilayers, resulting in larger applied fields to encourage domain growth and rotation in the field direction.

| Sample Number | $H_c \parallel$ (Oe) | $H_c \perp$ (Oe) | $H_s \perp$ (T $\pm$ 0.1T) |
|---------------|----------------------|------------------|----------------------------|
| SN63          | 350 ( $\pm$ 20)      | 520 ( $\pm$ 25)  | 4.37                       |
| SN64          | 422 ( $\pm$ 25)      | 507 ( $\pm$ 25)  | 4.98                       |
| SN65          | 547 ( $\pm$ 25)      | 805 ( $\pm$ 40)  | 4.04                       |
| SN66          | 318 ( $\pm$ 20)      | 161 ( $\pm$ 10)  | 3.66                       |
| SN68          | 544 ( $\pm$ 25)      | 222 ( $\pm$ 15)  | 2.84                       |
| SN120         | 541 ( $\pm$ 25)      | -                | -                          |
| SN121         | 620 ( $\pm$ 30)      | -                | -                          |
| SN122         | 86 ( $\pm$ 2)        | -                | -                          |
| SN124         | 353 ( $\pm$ 20)      | -                | -                          |
| SN134         | 265 ( $\pm$ 15)      | 666 ( $\pm$ 30)  | 4                          |
| SN135         | 249 ( $\pm$ 15)      | 700 ( $\pm$ 30)  | 5.46                       |
| SN136         | 244 ( $\pm$ 15)      | 223 ( $\pm$ 20)  | 5.01                       |
| SN137         | 263 ( $\pm$ 15)      | 732 ( $\pm$ 30)  | 4.04                       |
| SN138         | 282 ( $\pm$ 15)      | 2272 ( $\pm$ 50) | 4.52                       |

Table 5.6: Summary of the properties obtained from the parametrisation of the U/Gd hysteresis loops. Blanks have been left for those samples, which have not been measured with the field applied perpendicularly to the plane of the film.

As mentioned previously, in the chapters describing the growth and structural determination of the multilayers, the third U/Gd series of samples comprised a U-Gd alloy. This alloy is of an approximate U concentration of 5%. This low concentration is used to reduce the formation of U dimers or clusters in order to observe the effect of U atoms in a matrix of Gd. Although predominantly grown as a means for comparison with respect to the induced magnetisation and 5f-4f hybridisation extent, bulk measurements were still performed as a matter of course. Figure 5.12 shows the magnetisation as a function of applied field both parallel and

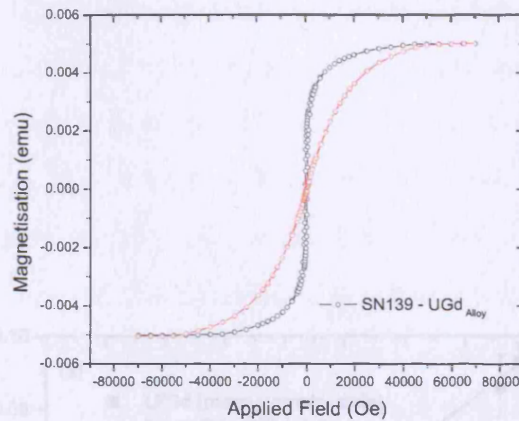


Figure 5.12: The magnetisation as a function of the applied magnetic field for sample SN139 - U-Gd alloy ( $\sim 5\%U$ ). The red curve denotes the response to a field applied perpendicular to the plane of the film and the black curve, a field applied parallel.

perpendicular to the plane of the film. The general shape resembles those observed for U/Gd multilayers. Taking the relative thickness of the respective components proposed in chapter 4, U-Gd ( $160\text{\AA}/2500\text{\AA}$ ), then the saturation moment normalised to the number of gadolinium atoms is  $\sim 5\mu_B/\text{Gd}$ .

### Saturation Magnetisation

Table 5.5 lists values of the measured saturation magnetisation (emu) and  $M_S$  in units of  $\mu_B/\text{Gd}$ . These are calculated, using measured values of the sample areas and gadolinium layer thicknesses and densities determined by X-ray reflectivity in order to normalise the saturation magnetisation by the number of Gd atoms in the sample.

Figure 5.13 shows both the measured values of the saturation magnetisation, normalised to the area and number of bilayer repeats within the sample, and values of the saturation magnetisation per gadolinium atom, as a function of the gadolinium layer thickness. Figure 5.13 (a) shows the straight line trend that the normalised, absolute saturation magnetisation is expected to follow as a function of Gd layer thickness. The close proximity of these data points to the straight line fit, shown in red, emphasizes the accuracy with which the layer thicknesses have been determined by X-ray reflectivity measurements and bears testament to the high quality growth



of the U/Gd system. The x-axis intercept represents the gadolinium layer thickness for which no observable magnetisation is expected, and is commonly ascribed the term 'dead' layer as seen in both the U/Fe and U/Co systems previously. In this case the thickness,  $t_{\text{Gd}}$ , is  $\sim 4.5\text{\AA}$  or 1.5ML (monolayers), where one monolayer is equivalent to the lattice spacing  $d_{\text{Gd}}$ , which from X-ray diffraction measurements is  $\sim 2.9\text{\AA}$ . The thickness of the dead layer is small when compared to the U/Fe ( $\sim 12\text{\AA}$ ) and U/Co ( $\sim 15\text{\AA}$ ) systems, which again supports the assertion that the U/Gd multilayers exhibit a much reduced interfacial diffusion and a more coherent growth, due to the closer lattice match, than those comprising uranium and the transition metal ferromagnets.

Figure 5.13 (b) shows the saturation magnetisation,  $M_{\text{S}}$ , as a function of  $t_{\text{Gd}}$  normalised to the number of gadolinium atoms. As discussed briefly in Chapter 2 and listed in table 5.2, the expected value for the gadolinium saturation magnetisation ought to be  $7.63\mu_{\text{B}}/\text{Gd}$ , but the clear tendency shown in our results is towards a value just over  $4\mu_{\text{B}}/\text{Gd}$  as the Gd layers become thick. Saturation magnetisations close to those found in the bulk metal have been reported in Fe/Gd [29] and Gd/Au systems, however, similarly large reductions to those described in our U/Gd system have been observed in Gd/V [27] and Gd/Mo [67] multilayers. In these instances there seems to be no clear argument as to the mechanism behind the magnetisation reduction. In this vein we set out to plot the trend, if any, of the saturation magnetisation as a function of the uranium layer thickness.

Figure 5.14 indicates that the presence of the uranium layers in between the magnetic gadolinium effectively reduces the ferromagnetic saturation, and that as  $t_{\text{U}}$  is increased this effect acts to further reduce  $M_{\text{S}}$  in an exponentially decaying trend that begins to plateau at uranium layer thicknesses approaching  $80\text{\AA}$ . The results suggest that the uranium is playing a major role in the reduction of the Gd moment, but the mechanism is not entirely clear. This could be caused by a strong electronic 5f-4f hybridisation, where the itinerant, uranium 5f electrons might have a 'damping' effect on the ferromagnetic ordering. Alternatively, this dramatic reduction might be simply a by-product of the structural changes that occur in the gadolinium layers as  $t_{\text{U}}$  is increased; the improved uranium crystallinity obtained

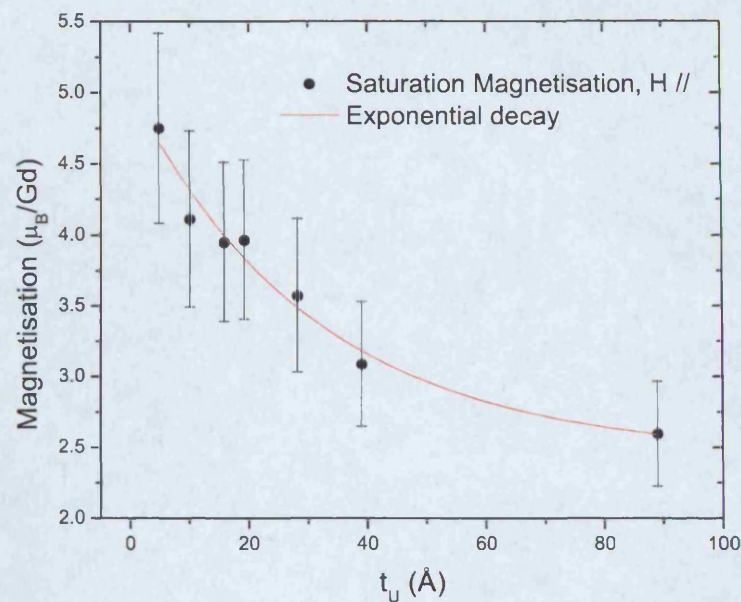


Figure 5.14: The variation of the saturation magnetisation as a function of the uranium layer thickness for constant  $t_{\text{Gd}} \sim 20\text{\AA}$ . The exponential decay trend line is shown as a guide to the eye.

with thicker U layers could provide a greater strain gradient through the gadolinium layers that acts to reduce the Gd moment or the interface region could provide a number of pinning centres, hindering the alignment of the gadolinium magnetic moments.

### Coercive Field

It was also useful to note any trends in the coercive fields as a function of  $t_U$ , figure 5.16, and of  $t_{\text{Gd}}$ , figure 5.15. In these cases the plots have been made of the coercive fields measured with the magnetic field applied in the plane of the films. The coercive field is a measure of the ease for which an applied magnetic field may rotate the magnetic moments, i.e. cause domain growth and rotation in the direction of the applied field. It is then possible to make qualitative suggestions as to the formation and quantity of magnetic domains within these multilayers based on the variation of  $H_C$  with gadolinium and uranium layer thicknesses respectively.

Figure 5.15 plots the coercive field as a function of gadolinium layer thickness for two cases, (a) and (b), where the samples have similar U layer thicknesses,  $\sim 20\text{\AA}$

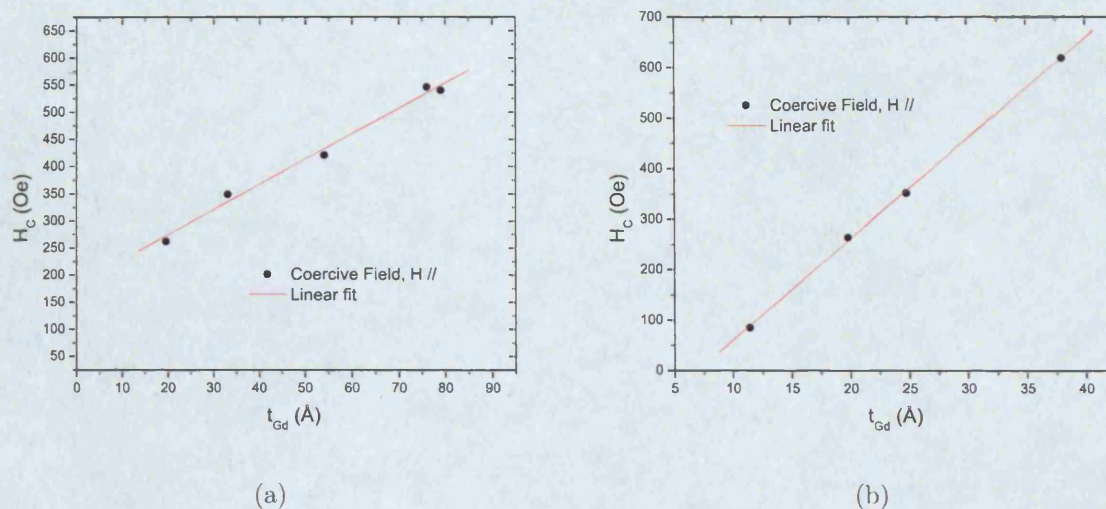


Figure 5.15: The dependence of the coercive field upon the gadolinium layer thickness for two values of constant  $t_U$  (a),  $\sim 20 \text{ \AA}$ , and (b),  $\sim 10 \text{ \AA}$ , with the applied field in the plane of the film.

and  $\sim 10 \text{ \AA}$  respectively. These show clear linear trends in  $H_C$ , that increase as  $t_{Gd}$  increases, indicating that the moments become harder to rotate into the direction of the applied field as the gadolinium layer thickness is increased. This could be understood simply as an increase in the number of domains, where the larger number of domain walls provide an energy barrier which requires a larger applied field to overcome it.

The relationship between  $t_U$  and  $H_C$  with the field applied parallel to the plane of the sample is more complicated. Figure 5.16 plots this relationship for multilayers with similar gadolinium layer thicknesses,  $\sim 20 \text{ \AA}$ . For samples with thin U layers, the coercive field decreases as  $t_U$  increases up to  $20 \text{ \AA}$ . At this point a minimum in the coercive field can be observed, after which  $H_C$  increases linearly with  $t_U$ . This relationship could also be explained in terms of domain formation. When the U layers are very thin, the increase in  $t_U$  could afford the formation of fewer, larger domains as the structural coherence improves through the multilayer stack. There is then a competition between the improvement in crystalline registry, forming larger domains through the multilayer stack and the formation of more domains as the layers become thicker.

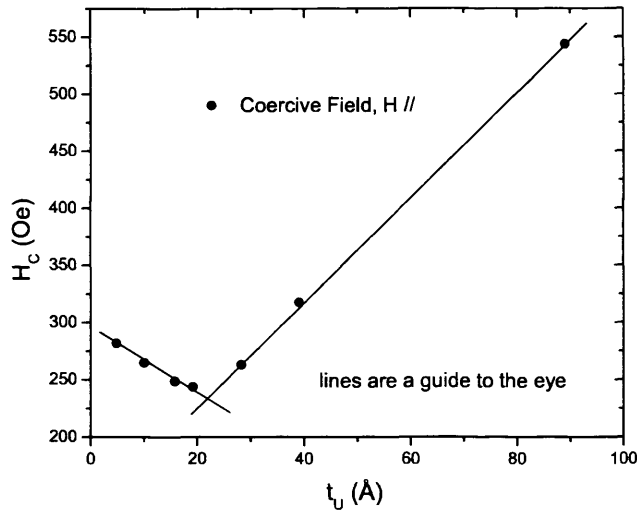


Figure 5.16: The dependence of the coercive field upon the uranium layer thickness for constant  $t_{Gd} \sim 20\text{\AA}$  with the magnetic field applied in the plane of the film.

### Effective Anisotropy

In bulk gadolinium, the moments align along the  $c$ -axis, which in our case is the direction of growth perpendicular to the film. However, the large demagnetising field, caused by the relatively two-dimensional shape of the multilayers causes the easy magnetisation axis to lie within the film plane. The anisotropy can be quantified in these systems and separated to reveal the magnitudes of the respective contributions. As mentioned in the earlier discussion on the effective anisotropy,  $K_{eff}$  can be determined from a consideration of the saturation magnetisation and the saturation field in the hard axis direction, which is taken perpendicular to the plane of the film. Equation 5.16 can then be rearranged to give,

$$K_{eff} = \frac{-H_S M_S}{2} \quad (5.22)$$

Table 5.7 shows the effective anisotropy values for several U/Gd samples and the respective saturation magnetisations in units of  $JTm^{-3}$ . The magnitudes of the effective anisotropy are comparable to those found in other multilayer systems [66], [68] and values of the volume and surface contributions are of a similar size to those ascertained for the Fe/Au [69], Ce/Fe [70] and U/Fe [49] systems.

As shown earlier, the effective anisotropy can be written in terms of the volume

| Sample Number | Composition  | Gd volume<br>( $\text{m}^3 \times 10^{-12}$ ) | $M_S$<br>( $\text{JTm}^{-3} \times 10^6$ ) | $K_{\text{eff}}$<br>( $\text{Jm}^{-3} \times 10^6$ ) |
|---------------|--|---|--|--|
| SN63          | [U <sub>26</sub> /Gd <sub>33</sub> ] <sub>20</sub>     | 1.28  | 1.11                                       | $-2.43 \pm 0.19$                                     |
| SN64          | [U <sub>26</sub> /Gd <sub>54</sub> ] <sub>20</sub>     | 1.32  | 1.12                                       | $-2.78 \pm 0.26$                                     |
| SN65          | [U <sub>26</sub> /Gd <sub>76</sub> ] <sub>20</sub>     | 1.77  | 1.14                                       | $-2.29 \pm 0.23$                                     |
| SN137         | [U <sub>24.8</sub> /Gd <sub>19.5</sub> ] <sub>30</sub> | 0.872   | 1.00                                       | $-2.03 \pm 0.20$                                     |
| SN66          | [U <sub>63.5</sub> /Gd <sub>20</sub> ] <sub>20</sub>   | 0.496   | 0.869                                      | $-1.59 \pm 0.19$                                     |
| SN68          | [U <sub>89</sub> /Gd <sub>20</sub> ] <sub>20</sub>     | 0.62  | 0.731                                      | $-1.04 \pm 0.12$                                     |
| SN138         | [U <sub>4.8</sub> /Gd <sub>20</sub> ] <sub>30</sub>    | 0.786   | 1.34                                       | $-3.02 \pm 0.31$                                     |

Table 5.7: Effective anisotropy values calculated for a selection of U/Gd multilayers. Those with constant U thickness of  $\sim 25\text{\AA}$  have been used to deduce the respective surface and volume contributions.

and surface contributions. This equation can be rearranged so that

$$t_{\text{Gd}}K_{\text{eff}} = K_V t_{\text{Gd}} + 2K_S \quad (5.23)$$

Figure 5.17 shows the change in  $t_{\text{Gd}}K_{\text{eff}}$  as the gadolinium layer thickness is varied for constant  $t_U$  of  $\sim 25\text{\AA}$ . The general trend observed can be fitted to a straight line, where the gradient gives the volume contribution  $-2.70 \pm 0.26 \times 10^6 \text{ Jm}^{-3}$  and the y-intercept is twice the surface contribution,  $K_S = 1.16 \pm 0.8 \times 10^{-3} \text{ Jm}^{-2}$ . These two competing effects indicate a possible crossover from an overall anisotropy aligning the moments within the plane of the film to a perpendicularly preferred orientation. This is represented by the x-intercept, which in this case is  $\sim 5\text{\AA}$ . This value suggests that for a [U<sub>25</sub>/Gd<sub><5</sub>] multilayer perpendicular magnetic anisotropy might be expected, leading to an easy axis oriented out of the plane of the film. The blue arrow shown on figure 5.17 shows the anisotropy values for U/Gd multilayers with  $t_{\text{Gd}}$  of  $20\text{\AA}$  and indicates increasing uranium layer thickness. This suggests that it may be possible to grow a U/Gd multilayer with thick U layers and thin Gd layers in order to provide some perpendicular magnetic anisotropy.

It is however, important to note that there are some major assumptions in this simplified volume and surface contribution extraction from the effective anisotropy;

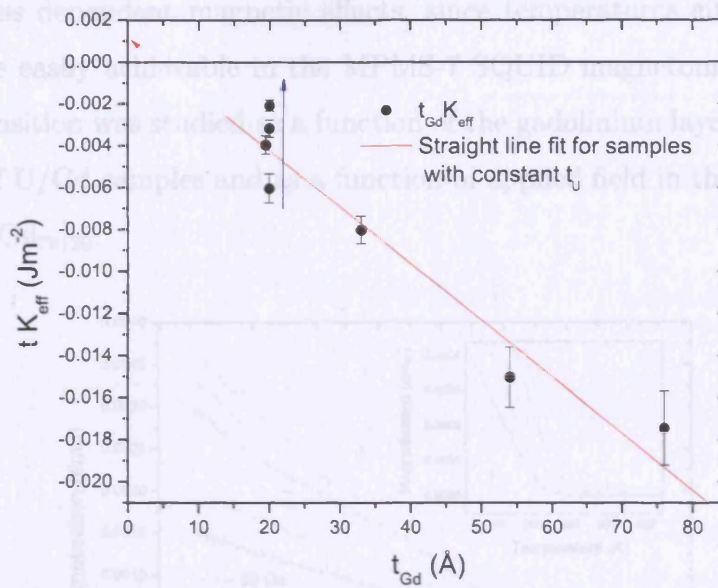


Figure 5.17: Graph of  $t_{\text{Gd}}k_{\text{eff}}$  vs  $t_{\text{Gd}}$  in order to determine the relative volume and surface contributions to the effective anisotropy of the multilayers. The blue arrow shows the effect of increasing uranium layer thickness on the effective anisotropy.

the anisotropy, localised at the interface region influences the magnetic moments within the bulk of the layer, which is only true if the anisotropy is much smaller than the intralayer exchange. The validity of the separation of the effective anisotropy into surface and volume terms becomes questionable when the layers are very thin and are almost entirely comprised of interface region. The volume anisotropy in this case is taken as independent of the thickness of the films, but it is possible in some multilayer systems, where the lattice mismatch between the respective species is low, to produce strain effects throughout the multilayer that introduce a magnetoelastic contribution that changes the magnetocrystalline anisotropy.

#### 5.8.4 Uranium/Gadolinium - Temperature Dependence

A large amount of the magnetisation measurements carried out on the U/Gd system concerned the temperature dependent properties of the magnetisation, due to the relatively low Curie temperature of gadolinium when compared to iron and cobalt, table 5.2. This critical temperature is of a convenient value for further investigating

layer thickness dependent magnetic effects, since temperatures either side of this transition are easily achievable in the MPMS-7 SQUID magnetometer. The ferromagnetic transition was studied as a function of the gadolinium layer thickness for a wide range of U/Gd samples and as a function of applied field in the case of sample SN64 -  $[U_{26}/Gd_{76}]_{20}$ .

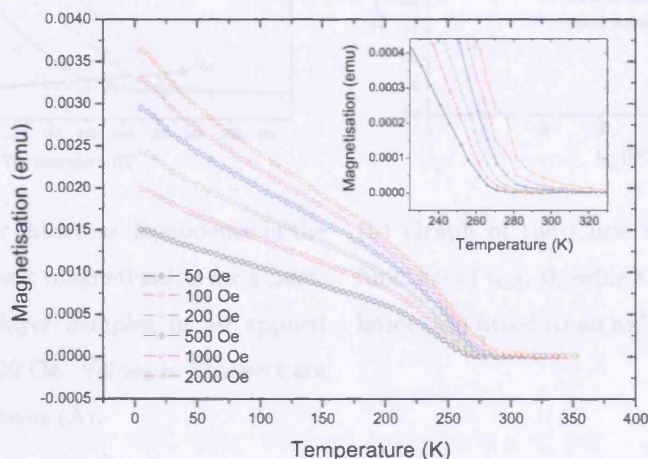
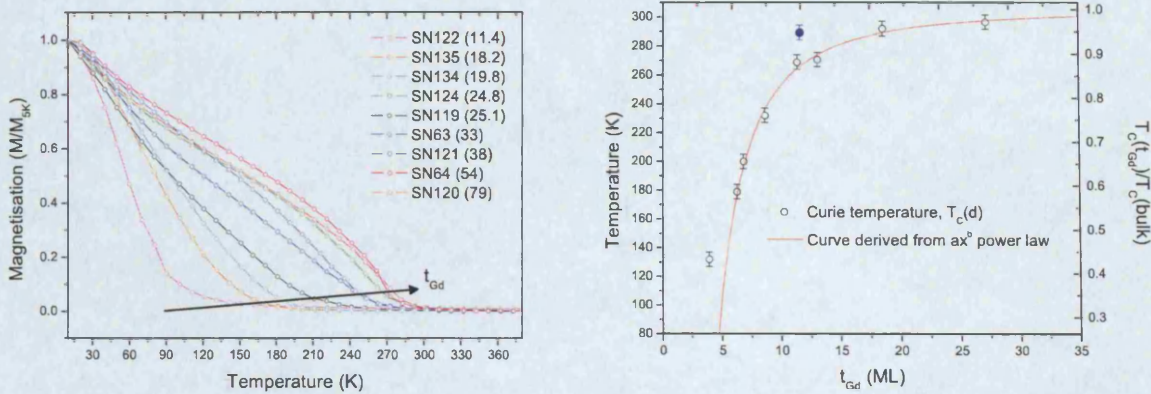


Figure 5.18: The temperature dependent magnetisation for a number of magnetic field values measured for sample SN64 -  $[U_{26}/Gd_{76}]_{20}$ .

Figure 5.18 presents the temperature dependent magnetisation (emu) for several applied magnetic field values. The insert shows a close-up view of the transition region and it is clear that the onset of magnetic ordering and the form of the initial magnetisation are dependent on the applied magnetic field. It is notoriously difficult to precisely determine the ferromagnetic transition (Curie) temperature from magnetisation measurements and most attempts are made to describe the paramagnetic phase, using the Curie-Weiss law for localised moments above  $T_C$ . In our case, with such a small quantity of material and a relatively large diamagnetic background, measurements of the paramagnetic susceptibility at these temperatures would be very difficult. It is reasonable, however, to label the Curie temperature based on the magnetisation in the ferromagnetic phase, as the 'knee' point of the temperature dependent curve. Although  $T_C$  is not known exactly, it is possible to make a layer thickness dependent study of the critical temperature. This has been undertaken for a range of U/Gd samples as a function of  $t_{Gd}$ , spanning all three series discussed,

and these have been carried out in an applied field of 1000 Oe.



(a) Gadolinium layer thickness dependence of the temperature dependent magnetisation for a number of U/Gd multilayer samples in an applied magnetic field of 1000 Oe. Values in brackets are the Gd layer thicknesses (Å). (b) Graph of the Curie temperature,  $T_C$ , as a function of  $t_{Gd}$ , showing the finite size scaling relationship fitted to an  $ax^b$  type power law.

Figure 5.19: Figures illustrating the finite size scaling effect of reduced layer thickness on the ferromagnetic transition temperature.

Figure 5.19 (b) shows the decrease in  $T_C$  as the gadolinium layers become thinner, where  $t_{Gd}$  has been converted into monolayers (ML) with 1ML taken as 2.9Å from the X-ray diffraction results. This trend follows the well known finite-size scaling behaviour and is commonly expressed in terms of the observed and bulk Curie temperatures,

$$\frac{T_C(bulk) - T_C(t_{Gd})}{T_C(bulk)} = C_0 \times t_{Gd}^{-\lambda} \quad (5.24)$$

$C_0$  is an arbitrary constant, which includes contributions from interlayer coupling effects and  $\lambda = 1/\nu$ , where  $\nu$  is the three-dimensional Ising critical exponent of the correlation length. This treatment of finite-size scaling behaviour well describes qualitatively, Ni [71], Fe [72], Co [73] and Gd [74] systems studied previously, but includes some assumptions about the nature of the system studied. The size of the magnetic moment is not taken into account and is assumed to carry an equivalent value per atom for different layer thicknesses. This requires a coherent multilayer

growth with little diffusion at the interfaces. Farle et al. [75] assert that *if  $T_C(t_{\text{ferro}})$  does not follow equation (5.24) then one does not have layer by layer growth.*

The data shown in figure 5.19 (b) were fitted to equation (5.24), such that  $C_0 = 13.4 \pm 2.5$  and  $\lambda = 1.90 \pm 0.09$ , giving  $\nu = 0.53$ . All of the measured data points fit closely to this curve, with the exception of the thinnest of the Gd layers and the point marked in blue, representing sample SN124, grown at an elevated substrate temperature of  $\sim 600\text{K}$ . The close fit to the finite-size scaling behaviour again indicates that the multilayers exhibit layer by layer growth with little diffusion at the interfaces and a good registry between the different atomic species. The assumption of a constant  $\mu_B/\text{Gd}$  value for varying Gd layer thicknesses is valid considering the magnetisation data presented earlier. Our values for  $C_0$  and  $\nu$  are similar in magnitude to those found in other studies and are especially close to those stated for Gd multilayers [75].

For U/Gd multilayers with the thinnest gadolinium layers, the observed  $T_C$  is much higher than that expected by following the finite-size scaling. This has also been observed in the Gd/W system [75], [76] and has been related to the cross-over from 3D to 2D magnetic behaviour, where theory predicts  $\nu = 1.00$  in the 2D regime. The data point highlighted in blue, SN124 (600K), also exhibits a  $T_C$  that is higher than that expected. This follows observations of the Gd/W system [75], where the increased  $T_C$  values for respective Gd layer thicknesses were attributed to the accommodation of misfit dislocations and the presence of large inhomogeneous strains, caused by steps and other defects at the interface. Recalling the X-ray diffraction data and figure 3.3 in section 3.1, as the substrate temperature is increased, the tendency is towards a more columnar growth mechanism. This gives a greater observed intensity in the high angle diffraction data, indicating a larger proportion of crystalline gadolinium, but could produce a large number of steps at the interfaces and subsequently a large number of areas with local strains.

## 5.9 Summary Analysis

The magnetisation measurements carried out for the U/Co and U/Fe systems were performed as a function of the applied field only, since the respective Curie temperatures were too high to perform any quantitative analysis of the temperature dependence of the magnetisation. The trends observed in the saturation magnetisation values for the U/Fe series of samples supported the results published previously [19], indicating a magnetically 'dead' layer of approximately 12Å present at the interfaces. This result is a likely consequence of the diffusion of Fe atoms into the uranium layers, which is supported by the observed X-ray diffraction measurements presented earlier. Trends observed in the magnetisation of U/Co samples exhibit much the same properties of those for the U/Fe system, yielding a magnetic dead layer of closer to 15Å, suggesting a greater diffusion of Co atoms into uranium than that of iron. These results again confirm the observations from the X-ray diffraction and X-ray reflectivity studies and indicate the existence of regions of Co and Fe within the multilayers, of different magnetic moment values. The property of varying magnetisation through the ferromagnetic layers can be investigated by polarised neutron reflectivity. This method allows simultaneous measurement of the magnetic moment and physical structure of the multilayer, by probing the neutron scattering length density as a function of depth through the multilayer.

A much more extensive investigation of the bulk magnetic properties of the U/Gd system has been undertaken. Field dependent measurements have revealed a complicated dependence of the coercive field upon  $t_U$  and a linear increase in  $H_C$  with  $t_{Gd}$ , as the domains increase in size. The absolute value of the saturation magnetisation decreases linearly with the thickness of the gadolinium layers to reveal a near negligible value for the dead layer, indicating a constant distribution of the magnetic moment throughout the Gd layers. This is further confirmed by the near constant value of  $M_S$  ( $\mu_B/Gd$ ) observed for samples with varying  $t_{Gd}$ . A more complex relationship is suggested by the trend observed for the saturation magnetisation as a function of the uranium layer thickness, where thicker uranium layers lead to reduced values of  $M_S$ . This effect could be caused by structural changes to the gadolinium layers as a consequence of the thicker uranium, i.e. as  $t_U$  increases, the

strain on the Gd layers is increased, resulting in a compression of the gadolinium and a reduction in the magnetic moment.

The effective anisotropy measured in these U/Gd multilayers is of a similar magnitude to that observed for U/Fe [49] and U/Ce [70] systems. Analysis of the results indicate volume and surface contributions that imply a perpendicular magnetic anisotropy acting to orient the moments out of the plane of the film that would be large enough to overcome the shape anisotropy at a  $t_{\text{Gd}}$  of  $\sim 5\text{\AA}$  for  $t_{\text{U}} = 25\text{\AA}$ . This Gd thickness might be increased by increasing the U layer thickness so that it might be possible to observe an easy axis of magnetisation oriented out of the plane in U/Gd films.

A study of the temperature dependence of the magnetisation has revealed a finite-size scaling relationship between the ferromagnetic ordering (Curie) temperature and the gadolinium layer thickness, which is consistent with behaviour observed in the Gd/W system [75]. Thin Gd layers suggest a transition from 3 dimensional to 2 dimensional behaviour at low values of  $t_{\text{Gd}}$ . Samples grown at elevated substrate temperatures exhibit values for  $T_{\text{C}}$  that are higher than expected, as a possible consequence of local interfacial strains, caused by a step like growth mechanism.

In order to further probe the bulk magnetic properties of U/Fe, U/Co and U/Gd multilayers, the polarised neutron reflectometry (PNR) technique has been employed to give a better understanding of the distribution of the magnetisation within the ferromagnetic layers. PNR should also be able to shed some light on the extent of the 5f-3d, 5f-4f hybridisations and the coupling mechanism between the respective layers.

## 5.10 Neutrons

In addition to an understanding of the physical structure of the multilayers it is important to look systematically at the magnetic properties that these samples exhibit. Neutrons are ideal probes to study the magnetism of materials and can simultaneously give information about the structure and magnetisation within the structure. In the realm of thin film science, the polarised neutron reflectivity (PNR) technique is employed to support results from X-ray reflectivity measurements and bulk magnetisation studies. PNR also enables a determination of magnetisation profiles within the magnetic layers and can detect coupling mechanisms through the non-magnetic spacer layer, giving some insight into the extent of any hybridisation between respective elements.

Initially, it is useful to introduce the relevant properties of the neutron and describe its interaction with matter at a fundamental level.

Neutrons were discovered by James Chadwick in 1932. They are spin  $1/2$  particles that consist of three quarks (udd), which result in an overall charge neutrality. However, there is an internal distribution of charge due to the three quarks that is responsible for a magnetic moment, which can then be exploited to study magnetic materials. For a sufficient production of neutrons it is only possible to use particular nuclear reactions, either fission or spallation. For the purpose of this thesis, the process of neutron spallation will be discussed, since the neutron scattering experiments were carried out on the CRISP reflectometer at the ISIS neutron spallation source.

This spallation process, figure 5.20, involves the bombardment of a heavy metal target by a beam of high-energy protons,  $\sim 800\text{MeV}$ . The protons are extracted from a synchrotron, supplied by a linac accelerator and are used to collide with a heavy metal, tantalum target. The nuclei of the target become energetically excited and release their energy by ejecting nucleons; approximately 15 neutrons are released for every proton-target collision. In the same way that X-ray photons have wavelengths of the order of atomic distances, which allow them to probe the structure of matter, neutrons too can have wavelengths of similar magnitude and are commonly described as epithermal neutrons. The neutrons that are released by the spallation process have very high energies and velocities and need to be slowed

## 5.10.1 Neutron Scattering

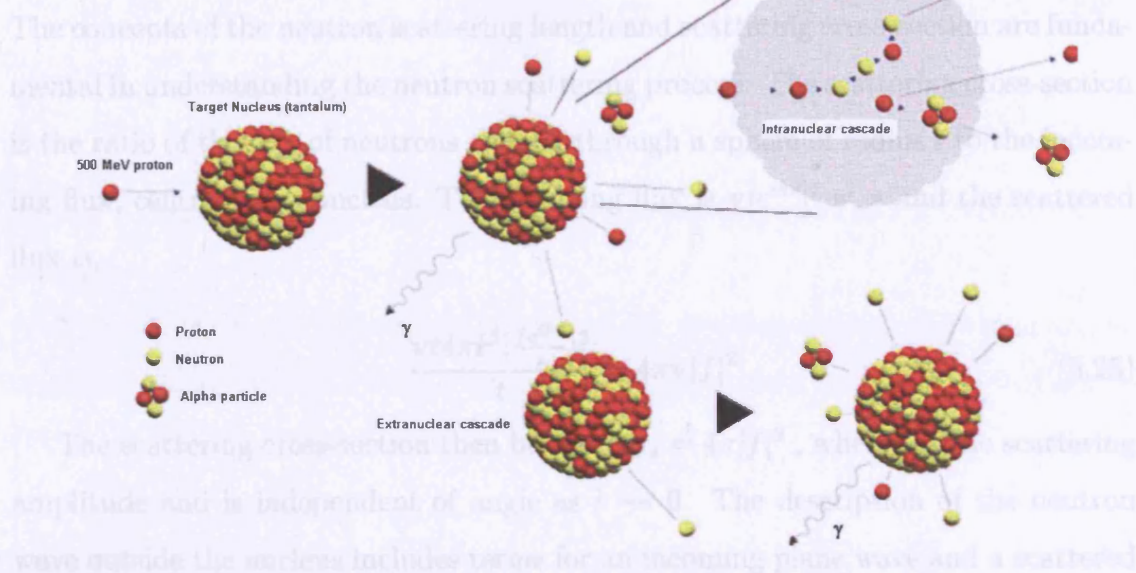


Figure 5.20: Schematic diagram showing the spallation process used to produce the neutron flux at the ISIS time-of-flight source at the Rutherford Appleton Laboratories.

to thermal energies. This is achieved by using hydrogenous moderators around the target, exploiting the large scattering cross-section of hydrogen. The moderator used for the CRISP instrument is liquid hydrogen at 20K, which provides a range of neutron wavelengths suitable for investigating relatively large nano-scale structures.

Before considering the mechanics of neutron scattering it is useful to remember how a neutron interacts with matter. The principle interactions between neutrons and atoms are the strong interaction with nuclei and the magnetic dipole interaction with unpaired electrons. The neutral charge of the neutron means that they are sensitive to the positions of the nuclei and are not affected by Coulombic forces, which allows for long penetration depths,  $\sim$ cm. The spin of the neutron can be used to investigate nuclear spin ordering, since the nuclear scattering will be spin-dependent. Magnetic excitations and structures can also be probed by neutron scattering, due to the coupling of the magnetic moment of the neutron and the magnetic moment of unpaired electrons.

### 5.10.1 Neutron Scattering

The concepts of the neutron scattering length and scattering cross-section are fundamental in understanding the neutron scattering process. The scattering cross-section is the ratio of the flux of neutrons passing through a sphere of radius  $r$  to the incoming flux, centred on a nucleus. The incoming flux is  $\mathbf{v}|e^{i\mathbf{k}\cdot\mathbf{r}}|^2 = \mathbf{v}$  and the scattered flux is,

$$\frac{\mathbf{v}t4\pi\mathbf{r}^2\left|\frac{fe^{i\mathbf{k}\cdot\mathbf{r}}}{r}\right|^2}{t} = 4\pi\mathbf{v}|f|^2 \quad (5.25)$$

The scattering cross-section then becomes  $\sigma_s = 4\pi|f|^2$ , where  $f$  is the scattering amplitude and is independent of angle as  $k \rightarrow 0$ . The description of the neutron wave outside the nucleus includes terms for an incoming plane wave and a scattered spherical wave.

$$\Psi(\mathbf{r}) = e^{i\mathbf{k}\cdot\mathbf{r}} + \frac{f}{r}e^{i\mathbf{k}\cdot\mathbf{r}} \quad (5.26)$$

Averaged over all possible angles between  $\mathbf{k}$  and  $\mathbf{r}$  gives,

$$\Psi(\mathbf{r}) = -\frac{1}{2ik}\frac{e^{i\mathbf{k}\cdot\mathbf{r}}}{r} + \left(f + \frac{1}{2ik}\right)\frac{e^{i\mathbf{k}\cdot\mathbf{r}}}{r} \quad (5.27)$$

The difference between the incoming and outgoing beams gives the neutron absorption cross-section,  $\sigma_a$ , such that the total interaction cross-section equates to the sum of both absorption and scattering components.

$$\sigma_t = \sigma_a + \sigma_s = \frac{4\pi}{k}\Im f \quad (5.28)$$

The scattering amplitude  $f = -b + ikb^2 + O(k^2)$  can be described in terms of the scattering length  $b$ , which is composed of real and imaginary parts:  $b = b' - ib''$ . The imaginary part of the scattering length describes the absorption of neutrons, caused by resonant effects with the nucleus. In an unpolarised system the scattering length is an average of the scattering lengths  $b^+$  and  $b^-$ , representing the two spin states of the neutron, spin up and spin down respectively:

$$\langle b \rangle = p_+b^+ + p_-b^- \quad (5.29)$$

$$p_+ = \frac{I + 1}{2I + 1} \quad (5.30)$$

$$p_- = \frac{I}{2I + 1} \quad (5.31)$$

$p_+$  and  $p_-$  represent the probabilities of the scattering lengths and  $I$ , the spin of the nucleus.

Initially, for low energy thermal neutrons, the neutron-nucleus scattering can be considered to be isotropic within the centre of mass system and can be described by the Fermi pseudopotential,

$$V(\mathbf{r}) = \frac{2\pi\hbar^2}{m} b\delta(\mathbf{r}) \quad (5.32)$$

However, due to the magnetic moment, caused by the distribution of charge within the neutron and the inherent spin of the neutron, the interaction is not solely concerned with the isotropic neutron-nucleus scattering; the neutron can also interact with unpaired electrons within the sample and with an external applied field, which introduces another potential term known as the Zeeman interaction. The potential now represents the neutron-nucleus, neutron-magnetisation and neutron-magnetic field interactions respectively where  $\mathbf{M}$  is the magnetisation parallel to the scattering vector.

$$V(\mathbf{r}) = \frac{2\pi\hbar^2}{m} Nb - \mu_0 g_n \mu_n \sigma_t \cdot \mathbf{M} - \mu_0 g_n \mu_n \sigma_t \cdot \mathbf{H} \quad (5.33)$$

Since we are particularly concerned with relatively large-scale structures in real space, we need to investigate features in  $Q$ -space that are small, which equates to scattering at small angles.

## 5.11 Polarised Neutron Reflectivity

Polarised neutron reflectivity (PNR) is the ideal technique to study magnetic multilayers, where it is possible to gain information about the chemical structure and the magnetisation simultaneously. A neutron reflectometer works in a similar way

to that used for X-rays and measures the reflectivity coefficient as a function of the neutron wavevector. The reflectivity can be treated by Parratt's recursive method described earlier, but with modifications to account for the sample magnetisation and the spin state of the neutron. In the case of neutron reflectivity the refractive index is dependent on the coherent scattering length.

$$n \approx 1 - \frac{2\pi}{k^2} Nb \quad (5.34)$$

Looking at this equation it is possible to have total external reflection of neutrons from a surface provided the scattering length is positive, which is the case for the majority of nuclei.

The potential involved in the neutron-sample interaction contains a term to describe the magnetisation,  $V_m$ .

$$V_{m,y}(z) = -\mu_n \cdot \mathbf{B}(z) = -\frac{2\pi\hbar^2}{m} p_m(z) \sin \theta \quad (5.35)$$

$$V = V_n \pm V_m = \frac{2\pi\hbar^2}{m} N(b \pm p_m) \quad (5.36)$$

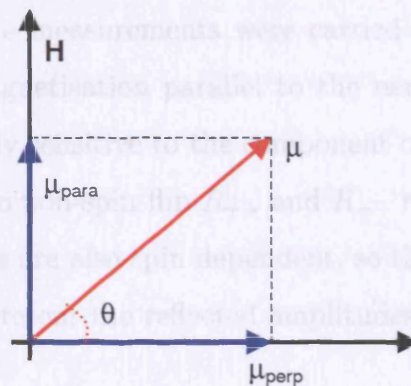


Figure 5.21: Orientation of the sample magnetisation,  $\mu$ , with respect to the applied field,  $H$ .

The magnetic potential,  $V_{m,y}(z)$  describes the magnetic moment of the neutron, scattering from a sample with its magnetisation aligned at an angle  $\theta$  to an axis perpendicular to the neutron moment. The scheme in figure 5.21 indicates the direction

of the applied magnetic field,  $\mathbf{H}$ , which is along the y axis, parallel to the neutron quantisation axis. In this case the z axis lies perpendicular to the magnetisation of the sample. The geometry of non-spin flip scattering describes the situation where the incident and reflected neutron spin directions are the same. In this case the reflected intensity is measuring only the component of the magnetisation parallel to the neutron spin, yielding the potentials and reflectivities  $V_{++}$ ,  $V_{--}$ ,  $R_{++}$  and  $R_{--}$  respectively.

The spin flip scattering measures the component of the magnetisation perpendicular to the neutron spin, still within the plane of the sample as a function of the depth z. In most systems the sample magnetisation will be aligned parallel to the applied field, but some magnetic structures such as helical and canted spins can be seen by using this type of scattering. In this case the potentials and reflectivities can be labelled  $V_{+-}$ ,  $V_{-+}$ ,  $R_{+-}$  and  $R_{-+}$ .

The potential of the neutron scattering from magnetic samples can be represented in a matrix form:

$$V = \begin{pmatrix} V_{++} & V_{+-} \\ V_{-+} & V_{--} \end{pmatrix} = \frac{2\pi\hbar^2}{m} N \begin{pmatrix} b & +p_{NSF} & p_{SF} \\ p_{SF} & b & -p_{NSF} \end{pmatrix} \quad (5.37)$$

In this work, all of the measurements were carried out with an applied field, saturating the sample magnetisation parallel to the neutron spin, so that the reflected intensities were only sensitive to the component of the magnetisation in this direction, corresponding to non-spin flip  $R_{++}$  and  $R_{--}$  reflectivities.

The Fresnel coefficients are also spin dependent, so that a matrix formalism can also be constructed to represent the reflected amplitudes from layer 1 (air) to layer n (substrate).

$$\mathbf{r}_{1\dots n} = \begin{pmatrix} \mathbf{r}_{1\dots n}^{\uparrow\uparrow} & \mathbf{r}_{1\dots n}^{\uparrow\downarrow} \\ \mathbf{r}_{1\dots n}^{\downarrow\uparrow} & \mathbf{r}_{1\dots n}^{\downarrow\downarrow} \end{pmatrix} \quad (5.38)$$

The reflected amplitude can be treated in the same way as the X-ray result in equation (4.41), but with the phase factor, p replaced with a propagation matrix,  $P_j$  to account for the phase of both spin up and spin down states, where  $q_j$  is the perpendicular wavevector transfer in a layer j and  $d_j$  is the thickness of the jth layer.

$$P_j = \begin{pmatrix} e^{iq_j^\uparrow d_j} & 0 \\ 0 & e^{iq_j^\downarrow d_j} \end{pmatrix} \quad (5.39)$$

The Fresnel equations become,

$$r_{j,j+1}^{\uparrow\uparrow} = \frac{q_j^\uparrow - q_{j+1}^\uparrow}{q_j^\uparrow + q_{j+1}^\uparrow} \quad (5.40)$$

$$t_{j,j+1}^{\uparrow\uparrow} = \frac{2q_j^\uparrow}{q_j^\uparrow + q_{j+1}^\uparrow} \quad (5.41)$$

The reflected intensities can be derived from the Parratt recursive method outlined earlier, with the exception that the wavevectors are spin-dependent. The roughness is modeled as an error function perturbation to the interface, as was used for the case of X-ray reflectivity.

The production of two reflected intensity curves relating to the two spin states of the neutron has features that can be difficult to resolve so it can be more useful to simulate the asymmetry of the data sets. The asymmetry is the ratio of the difference between the two curves to the sum of the reflected intensities.

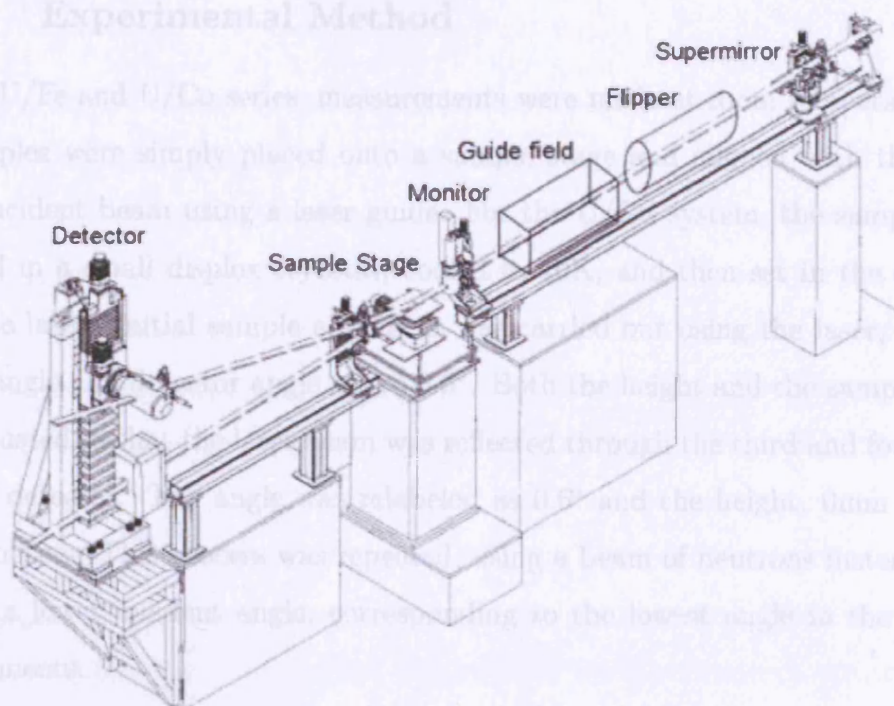
$$Asymmetry = \frac{R_{++}(\mathbf{Q}) - R_{--}(\mathbf{Q})}{R_{++}(\mathbf{Q}) + R_{--}(\mathbf{Q})} \quad (5.42)$$

The experiments described in this thesis were performed on the CRISP reflectometer at the ISIS neutron spallation source. A specific consideration for carrying out experiments at a spallation source, where the neutrons arrive in a pulse of a range of wavelengths is that a time-of-flight experimental set-up is used.

The CRISP instrument (figure 5.22) is situated after the liquid hydrogen moderator at 20K and analyses a wavelength band of 0.5 - 6.5 Å. The neutron beam arrives at the experimental hutch at an inclination angle of 1.5° and the entrance slit provides a cross-section that is 40mm wide and between 0.5 and 6mm high. The wavelength band is defined by a disc chopper with an aperture and a nimonic chopper is used for pulse suppression. The first object that the beam encounters is known as a frame-overlap mirror, which uses a nickel-coated, silicon wafer to filter out neutrons with wavelengths,  $\lambda \geq 13\text{Å}$ . This is due to the fact that the neutrons arrive in pulses of 50Hz and in order to distinguish between separate pulses it is

## 5.11.1 Experimental Method

For the U/Fe and U/Cu series measurements were the samples were simply placed into the centre of the incident beam using a laser guide mounted in a small display, and which set the centre of the guide to the initial sample position. Both the height and the sample angles were adjusted using a turntable. The neutron beam was reflected through the third and fourth slits into the detector. The neutron path is shown in dashed lines in the diagram.



Since the neutron measurements are wavelength dependent in this case, it was

Figure 5.22: Layout of the CRISP neutron reflectometer at the ISIS neutron spallation source, showing set-up for polarised neutron reflectivity without polarisation analysis in the specular geometry. Dashed lines show the neutron path through the apparatus to the detector.

important not to allow the slowest neutrons from one to interfere with another. The neutrons are then polarised by a supermirror, which has an efficiency of  $\sim 99.95\%$ . A non-adiabatic spin flipper is used to select the neutron spin direction and the polarised neutrons then travel through a guide field to prevent polarisation relaxation, through a second collimation slit and then through a monitor to measure the incident flux. The neutrons now reach the sample, which is magnetised by a maximal applied field of  $\sim 4.4\text{kOe}$  that is applied in the same direction as the guide field to prevent loss of polarisation. The sample sits approximately 10m from the moderator and reflects neutrons through two further slits to the detector, 1.75m away.

The time-of-flight resolution is a function of the angular and time resolutions; in this case  $\delta t$  is the pulsed time width and  $t$  is the time of flight of the neutron.

$$\left(\frac{\delta q}{q}\right)^2 = \left(\frac{\delta\theta}{\theta}\right)^2 + \left(\frac{\delta t}{t}\right)^2 \quad (5.43)$$

### 5.11.1 Experimental Method

For the U/Fe and U/Co series, measurements were made at room temperature and the samples were simply placed onto a sample stage and aligned with the centre of the incident beam using a laser guide. For the U/Gd system, the samples were mounted in a small displax cryostat, cooled to 10K, and then set in the centre of the guide laser. Initial sample alignment was carried out using the laser, with the sample angle and detector angle set to  $0.6^\circ$ . Both the height and the sample angles were adjusted so that the laser beam was reflected through the third and fourth slits into the detector. The angle was relabeled as  $0.6^\circ$  and the height, 0mm to allow for any offsets. This process was repeated, using a beam of neutrons instead of the laser at a lower incident angle, corresponding to the lowest angle in the planned measurements.

Since the neutron measurements are wavelength dispersive in this case, it was necessary to take specular measurements at several angles in order to gain enough data over the required Q-range. Most results were obtained at angles,  $0.25^\circ$ ,  $0.6^\circ$ ,  $1.2^\circ$  and  $2.0^\circ$  over a period of 15 hours, to obtain reasonable data to  $0.25\text{\AA}^{-1}$  in Q.

The data were manipulated, using the POL program within the OpenGenie computer package. In the case of multiple angles, the data sets have to be rebinned and combined to give a complete picture of the reflected intensity.

The xPOLLY program written by S.Langridge [4] was used to simulate the polarised neutron data. The input parameters include the relevant layer thickness, roughness, density and magnetisation ( $\mu_B/\text{atom}$ ). The anomalous dispersion corrections used in the X-ray reflectivity simulation are replaced by the real and imaginary components of the neutron scattering length. The simulated data are sensitive to the distribution of the magnetisation and coupling nature of the ferromagnetic layers, so it is possible to model these factors in the input parameters. The simulations were then fitted to the data, using the same minimisation procedures used to fit the X-ray reflectivity. In addition to the two separate curves it is also possible to fit the data to the asymmetry of the polarised neutron reflectivity.

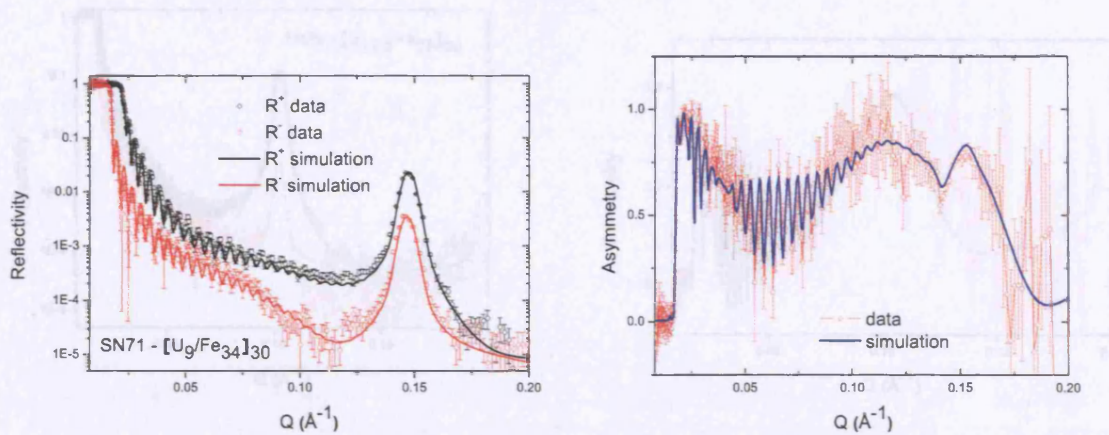
### 5.11.2 Results

Polarised neutron reflectivity measurements have been carried out on a selection of U/Fe, U/Co and U/Gd samples. In the case of the iron and cobalt systems the data were taken at room temperature, whereas the U/Gd multilayers were cooled to 10K. A magnetic field of 4.4kOe, large enough to magnetically saturate the samples, was applied in all cases, within the plane of the multilayer samples, parallel to the spin of the neutron, perpendicular to the direction of motion. These measurements were taken without polarisation analysis so that only the non spin-flip scattering was investigated. The xPOLLY simulation program was used to model the spin-up and spin-down reflectivities,  $R_{++}$  and  $R_{--}$ . The following sections describe the experimental data and fitted simulations for the specular reflectivity and the asymmetry. Summary tables report results from the simultaneous structural and magnetic characterisation and relay the models used.

### 5.11.3 Uranium/Iron

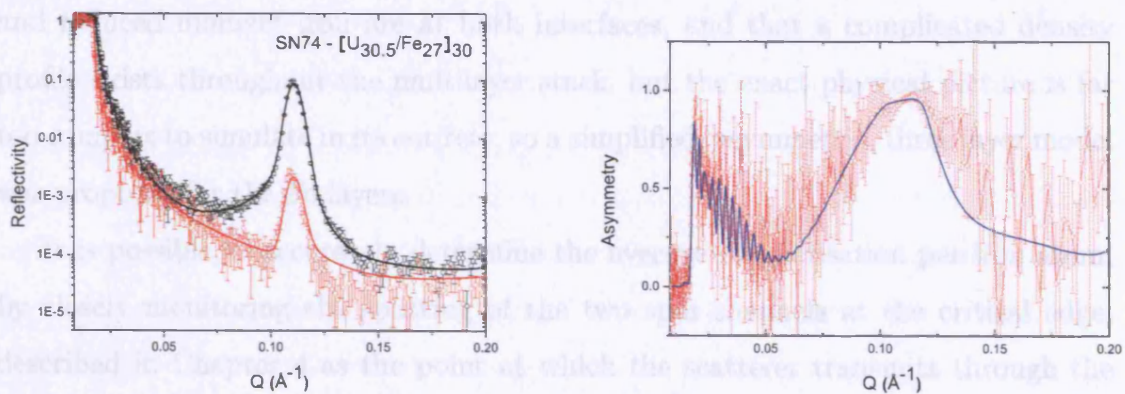
Samples SN71, SN74 and SN75 were investigated, using PNR to simultaneously confirm the multilayer structure as modelled for X-ray reflectivity, the value of the magnetic moment per Fe atom at saturation determined by SQUID magnetometry, and to probe the distribution of magnetisation within the ferromagnetic layers and the coupling between the layers. Figures 5.23, 5.24 and 5.25 show the specular reflected intensities for both spin up (black) and spin down (red) channels and the fitted, simulations to these data accompanied by graphs describing the asymmetry.

The model used to simulate the reflectivity data included three types of iron, as suggested by Beesley et al. [19] [49] as a direct consequence of results obtained from SQUID magnetometry and Mössbauer spectroscopy. The growth mechanism assumed for the U/Fe system was as follows; Fe atoms sputtered onto an uranium layer diffuse into the U layer to produce a graduated alloy region, comprising of a non-ferromagnetic iron component close to the bulk of the U layer, carrying no measurable magnetic moment, then a gradual increase in moment as the iron layer becomes thicker, and finally the bulk magnetic moment of  $2.2\mu_B$  for the solely crys-



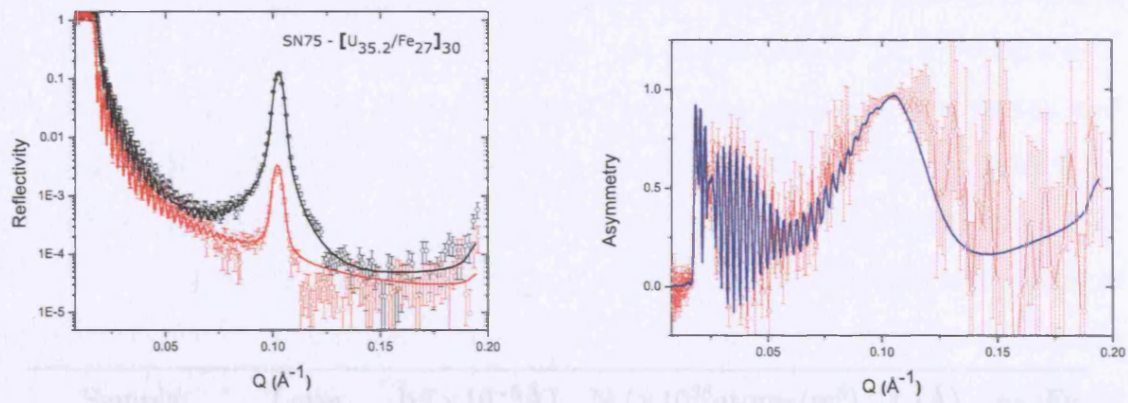
(a) Experimental data and fitted, simulated curves for the specular reflectivity in a saturation field. The black points (curve) denote the  $R_{++}$  channel and the red points (curve), the  $R_{--}$ . (b) Experimental data and fitted, simulated curve (blue line), describing the asymmetry; the ratio of the difference between the two spin channels to the sum.

Figure 5.23: The polarised neutron reflectivity data measured in the specular geometry at 300K and 4.4kOe simulated by the xPOLLY program for sample SN71 -  $[U_9/Fe_{34}]_{30}$ .



(a)  $R_{++}$  (black) and  $R_{--}$  (red) channels of the polarised neutron reflectivity in the specular geometry under an applied saturation field. (b) Experimental data and fitted, simulated curve (blue line), describing the asymmetry.

Figure 5.24: The polarised neutron reflectivity data measured in the specular geometry at 300K and 4.4kOe simulated by the xPOLLY program for sample SN74 -  $[U_{30.5}/Fe_{27}]_{30}$ .



(a)  $R_{++}$  (black) and  $R_{--}$  (red) channels of the polarised neutron reflectivity in the specular geometry under an applied saturation field. (b) Experimental data and fitted, simulated curve (blue line), describing the asymmetry.

Figure 5.25: The polarised neutron reflectivity data measured in the specular geometry at 300K and 4.4kOe simulated by the xPOLLY program for sample SN75 -  $[\text{U}_{35.2}/\text{Fe}_{27}]_{30}$

talline iron component. The Fe-U interface at the top of the layer was assumed to have a much more sharply contrasted region, since the U atoms are far less likely to diffuse into the Fe layers. In reality it is likely that components of the non-magnetic and reduced moment iron are at both interfaces, and that a complicated density profile exists throughout the multilayer stack, but the exact physical picture is far too complex to simulate in its entirety, so a simplified, asymmetric, three layer model was proposed for the Fe layers.

It is possible to accurately determine the average magnetisation per iron atom, by closely monitoring the splitting of the two spin channels at the critical edge, described in Chapter 4 as the point at which the scatterer transmits through the multilayer and no longer undergoes total external reflection. In our case, the scatterer is the neutron, which even at very small incident angles are able to transmit through the entire multilayer stack. It is in this region of the reflectivity curve that the splitting of the two spin channels is sensitive to the magnetisation of the whole sample. The distribution of the magnetisation within the Fe layers was then probed by varying the respective thicknesses of the three Fe components, keeping the average  $\mu_{\text{B}}/\text{Fe}$  constant.

| Sample   | Layer          | $b$ ( $\times 10^{-5} \text{ \AA}$ ) | $N$ ( $\times 10^{28} \text{ atoms/m}^3$ ) | $t$ ( $\text{ \AA}$ ) | $\mu_B/\text{Fe}$ |
|--|----------------|--------------------------------------|--|-----------------------|-------------------|
| SN71   | $Fe_{bulk}$    | 9.54                                 | 8.4  | 18.1                  | 2.2               |
| [U <sub>9</sub> /Fe <sub>34</sub> ] <sub>30</sub>    | $Fe_{reduced}$ | 9.54                                 | 7.3  | 11                    | 0.9               |
|  | $Fe_{alloy}$   | 9.54                                 | 7  | 5                     | 0                 |
|  | U              | 8.417                                | 4.7  | 9                     | 0                 |
| SN74   | $Fe_{bulk}$    | 9.54                                 | 8.4  | 14                    | 2.2               |
| [U <sub>35.2</sub> /Fe <sub>27</sub> ] <sub>30</sub> | $Fe_{reduced}$ | 9.54                                 | 6.8  | 9                     | 0.7               |
|  | $Fe_{alloy}$   | 9.54                                 | 6.5  | 4                     | 0                 |
|  | U              | 8.417                                | 4.7  | 35.2                  | 0                 |
| SN75   | $Fe_{bulk}$    | 9.54                                 | 8.4  | 14                    | 2.2               |
| [U <sub>30.5</sub> /Fe <sub>27</sub> ] <sub>30</sub> | $Fe_{reduced}$ | 9.54                                 | 6.8  | 8                     | 0.4               |
|  | $Fe_{alloy}$   | 9.54                                 | 6  | 5                     | 0                 |
|  | U              | 8.417                                | 4.7  | 30.5                  | 0                 |

Table 5.8: Summary of the input parameters used to simulate the polarised neutron reflectivity data, fitted using the xPOLLY [4] program. Table includes the asymmetric, three component iron layer model with values for the respective densities and magnetic moments.

The input parameters consisted of the real and imaginary parts of the neutron scattering length,  $b$  ( $\times 10^{-5}\text{\AA}$ ), the atomic number density,  $N$  ( $\times 10^{28}\text{atoms/m}^3$ ), the magnetic moment per atom ( $\mu_B/\text{atom}$ ), the angle between the moments and the applied field,  $\theta$  (taken to be  $0^\circ$  in our case, since a magnetic field large enough to saturate the iron layers was applied), and the layer thickness,  $t$  ( $\text{\AA}$ ). The coupling between the iron layers was chosen to be ferromagnetic since there were no observable half order Bragg peaks, indicative of an antiferromagnetically coupled multilayer system. The instrumental resolution (3.32) and the magnitude of the background, experimental noise were also input. Table 5.8 summarises the parameters determined for the U/Fe series of samples. The three component Fe layer model can be represented as a two layer system of bulk magnetisation and magnetically 'dead' iron respectively, which gives  $10 \leq t_{\text{Fe}}(\text{\AA}_{\text{dead}}) \leq 11.5$ . SQUID magnetometry indicated a magnetically dead iron layer of  $\sim 11\text{\AA}$ , see figure 5.6 (b).

| Sample | Composition                             | $N_{\text{X-ray}}$<br>( $\times 10^{28}\text{atoms/m}^3$ ) | $N_{\text{PNR}}$<br>( $\times 10^{28}\text{atoms/m}^3$ ) | $m_{\text{SQUID}}$<br>$\mu_B/\text{Fe}$ | $m_{\text{PNR}}$<br>$\mu_B/\text{Fe}$ |
|--------|---|--|--|---|---------------------------------------|
| SN71   | $[\text{U}_9/\text{Fe}_{34}]_{30}$      | 8.09   | 7.84   | $1.4 \pm 0.16$                          | 1.46                                  |
| SN74   | $[\text{U}_{35.2}/\text{Fe}_{27}]_{30}$ | 8.11   | 7.59   | $1.23 \pm 0.15$                         | 1.37                                  |
| SN75   | $[\text{U}_{30.5}/\text{Fe}_{27}]_{30}$ | 8.13   | 7.48   | $1.2 \pm 0.15$                          | 1.26                                  |

Table 5.9: Comparison of the averaged densities and magnetic moment values as determined from PNR, with those obtained using SQUID magnetometry and X-ray reflectivity techniques.

The average values for the Fe and U layer densities and magnetic moment values obtained from PNR were compared to those obtained from bulk magnetic measurements and the fitted X-ray reflectivity parameters, these are shown in table 5.9. Figure 5.26 shows the saturation moment ( $\mu_B/\text{Fe}$ ) as a function of the iron layer thickness, comparing values obtained using SQUID magnetometry and polarised neutron reflectometry.

The mean densities determined from X-ray and neutron reflectometry techniques are similar in magnitude for all the samples measured. The values of the saturation magnitude ( $\mu_B/\text{Fe}$ ) determined by PNR, and averaged over the entire Fe layer, fall

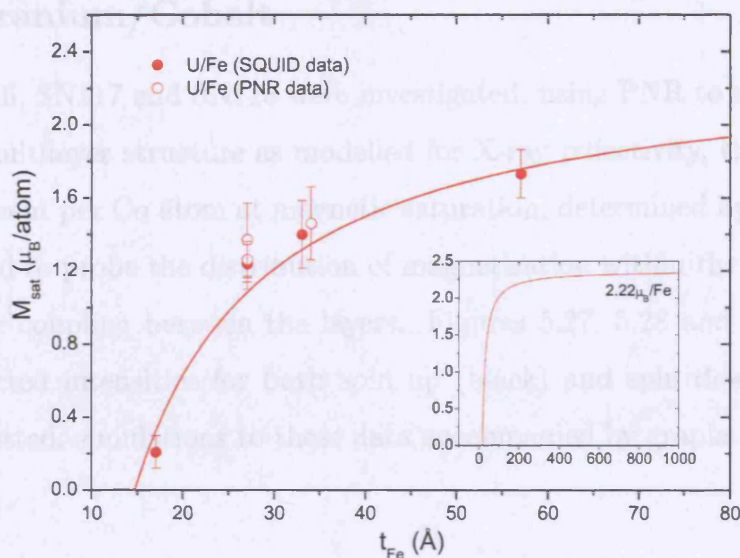


Figure 5.26: Comparison of the saturation magnetisation values ( $\mu_{\text{B}}/\text{Fe}$ ) as determined by SQUID magnetometry and PNR, averaged over the entire Fe layer, as a function of the iron layer thickness.

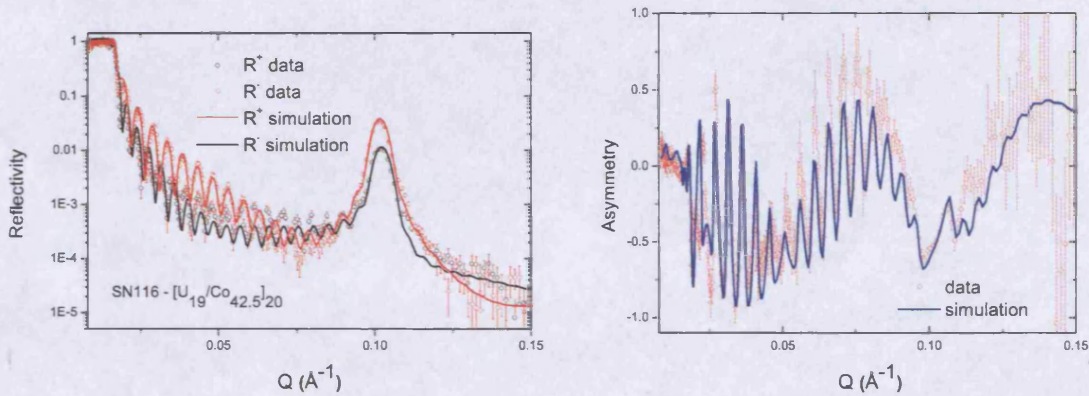
on the trend line observed in the magnetisation study described earlier. These supporting results and the model used to simulate the neutron reflectivity data lend further weight to the existence of regions of iron with varying values of magnetic moment, a conclusion reached in the published work by Beesley et al. [19].

Figure 5.27: The polarized neutron reflectivity data measured in the specular geometry at 300K and 340K simulated by the xPOLLY program for sample SN11P ( $\text{Co}_{0.11}\text{Fe}_{0.89}/\text{U}_{0.5}\text{Fe}_{0.5}$ ).

As a simplification of the model used to simulate the reflectivity from U/Fe multilayers, the cobalt was divided into two discrete layers – one of bulk crystalline cobalt with the bulk density and magnetic moment ( $1.7 \mu_{\text{B}}/\text{Co}$ ), and the other as a reduced density, magnetic ‘dead’ layer. As assumed for the U/Fe system, the Co was considered as diffusing mainly into the U layers on deposition, so that the majority of the alloying would take place at the U-Co interface and not at the Co-U interface. The original two-layer model was used to provide self-consistent, and density profile

### 5.11.4 Uranium/Cobalt

Samples SN116, SN117 and SN118 were investigated, using PNR to simultaneously confirm the multilayer structure as modelled for X-ray reflectivity, the value of the magnetic moment per Co atom at magnetic saturation, determined by SQUID magnetometry, and to probe the distribution of magnetisation within the ferromagnetic layers and the coupling between the layers. Figures 5.27, 5.28 and 5.29 show the specular reflected intensities for both spin up (black) and spin down (red) channels and the fitted, simulations to these data accompanied by graphs describing the asymmetry.

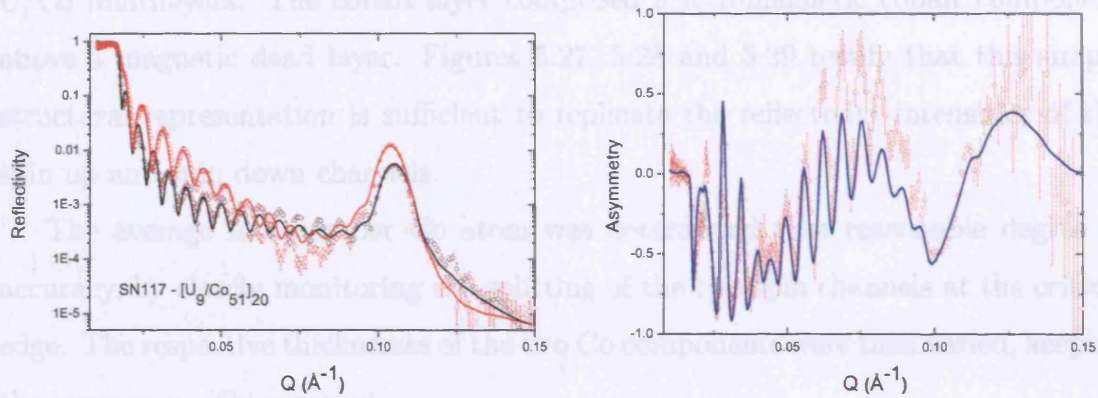


(a)  $R_{++}$  (black) and  $R_{--}$  (red) channels of the polarised neutron reflectivity in the specular geometry under an applied saturation field.

(b) Experimental data and fitted, simulated curve (blue line), describing the asymmetry.

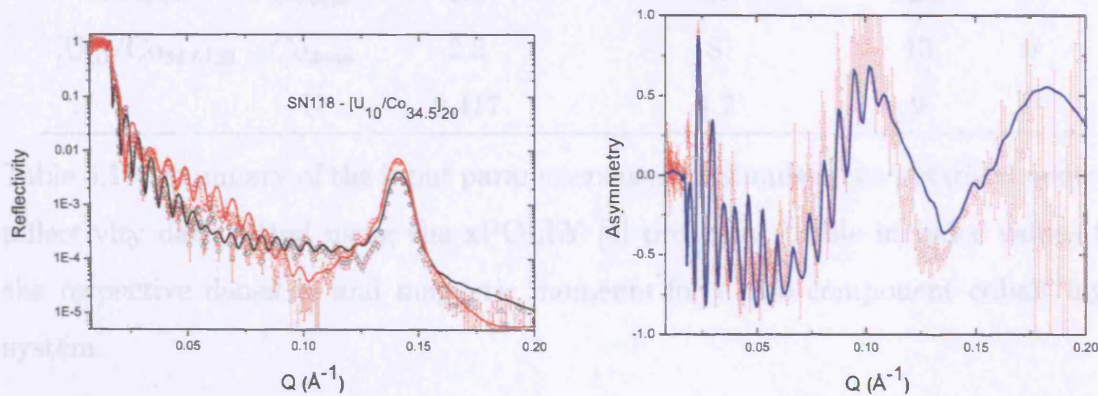
Figure 5.27: The polarised neutron reflectivity data measured in the specular geometry at 300K and 4.4kOe simulated by the xPOLLY program for sample SN116 –  $[\text{Co}_{42.5}/\text{U}_{19}]_{20}$

As a simplification of the model used to simulate the reflectivity from U/Fe multilayers, the cobalt was divided into two discrete layers - one of bulk crystalline cobalt with the bulk density and magnetic moment ( $1.7\mu_{\text{B}}/\text{Co}$ ), and the other as a reduced density, magnetic 'dead' layer. As assumed for the U/Fe system, the Co was considered as diffusing mainly into the U layers on deposition, so that the majority of the alloying would take place at the U-Co interface and not at the Co-U interface. This crude, two-layer model was used to provide a magnetisation and density profile



(a)  $R_{++}$  (black) and  $R_{--}$  (red) channels of the polarised neutron reflectivity in the specular geometry under an applied saturation field. (b) Experimental data and fitted, simulated curve (blue line), describing the asymmetry.

Figure 5.28: The polarised neutron reflectivity data measured in the specular geometry at 300K and 4.4kOe simulated by the xPOLLY program for sample SN117 -  $[\text{U}_9/\text{Co}_{51}]_{15}$



(a)  $R_{++}$  (black) and  $R_{--}$  (red) channels of the polarised neutron reflectivity in the specular geometry under an applied saturation field. (b) Experimental data and fitted, simulated curve (blue line), describing the asymmetry.

Figure 5.29: The polarised neutron reflectivity data measured in the specular geometry at 300K and 4.4kOe simulated by the xPOLLY program for sample SN118 -  $[\text{U}_{10}/\text{Co}_{34.5}]_{20}$

within the cobalt layers, as a simplification of the actual physical structure of the U/Co multilayers. The cobalt layer comprised a ferromagnetic cobalt component above a magnetic dead layer. Figures 5.27, 5.28 and 5.29 testify that this simple structural representation is sufficient to replicate the reflectivity intensities of the spin up and spin down channels.

The average moment per Co atom was determined to a reasonable degree of accuracy, by closely monitoring the splitting of the two spin channels at the critical edge. The respective thicknesses of the two Co components were then varied, keeping the average  $\mu_B/\text{Co}$  constant.

| Sample   | Layer       | $b$ ( $\times 10^{-5}\text{\AA}$ ) | $N$ ( $\times 10^{28}\text{atoms/m}^3$ ) | $t$ ( $\text{\AA}$ ) | $\mu_B/\text{Co}$ |
|--|-------------|------------------------------------|--|----------------------|-------------------|
| SN116  | $Co_{bulk}$ | 2.5                                | 8.9                                      | 25                   | 1.7               |
| [Co <sub>42.5</sub> /U <sub>19</sub> ] <sub>20</sub> | $Co_{dead}$ | 2.5                                | 8.5                                      | 17                   | 0                 |
|  | U           | 8.417                              | 4.6                                      | 20                   | 0                 |
| SN117  | $Co_{bulk}$ | 2.5                                | 8.9                                      | 39                   | 1.7               |
| [U <sub>9</sub> /Co <sub>51</sub> ] <sub>15</sub>    | $Co_{dead}$ | 2.5                                | 8.3                                      | 12                   | 0                 |
|  | U           | 8.417                              | 4.6                                      | 9                    | 0                 |
| SN118  | $Co_{bulk}$ | 2.5                                | 8.8                                      | 22.5                 | 1.7               |
| [U <sub>10</sub> /Co <sub>34.5</sub> ] <sub>20</sub> | $Co_{dead}$ | 2.5                                | 8  | 13                   | 0                 |
|  | U           | 8.417                              | 4.7                                      | 9                    | 0                 |

Table 5.10: Summary of the input parameters used to simulate the polarised neutron reflectivity data, fitted using the xPOLLY [4] program. Table includes values for the respective densities and magnetic moments for a two component cobalt layer system.

As for the U/Fe series, the input parameters consisted of the real and imaginary parts of the neutron scattering length,  $b$  ( $\times 10^{-5}\text{\AA}$ ), the atomic number density,  $N$  ( $\times 10^{28}\text{atoms/m}^3$ ), the magnetic moment per atom ( $\mu_B/\text{atom}$ ), the angle between the moments and the applied field,  $\theta$  (taken to be  $0^\circ$  in our case, since a magnetic field large enough to saturate the cobalt layers was applied), and the layer thickness,  $t$  ( $\text{\AA}$ ). The coupling between the cobalt layers was chosen to be ferromagnetic since there were no observable half order Bragg peaks, indicative of an antiferromagnetically

coupled multilayer system. The instrumental resolution (3.32) and the magnitude of the background, experimental noise were also input. Table 5.10 summarises the parameters determined for the U/Co series of samples.

| Sample | Composition  | $N_{X\text{-ray}}$<br>( $\times 10^{28}$ atoms/m $^3$ ) | $N_{\text{PNR}}$<br>( $\times 10^{28}$ atoms/m $^3$ ) | $m_{\text{SQUID}}$<br>$\mu_{\text{B}}/\text{Co}$ | $m_{\text{PNR}}$<br>$\mu_{\text{B}}/\text{Co}$ |
|--------|--|---|---|--|--|
| SN116  | [Co <sub>42.5</sub> /U <sub>19</sub> ] <sub>20</sub> | 8.60  | 8.64  | 1.10 $\pm$ 0.23                                  | 1.02   |
| SN117  | [U <sub>9</sub> /Co <sub>51</sub> ] <sub>15</sub>    | 8.65  | 8.76  | -  | 1.30   |
| SN118  | [U <sub>10</sub> /Co <sub>34.5</sub> ] <sub>20</sub> | 8.56  | 8.59  | -  | 1.11   |

Table 5.11: Comparison of the averaged densities and magnetic moment values as determined from PNR, with those obtained using SQUID magnetometry and X-ray reflectivity techniques.

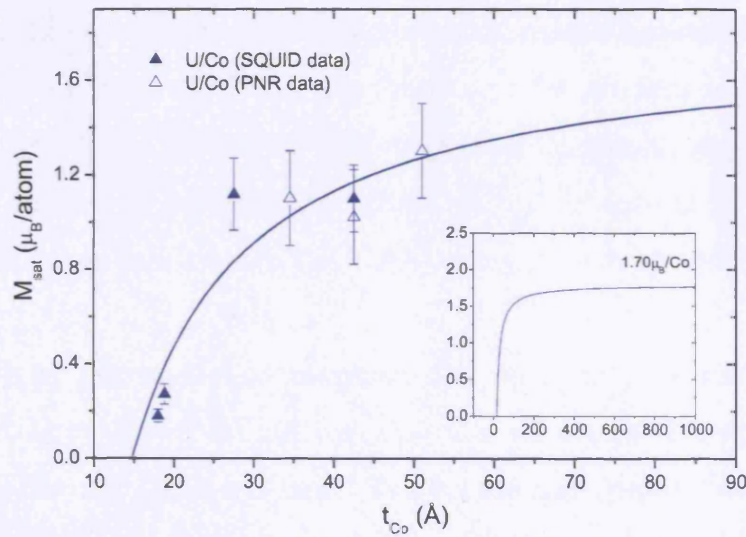


Figure 5.30: Comparison of the saturation magnetisation values ( $\mu_{\text{B}}/\text{Co}$ ) as determined by SQUID magnetometry and PNR, averaged over the entire Co layer, as a function of the cobalt layer thickness.

The average values for the Co and U layer densities and magnetic moment values obtained from PNR were compared to those obtained from bulk magnetic measurements and the fitted X-ray reflectivity parameters, these are shown in table 5.11. Figure 5.30 shows the saturation moment ( $\mu_{\text{B}}/\text{Co}$ ) as a function of the cobalt layer

thickness, comparing values obtained using SQUID magnetometry and polarised neutron reflectometry.

The mean densities determined from X-ray and neutron reflectometry techniques are similar in magnitude for all the samples measured. The values of the saturation magnitude ( $\mu_B/\text{Co}$ ) determined by PNR, and averaged over the entire Co layer, fall on the trend line observed in the magnetisation study described earlier.

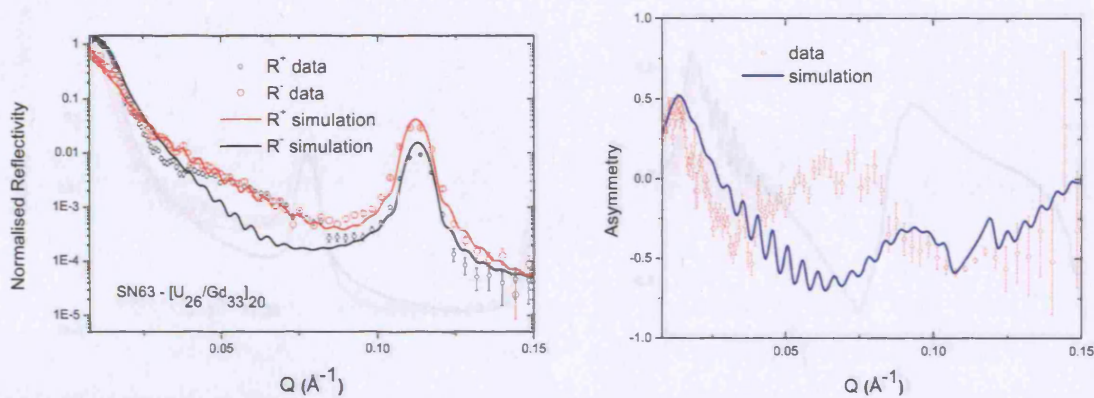
### 5.11.5 Uranium/Gadolinium

Samples SN63, SN65, SN67 and SN124 were investigated, using PNR to simultaneously confirm the multilayer structure as modelled for X-ray reflectivity, the value of the magnetic moment per Gd atom at saturation determined by SQUID magnetometry, and to probe the distribution of magnetisation within the ferromagnetic layers and the coupling between the layers. The PNR measurements were taken at a temperature of 10K in all cases, to ensure that the Gd layers were significantly below their respective Curie temperatures. Figures 5.31, 5.33, 5.32 and 5.34 show the specular reflected intensities for both spin up (black) and spin down (red) channels and the fitted, simulations to these data accompanied by graphs describing the asymmetry. For samples SN63 and SN67, data was also collected for the reflected intensities at 300K.

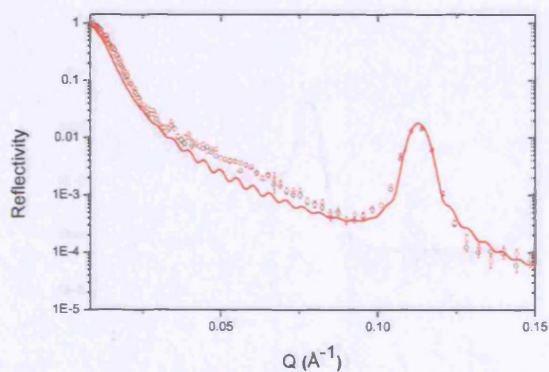
The magnetisation measurements discussed earlier did not indicate the presence of a magnetic 'dead' layer and implied a near constant saturation moment (reduced from the bulk value of  $7.63\mu_B$ ) as a function of the gadolinium layer thickness ( $\sim 4\mu_B/\text{Gd}$ ). The X-ray diffraction and magnetisation results suggested a much more reduced amount of diffusion than that seen in the case of U/Fe and U/Co multilayers, and as a consequence the U/Gd samples were modelled as a simple bilayer.

The reflectivity curves and consequently the asymmetry, as simulated by the simple U/Gd bilayer model, do not resemble the experimental data as closely as those of the U/Fe and U/Co systems. The mechanism responsible for the large reduction in saturation magnetic moment of the Gd layers is not clear. It is possible that this effect is manifest in the neutron reflectivity, but attempts to model the gadolinium layers with a more complex distribution of magnetic moment have not replicated the experimental data to any greater degree than the simple, constant moment model. The total moment exhibited by the U/Gd samples was determined as for the U/Fe and U/Co systems, by reproducing the splitting of the spin up and spin down reflectivity channels the critical edge region.

The input parameters consisted of the real and imaginary parts of the neutron scattering length,  $b$  ( $\times 10^{-5}\text{\AA}$ ), the atomic number density,  $N$  ( $\times 10^{28}\text{atoms/m}^3$ ), the

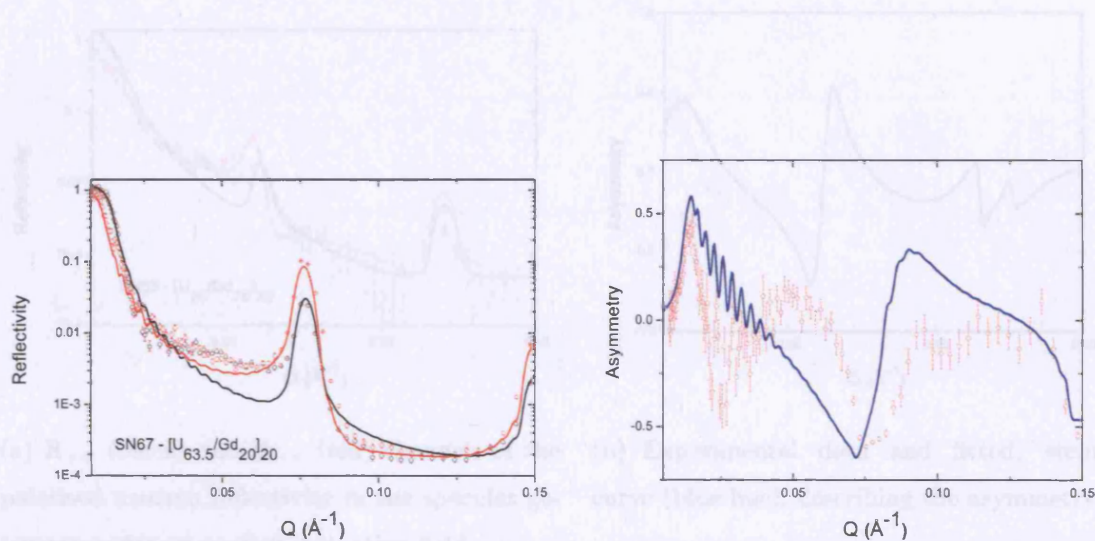


(a)  $R_{++}$  (black) and  $R_{--}$  (red) channels of the polarised neutron reflectivity in the specular geometry under an applied saturation field. (b) Experimental data and fitted, simulated curve (blue line), describing the asymmetry.

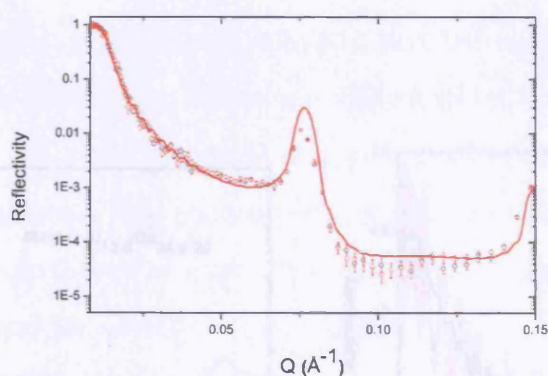


(c) Experimental data and fitted, simulated curve (red line), describing the reflected intensity observed at room temperature (300K).

Figure 5.31: The polarised neutron reflectivity data measured in the specular geometry at 10K/300K in an applied magnetic field of 4.4kOe, simulated using the xPOLLY program for sample SN63 -  $[\text{U}_{26}/\text{Gd}_{33}]_{20}$ .

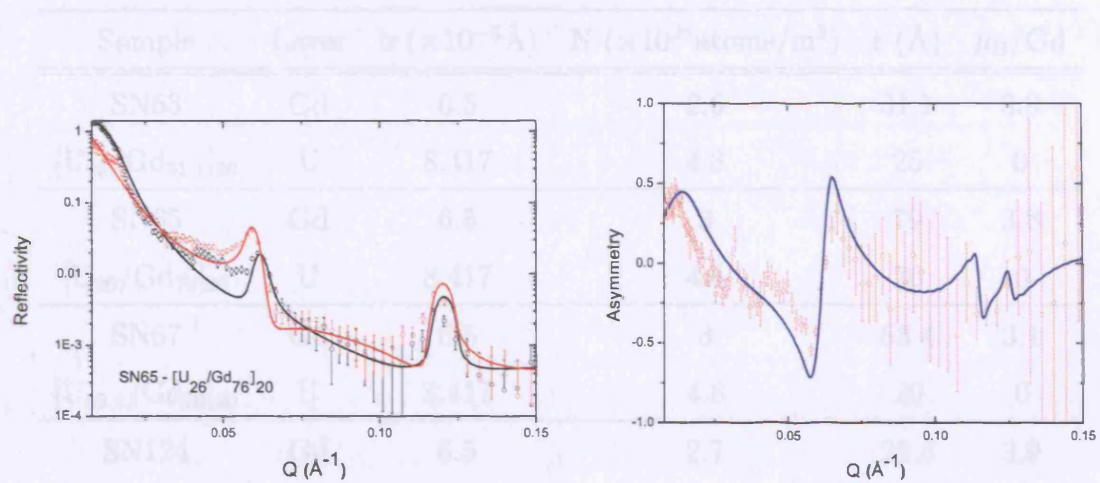


(a)  $R_{++}$  (black) and  $R_{--}$  (red) channels of the polarised neutron reflectivity in the specular geometry under an applied saturation field. (b) Experimental data and fitted, simulated curve (blue line), describing the asymmetry.



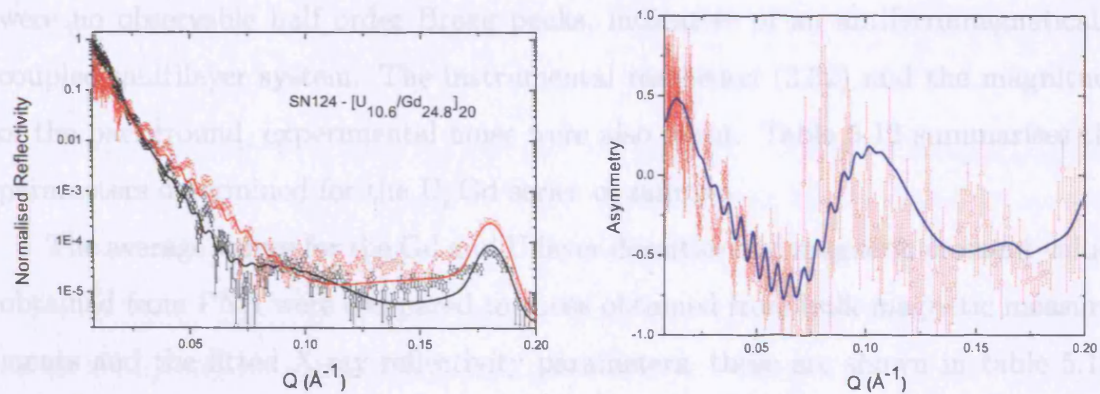
(c) Experimental data and fitted, simulated curve (red line), describing the reflected intensity observed at room temperature (300K).

Figure 5.32: The polarised neutron reflectivity data measured in the specular geometry at 10K/300K in an applied magnetic field of 4.4kOe, simulated using the xPOLLY program for sample SN67 -  $[U_{63.5}/Gd_{20}]_{20}$ .



(a)  $R_{++}$  (black) and  $R_{--}$  (red) channels of the polarised neutron reflectivity in the specular geometry under an applied saturation field. (b) Experimental data and fitted, simulated curve (blue line), describing the asymmetry.

Figure 5.33: The polarised neutron reflectivity data measured in the specular geometry at 10K/300K in an applied magnetic field of 4.4kOe, simulated using the xPOLLY program for sample SN65 -  $[\text{U}_{26}/\text{Gd}_{76}]_{20}$ .



(a)  $R_{++}$  (black) and  $R_{--}$  (red) channels of the polarised neutron reflectivity in the specular geometry under an applied saturation field. (b) Experimental data and fitted, simulated curve (blue line), describing the asymmetry.

Figure 5.34: The polarised neutron reflectivity data measured in the specular geometry at 10K/300K in an applied magnetic field of 4.4kOe, simulated using the xPOLLY program for sample SN124 -  $[\text{U}_{10.6}/\text{Gd}_{24.8}]_{20}$ .

| Sample                                  | Layer | $b$ ( $\times 10^{-5} \text{ \AA}$ ) | $N$ ( $\times 10^{28} \text{ atoms/m}^3$ ) | $t$ ( $\text{ \AA}$ ) | $\mu_B/\text{Gd}$ |
|---|-------|--------------------------------------|--|-----------------------|-------------------|
| SN63                                    | Gd    | 6.5                                  | 2.6  | 31.1                  | 3.9               |
| $[\text{U}_{25}/\text{Gd}_{31.1}]_{20}$ | U     | 8.417                                | 4.8  | 25                    | 0                 |
| SN65                                    | Gd    | 6.5                                  | 3  | 79                    | 3.8               |
| $[\text{U}_{26}/\text{Gd}_{79}]_{20}$   | U     | 8.417                                | 4.6  | 26                    | 0                 |
| SN67                                    | Gd    | 6.5                                  | 3  | 63.4                  | 3.1               |
| $[\text{U}_{63.4}/\text{Gd}_{20}]_{20}$ | U     | 8.417                                | 4.8  | 20                    | 0                 |
| SN124                                   | Gd    | 6.5                                  | 2.7  | 25.8                  | 3.9               |
| $[\text{U}_9/\text{Gd}_{25.8}]_{20}$    | U     | 8.417                                | 4.8  | 9                     | 0                 |

Table 5.12: Summary of the input parameters used to simulate the polarised neutron reflectivity data, fitted using the xPOLLY [4] program. Table includes values for the respective densities and magnetic moments.

magnetic moment per atom ( $\mu_B/\text{atom}$ ), the angle between the moments and the applied field, theta (taken to be  $0^\circ$  in our case, since a magnetic field large enough to saturate the gadolinium layers was applied), and the layer thickness,  $t$  ( $\text{ \AA}$ ). The coupling between the gadolinium layers was chosen to be ferromagnetic since there were no observable half order Bragg peaks, indicative of an antiferromagnetically coupled multilayer system. The instrumental resolution (3.32) and the magnitude of the background, experimental noise were also input. Table 5.12 summarises the parameters determined for the U/Gd series of samples.

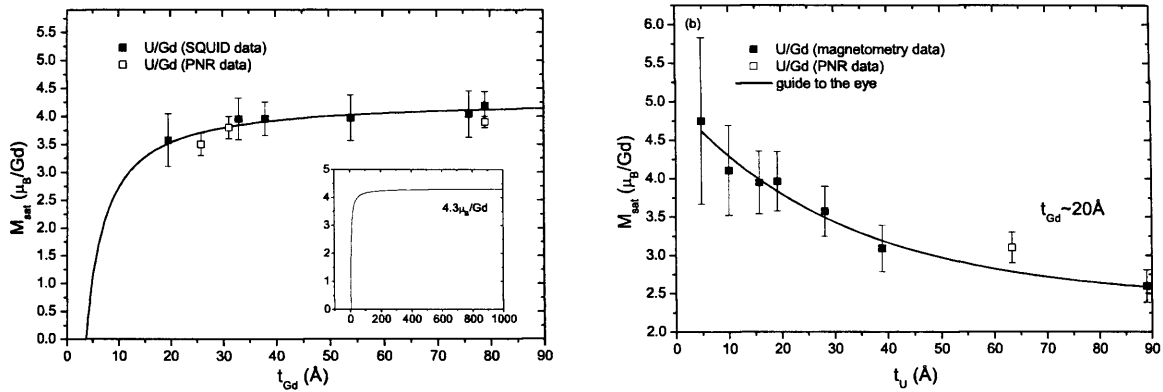
The average values for the Gd and U layer densities and magnetic moment values obtained from PNR were compared to those obtained from bulk magnetic measurements and the fitted X-ray reflectivity parameters, these are shown in table 5.13. Figure 5.35 shows the saturation moment ( $\mu_B/\text{Gd}$ ) as a function of the cobalt layer thickness, comparing values obtained using SQUID magnetometry and polarised neutron reflectometry.

The mean densities determined from X-ray and neutron reflectometry techniques are similar in magnitude for all the samples measured. The values of the saturation magnitude ( $\mu_B/\text{Gd}$ ) determined by PNR, and averaged over the entire Gd layer, fall on the trend lines observed in the magnetisation study described earlier and are

| Sample | Composition  | $N_{X\text{-ray}} \times 10^{28}$<br>(atoms/m <sup>3</sup> ) | $N_{\text{PNR}} \times 10^{28}$<br>(atoms/m <sup>3</sup> ) | $m_{\text{SQUID}}$<br>$\mu_{\text{B}}/\text{Gd}$ | $m_{\text{PNR}}$<br>$\mu_{\text{B}}/\text{Gd}$ |
|--------|--|--|--|--|--|
| SN63   | [U <sub>25</sub> /Gd <sub>31.1</sub> ] <sub>20</sub> | 8.60   | 8.64   | 3.96 ± 0.48                                      | 3.9  |
| SN65   | [U <sub>26</sub> /Gd <sub>79</sub> ] <sub>20</sub>   | 8.65   | 8.76   | 4.04 ± 0.42                                      | 3.8  |
| SN67   | [U <sub>63.4</sub> /Gd <sub>20</sub> ] <sub>20</sub> | 8.56   | 8.59   | -  | 3.1  |
| SN124  | [U <sub>9</sub> /Gd <sub>25.8</sub> ] <sub>20</sub>  | 8.56   | 8.59   | 3.34 ± 0.46                                      | 3.5  |

Table 5.13: Comparison of the averaged densities and magnetic moment values as determined from PNR, with those obtained using SQUID magnetometry and X-ray reflectivity techniques.

represented in figures 5.35 (a) and 5.35 (b).



(a) Saturation magnetisation values ( $\mu_{\text{B}}/\text{Gd}$ ) determined by SQUID magnetometry and PNR as a function of the Gd layer thickness.

(b) Saturation magnetisation values ( $\mu_{\text{B}}/\text{Gd}$ ) determined by SQUID magnetometry and PNR as a function of the U layer thickness.

Figure 5.35: Comparison of the magnetic moment values per Gd atom, determined by bulk magnetisation measurements and polarised neutron reflectometry in a saturation field, as a function of  $t_{\text{Gd}}$  (a) and  $t_{\text{U}}$  (b).

### 5.11.6 Summary Analysis

The polarised neutron reflectivity technique provides simultaneous information on the chemical structure and magnetic moment values at saturation. This allows direct comparison with X-ray reflectivity data and SQUID magnetometry measurements.

The respective intensities of the spin up and spin down states are also sensitive to some degree of the distribution of the magnetisation within the ferromagnetic layers, so it is also possible to infer some detail about the magnetic structure of the layers, which can be linked to results obtained of the crystalline structure, using X-ray diffraction.

However, it is more difficult to extract any evidence of hybridisation between the 5f and 3d states in the U/Fe and U/Co systems or between the 5f and 4f electrons in the U/Gd series. Any induced polarisations on the U sites are too small to be detected in the PNR data. In certain circumstances it may be possible to observe these small moments. This can be achieved by matching the respective U/ferromagnet layer thicknesses to cause an extinction of the even order Bragg peaks, providing a greater sensitivity to the magnetisation alone. In any case, the only samples consisting of thickness matched layers were too thin for any more than the first Bragg peak to be observed in the PNR data.

It was possible to closely simulate the neutron reflectivity data for both spin channels, and consequently the asymmetry, for U/Fe and U/Co systems. The models included regions of magnetisation equivalent in magnitude to those observed in bulk crystals of the respective elements, and regions of reduced or completely 'dead' magnetic material. The average layer thicknesses and other structural parameters closely agreed with those determined by X-ray reflectivity and the average values of  $\mu_B/\text{atom}$  agreed between the PNR and bulk magnetometry techniques. The distribution of magnetic moment within the ferromagnetic layers, determined by PNR, closely resembled the amorphous  $\rightarrow$  crystalline transition in growth, reflected in the X-ray diffraction data.

As observed in the bulk magnetisation and X-ray results described earlier in this chapter and in chapter 4, the properties exhibited by U/Gd multilayers are markedly different from those of the U/Fe and U/Co systems. The simulations of the U/Gd polarised neutron reflectivity were based on a simple bilayer model, that did not account for any distribution in the magnetisation. The splitting of the spin up and spin down channels of the reflectivity were well replicated at the Bragg peak and critical edge positions, but the regions in between the Bragg peaks, commonly

observed in the X-ray reflectivity measurements to be dependent upon the overlayer structure, could not be simulated with a simple niobium/niobium oxide surface layer.

The saturation magnetisations determined by the simulation of the PNR data at the critical edge agreed with bulk magnetisation measurements and described gadolinium layers with  $M_S$  of  $\sim 4\mu_B/\text{Gd}$ , a value significantly reduced from the bulk value of  $7.63\mu_B$ . The future difficulty lies in discovering the mechanism behind this large observed reduction in saturation magnetisation.

# Chapter 6

## Element Specific Characterisation

The techniques used to magnetically characterise the multilayer systems to this point have been sensitive to the magnetisation from the entire sample; a signal dominated by the ferromagnetic layers. Although it has been possible to probe the distribution of magnetisation within the ferromagnetic layers, the detection of any uranium magnetism has been difficult. It is possible however, with the advent of modern synchrotron X-ray sources, to use intense beams of circularly polarised X-rays, tuned to specific energy levels, to probe the magnetisation within individual components of a multilayer system. To date, most of the studies reporting induced magnetic moments have focused on the 3d, 4d and 5d transition metal series [77]. Specifically, we have used X-ray magnetic circular dichroism (XMCD) to investigate the magnitude of spin and orbital components of the induced U 5f magnetic moment, if any, and propose a magnetisation profile based on values obtained from a series of samples. X-ray resonant magnetic scattering (XRMS) has also been utilised, particularly X-ray resonant magnetic reflectivity (XRMR), to directly probe the distribution of magnetic moment within the layers of selected elements.

Before a more complete discussion of the XMCD and XRMR effects, it is important to introduce the nomenclature commonly used (and used within this thesis) to label absorption edges. The X-ray absorption edges correspond to quantum mechanical, electronic energy levels. These are listed together with their corresponding spectroscopic notations in table 6.1.

| Energy Level(Q.M)  | Spectroscopic notation |
|--------------------|------------------------|
| $1s$               | K                      |
| $2s$               | $L_I$                  |
| $2p_{\frac{1}{2}}$ | $L_{II}$               |
| $2p_{\frac{3}{2}}$ | $L_{III}$              |
| $3s$               | $M_I$                  |
| $3p_{\frac{1}{2}}$ | $M_{II}$               |
| $3p_{\frac{3}{2}}$ | $M_{III}$              |
| $3d_{\frac{3}{2}}$ | $M_{IV}$               |
| $3d_{\frac{5}{2}}$ | $M_V$                  |
| $\vdots$           | $\vdots$               |

Table 6.1: X-ray spectroscopic notation used to describe elemental energy levels.

## 6.1 X-ray Magnetic Circular Dichroism

The term dichroism refers to a dependence on photon polarisation states of the absorption of electromagnetic radiation, discussed in chapter 4. Magnetically dichroic materials exhibit a polarisation dependence due to anisotropic magnetisation distributions, created by unpaired electrons. In this case, attenuation coefficients can vary as the incident photon polarisation is changed with respect to the magnetic easy axis. X-ray magnetic circular dichroism (XMCD) is the difference in absorption between left and right-handed, circularly polarised X-rays, which can be probed by manipulating the photon helicity or the magnetisation direction of the sample.

The most common methods that exploit this effect experimentally use either a transmission or fluorescence yield geometry. The simplest of these is the measurement in transmission, where without magnetisation the intensity of the attenuated beam is given by eqn (4.25). If the beam experiences a magnetisation, the attenuation coefficient is then modified by an amount  $\Delta\mu$ , which is additive if the photon helicity and magnetisation directions are parallel and subtractive if they are

antiparallel. The transmitted dichroic intensity [51] can be written,

$$I_{XMCD} = I_0 (e^{(-\mu+\Delta\mu)z} - e^{(-\mu-\Delta\mu)z}) \sim -2I_0z\Delta\mu e^{-\mu z} \quad (6.1)$$

This intensity can be extracted by measuring the change in intensity as the photon helicity or the sample magnetisation direction is alternated.

The underlying process in XMCD involves the transfer of angular momentum from the incident photon to the sample. The helicity of the X-ray photon,  $\sigma = \pm 1$  determines the respective attenuation coefficients which are directly sensitive to the orbital electronic polarisation. This excitation is dominated by the interaction of the electric field of the photon and the electric dipole moment operator, due to the typical X-ray wavelengths used in dichroism experiments, which are much larger than the core level dimensions. It is then possible to calculate electronic transition rates within the electric dipole approximation, by determining the dipole matrix elements, which involve the spatial wave functions of initial and final states. The parity of these states are given by their orbital quantum numbers,  $l$ . It is only possible to obtain a non-vanishing matrix element of initial and final states, according to the dipole transition selection rule.

$$\Delta l = \pm 1 \quad (6.2)$$

The conservation of momentum dictates that the angular momentum of the photon annihilated in the absorption process will be transferred to the sample so that the total electronic angular momentum will be modified by an amount  $\sigma\hat{\mathbf{q}}$ , where  $\sigma$  represents the helicity of the photon ( $\pm 1$  for right-handed and left-handed circular polarisation respectively) and  $\hat{\mathbf{q}}$  is the unit vector of the angular momentum in the direction of propagation. The projection of the angular momentum along the magnetic easy axis is then modified by the scalar product of its unit vector and  $\sigma\hat{\mathbf{q}}$ , which results in a change in angular momentum projection,  $\nu = \pm 1$  that depends on whether the photon helicity is parallel or antiparallel to the magnetisation direction. This gives rise to the magnetic quantum number selection rule,

$$\Delta m = \pm 1, 0 \quad (6.3)$$

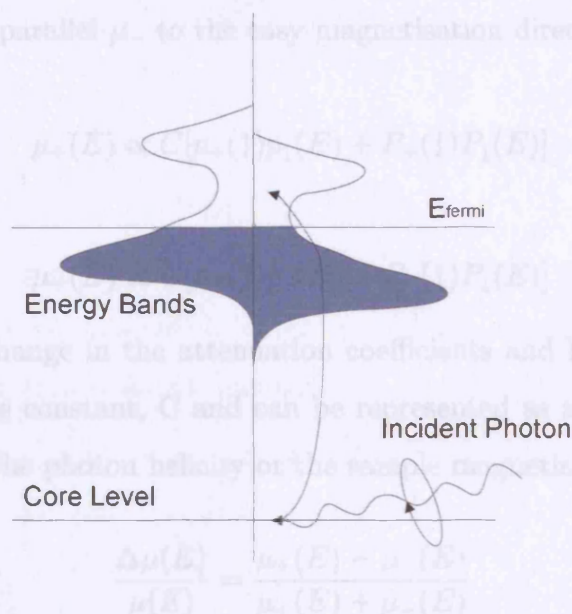


Figure 6.1: In the spin-dependent photoabsorption process a circularly polarised photon excites an electron from the core level, which gains a spin-polarisation. The photoelectron is then captured into a vacancy in the valence band.

This process is not only sensitive to a net orbital polarisation, but can probe magnetisation from both spin and orbital polarisations due to the spin-orbit coupling with the atomic states, which not only splits states with the same orbital angular momentum quantum number,  $l$ , into states of different total angular momentum,  $j$ , but also distorts the radial wave functions, which affects the transition rates and photon attenuation.

Figure 6.1 represents the process of spin-dependent absorption of circularly polarised X-rays. The process can be divided into two stages [78]; firstly, the excitation of an electron from a core level gains spin polarisation. The photoelectron is then promoted to an unoccupied valence state. The transition rates are dependent on the number of available final states with spin parallel to the spin of the photoelectron. Since the photoelectron spin is determined by the helicity of the incoming photon, there will be a difference in transition rates between left and right-handed, circularly polarised X-rays.

By applying Fermi's Golden Rule, describing the relative weights of the photoelectron spin-polarisation  $p_{\pm}(\uparrow, \downarrow)$  and the unoccupied density of states  $p_{\uparrow, \downarrow}(E)$  it is possible to form expressions for the attenuation coefficients with the photon helicity

parallel  $\mu_+$  and antiparallel  $\mu_-$  to the easy magnetisation direction.

$$\mu_+(E) \propto C[p_+(\uparrow)p_\uparrow(E) + P_+(\downarrow)P_\downarrow(E)] \quad (6.4)$$

$$\mu_-(E) \propto C[p_-(\uparrow)p_\uparrow(E) + P_-(\downarrow)P_\downarrow(E)] \quad (6.5)$$

The fractional change in the attenuation coefficients and hence the absorption rates cancels out the constant,  $C$  and can be represented as an asymmetry signal, by either reversing the photon helicity or the sample magnetisation direction.

$$\frac{\Delta\mu(E)}{\mu(E)} = \frac{\mu_+(E) - \mu_-(E)}{\mu_+(E) + \mu_-(E)} \quad (6.6)$$

Reversing the helicity or the sample magnetisation acts to change the sign of the photoelectron polarisation but not the magnitude, so that  $p_+(\uparrow) = p_-(\downarrow) = p_\uparrow$  and  $p_+(\downarrow) = p_-(\uparrow) = p_\downarrow$ , which can be determined, using the Clebsch-Gordan coefficients. It is then possible to expand the expression for the asymmetry to give,

$$\frac{\Delta\mu(E)}{\mu(E)} = \left( \frac{p_\uparrow - p_\downarrow}{p_\uparrow + p_\downarrow} \right) \left( \frac{p_\uparrow(E) - p_\downarrow(E)}{p_\uparrow(E) + p_\downarrow(E)} \right) = 2P_e \frac{\rho_s(E)}{\rho(E)} \quad (6.7)$$

$\rho_s$  is the spin-polarised density of states, which is the average density for spin-up and spin-down states and  $\rho(E)$  is the charge density.  $P_e$  is the photoelectron polarisation.

The major advantage of the XMCD technique is that it is possible to evaluate the separate contributions of the orbital and spin magnetic moments,  $m_{\text{orb}}$  and  $m_{\text{spin}}$  respectively, which can provide better understanding of the origin of the observed macroscopic magnetic properties. This is achieved by the application of the magneto optical sum rules [79], which relate integrals of the dichroic signal over particular absorption edges directly to  $m_{\text{orb}}$  and  $m_{\text{spin}}$ . These sum rules are based on a single ion approximation that relates the optical cross section to the average orbital and spin moments of the conduction band ground states. Thole et al. in 1992 [80] calculated the ground state expectation value of the orbital angular momentum operator  $\langle L_z \rangle$  by measuring the difference between the integrated intensities for left

and right circularly polarised X-rays. The orbital magnetic moment can then be calculated since,

$$m_{orb} = -\frac{\langle L_z \rangle \mu_B}{\hbar} \quad (6.8)$$

Carra et al. in 1993 [81] then derived an independent determination of the ground state expectation value of the effective spin moment operator  $\langle S_e \rangle$ , which is a combination of the spin moment operator  $\langle S_z \rangle$  and the magnetic dipole operator  $\langle T_z \rangle$  such that,

$$\langle S_e \rangle = \langle S_z \rangle + 3\langle T_z \rangle \quad (6.9)$$

and,

$$m_{spin} = -2\frac{\langle S_z \rangle \mu_B}{\hbar} \quad (6.10)$$

The magnetic dipole operator describes any correlation between the spin and the electron distribution around the absorbing atom and is strongly influenced by spin anisotropy (caused by the spin-orbit interaction) or crystal field effects. In itinerant electronic systems the  $\langle T_z \rangle$  term is very weak and the ratios of  $\langle T_z \rangle / \langle S_z \rangle$  for bcc iron and hcp cobalt have been found of -0.38% and -0.26% [82] respectively, which are negligible in the sum rule calculations. In 5f electron systems however it is necessary to consider an intermediate spin-orbit coupling scheme where the  $\langle T_z \rangle$  term becomes a significant one, such that van der Laan and Thole [83] found  $\langle T_z \rangle / \langle S_z \rangle$  ratios of +15% and -43% for 5f<sup>2</sup> and 5f<sup>3</sup> configurations respectively.

The integrals of the observed XMCD signals and the  $\langle L_z \rangle$  and  $\langle S_e \rangle$  terms are related by,

$$\langle L_z \rangle = \frac{3n_h \int_{M_{IV}+M_V} \Delta\gamma(E) dE}{\int_{M_{IV}+M_V} (\gamma^+(E) + \gamma^-(E) + \gamma^{iso}(E)) dE} \quad (6.11)$$

$$\langle S_e \rangle = \frac{3n_h \left( 2 \int_{M_V} \Delta\gamma(E) dE - 3 \int_{M_{IV}} \Delta\gamma(E) dE \right)}{4 \left( \int_{M_{IV}+M_V} (\gamma^+(E) + \gamma^-(E) + \gamma^{iso}(E)) dE \right)} \quad (6.12)$$

where  $n_h$  are the number of holes present in the 5f shell for a specific configuration.  $\Delta\gamma$  is the dichroic signal,  $\gamma^\pm$  are the absorption coefficients for RCP and

LCP photons and  $\gamma^{\text{iso}}$  is the isotropic absorption, equivalent to the average of the absorption for both helicities.

### 6.1.1 Experimental Method

The main drive of this study was to investigate the polarisation, if any, of the U 5f electrons in the U/Fe, U/Co and U/Gd multilayer systems. To this end, the XMCD signal was measured at the uranium  $M_4$  and  $M_5$  edges. Other transitions were also probed however, in order to investigate the nature of the magnetic elements. All of the relevant transitions probed are summarised in table 6.2.

| Resonant Edge | Energy (keV) | Transition  |
|---------------|--------------|---|
| $UM_{IV}$     | 3.728        | $U3d_{3/2} \rightarrow U5f_{5/2}$                   |
| $UM_V$        | 3.552        | $U3d_{5/2} \rightarrow U5f_{5/2}$ or $5f_{7/2}$     |
| $FeK$         | 7.112        | $Fe1s \rightarrow Fe4p_{1/2}$ or $4p_{3/2}$         |
| $FeL_{II}$    | 0.720        | $Fe2p_{1/2} \rightarrow Fe3d_{3/2}$                 |
| $FeL_{III}$   | 0.707        | $Fe2p_{3/2} \rightarrow Fe3d_{3/2}$ or $3d_{5/2}$   |
| $GdL_{II}$    | 7.930        | $Gd2p_{1/2} \rightarrow Gd5d_{3/2}$                 |
| $GdL_{III}$   | 7.243        | $Gd2p_{3/2} \rightarrow Gd5d_{3/2}$ or $Gd5d_{5/2}$ |

Table 6.2: Electric dipole transitions for resonant energies, investigated during the course of this thesis.

All of the XMCD measurements performed during the course of this thesis were carried out on the ID12 beamline, dedicated to the study of polarisation dependent X-ray absorption at the European Synchrotron Radiation Facility (ESRF) in Grenoble, working with F. Wilhelm and A. Rogalev. Figure 6.2 is a diagram of the main apparatus comprising the ID12 beamline. A more detailed description of the beamline has been given by Goulon et al. [84].

The ID12 beamline is situated on an insertion device, or straight section of the storage ring and has specific undulators available for certain energy ranges. To probe the U M edges, the first harmonic of the electromagnetic permanent hybrid undulator (EMPHU) was used, the second harmonic of the Apple II undulator was employed for the investigation of Fe K, Gd  $L_{II}$  and  $L_{III}$  edges. A combination of

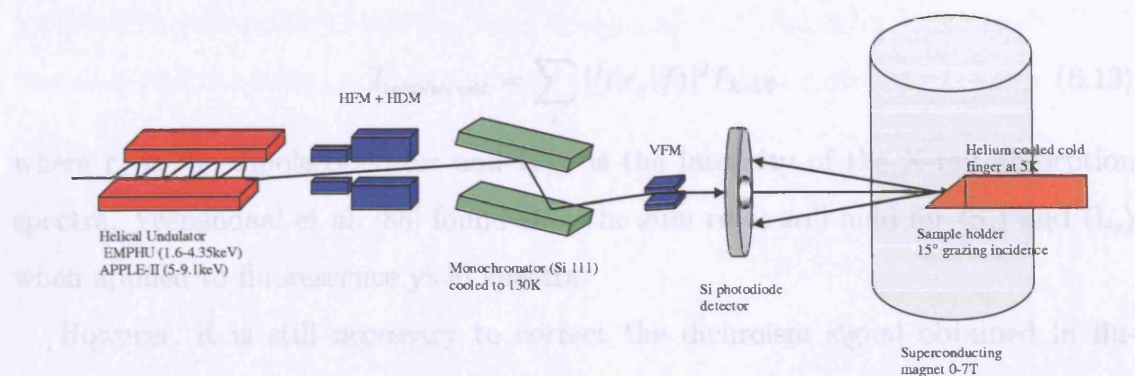


Figure 6.2: Schematic layout of the ID12 beamline.

horizontal deflecting mirrors and a focusing mirror were used to focus the beam onto the fixed exit, double crystal monochromator. The monochromator consists of a pair of Si(111) crystals at  $\sim 230\text{K}$  that provide a circular polarisation efficiency of 35% at the  $\text{UM}_V$  edge and 45% at the  $\text{UM}_{IV}$  edge.

The experiment was carried out in the backscattering geometry, measuring the total fluorescence yield, since the relatively thick sapphire substrates were not suitable for transmission. The samples were mounted onto copper stubs at an angle of  $15^\circ$  to the incoming beam in the vertical plane, using a heat conductive epoxy. The sample was then positioned onto the cold finger of a constant flow, liquid helium cryostat, which was kept at  $\sim 5\text{K}$ . The incident beam passed through a hole in the silicon photodiode detector, which measured the fluorescence signal scattered back from the sample. The temperature dependent dark current, responsible for a large quantity of background noise, was significantly reduced by exploiting a synchronous detection technique based on a square wave modulation of the X-ray beam. This was achieved by using a beam chopper, upstream from the monochromator, in conjunction with a lock-in amplifier to discriminate between the incident flux and the background noise.

The fluorescence yield method is only valid if the separation of the final states of the transition is larger than the mean lifetime broadening. This means that the decay at certain energies depends only on the initial  $i$  and final states  $f$ , giving rise to an incoherent fluorescence yield [85],

$$I_{incoherent} = \sum_i |\langle i|r_q|f\rangle|^2 I_{XAS} \quad (6.13)$$

where  $r_q$  is the dipole operator and  $I_{XAS}$  is the intensity of the X-ray absorption spectra. Veenendaal et al. [86] found that the sum rules still hold for  $\langle S_z \rangle$  and  $\langle L_z \rangle$  when applied to fluorescence yield spectra.

However, it is still necessary to correct the dichroism signal obtained in fluorescence yield for absorption effects. This correction is relatively easy in bulk samples by measuring the total electron yield spectrum, which detects the number of secondary electrons, produced mainly by Auger type decays. This spectrum is proportional to the absorption cross-section if the light is absorbed on a length scale significantly longer than the escape depth of the secondary electrons. For thin films, the absorption correction is more complicated. Attenuation variations occur within the sample, which lead to energy dependent penetration depths that effect the resonant intensity. These attenuation variations are often referred to as self absorption corrections (SAC). It is possible to relate the absorption coefficient to the intensity normalised to the incident flux,

$$I_{norm}(E) = B \frac{\mu_a(E)}{\mu_{total}(E) + A} f(E) \quad (6.14)$$

in this case B is a constant, dependent on the experimental geometry.  $\mu_a$  is the absorption coefficient associated with the production of a hole in a specific energy level,  $\mu_{total}$  is the sum of the coefficients from other energy levels and atomic species and  $\mu_a$ .  $A = (\sin \alpha / \sin \beta) \gamma_{total}(E_f)$ , where  $\alpha$  is the angle between the sample surface and the incident photon beam,  $\beta$  is the angle between the fluorescent photon and the sample surface and  $E_f$  is the energy resulting from the entire decay process.

$$f(E) = 1 - e^{-\left(\frac{\gamma_{total}(E)}{\sin \alpha} + \frac{\gamma_{total}(E_f)}{\sin \beta}\right)d} \quad (6.15)$$

where d is the sample thickness. This treatment of self absorption corrections [87] requires modifications in order to encompass typical multilayer parameters that describe the variation in absorption with depth and account for the incoming and outgoing beam angles. A program to calculate corrections to the XMCD spectra

collected in fluorescence yield has been developed by F. Wilhelm et al. at the ID12 beamline and has been applied to some of experimental data presented in this thesis.

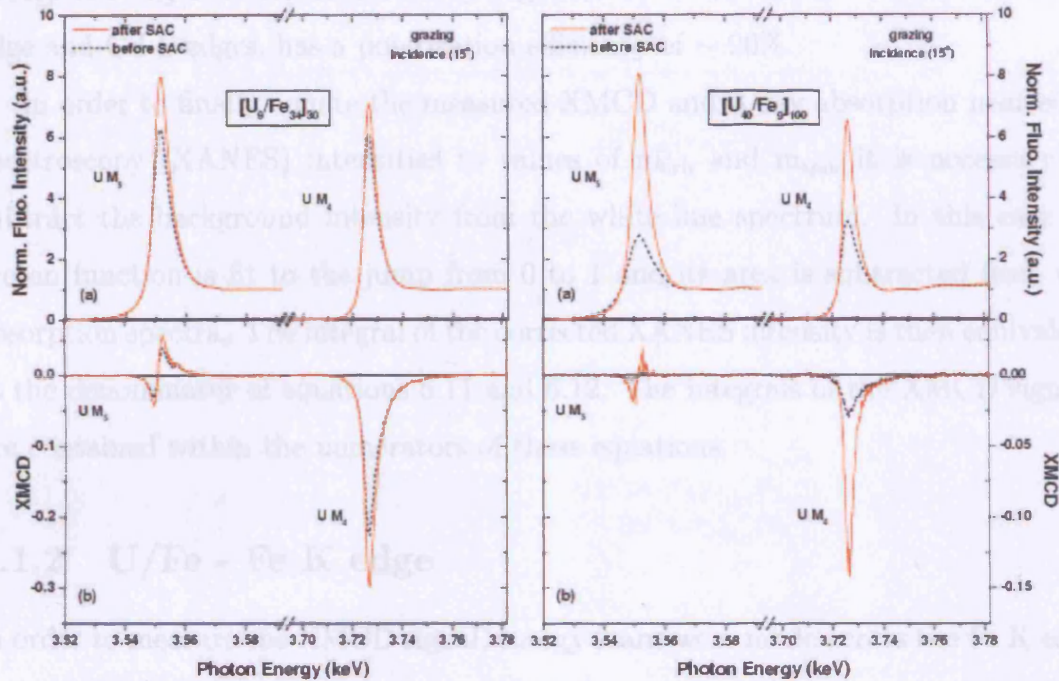


Figure 6.3: Example of the self absorption corrections for two example U/Fe samples. The correction clearly becomes more significant for thick uranium layers.

Once the data were collected, the X-ray absorption spectra were normalised, so that the intensity far below the resonance edge in energy was set to 0 and the intensity far above it was set to 1. The XMCD signal was then normalised to the white line. The self-absorption corrections were then performed to account for the attenuation profile through the multilayers.

The intensity of the uranium M edges and the gadolinium L edges must then be normalised according to the respective branching ratios, which is a function of the number of initial available states. For the  $UM_{IV}$  edge the initial states can take the values  $m_j = -3/2, -1/2, 1/2,$  and  $3/2$  whereas  $m_j = -5/2, -3/2, -1/2, 1/2, 3/2, 5/2$  are the allowed initial states of the  $UM_V$  edge, leading to a ratio of 1:2/3 ( $UM_V : UM_{IV}$ ). The Gd  $L_{II}$  edge initial states have allowed values  $m_j = -1/2, 1/2$  and the Gd  $L_{III}$  has  $m_j = -3/2, -1/2, 1/2,$  and  $3/2$ , which results in a branching ratio of 1:2. The final correction to the experimental data takes into account the circular

polarisation efficiency of the monochromatic beam, which is 45% and 35% at the  $UM_{IV}$  and  $UM_V$  edges respectively. The Apple II undulator, used to investigate the absorption edges in the harder X-ray regime, which in our case includes the Fe K edge and Gd L edges, has a polarisation efficiency of  $\sim 90\%$ .

In order to finally equate the measured XMCD and X-ray absorption near edge spectroscopy (XANES) intensities to values of  $m_{orb}$  and  $m_{spin}$  it is necessary to subtract the background intensity from the white line spectrum. In this case an arctan function is fit to the jump from 0 to 1 and its area is subtracted from the absorption spectra. The integral of the corrected XANES intensity is then equivalent to the denominator of equations 6.11 and 6.12. The integrals of the XMCD signals are contained within the numerators of these equations.

### 6.1.2 U/Fe - Fe K edge

In order to measure the XMCD signal, energy scans were made across the Fe K edge from 7100eV to 7150eV in 400 steps of 0.375eV, counting for 1s per data point. The circular polarisation was flipped 5 times with the field applied parallel to the beam direction. The magnetisation direction was then reversed, antiparallel to the beam direction and the polarisation again flipped. The intensity subscript represents the field direction, + is parallel and - is antiparallel to the direction of propagation of the incident photons. The bracketed symbol represents the direction of circular polarisation (+) is RCP and (-) is LCP. In this case the difference between average  $I_+(+)$  and  $I_+(-)$  values give the XMCD in one field direction and  $I_+(+) - I_+(-)$  gives the XMCD with  $\mathbf{H}$  antiparallel. The signals are compared for both magnetic field directions, where the reversibility of the XMCD intensity supports its magnetic origin.

The Fe K edge was investigated for samples SN71 [ $U_9/Fe_{34}$ ]<sub>30</sub>, SN72 [ $U_{23.5}/Fe_{17}$ ]<sub>10</sub> and SN73 [ $U_{30.5}/Fe_{14}$ ]<sub>10</sub>. These samples were used to compare results between the earlier work of Angela Beesley [49] and samples grown on sapphire substrates with Nb buffers and capping layers [23]. The composition was chosen to look closely at the iron thickness near to the crystalline/non-crystalline (magnetic/non-magnetic) boundary seen in the high angle diffraction and SQUID magnetometry results. The

measurements were carried out at a temperature of 5K in a magnetic field of 1T, magnetically saturating the samples in the plane of the film. Figure 6.4 shows the normalised XMCD intensity and X-ray absorption near-edge spectroscopy (XANES).

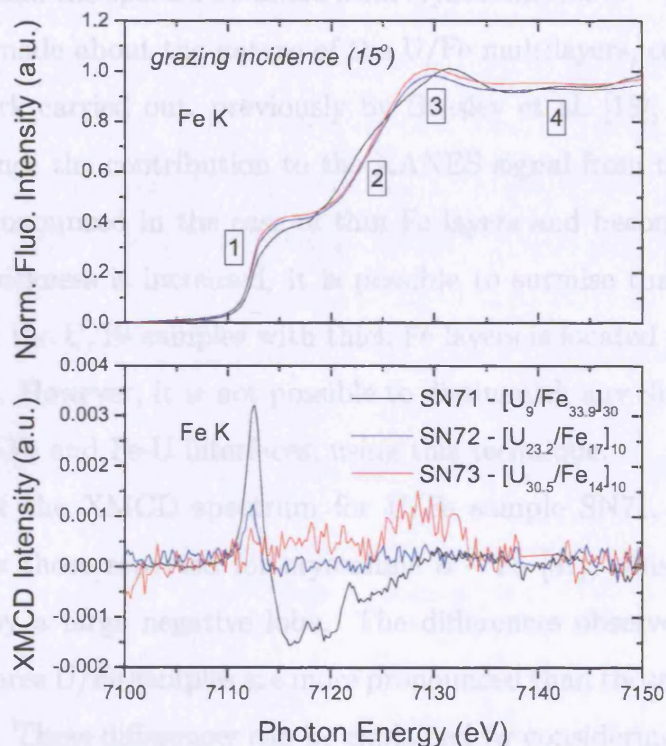


Figure 6.4: XANES and XMCD signals for three U/Fe samples of varying structural composition across the Fe K edge.

The XANES spectra seen in the normalised fluorescence are shown in figure 6.4 for three U/Fe samples, mapping the transition from crystalline bcc  $\alpha$  - Fe to an amorphous iron or U-Fe alloy layer. Although at first glance the XANES spectra appear very similar for all three U/Fe samples, there are subtle differences that can be observed in certain regions (numbered 1-4). The intensity of the pre-edge feature, region 1, carries more intensity for the thin Fe layers than for the thicker, crystalline Fe sample. The characteristic shoulder located in region 2 at 7.125keV corresponds to that observed for  $\alpha$  - Fe and is not present at all in the amorphous, U-Fe alloy samples. Region 3 shows the maximum of the edge, which is shifted to lower energies ( $\sim -2$ eV) for the U/Fe samples comprised of non-crystalline iron. The first oscillation of the energy dependent X-ray absorption fine structure (EXAFS) can be

seen in the XANES spectrum of the thick Fe layer sample, but is shifted to higher energies for those samples with thin Fe layers. In fact, overall, the XANES spectra of the thin Fe layer samples more closely resemble those reported for amorphous Fe [88] [89] [90] than the spectra obtained from crystalline bcc  $\alpha$  – Fe. This confirms the conclusions made about the nature of the U/Fe multilayers, concerning thin Fe layers in the work carried out, previously by Beesley et al. [18], using Mössbauer spectroscopy. Since the contribution to the XANES signal from the amorphous Fe is much more pronounced in the case of thin Fe layers and becomes less visible as the iron layer thickness is increased, it is possible to surmise that the amorphous Fe component in the U/Fe samples with thick Fe layers is located principally at the interface regions. However, it is not possible to distinguish any differences between the respective U-Fe and Fe-U interfaces, using this technique.

The shape of the XMCD spectrum for U/Fe sample SN71, thick iron layer, closely resembles those reported for crystalline  $\alpha$  – Fe [91], consisting of a sharp peak, followed by a large negative lobe. The differences observed in the XMCD spectra for the three U/Fe samples are more pronounced than those described for the XANES spectra. These differences can be explained by considering the origin of the dichroism effect at the Fe K edge. The K edge reflects the orbital polarisation of the electronic p states in the differential form  $d\langle L_z \rangle / dE$ , which means that in its integral form, the XMCD is a measure of the orbital magnetism of the Fe 4p shell (considering only dipole transitions) [92]. The XMCD spectrum at the Fe K edge can then be interpreted as the exchange and spin-orbit splitting of the final 4p states [93]. As the Fe layers become thinner, the distinctive shape observed in the XMCD spectra, a consequence of the ferromagnetic state of crystalline  $\alpha$  – Fe, changes dramatically. For sample SN73, comprising the thinnest Fe layers, the XMCD signal is completely different from that observed for ferromagnetic iron and it is reasonable to conclude that there is very little, or no ferromagnetic iron component present at all. A link can then be made between the observation of amorphous iron and 'non-magnetic' (non-ferromagnetic) iron, supporting results obtained, using Mössbauer spectroscopy [19].

### 6.1.3 U/Fe - U $M_{IV}$ and $M_V$ edges

In order to investigate any induced effects on the uranium layers, caused by a polarisation from the iron, the large resonant enhancements of the uranium M edges were exploited. At the U edges a field of 1T was applied to saturate the sample. The polarity of the incoming X-ray photons was flipped three times (+--+--) at each energy point, counting for 1s with a reversal time of 160ms. The sign of the magnetic field was then reversed and the polarity flipped again.

The U M edges were investigated for samples SN71 [ $U_9/Fe_{34}$ ]<sub>30</sub>, SN72 [ $U_{23.5}/Fe_{17}$ ]<sub>10</sub> and SN73 [ $U_{30.5}/Fe_{14}$ ]<sub>10</sub>. The measurements were carried out at a temperature of 5K in a magnetic field of 1T, magnetically saturating the samples in the plane of the film. Figure 6.5 shows the normalised XMCD intensity and X-ray absorption near-edge spectroscopy (XANES) at both the U  $M_{IV}$  and  $UM_V$  edges.

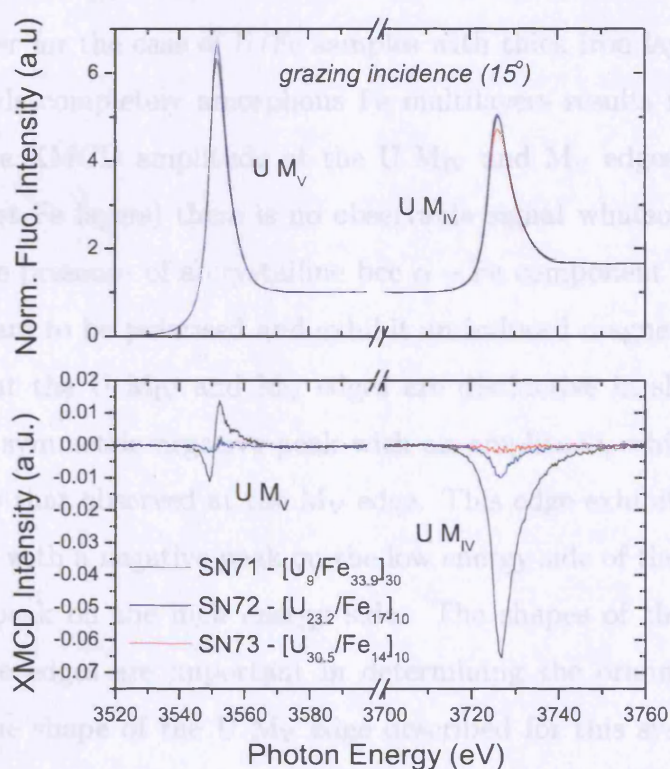


Figure 6.5: XANES and XMCD signals for three U/Fe samples of varying structural composition across the Fe K edge.

The spectra shown in figure 6.5 do not include SAC, but provide a qualitative picture of the uranium XANES and XMCD spectra, as a function of the iron layer

thickness, across the transition from amorphous to crystalline iron. Contrary to the Fe K edge XANES spectra, those observed at the U  $M_{IV}$  and  $M_V$  edges are similar in amplitude and spectral shape, independent of the Fe layer thickness. The U  $M_{IV}$  edge corresponds to transitions from the  $3d_{3/2}$  to the  $5f_{5/2}$  level, whereas the U  $M_V$  absorption edge signal is dependent upon transitions from the  $3d_{5/2}$  to the  $5f_{5/2}$  and  $5f_{7/2}$  levels (the majority of the transitions at the U  $M_V$  edge have final states at the  $5f_{7/2}$  level), see table 6.2. The electric dipole selection rules then determine that the U  $M_{IV}$  and U  $M_V$  absorption signals are dependent on the number of  $5f_{5/2}$  and  $5f_{7/2}/5f_{5/2}$  holes respectively [94] [95] [96].

The existence of the observed XMCD signal at the U M edges indicates that the uranium atoms carry an induced magnetic moment, but the mechanism responsible for the polarisation of the uranium layers is not obvious. Figure 6.5 shows a clear trend in the XMCD signal as a function of the Fe layer thickness. The signal is appreciably larger for the case of U/Fe samples with thick iron layers, whereas the transition towards completely amorphous Fe multilayers results in a reduction in magnitude of the XMCD amplitude at the U  $M_{IV}$  and  $M_V$  edges and in the case of SN73 (thinnest Fe layers) there is no observable signal whatsoever. This trend suggests that the presence of a crystalline bcc  $\alpha$  – Fe component is required if the uranium atoms are to be polarised and exhibit an induced magnetic moment. The XMCD signals at the U  $M_{IV}$  and  $M_V$  edges are distinctive in shape; the U  $M_{IV}$  edge is a nearly symmetric negative peak with an amplitude, which is almost four times as large as that observed at the  $M_V$  edge. This edge exhibits an asymmetric dispersive shape with a negative peak on the low energy side of the absorption edge and a positive peak on the high energy side. The shapes of the XMCD signals at the respective edges are important in determining the origin of the uranium polarisation. The shape of the U  $M_V$  edge described for this system is markedly different from that observed in the UAs/Co system [17], where the uranium atoms carry an inherent magnetic moment, and the shape is also different to that observed for polycrystalline  $UFe_2$  [97], suggesting that we have neither an inherent uranium moment nor the presence of an  $UFe_2$  alloy at the U/Fe interfaces. A comparison between the XANES and XMCD spectra for a U/Fe multilayer sample and a  $UFe_2$

single crystal is shown in figure 6.6.

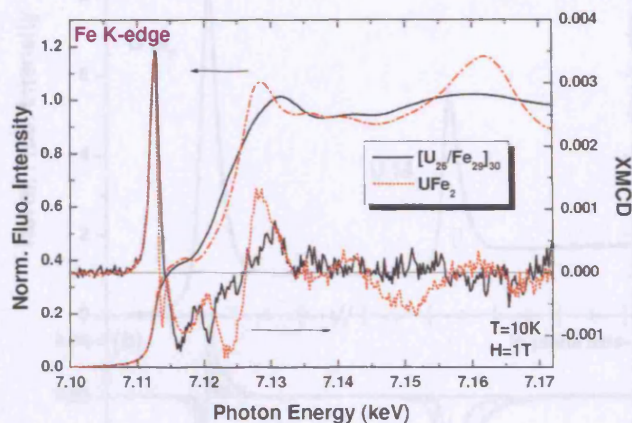


Figure 6.6: Comparison between the observed XANES and XMCD signals for a  $[U_{26}/Fe_{29}]_{30}$  multilayer and a  $UFe_2$  single crystal.

The discussion of  $UFe_2$  as a source of the induced uranium moment results from a consideration of the formation of U-Fe intermetallic alloys at the U/Fe multilayer interface. The only known ferromagnetic compound in the U-Fe phase diagram is that of  $UFe_2$ , which carries a magnetic moment of  $\sim 1.2\mu_B$  per molecule, as described in chapter 2. However, there is practically no magnetic moment observed on the U site, since the orbital and spin components of the magnetisation are aligned oppositely to one another and are similar in magnitude ( $0.23\mu_B$ ) [43]. The  $UFe_2$  Curie temperature is 165K in the bulk, likely to be further reduced in a multilayer due to finite-size scaling effects. Since the induced U magnetic moment in U/Fe multilayers persisted up to room temperature, 300K, the observed polarisation cannot be attributed to the presence of any  $UFe_2$  at the U/Fe interface. To further substantiate this claim, clear differences can be seen in both the XANES and XMCD spectral shapes, between a U/Fe multilayer with reasonably thick Fe layers and a  $UFe_2$  single crystal, figure 6.6.

A more thorough investigation of the XMCD signal dependence at the U M edges as a function of U layer thickness has been undertaken [23], including self absorption corrections (SAC), figure 6.7. A clear trend is visible, considering the four samples included in the figure, which possess roughly equivalent Fe layer thicknesses ( $\sim 30\text{\AA}$ ). The shape of the curves at the respective edges does not change with varying  $t_U$ ,

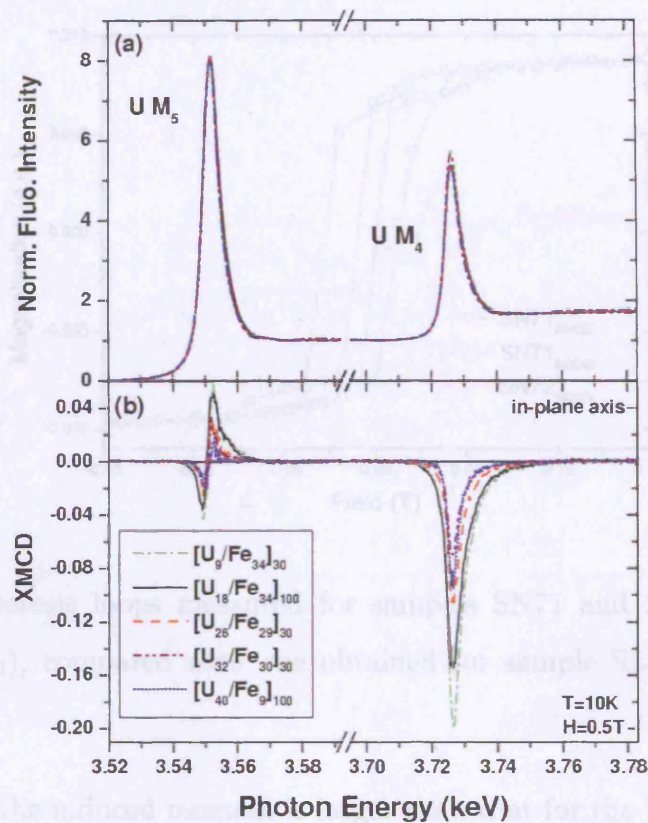


Figure 6.7: XANES and XMCD signals for a selection of U/Fe multilayers, with varying  $t_U$  and constant  $t_{Fe}$ .

although the amplitude in the signals decrease as the uranium layers become thicker. This result implies that the distribution of the induced U 5f magnetic moment, polarised by the iron layers, is not constant throughout the U layer and that the U atoms located nearest to the interfaces are far more likely to be polarised.

In order to ensure that the samples were in an applied magnetic field large enough to completely saturate the magnetisation, element-specific hysteresis loops were measured, by measuring the maximum of the U  $M_{IV}$  edge XMCD signal at 5K as a function of the applied field. In systems where the magnetic moment is purely induced, Ni/Pt [77], the hysteretic behaviour of the polarisation closely follows that of the ferromagnetic element.

On inspection of figure 6.8, the hysteresis loops as determined by XMCD and SQUID magnetometry can be directly compared for the U/Fe multilayer sample SN71. The general shape of the magnetisation curves are very similar, although the

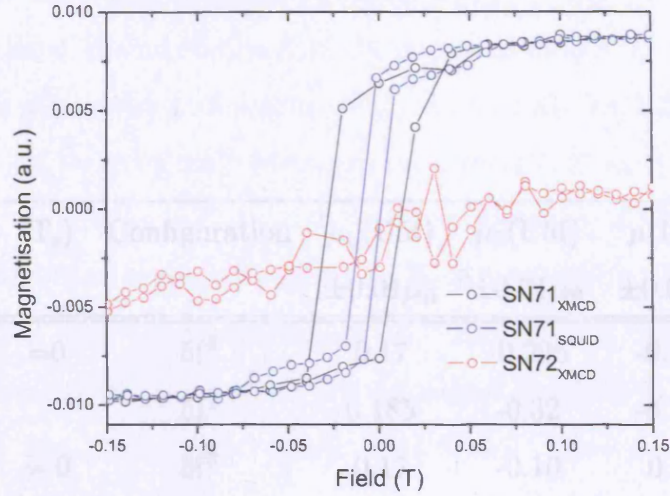


Figure 6.8: Hysteresis loops measured for samples SN71 and SN72 ( $[U_{34}/Fe_9]_{30}$  and  $[U_{23.2}/Fe_{17}]_{10}$ ), compared with one obtained for sample SN71, using SQUID magnetometry.

coercive field for the induced moment is larger than that for the bulk sample. This suggests that the induced U magnetic moments are more difficult to align with the applied magnetic field than the moments of the Fe layers, possibly as a consequence of pinning at the site of defects in the interface regions, where the uranium is likely to be polarised. The fact that the evolution of the induced magnetisation follows that of the bulk multilayer sample supports the idea that the observed U moment is a consequence of a 5f-3d hybridisation at the U/Fe interface.

Having established that the applied fields are large enough to saturate the induced U magnetic moments, it is possible to extract orbital and spin magnetic moments, using magneto-optical sum rules [80] [81]. It is first important to recall the sum rules for the XMCD spectra at the U  $M_{IV}$  and  $M_V$  edges, equations (6.11) and (6.12), which determine the ground state expectation values of the z component of the orbital magnetic moment  $\langle L_z \rangle$  and the effective 5f spin magnetic moment,  $\langle S_e \rangle$ . The effective spin moment can be written in terms of the z component of the 5f spin magnetic moment and the expectation value of the z projection of the magnetic dipole operator,  $\langle T_z \rangle$ , see equation (6.9).

In our case, the number of 5f holes,  $n_h$ , is  $14 - n_e$ , where  $n_e$  is the number of

| Sample  | $\langle T_z \rangle$ | Configuration   | $\mu_L(\text{U}5f)$ | $\mu_S(\text{U}5f)$ | $\mu(\text{U}5f)$ | $\mu_L/\mu_S$ |
|---|-----------------------|-----------------|---------------------|---------------------|-------------------|---------------|
|   |                       |                 | $\pm 0.01\mu_B$     | $\pm 0.01\mu_B$     | $\pm 0.02\mu_B$   |               |
| SN71<br>[U <sub>9</sub> /Fe <sub>34</sub> ] <sub>30</sub>   | =0                    | 5f <sup>3</sup> | 0.17                | -0.295              | -0.125            | -0.58         |
|   |                       | 5f <sup>2</sup> | 0.185               | -0.32               | -0.135            | -0.58         |
|   | ≠ 0                   | 5f <sup>3</sup> | 0.17                | -0.10               | 0.07              | -1.66         |
|   |                       | 5f <sup>2</sup> | 0.185               | -0.07               | 0.11              | -2.60         |
| S3.6<br>[U <sub>18</sub> /Fe <sub>34</sub> ] <sub>100</sub> | =0                    | 5f <sup>3</sup> | 0.135               | -0.25               | -0.115            | -0.54         |
|   |                       | 5f <sup>2</sup> | 0.145               | -0.275              | -0.13             | -0.54         |
|   | ≠ 0                   | 5f <sup>3</sup> | 0.135               | -0.09               | 0.045             | -1.53         |
|   |                       | 5f <sup>2</sup> | 0.145               | -0.06               | 0.085             | -2.41         |
| S2.9<br>[U <sub>26</sub> /Fe <sub>29</sub> ] <sub>30</sub>  | =0                    | 5f <sup>3</sup> | 0.09                | -0.15               | -0.06             | -0.595        |
|   |                       | 5f <sup>2</sup> | 0.095               | -0.165              | -0.07             | -0.595        |
|   | ≠ 0                   | 5f <sup>3</sup> | 0.09                | -0.05               | 0.035             | -1.71         |
|   |                       | 5f <sup>2</sup> | 0.095               | -0.035              | 0.06              | -2.69         |
| SN75<br>[U <sub>32</sub> /Fe <sub>30</sub> ] <sub>30</sub>  | =0                    | 5f <sup>3</sup> | 0.05                | -0.09               | -0.04             | -0.54         |
|   |                       | 5f <sup>2</sup> | 0.054               | -0.10               | -0.046            | -0.54         |
|   | ≠ 0                   | 5f <sup>3</sup> | 0.05                | -0.032              | 0.018             | -1.54         |
|   |                       | 5f <sup>2</sup> | 0.054               | -0.023              | 0.029             | -2.41         |

Table 6.3: Induced U 5f orbital, spin and total magnetic moments, determined by XMCD for a selection of U/Fe multilayer samples. Results are shown, with and without the inclusion of the  $\langle T_z \rangle$  term for U 5f<sup>2</sup> and 5f<sup>3</sup> configurations. The measurements were made at 5K in an applied field of 10kOe, large enough to magnetically saturate the U moments.

electrons in the 5f shell, which is dependent on the uranium valence state. For a  $5f^2$  configuration  $n_h = 12$  and the ratio of the magnetic dipole operator to the spin magnetic moment along the z direction,  $\langle T_z \rangle / \langle S_z \rangle = 1.16$ , for a  $5f^3$  configuration  $n_h = 11$  and  $\langle T_z \rangle / \langle S_z \rangle = 0.62$  [83]. Although the inclusion of the  $\langle T_z \rangle$  term is valid in an atomic-like picture, it is likely that the delocalisation of the 5f electrons in the case of U/Fe multilayers could lead to an almost negligible  $\langle T_z \rangle$  contribution. We have considered both cases, determining the spin, orbital and total magnetic moments for  $5f^2$  and  $5f^3$  configurations, for samples characterised within the body of this thesis and samples described previously [18] [49]. These results are listed in table 6.3.

The induced U magnetic moment values change dramatically depending on whether the  $\langle T_z \rangle$  term is included or not. Previous studies do not provide a definitive answer as to whether the magnetic dipole operator should be considered when evaluating the spin and orbital moments of an *induced* magnetic moment, but they give a feel for the systems in which the dipole term is likely to feature and the systems in which it is not. In the case of the highly anisotropic uranium compound, US, the  $\langle T_z \rangle$  term is important [98] and its magnitude has been confirmed; experimentally, using XMCD and polarised neutron diffraction techniques within the sum rule approximations [83], and theoretically [99]. The binary,  $UFe_2$  compound exhibits a negligible U 5f magnetic moment, which is reproduced theoretically, taking  $\langle T_z \rangle$  to be zero [97]. The magnitude of the dipole term was also considered to be small in the determination of the U magnetic moments in the UAs/Co multilayer system, using *ab initio* calculations [100].

So far, only uranium compounds carrying an intrinsic magnetic moment have been considered, but it is possible to make assumptions about the inclusion of the dipole operator from general considerations of the uranium environment in the U/Fe multilayer system. The X-ray diffraction results discussed in chapter 4 indicated that the U layers are polycrystalline. In this instance, the cubic site symmetry and the strong spin orbit coupling of the uranium [101] could result in a much smaller  $\langle T_z \rangle$  contribution to the effective spin magnetic moment than that derived from a purely atomic picture [83].

Recently, the electronic and magnetic properties of U/Fe multilayer thin films have been investigated theoretically, using density functional theory (DFT) [2]. The calculations considered an idealised U/Fe system, consisting of 1ML of  $\alpha$ -U grown in the 001 orientation and 3ML of bcc  $\alpha$ -Fe, oriented 110. The results predicted an induced uranium magnetic moment, and furthermore, suggested that the uranium would be polarised in an opposite direction to the magnetisation of the iron layers and would be confined to the interface region, with no appreciable moment more than  $\sim 2\text{\AA}$  from the U-Fe or Fe-U interfaces. Although our system is far from ideal, including a large number of structural defects, lattice strains and alloyed regions caused by interdiffusion, it is still likely that the main features of the DFT calculations will be observed; the U moments aligned anti parallel to the iron layers at the U/Fe interfaces and the majority of the induced moment detected on the U atoms closest to the iron layers. On inspection of the results summarised in table 6.3, the total induced magnetic moment is aligned antiparallel to the iron layers only when the  $\langle T_z \rangle$  term is assumed to be zero.

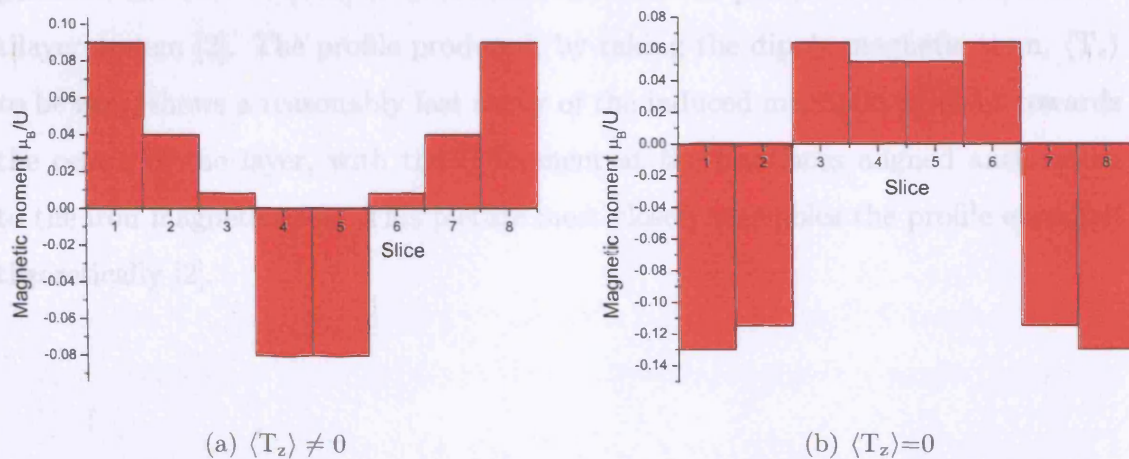


Figure 6.9: Profiles of the induced uranium magnetic moment, determined by the evolution of the total induced magnetic moment, as calculated using the XMCD sum rules. Slices are  $4\text{\AA}$ .

Table 6.3 shows that the induced 5f magnetic moment value per U atom varies with uranium layer thickness. This observation is important, since it implies that the polarisation is not constant through the uranium layer. The four samples listed in table 6.3 have approximately constant  $t_{\text{Fe}}$  and different  $t_{\text{U}}$ . It is then possible to

draw a profile of the induced U 5f moment, from the values of  $\mu_B/U$  for each sample, but some assumptions are necessary in this case; the valence state is not known in this system, so for the purpose of this exercise a  $5f^{2.5}$  electronic configuration has been adopted. This simplified model neglects interactions between the respective slices and assumes that the roughness, interfacial diffusion and strains are the same for all of the U/Fe samples. This treatment also ignores any any differences between the nature of the U-Fe interface and the Fe-U interface, in terms of varying degrees of implantation as discussed in earlier chapters, and therefore by definition the U magnetic moment profile is confined to be symmetric. The profiles of the induced U 5f magnetic moment for a  $[U_{32}/Fe_{30}]_{30}$  multilayer, with the U layer separated into 8 slices, are shown in figure 6.9 for the two cases  $\langle T_z \rangle \neq 0$  and  $\langle T_z \rangle = 0$ .

Qualitatively, both profiles show some form of oscillating moment, which indicates that there may be some RKKY type interaction through the uranium layers or it could be a consequence of the structural alloy profile at the interfaces, which would also lead to a less sharp decay of the polarisation, as expected in the surface polarisation of  $\alpha - U$  [102] or in the DFT calculations performed on the U/Fe multilayer system [2]. The profile produced, by taking the dipole magnetic term,  $\langle T_z \rangle$  to be zero, shows a reasonably fast decay of the induced magnetic moment towards the centre of the layer, with the U moment at the interfaces aligned antiparallel to the iron magnetisation. This picture most closely resembles the profile expected theoretically [2].

### 6.1.4 U/Co - U $M_{IV}$ edge

The hybridisation of the 5f-3d electronic states, observed in the U/Fe multilayer system as a polarisation of the U layers, giving an induced U 5f magnetic moment, was further investigated in the U/Co multilayer system. Earlier structural and bulk magnetic measurements (chapters 4 and 5) indicated that the U/Fe and U/Co systems were very similar in terms of their physical and magnetic properties. Since iron and cobalt are neighbours in the periodic table and both exhibit 3d band ferromagnetism at room temperature, a similar electronic interaction was initially expected between the 3d cobalt and the 5f uranium electrons.

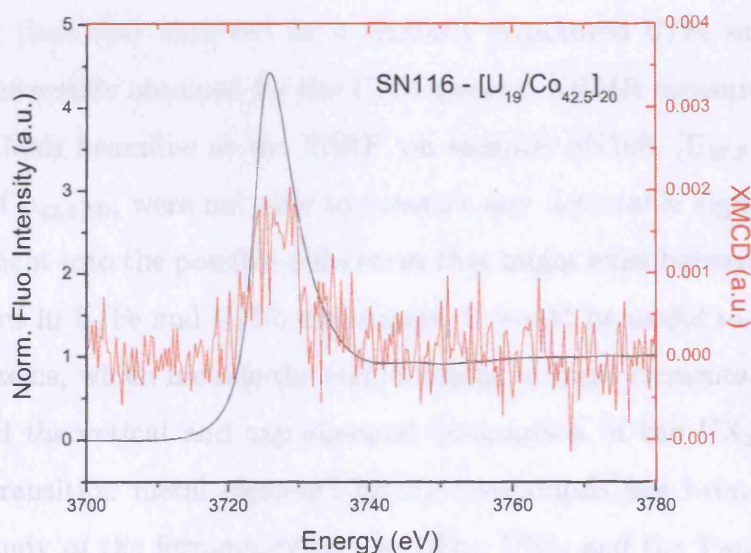


Figure 6.10: XANES and XMCD spectra at the U  $M_{IV}$  edge for U/Co sample SN116, comprising thick Co layers and thin U layers in order to achieve a maximal observed XMCD signal.

As for the U/Fe system, the large resonant enhancements of the uranium M edges were exploited to probe the polarisation of the U layers. A field of 10kOe was applied to saturate the sample, at a temperature of  $\sim 5$ K. The polarity of the incoming X-ray photons was flipped three times (+--+ -) at each energy point, counting for 1s with a reversal time of 160ms. The sign of the magnetic field was then reversed and the polarity flipped again. A reversal of the XMCD spectrum (determined by the difference in fluorescence with RCP and LCP X-ray photons),

as the field is flipped, confirms the magnetic origin of the signal as opposed to some experimental artifact.

As an initial study of this system, a sample was chosen with thin U layers and thick Co layers, which would provide the most ideal conditions for the observation of any induced magnetic moment on the uranium layers. Sample SN116 ( $[\text{U}_{19}/\text{Co}_{42.5}]_{20}$ ) was measured at the U  $M_{IV}$  edge (figure 6.10), which has been shown to provide a larger signal at resonance than the U  $M_V$  edge in other uranium multilayer systems [23].

Figure 6.10 shows the U  $M_{IV}$  edge XANES and XMCD signals. The XMCD amplitude is hardly detectable above the background noise (almost one hundred times smaller than that observed for a similarly structured U/Fe sample), a stark contrast to the results obtained for the U/Fe system. XRMR measurements carried out on the XMaS beamline at the ESRF, on samples SN108,  $[\text{U}_{27.5}/\text{Co}_{27.5}]_{30}$ , and SN116,  $[\text{U}_{19}/\text{Co}_{42.5}]_{20}$ , were not able to measure any detectable signal. In order to gain some insight into the possible differences that might exist between the observed U polarisations in U/Fe and U/Co multilayers, it would be useful to compare other magnetic systems, which include the combinations of these elements.

A detailed theoretical and experimental comparison of the  $\text{UX}_2$  ( $X = 3d$ , ferromagnetic transition metal element) binary compounds has been reported in a theoretical study of the ferromagnetism in  $\text{UFe}_2$ ,  $\text{UNi}_2$  and the Pauli paramagnet,  $\text{UCo}_2$ , in terms of the nature of the uranium 5f electrons and the 3d-5f hybridisation, by Severin et al. [44]. These properties can be understood by considering the density of states (DOS) of the 3d and 5f bands in the vicinity of the Fermi energy. In the  $\text{UFe}_2$  compound there is a large overlap in energy of the 3d band of Fe and the U 5f band, where the strong hybridisation causes 3d-5f mixing at the Fermi level, resulting in a ferromagnetism driven principally by the iron atoms. In  $\text{UCo}_2$  the energy of the 3d band is lowered with respect to the U 5f electrons, which leads to a reduced DOS between the bands. The extra electron in cobalt places the Fermi energy directly in this low DOS region, and consequently the  $\text{UCo}_2$  compound is then non-ferromagnetic. In  $\text{UNi}_2$  the 3d band is lowered still further in energy, resulting in an almost negligible amount of 3d-5f hybridisation. The extra electron in nickel

with respect to cobalt however, places the Fermi level into the U 5f dominated part of the DOS. This leads to a ferromagnetically ordered UNi<sub>2</sub> compound dominated by the uranium atoms. It is then possible, from a consideration of the likely interactions at the U/X interfaces and the extent of the 3d-5f hybridisation discussed [44], to explain the observed trend in U polarisation from the U/Fe to the U/Co system.

An interesting additional point is made with respect to UFe<sub>2</sub>. This compound possesses a lower Curie temperature than for binary, rare-earth iron compounds and exhibits a heavily reduced iron magnetic moment. These properties are resolved as a suppression of the magnetism by the U 5f electrons. This could be an important factor, concerning the reduced magnetic moments seen in all of the U multilayer systems.

6.1.5 U/Gd - Gd L<sub>II</sub> and L<sub>III</sub> edges

The U/Gd system was investigated, using the XMCD technique, to probe the extent of the 4f-5f hybridisation, which might be observed as an induced U moment. This study would provide an interesting comparison between the 3d-5f systems considered previously, and investigations at the Gd L edges might shed some light on the reduced magnetic moment values determined by SQUID magnetometry.

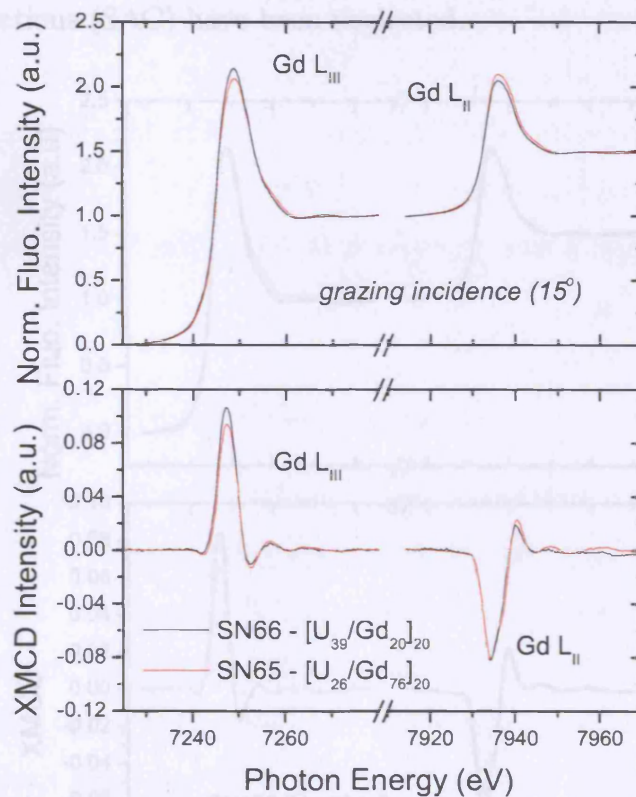


Figure 6.11: XANES and XMCD signals for U/Gd samples SN65 and SN66.

Employing the Apple-II helical undulator, energy scans were made across the Gd L<sub>II</sub> edge from 7915eV to 7975eV in 300 steps of 0.2eV, and across the Gd L<sub>III</sub> edge from 7228eV to 7284eV in 280 steps of 0.2eV, counting for 1s per data point. A field of 1T was applied to saturate the sample, at a temperature of  $\sim 5$ K. The circular polarisation was flipped 5 times with the field applied parallel to the beam direction. The magnetisation direction was then reversed, antiparallel to the beam direction and the polarisation again flipped.

Figure 6.11 shows the XANES and XMCD spectra for two U/Gd multilayer

samples, one with thick Gd layers and the other with thin Gd layers. The XANES spectra show no distinctive differences between the two samples and the XMCD signals have similar shapes and amplitudes to one another, which suggests that there is no appreciable difference in the magnitude of the observed magnetic moment for thick and thin Gd layers, a result supported by the SQUID magnetometry measurements presented in chapter 5. The XMCD spectra presented here have been normalised to the white line and corrected according to the branching ratio, but self absorption corrections (SAC) have been neglected.

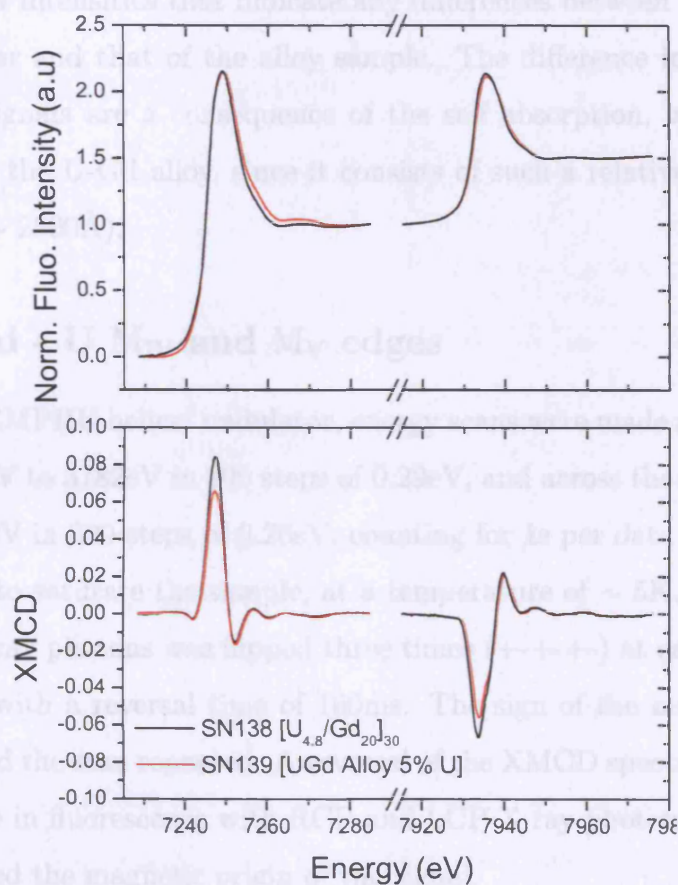


Figure 6.12: XANES and XMCD signals for U/Gd sample SN138 and U-Gd alloy, SN139.

A comparison of the Gd  $L_{II}$  edge XMCD intensity with that observed in Gd/Fe multilayers by Choi et al. [103] before branching ratio correction, shows that the shape and amplitudes are similar. In the report by Choi, the edge-jump, normalised Gd XMCD peak at 10K is quoted as 'in agreement' with bulk gadolinium. This ob-

servation does not agree with our own measurements, where SQUID magnetometry has indicated a reduced saturation magnetisation. However, the L edges probe only the 5d states, which should reflect the magnetic 4f shell, due to the strong 4f-5d intra-atomic exchange coupling. It is possible that a suppression of the magnetism of the Gd 4f electrons by the U 5f states, an effect alluded to in the work by Severin et al. [44], might not affect the 5d conduction band.

Figure 6.12 shows the XANES and XMCD spectra at the Gd  $L_{II}$  and  $L_{III}$  edges for U/Gd multilayer sample SN138 and a U-Gd alloy. There are no obvious features in the fluorescent intensities that indicate any differences between the Gd comprising the multilayer and that of the alloy sample. The difference in the amplitudes of the XMCD signals are a consequence of the self absorption, which carries the largest effect for the U-Gd alloy, since it consists of such a relatively large amount of gadolinium ( $\sim 2500\text{\AA}$ ).

### 6.1.6 U/Gd - U $M_{IV}$ and $M_V$ edges

Employing the EMPHU helical undulator, energy scans were made across the U  $M_{IV}$  edge from 3695eV to 3782eV in 300 steps of 0.29eV, and across the U  $M_V$  edge from 3520eV to 3598eV in 300 steps of 0.26eV, counting for 1s per data point. A field of 1T was applied to saturate the sample, at a temperature of  $\sim 5\text{K}$ . The polarity of the incoming X-ray photons was flipped three times (+--+--) at each energy point, counting for 1s with a reversal time of 160ms. The sign of the magnetic field was then reversed and the scan repeated. A reversal of the XMCD spectrum (determined by the difference in fluorescence with RCP and LCP X-ray photons), as the field is flipped, confirmed the magnetic origin of the signal.

Figure 6.13 shows the normalised XMCD intensity and X-ray near-edge spectroscopy (XANES) spectra at both the U  $M_{IV}$  and  $M_V$  edges for a range of U/Gd multilayer samples, comprising approximately constant Gd layer thicknesses, but varying U layer thicknesses. This figure also displays the results for a U-Gd alloy sample ( $\sim 5\%$  U).

The observation of an XMCD signal at the U M edges indicates that the uranium atoms carry an induced magnetic moment. However, the magnitude of the signal

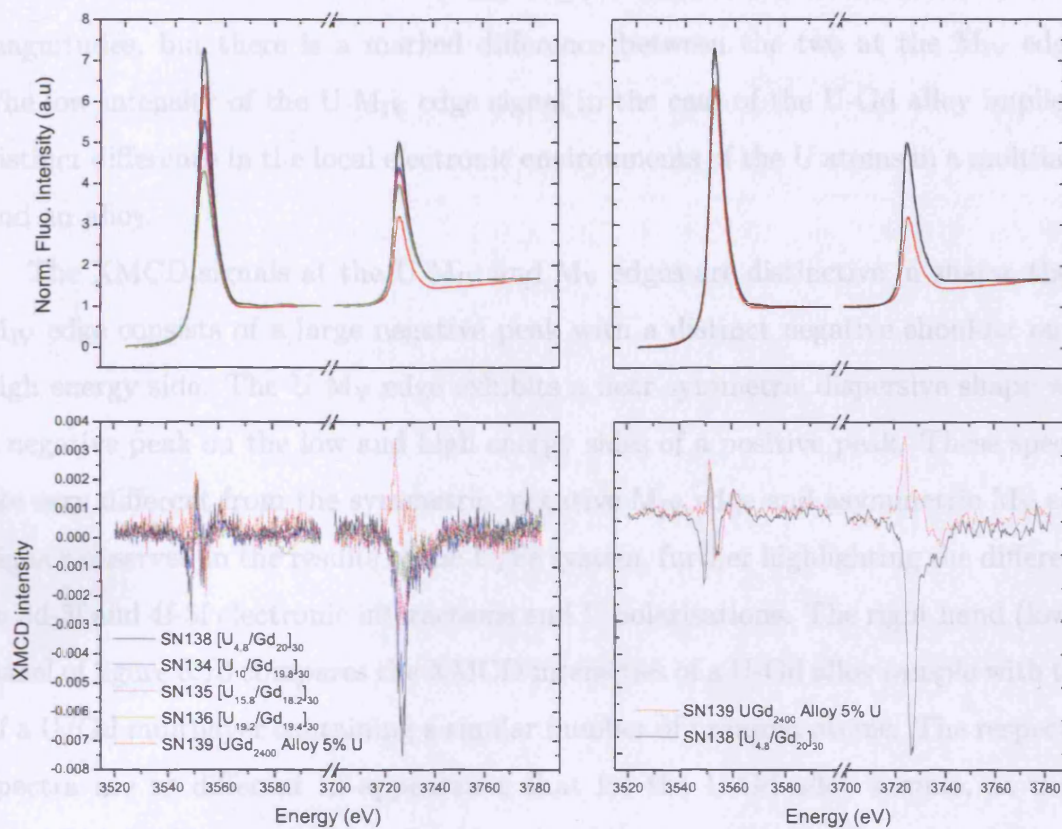


Figure 6.13: XANES and XMCD signals at the U  $M_{IV}$  and  $M_V$  edges, normalised to the white line and corrected for the respective branching ratio, but not including SAC. The left panels compare spectra for a series of U/Gd multilayers with varied U layer thicknesses, but constant  $t_{Gd}$ , the right panels show a clearer comparison of the spectra observed for a multilayer and that of a U-Gd alloy sample.

is considerably smaller (almost two orders of magnitude) than that observed for a similarly structured U/Fe multilayer. This indicates a much weaker 4f-5f hybridisation in the U/Gd system, perhaps as a consequence of the localised nature of the 4f gadolinium electrons.

The XANES spectra show the distinct white line shapes at the U M edges, seen in the study of the U/Fe and U/Co systems. The differences in amplitude result directly from self absorption effects, where the most dramatic effect can be observed for SN136 (shown in green), the sample with the thickest U layers. The right panel compares the U-Gd alloy sample with that of a U/Gd multilayer containing a similar

number of uranium atoms. The U  $M_V$  edge intensities exhibit similar shapes and magnitudes, but there is a marked difference between the two at the  $M_{IV}$  edges. The low intensity of the U  $M_{IV}$  edge signal in the case of the U-Gd alloy implies a distinct difference in the local electronic environments of the U atoms in a multilayer and an alloy.

The XMCD signals at the U  $M_{IV}$  and  $M_V$  edges are distinctive in shape; the U  $M_{IV}$  edge consists of a large negative peak with a distinct negative shoulder on its high energy side. The U  $M_V$  edge exhibits a near symmetric dispersive shape with a negative peak on the low and high energy sides of a positive peak. These spectra are very different from the symmetric, negative  $M_{IV}$  edge and asymmetric  $M_V$  edge signals observed in the results of the U/Fe system, further highlighting the difference in 3d-5f and 4f-5f electronic interactions and U polarisations. The right hand (lower) panel of figure 6.13 compares the XMCD intensities of a U-Gd alloy sample with that of a U/Gd multilayer containing a similar number of uranium atoms. The respective spectra are so different in appearance that for the U-Gd alloy sample, at the U  $M_V$  edge the first negative peak is completely absent. At the  $M_{IV}$  edge the signal is opposite in sign to that of the U/Gd multilayers. These differences emphasize the fact that the uranium atoms in a U-Gd alloy are exposed to a very different environment magnetically, than those in a U/Gd multilayer. These results support the SQUID magnetometry and X-ray diffraction measurements, which suggest a very small amount of U-Gd alloy present in the multilayer samples, if any.

A clear trend is visible, considering the four samples included in the figure, which possess roughly equivalent Gd layer thicknesses ( $\sim 20\text{\AA}$ ). The shape of the curves at the respective edges does not change with varying  $t_U$ , although the amplitude in the signals decrease as the uranium layers become thicker. This result implies that the distribution of the induced U 5f magnetic moment, polarised by the gadolinium layers, is not constant throughout the U layer and that a U moment profile exists within the uranium layers. In order to provide a profile of the induced moment, it is first necessary to extract the orbital and spin magnetic moments from the XMCD spectra. This is achieved, using the magneto-optical sum rules [80] [81] as described for the induced U 5f moment of the U/Fe system. Values of the spin, orbital and

| Sample  | $\langle T_z \rangle$ | Config.         | $\mu_L(\text{U}5f)$<br>$\pm 0.0005\mu_B$ | $\mu_S(\text{U}5f)$<br>$\pm 0.0005\mu_B$ | $\mu(\text{U}5f)$<br>$\pm 0.001\mu_B$ | $\mu_L/\mu_S$ |
|---|-----------------------|-----------------|--|--|---------------------------------------|---------------|
| SN134<br>[U <sub>10</sub> /Gd <sub>19.8</sub> ] <sub>30</sub>   | =0                    | 5f <sup>3</sup> | 0.00816                                  | -0.0140                                  | -0.00581                              | -0.58         |
|   |                       | 5f <sup>2</sup> | 0.00890                                  | -0.0152                                  | -0.00634                              | -0.58         |
|   | ≠ 0                   | 5f <sup>3</sup> | 0.00816                                  | -0.00489                                 | 0.00328                               | -1.67         |
|   |                       | 5f <sup>2</sup> | 0.00890                                  | -0.00340                                 | 0.00550                               | -2.95         |
| SN135<br>[U <sub>15.8</sub> /Gd <sub>18.2</sub> ] <sub>30</sub> | =0                    | 5f <sup>3</sup> | 0.00663                                  | -0.0101                                  | -0.00344                              | -0.66         |
|   |                       | 5f <sup>2</sup> | 0.00724                                  | -0.0110                                  | -0.00375                              | -0.66         |
|   | ≠ 0                   | 5f <sup>3</sup> | 0.00663                                  | -0.00352                                 | 0.00311                               | -1.88         |
|   |                       | 5f <sup>2</sup> | 0.0724                                   | -0.00245                                 | 0.00478                               | -2.95         |
| SN136<br>[U <sub>19.2</sub> /Gd <sub>19.4</sub> ] <sub>30</sub> | =0                    | 5f <sup>3</sup> | 0.00428                                  | -0.00633                                 | -0.00204                              | -0.68         |
|   |                       | 5f <sup>2</sup> | 0.00467                                  | -0.00690                                 | -0.00223                              | -0.68         |
|   | ≠ 0                   | 5f <sup>3</sup> | 0.00428                                  | -0.00221                                 | 0.00207                               | -1.94         |
|   |                       | 5f <sup>2</sup> | 0.00467                                  | -0.00154                                 | 0.00313                               | -3.03         |
| SN138<br>[U <sub>4.8</sub> /Gd <sub>20</sub> ] <sub>30</sub>    | =0                    | 5f <sup>3</sup> | 0.0115                                   | -0.0201                                  | -0.00857                              | -0.57         |
|   |                       | 5f <sup>2</sup> | 0.0126                                   | -0.0219                                  | -0.00935                              | -0.57         |
|   | ≠ 0                   | 5f <sup>3</sup> | 0.0115                                   | -0.00702                                 | 0.00450                               | -1.64         |
|   |                       | 5f <sup>2</sup> | 0.0126                                   | -0.00489                                 | 0.00767                               | -2.57         |
| SN139<br>U – Gd <sub>alloy</sub><br>(~ 5%U)                     | =0                    | 5f <sup>3</sup> | -0.00449                                 | 0.00432                                  | -0.00018                              | -1.04         |
|   |                       | 5f <sup>2</sup> | -0.00490                                 | 0.00471                                  | 0.00020                               | -1.04         |
|   | ≠ 0                   | 5f <sup>3</sup> | -0.00449                                 | -0.00151                                 | 0.00299                               | -2.98         |
|   |                       | 5f <sup>2</sup> | -0.00490                                 | 0.00105                                  | 0.00385                               | -4.67         |

Table 6.4: Induced U 5f orbital, spin and total magnetic moments, determined by XMCD for a selection of U/Gd multilayer samples. Results are shown, with and without the inclusion of the  $\langle T_z \rangle$  term for U 5f<sup>2</sup> and 5f<sup>3</sup> configurations. The measurements were made at 5K in an applied field of 1T, large enough to magnetically saturate the U moments.

total induced U 5f moment, and the ratio of orbital to spin moment are summarised in table 6.4 for U  $5f^2$  and  $5f^3$  configurations, including the  $\langle T_z \rangle$  term and taking  $\langle T_z \rangle = 0$ .

### 6.1.7 Summary Analysis

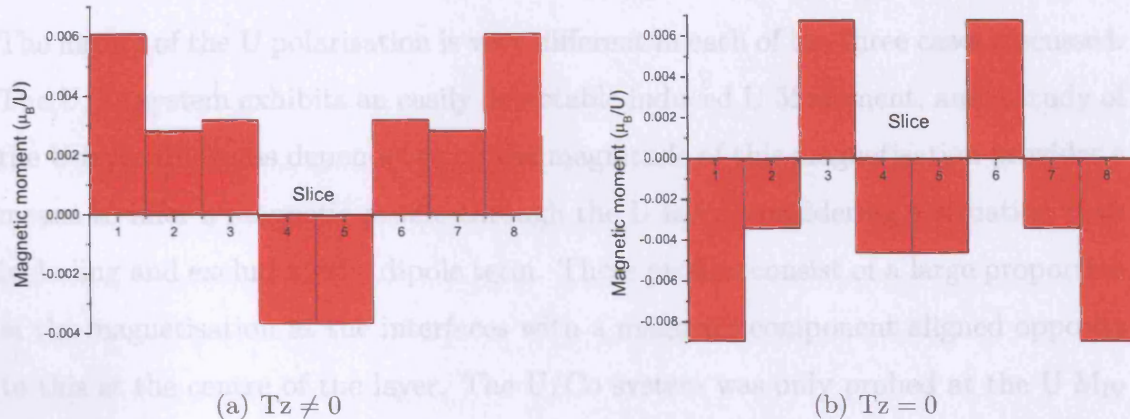


Figure 6.14: Profiles of the induced U 5f magnetic moment, determined by a comparison of the total U moments for the series of U/Gd samples in table 6.4, considering a  $5f^{2.5}$  configuration. Slices are  $2.5\text{\AA}$ .

The four U/Gd samples listed in table 6.4 have approximately constant  $t_{\text{Gd}} \sim 20\text{\AA}$  and different  $t_{\text{U}}$ . It is then possible to draw a profile of the induced U 5f moment, from the values of  $\mu_B/U$  for each sample. Since the valence state is not known in this system a  $5f^{2.5}$  electronic configuration has been adopted, by taking the average of the moment values for the  $5f^2$  and  $5f^3$  configurations. This is a simplistic method for modeling the U moment profile through the uranium layers, and it assumes that there are no interactions between the U 'slices' and that the U-Gd and Gd-U interfaces are equivalent. Although these assumptions might have been a little too idealistic in the case of the U/Fe system, where a large amount of interfacial diffusion is expected from the X-ray diffraction spectra and SQUID magnetometry results, the U/Gd system exhibits a much more coherent layer by layer growth, with less interdiffusion. The profiles of the induced U 5f magnetic moment for a  $[\text{U}_{20}/\text{Gd}_{20}]_{30}$  multilayer, with the U layer separated into 8 slices, are shown in figure 6.14 for the two cases (a)  $\langle T_z \rangle \neq 0$  and (b)  $\langle T_z \rangle = 0$ .

Qualitatively, both profiles show some form of oscillating moment, which indicates that there may be some RKKY type interaction through the uranium layers

similar to the indirect exchange mechanism responsible for the observation of ferromagnetic ordering in the gadolinium itself.

### 6.1.7 Summary Analysis

The nature of the U polarisation is very different in each of the three cases discussed. The U/Fe system exhibits an easily detectable induced U 5f moment, and a study of the U layer thickness dependence on the magnitude of this magnetisation provides a means to infer a magnetic profile through the U layer, considering a situation both including and excluding the dipole term. These profiles consist of a large proportion of the magnetisation at the interfaces with a magnetic component aligned opposite to this at the centre of the layer. The U/Co system was only probed at the U  $M_{IV}$  edge, for one example sample. The signal at this edge was barely detectable above the background noise and was more than two orders of magnitude smaller than that observed for the U/Fe system. This could be an effect comparable to that observed in the binary compound system discussed in detail by Severin et al. [44], where the larger separation between the 5f and 3d bands in the case of U/Co, leads to a negligible 5f-3d hybridisation.

The magnitudes of the magnetic moments induced in the uranium layers of the U/Gd samples were much smaller than those found for the U/Fe system and the XMCD signals were very different in shape, indicating that the polarisations are an effect induced by the hybridisations of the U 5f states with the 3d and 4f bands respectively. The oscillatory nature of the induced U moment profile in the case of U/Gd samples, could be due to an RKKY-type coupling between neighbouring Gd layers.

It is possible to further probe the profile of the induced magnetisation within the U layers, by employing the technique of X-ray resonant magnetic reflectivity. This technique is sensitive to the distribution of the magnetic moment as a function of the depth through the uranium layers. The following section details the relevant theory describing X-ray magnetic scattering, the experimental conditions and the results of XRMR measurements carried out on selected U/Fe samples.

## 6.2 X-ray Magnetic Scattering

X-ray scattering and photon absorption processes are closely related to one another. In fact, the attenuation coefficient,  $\mu$  is the product of the density of scatterers,  $n_0$  and the total scattering cross-section,  $\sigma_{tot}$ , which includes the imaginary part of the forward scattering length.

In chapter 4 the scattering of X-rays from materials was discussed in detail, but the interaction with magnetic ions and its effect on the scattered intensity was not approached. Under experimental circumstances discussed so far, contributions from magnetic scattering would be negligible. However, in certain conditions it is possible to distinguish between charge and magnetic scattering and even between orbital and spin contributions.

In order to consider the implications of scattering from a magnetic ion it is important to recollect the Hamiltonian, equation (4.1.2). The term quadratic in  $\mathbf{A}$  is associated with the Thomson scattering described earlier and the  $\mathbf{p} \cdot \mathbf{A}$  term drives the photoelectric absorption process. It is possible for the  $\mathbf{p} \cdot \mathbf{A}$  term to produce scattering effects, by employing second-order perturbation theory. The interaction of X-rays with the spin of atomic scatterers can be represented as a Zeeman term in the Hamiltonian,

$$H_{Zeeman} = 2\mu_B \mathbf{S} \cdot \mathbf{H} \quad (6.16)$$

where  $\mathbf{S}$  is the electronic spin and  $\mathbf{H} = \nabla \times \mathbf{A}$  is the photon magnetic field. The prefactor  $2\mu_B$  is the product of the Bohr magnetic moment and the spin gyromagnetic ratio. The electron motion through the electric field of the incident photon induces a magnetic field, which interacts with the spin of the electron to produce a spin-orbit interaction,  $\mathbf{S} \cdot (\mathbf{A} \times \mathbf{E})$ , treated by first-order perturbation theory. The spin contribution to the scattering length can be summarised as,

$$i\tau(\mathbf{F}_s(\mathbf{k}) \cdot \mathbf{B}) \quad (6.17)$$

$$\mathbf{B} = (\boldsymbol{\varepsilon}' \times \boldsymbol{\varepsilon}) - (\hat{\mathbf{q}}' \times \boldsymbol{\varepsilon}') \times (\hat{\mathbf{q}} \times \boldsymbol{\varepsilon}) + (\hat{\mathbf{q}}' \cdot \boldsymbol{\varepsilon})(\hat{\mathbf{q}}' \times \boldsymbol{\varepsilon}') - (\hat{\mathbf{q}} \cdot \boldsymbol{\varepsilon}')(\hat{\mathbf{q}} \times \boldsymbol{\varepsilon}) \quad (6.18)$$

$\mathbf{F}_s$  is the Fourier transform of the spin density per unit cell or spin unit cell structure factor,  $\tau$  is the ratio of the photon energy to the rest mass energy of the electron and  $\varepsilon$  and  $\varepsilon'$  are the primary and secondary photon polarisation vectors.

The orbital motion of the electron results in a term added to the scattering length, which describes the change from a stationary frame of reference to a moving one and contributes to the  $\mathbf{p} \cdot \mathbf{A}$  term of the Hamiltonian. The orbital contribution to the scattering length is then,

$$i\tau(\mathbf{F}_1 \cdot \mathbf{B}_0) \quad (6.19)$$

$\mathbf{F}_1$  is the orbital angular momentum unit cell structure factor and  $\mathbf{B}_0$  is the component of  $(\varepsilon \times \varepsilon')$  perpendicular to the scattering vector  $\mathbf{k}$ .

$$B_0 = (\varepsilon \times \varepsilon') - \hat{\mathbf{k}} \left[ \hat{\mathbf{k}} \cdot (\varepsilon \times \varepsilon') \right] \quad (6.20)$$

The difference between  $\mathbf{B}$  and  $\mathbf{B}_0$  highlights the different contributions that the spin and orbital momentum make to the non-resonant scattering amplitude, which allows them to be distinguished experimentally [104] [105]. The charge and magnetic scattering lengths can be evaluated as,

$$f_c = -r_e(\varepsilon' \cdot \varepsilon)F_c \quad (6.21)$$

$$f_m = r_e i\tau(\mathbf{F}_s \cdot \mathbf{B} + \mathbf{F}_1 \cdot \mathbf{B}_0) \quad (6.22)$$

Magnetic corrections to the Thomson scattering cross-section were first predicted in 1954 [106] and X-rays were described as a possible tool for determining magnetic structures [107]. For non-resonant scattering processes, Blume [104] estimated the ratio between pure magnetic and charge cross-sections,

$$\frac{\sigma_{magnetic}}{\sigma_{charge}} \approx \left( \frac{\hbar\omega}{mc^2} \right)^2 \frac{N_m^2}{N^2} \langle S \rangle^2 \frac{f_m^2}{f_c^2} \quad (6.23)$$

The first term is the square of the ratio of the photon energy to the energy of the electron.  $N_m$  is the number of magnetic electrons per atom and  $N$  is the total number of electrons per atom.  $\langle S \rangle$  is the expectation value of the spin operator,

which is unity at low temperatures and approaches zero at the Curie temperature. Values of this ratio are of the order  $\sim 10^{-4}$  for magnetic elements considered in this work and energies in the hard X-ray range.

Although the magnetic cross-section is very weak in comparison to that for the charge scattering it is still possible to observe pure magnetic diffraction peaks in certain antiferromagnetic crystals [108] [109] at reciprocal lattice points, where there is no charge scattering contribution, due to space group symmetry. Ferromagnets are much more difficult to resolve, since both the charge and magnetic Bragg reflections overlap. With the magnetic and charge scattering in phase, the scattering cross-section becomes,

$$\frac{d\sigma}{d\Omega} = |f_m + f_c|^2 = f_c^2 + f_m^2 + 2f_c f_m \quad (6.24)$$

The third term in equation (6.2) represents the magnetic-charge interference. This interference term allows the experimental determination of magnetic scattering in ferromagnets. It is both linear in  $\tau$  and linear in the magnetic orientation, which means that it is much stronger than pure magnetic scattering and it can be separated from the dominant charge scattering, by manipulating an external magnetic field.

The magnetic and charge scattering amplitudes are completely out of phase, which implies a lack of constructive interference, at least for centrosymmetric crystal structures. It is possible to induce an interference by using a circularly polarised incident beam or by tuning the photon energy close to that of an absorption edge of an element within the sample.

## 6.3 X-ray Resonant Magnetic Scattering

The resonant scattering process affects the scattered intensity by modifying the dispersive and absorptive parts of the atomic scattering amplitude,  $f'(\omega)$  and  $f''(\omega)$ , respectively. Recalling equation (4.1.2), the dispersion corrections have no  $Q$ -dependence to a good approximation, because they are dominated by electrons in the inner most shells, which are confined spatially. The incident X-ray photons tuned to an absorp-

tion edge (resonant energy) excite electrons from a bound inner shell to an unfilled energy state. The electrons then decay back into their initial state, emitting an elastically scattered photon of energy equivalent to the incident X-ray beam.

The Pauli exclusion principle only allows transitions into unoccupied orbitals and exchange induced orbital splittings. These transitions are sensitive to the spin polarisation of the electronic bands and result in predominantly electric dipole and quadrupole terms in the magnetic cross-section. For an electric  $2^L$  – pole resonance in a magnetic ion, the resonant contribution ( $f_{EL}^e$ ) to the coherent scattering amplitude [110] is given by,

$$f_{EL}^e(\omega) = \frac{4\pi}{|k|} f_D \sum_{M=L}^L \left[ \hat{\varepsilon}'^* \cdot \mathbf{Y}_{LM}^{(e)}(\hat{\mathbf{k}}') \mathbf{Y}_{LM}^{(e)*}(\hat{\mathbf{k}}) \cdot \hat{\varepsilon} \right] F_{LM}^{(e)}(\omega) \quad (6.25)$$

$\mathbf{Y}_{LM}^{(e)}(\hat{\mathbf{k}})$  are the vector spherical harmonics, which contain the photon polarisation dependence of the transition.  $\lambda$  is the photon wavelength,  $f_D$  is the Debye-Waller factor,  $\varepsilon$  and  $\varepsilon'$  are the polarisation vectors of the incident and scattered X-ray beams, respectively.  $F_{LM}^{(e)}(\omega)$  is the dimensionless transition matrix element, which determines the strength of the resonance,

$$F_{LM}^{(e)}(\omega) = \sum_{\alpha, \eta} \frac{p_\alpha p_\alpha(\eta)}{\chi(\alpha, \eta) - i} \frac{\Gamma_x(\alpha M \eta)}{\Gamma(\eta)} \quad (6.26)$$

$p_\alpha$  and  $p_\alpha(\eta)$  are the probabilities that the ion is in an initial ground state,  $\alpha$ , or that a transition from an initial state to an excited state,  $\eta$  has occurred. These probabilities are determined by the overlap integrals of initial and final states.  $\Gamma_x$  is the partial line width for the radiative decay process from the excited state to the initial state and  $\Gamma$  is the total line width of the decay of both radiative and non-radiative processes.

$$\chi(\alpha, \eta) = \frac{2(E_\eta - E_\alpha - \hbar\omega)}{\Gamma} \quad (6.27)$$

This term gives the deviation in energy from the resonance, providing a strong energy dependence in the matrix element  $F_{LM}^{(e)}$ .

The strongest contributions to the magnetic scattering cross-section usually come

from the electric dipole transitions. Hannon [110] treats the case for a dipole transition with  $\Delta l = 1$  and  $\Delta M = 0, \pm 1$ , table 6.2 shows the elemental transitions investigated during the course of this thesis. By notating the unit vector of the magnetic moment of the  $n$ th ion as  $\hat{z}_n$ , the spherical harmonics can be written for such transitions as,

$$[\hat{\varepsilon}' \cdot \mathbf{Y}_{1\pm 1}(\hat{\mathbf{k}}') \mathbf{Y}_{1\pm 1}^*(\hat{\mathbf{k}} \cdot \hat{\varepsilon})] = \left( \frac{3}{16\pi} \right) [\hat{\varepsilon}' \cdot \hat{\varepsilon} \mp i(\hat{\varepsilon}' \times \hat{\varepsilon} \cdot \hat{z}_n - (\hat{\varepsilon}' \cdot \hat{z}_n)(\hat{\varepsilon} \cdot \hat{z}_n)] \quad (6.28)$$

and

$$[\hat{\varepsilon}' \cdot \mathbf{Y}_{10}(\hat{\mathbf{k}}') \mathbf{Y}_{10}^*(\hat{\mathbf{k}} \cdot \hat{\varepsilon})] = \left( \frac{3}{8\pi} \right) [(\hat{\varepsilon}' \cdot \hat{z}_n)(\hat{\varepsilon} \cdot \hat{z}_n)] \quad (6.29)$$

Substituting these terms into equation (6.3) gives the resonant magnetic scattering amplitude for dipole transitions.

$$f_{nE1}^{Xres} = [(\hat{\varepsilon}' \cdot \hat{\varepsilon})F^{(0)} - i(\hat{\varepsilon}' \times \hat{\varepsilon}) \cdot \hat{z}_n F^{(1)} + (\hat{\varepsilon}' \cdot \hat{z}_n)(\hat{\varepsilon} \cdot \hat{z}_n)F^{(2)}] \quad (6.30)$$

where the coefficient of the first term  $F^{(0)} = (\frac{3}{4k})[F_{11} + F_{1-1}]$  the second term  $F^{(1)} = (\frac{3}{4k})[F_{11} - F_{1-1}]$  and  $F^{(2)} = (\frac{3}{4k})[2F_{10} - F_{11} - F_{1-1}]$ .

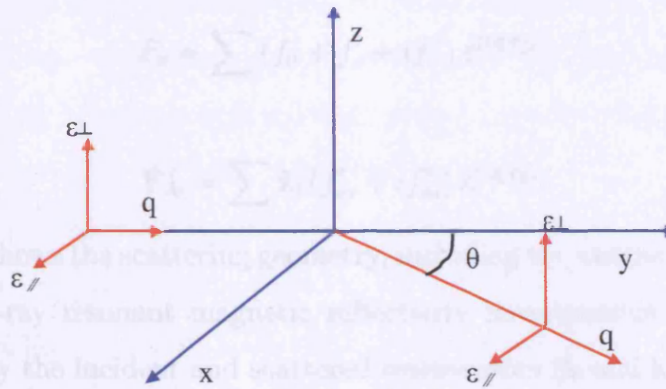


Figure 6.15: Schematic diagram, describing the scattering geometry and the linear and orthogonal components of the polarisation vectors.

A representation of an elastic scattering geometry is shown in figure 6.15, which includes the linear and orthogonal components of the polarisation vectors. In this case the respective components can be expressed as follows:

$$\varepsilon = \varepsilon_{\perp}(z) + \varepsilon_{\parallel}(y) = (\varepsilon_{\perp}, \varepsilon_{\parallel}, 0) \quad (6.31)$$

where  $\varepsilon = \varepsilon'$  and  $\varepsilon \cdot \varepsilon' = 1$  for the forward scattering length.

$$\varepsilon \times \varepsilon' = x (\varepsilon_{\perp} \varepsilon_{\parallel} - \varepsilon_{\parallel} \varepsilon_{\perp}) \quad (6.32)$$

The second term of equation (6.30) is sensitive to the sample magnetisation. This can be realised experimentally by calculating the difference in intensity of the scattered signal, measured with right and left circularly polarised light. However, this interference signal is only sensitive to the component of the magnetisation parallel to the scattering plane [111]. It is possible to make use of this form of scattering in a reflection geometry, in order to gain information about the distribution of the magnetisation along the z-axis.

## 6.4 X-ray Resonant Magnetic Reflectivity

Considering the X-ray resonant magnetic scattering process in a specular reflection geometry, the charge and magnetic structure factors are;

$$F_c = \sum (f_0 + f'_c + i f''_c) e^{(i\mathbf{q} \cdot \mathbf{r}_j)} \quad (6.33)$$

$$\mathbf{F}_m = \sum \hat{\mathbf{z}}_j (f'_m + i f''_m) e^{(i\mathbf{q} \cdot \mathbf{r}_j)} \quad (6.34)$$

Figure 6.16 shows the scattering geometry, including the magnetisation direction, for a typical X-ray resonant magnetic reflectivity measurement. The scattering plane, defined by the incident and scattered wavevectors ( $\mathbf{k}$  and  $\mathbf{k}'$  at an angle  $\theta$  to the y axis), is parallel to the yz plane, where the z-axis is defined as perpendicular to the multilayer surface.

The experimentally determined quantity is the difference between the reflected intensities for right and left circularly polarised X-rays. Since the intensities are the square of the resonant scattering factors, there are cross-terms in the magnetic and

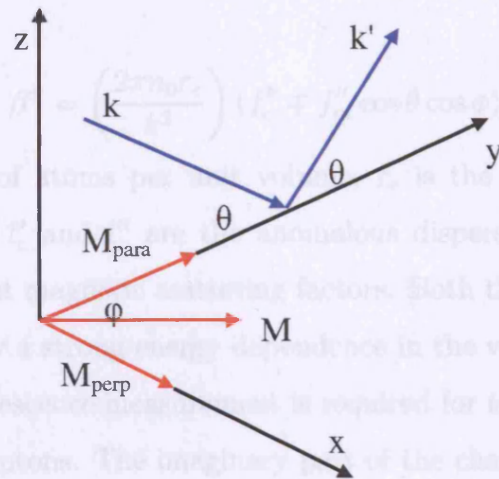


Figure 6.16:

charge dependent scattering factors, which result in a magnetic-charge interference given by,

$$I^+ - I^- = -2 \left( \hat{\mathbf{k}} + \hat{\mathbf{k}}' \cos 2\theta \right) \cdot (F'_c \mathbf{F}'_m + F''_c \mathbf{F}''_m) \quad (6.35)$$

Here, the charge structure factor and the resonant magnetic structure factor have been separated into their respective real and imaginary parts, which are real quantities for the case of centrosymmetric structures. The first term indicates that the magnetic charge interference is only sensitive to the magnetisation component parallel to  $\hat{\mathbf{k}} + \hat{\mathbf{k}}' \cos 2\theta$  in the scattering plane.

The reflected intensity for multilayer samples was treated using the method described in chapter 4. Recalling the equation for the refractive index and the scattering geometry displayed in figure 6.16, the refractive index for left and right helicity, circularly polarised X-rays becomes,

$$n^\pm = 1 - \delta^\pm + i\beta^\pm \quad (6.36)$$

where,

$$\delta^\pm = \left( \frac{2\pi n_0 r_e}{k^2} \right) (f_0 + f'_c \mp f'_m \cos \theta \cos \phi) \quad (6.37)$$

and

$$\beta^{\pm} = \left( \frac{2\pi n_0 r_e}{k^2} \right) (f_c'' \mp f_m'' \cos \theta \cos \phi) \quad (6.38)$$

$n_0$  is the number of atoms per unit volume,  $r_e$  is the radius of the electron,  $f_0 = Z$ , proton number,  $f_c'$  and  $f_c''$  are the anomalous dispersion corrections and  $f_m'$  and  $f_m''$  are the resonant magnetic scattering factors. Both the charge and magnetic scattering factors show a strong energy dependence in the vicinity of an absorption edge, such that a fluorescence measurement is required for the case of right and left circularly polarised photons. The imaginary part of the charge scattering factor,  $f_c''$  can be derived from the non-magnetic absorption  $(I^+ + I^-)/2$ , while the magnetic scattering factor,  $f_m''$  is related to the XMCD absorption coefficient,  $\mu_m$ ,

$$\mu_m = - \left( \frac{8\pi n_0 r_e}{k} \right) (\hat{\mathbf{k}} \cdot \hat{\mathbf{z}}) f_m'' \quad (6.39)$$

It is then possible to relate the real and imaginary parts of the respective scattering factors.

The behaviour of the dispersion corrections through a resonance edge can be modelled by a superposition of harmonic oscillators, described by oscillator strengths,  $g(\omega_s)$ , proportional to the absorption cross-section,  $\sigma_a$ . The expression for the real part of the dispersion corrections,  $f'$  can then be written in terms of a weighted superposition of single oscillators.

$$f'(\omega) = \sum_s g(\omega_s) f'_s(\omega_s, \omega) \quad (6.40)$$

The  $f''$  term can be related to the absorption cross-section via the optical theorem to yield,

$$f''(\omega) = - \left( \frac{\omega}{4\pi r_0 c} \right) \sigma_a(\omega) \quad (6.41)$$

The Kramers-Kronig relations [112] can be used to relate the values of  $f'$  and  $f''$ . These relations are derived from Cauchy's theorem, treating single oscillators, but can be used to encompass  $f'(\omega)$  and  $f''(\omega)$ , since they are linear superpositions of single oscillators. The Kramers-Kronig equations can be written,

$$f'(\omega) = \frac{1}{\pi} P \int_{-\infty}^{+\infty} \frac{f''(\omega')}{(\omega' - \omega)} d\omega' = \frac{2}{\pi} P \int_0^{+\infty} \frac{\omega' f''(\omega')}{(\omega'^2 - \omega^2)} d\omega' \quad (6.42)$$

$$f''(\omega) = -\frac{1}{\pi} P \int_{-\infty}^{+\infty} \frac{f'(\omega')}{(\omega' - \omega)} d\omega' = -\frac{2\omega}{\pi} P \int_0^{+\infty} \frac{f'(\omega')}{(\omega'^2 - \omega^2)} d\omega' \quad (6.43)$$

where P stands for principal value and refers to the fact that the integral is performed from  $-\infty$  to  $(\omega - \epsilon)$  and from  $(\omega + \epsilon)$  to  $+\infty$  in the limit of  $\epsilon \rightarrow 0$ .

In our case we are interested in measuring the X-ray resonant magnetic scattering at the U  $M_{IV}$  and  $M_V$  edges, which have enormous resonant enhancements to the scattering factors. It is therefore necessary to measure the resonant magnetic reflectivity as a function of energy, sampling a reasonable number of data points in energy parameter space to allow for a decent model of the magnetic and nonmagnetic absorption. Due to the large numbers of experimental and sample dependent parameters involved in X-ray resonant magnetic reflectivity studies, a good knowledge of the sample structure is essential to provide a reliable picture of the magnetisation distribution within the uranium layers.

The following section details the experimental set-up and simulation package, used to investigate a restricted selection of U/Fe samples.

### 6.4.1 Experimental Method

The XRMR measurements were carried out at the XMaS, beamline BM28 at the ESRF in Grenoble. This beamline is situated on a bending magnet section of the synchrotron, and although the incident flux is significantly lower than that found on an insertion device, the optics and experimental hutch set-up have been designed specifically for the study of X-ray magnetic scattering and the photon flux has been optimised at energies in the vicinity of the U M edges. A complete description of the beamline optics and experimental capabilities has been given by Brown et al. [113].

The major X-ray optics components consist of a fixed-exit, water-cooled, double crystal (Si 111) monochromator that is used to tune the energy of the incident photons, with an energy resolution of better than 0.0003%. A rhodium coated, single crystal, silicon, toroidal mirror is used to provide a focus of  $\sim 0.8$ mm vertically and

$\sim 0.3\text{mm}$  horizontally at the sample position. A double mirror harmonic rejection assembly, constructed of Pyrex was used to discriminate the higher, unwanted harmonics of the monochromator from the fundamental wavelength. The sample views the X-ray beam on orbit, so that the incident flux is linearly polarised. It is possible to obtain circularly polarised light either by using X-rays emitted above or below the electron orbit, or, as in our case, using a diamond (111) single crystal, quarter wave phase plate. In order to preserve as much flux as possible, necessary at the relatively low energies of the uranium M edges, the majority of the experimental components were kept under high vacuum.

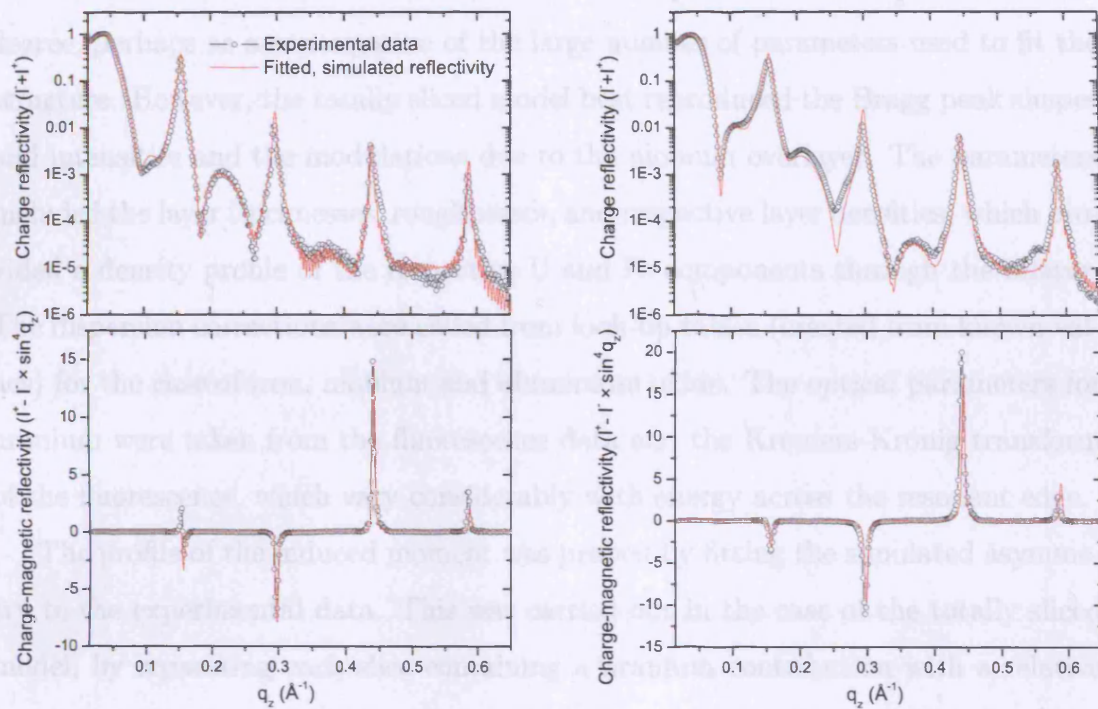
The samples were mounted onto copper stubs and attached to a magnet assembly, consisting of water-cooled pole pieces, generating an applied magnetic field of several hundred gauss. This field was large enough to saturate the iron moments, but small enough to be flipped quickly. The pole pieces were arranged so that they could provide a field aligned parallel to the incoming X-ray beam, necessary to detect the charge interference scattering described earlier. The magnet array was fixed onto a precision sample mount on an 11 circle Huber diffractometer and a Bicron detector was mounted onto the  $2\theta$  arm.

The beam position was first set to the centre of rotation of the diffractometer, using a centering pin mounted onto the sample stage. This was then replaced by the sample and magnet array, which were then set to the same position as the pin. The sample was then aligned, using the incident X-ray beam so that it was both in the centre of rotation of the diffractometer and that the beam was incident on the centre of the sample. This alignment process involved the detection of any offset in  $\theta$ , half cutting the beam at  $\theta = 2\theta = 0$ , and the detection of any  $\chi$  offset. Flexible bellows at the entrance and exit positions with respect to the X-ray beam incident on the sample, allowed a high vacuum to be maintained over this section of the beam path. Vertical and horizontal slits and attenuators were positioned at various points along the beam path and these were used to define the incident beam size and reduce the flux where necessary, to avoid saturation of the detector.

### 6.4.2 Results - SN71 [U<sub>9</sub>/Fe<sub>34</sub>]<sub>30</sub>

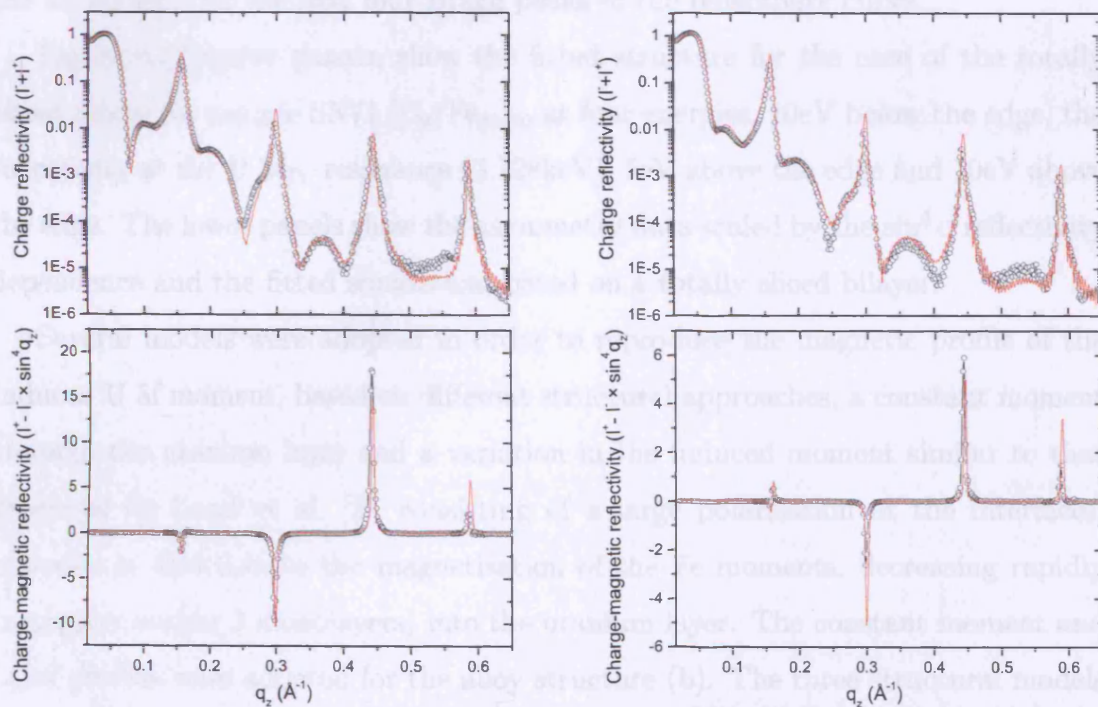
The measurements were carried out on two U/Fe samples, SN71 [U<sub>9</sub>/Fe<sub>34</sub>]<sub>30</sub> and SN74 [U<sub>32</sub>/Fe<sub>27</sub>]<sub>30</sub>, with thin and thick U layers respectively, but with similar Fe components. These samples were chosen to study the profile of the induced U 5f magnetic moment as a function of depth through the sample and to observe the persistence of this induced polarisation for the case of thicker U layers. Measurements of the reflectivity were made across the U M<sub>IV</sub> edge (3.728keV) at room temperature, for circularly polarised X-rays in an applied field, reversed at each data point along the reflectivity curve. A total of 17 energies were probed from 20eV below the M<sub>IV</sub> edge to 20eV above, providing a map of the X-ray reflectivity and magnetic asymmetry as a function of Q (Å<sup>-1</sup>) and of energy. In order to obtain values for the anomalous dispersion corrections across the resonance edge as discussed earlier, it was necessary to take a measurement of the X-ray fluorescence spectrum. This was achieved by fixing the detector perpendicular to the sample, minimising the intensity contribution from scattering events and measuring the intensity as a function of energy.

A simulation program has been developed by Alessandro Mirone and Simon Brown at the ESRF, which models the reflectivity data and the magnetic asymmetry as a function of energy across an absorption edge. This program is based on the theory behind X-ray resonant magnetic reflectivity described previously in the text. The sensitivity of the resonant scattering to the uranium component of the multilayers allows for a much more detailed description of the physical structure, especially in the interface region. The structure was fitted to three models, using an amoeba-type minimising procedure, designed to avoid local minima and recover a global minimum for a large parameter space. These models were based on (a) a clean interface with a large interfacial roughness, (b) a simple bilayer structure with alloy regions at the U-Fe and Fe-U interfaces and (c) a bilayer sliced into twenty alloyed components. The large number of energies, used to probe the variation in the optical parameters across the U M<sub>IV</sub> edge should provide a contrast that can distinguish between diffuse and rough interfaces, effects that cannot be distinguished using conventional X-ray reflectivity at a single energy.



(a) 3.718eV

(b) 3.728eV



(c) 3.733eV

(d) 3.738eV

Figure 6.17: Four example energies of the 17-energy mesh describing the X-ray resonant charge reflectivity and the asymmetry, showing the first four Bragg peaks for sample SN71  $[\text{U}_9/\text{Fe}_{34}]_{30}$ .

All three models were able to reproduce the experimental data to a reasonable degree, perhaps as a consequence of the large number of parameters used to fit the structure. However, the totally sliced model best reproduced the Bragg peak shapes and intensities and the modulations due to the niobium overlayer. The parameters included the layer thicknesses, roughnesses, and respective layer densities, which provided a density profile of the respective U and Fe components through the bilayer. The dispersion corrections were called from look-up tables (created from known values) for the case of iron, niobium and aluminium oxide. The optical parameters for uranium were taken from the fluorescence data and the Kramers-Kronig transform of the fluorescence, which vary considerably with energy across the resonant edge.

The profile of the induced moment was probed by fitting the simulated asymmetry to the experimental data. This was carried out in the case of the totally sliced model, by separating each slice containing a uranium contribution with a relative density greater than 0.001 into a magnetic and a non-magnetic part. The size of the moment is then fitted for each slice (in arbitrary units) in order to best reproduce the asymmetry for the first four Bragg peaks of the reflectivity curve.

Figure 6.17 upper panels, show the fitted structure for the case of the totally sliced model for sample SN71 [U<sub>9</sub>/Fe<sub>34</sub>]<sub>30</sub> at four energies, 10eV below the edge, the reflectivity at the U M<sub>IV</sub> resonance (3.728keV), 5eV above the edge and 10eV above the edge. The lower panels show the asymmetry data scaled by the  $\sin^4 q$  reflectivity dependence and the fitted simulation, based on a totally sliced bilayer.

Several models were adopted in order to reproduce the magnetic profile of the induced U 5f moment, based on different structural approaches, a constant moment through the uranium layer and a variation in the induced moment similar to that proposed by Laref et al. [2], consisting of a large polarisation at the interfaces, opposite in direction to the magnetisation of the Fe moments, decreasing rapidly (negligible within 2 monolayers) into the uranium layer. The constant moment and Laref profiles were adopted for the alloy structure (b). The three structural models proposed earlier were adapted to simulate the profile of the induced moment, by (a) slicing the U component of the simple U/Fe bilayer into four and separating the U slices into magnetic and non-magnetic components, (b) slicing the U component

into four and separating these and the U-Fe and Fe-U alloy regions into magnetic and non-magnetic components, and (c) separating each slice of the totally sliced model containing a uranium contribution with a relative density greater than 0.001 into a magnetic and a non-magnetic part.

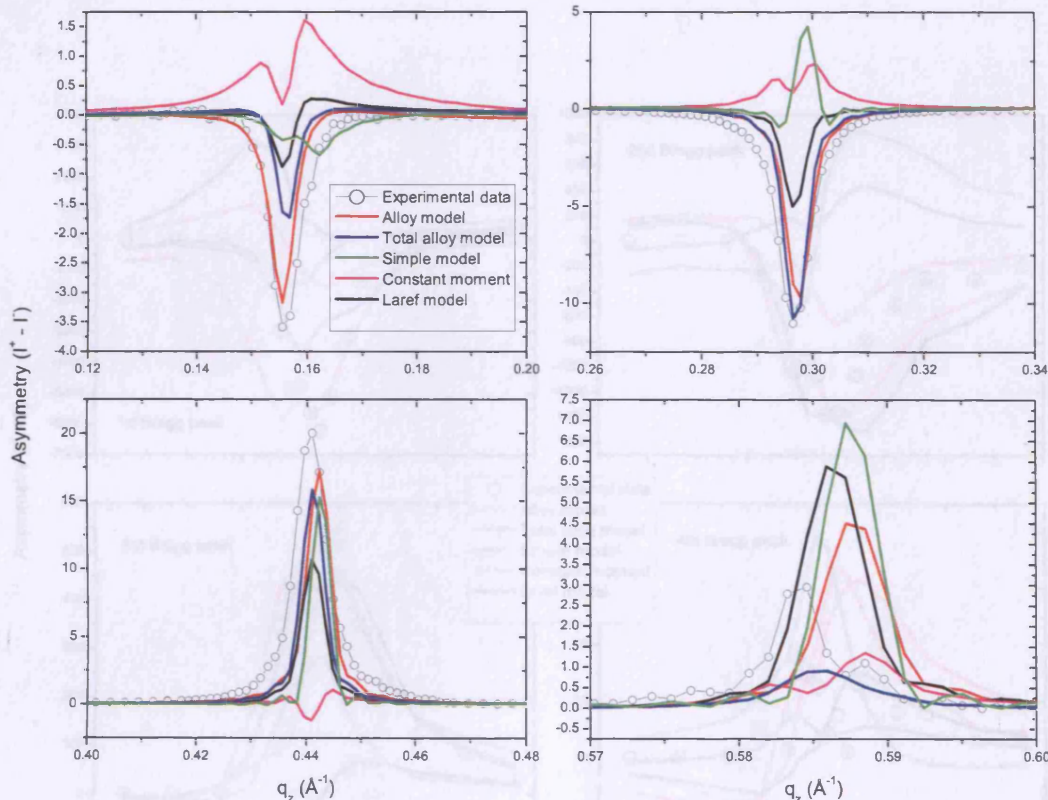


Figure 6.18: Asymmetry as a function of  $q$  in the vicinity of the first four Bragg peaks, showing results from several different structural and magnetic models.

Figure 6.18 compares the simulated asymmetry determined by the five proposed models at the four Bragg peaks as a function of wavevector momentum transfer,  $q$  ( $\text{\AA}^{-1}$ ). It is clear that the alloy and totally sliced models best represent the asymmetry data, but these models are best compared as a function of energy.

Figure 6.19 compares the simulated asymmetry determined by the five proposed models at the Bragg peak positions, as a function of energy. The change in the Bragg peak position with energy was accounted for. It is clear from these representations that the constant moment, Laref and simple bilayer structure models do not well

reproduce the experimental data. It seems clear that in order to reproduce the periodicity and intensity variation of the asymmetry at the four Bragg peaks the structural regions of uranium within a bilayer need to be  $\sim 15\text{\AA}$  apart, a situation which is not possible when the structure is confined to a simple bilayer with non diffuse, rough interfaces.

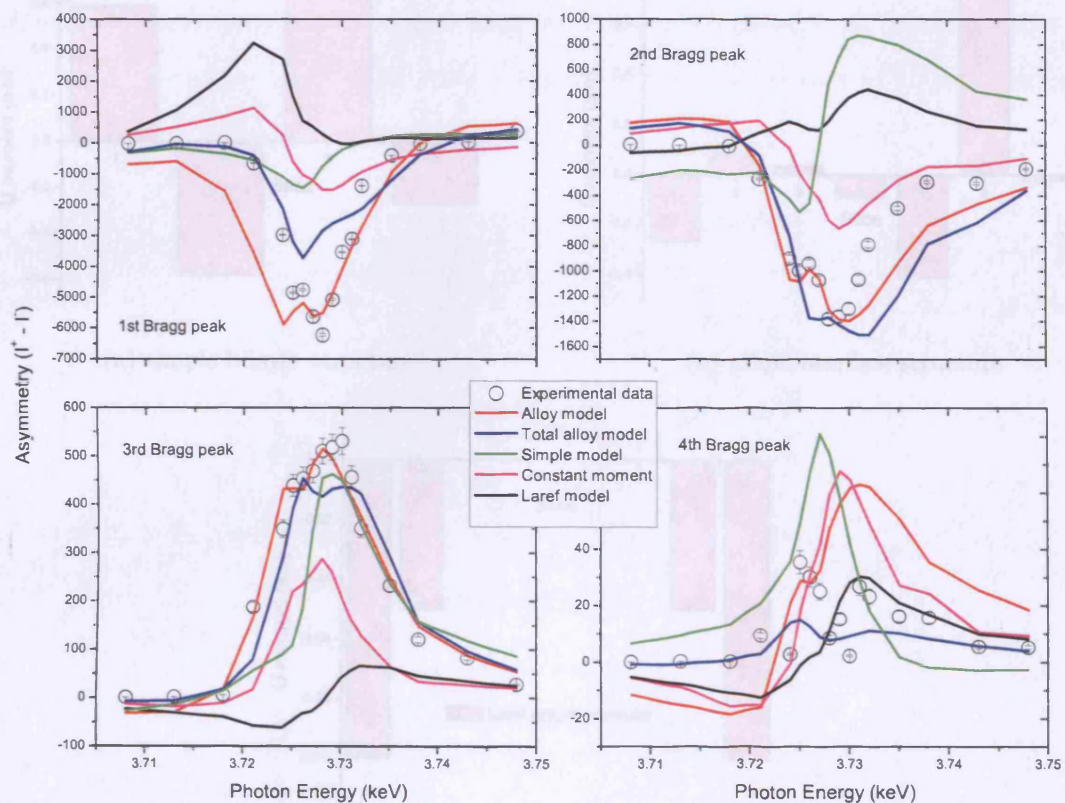


Figure 6.19: The asymmetry at the first four Bragg peaks as a function of energy across the U  $M_{IV}$  edge, showing results from several different structural and magnetic models.

Figure 6.20 shows the fitted profiles for the simple bilayer model and a representation of the model proposed by Laref et al. [25]. The constant moment was not expected to well represent the data, since the hybridization responsible for the observed  $\tilde{U}$  polarization is understood to be located at the interface and consequently the moment value should decrease

reproduce the experimental data. It seems clear that in order to reproduce the periodicity and intensity variation of the asymmetry at the four Bragg peaks the extremal regions of uranium within a bilayer need to be  $\sim 15\text{\AA}$  apart; a situation which is not possible when the structure is confined to a simple bilayer with non-diffuse, rough interfaces.

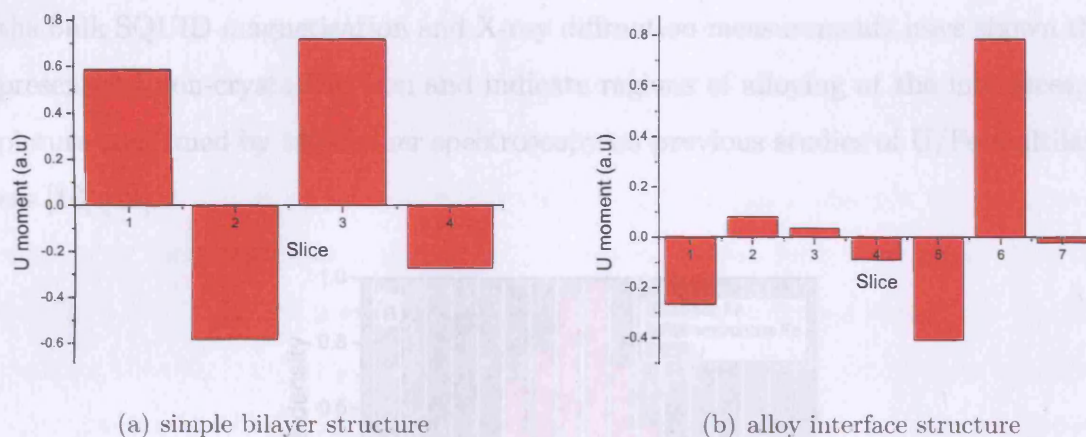


Figure 6.20: Profiles of the induced uranium magnetic moment, for the case of a simple bilayer structure and one containing alloyed interfaces. An idealised profile similar to that proposed by Laref et al. [2] is shown for comparison.

Figure 6.20 shows the fitted profile for the simple bilayer model and a representation of the model proposed by Laref et al. [2]. The constant moment was not expected to well represent the data, since the hybridisation responsible for the observed U polarisation and consequently the induced U 5f moment takes place at the interface region via a direct exchange mechanism, which is known to decrease

rapidly away from interface regions. Some RKKY-type exchange is also possible, but this would provide some oscillatory nature to the induced moment, and it is often a much weaker effect than the direct exchange. The Laref model [2] was based on an extremely idealised U/Fe system, with clean interfaces and a superlattice structure taking on the average lattice spacing of the  $\alpha$ -U (001) and Fe (110) respectively. This is most definitely not the situation we are faced with here, since the bulk SQUID magnetisation and X-ray diffraction measurements have shown the presence of non-crystalline iron and indicate regions of alloying at the interfaces, a picture confirmed by Mössbauer spectroscopy on previous studies of U/Fe multilayers [18] [19].

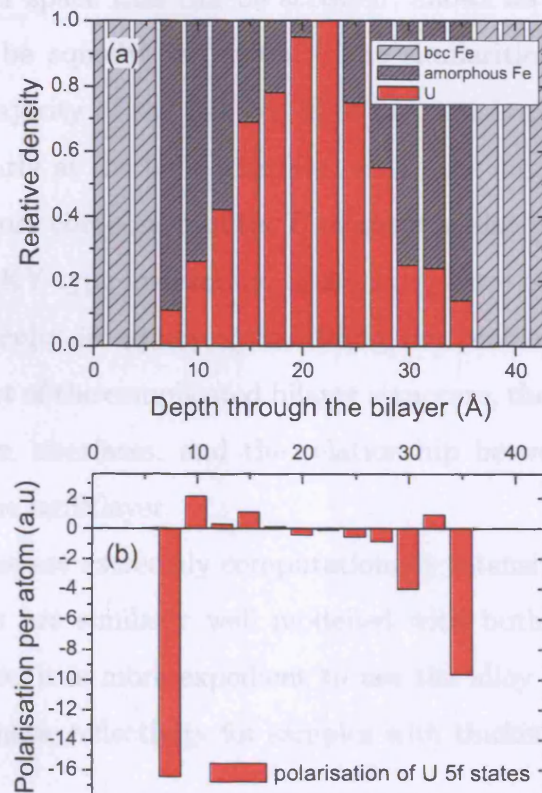


Figure 6.21: Density profile of the uranium present in sample SN71 from the fitted simulation to the X-ray resonant charge reflectivity data and the magnetic profile determined from the simulation of the asymmetry data.

Figure 6.21 shows the profile of the uranium density, determined from the fitting of the structure for the totally sliced model. Either side of this profile are iron layers

with densities close to the bulk Fe value. This density variation suggests that Fe-U interfaces are considerably less diffuse than U-Fe, which can be understood in terms of the unlikely implantation of U into Fe compared with the expected Fe diffusion into U.

The alloy and totally sliced models well represent the asymmetry at the Bragg peak positions as a function of energy and  $q$ . The profiles of these two models are shown in figures 6.20 and 6.21. The magnetic moment values, although arbitrary, have been normalised to the density of the respective layers to give an induced moment per U atom for each slice. The differences between the two profiles, which both simulate the experimental data to a reasonable degree, suggest that the large amount of parameter space that can be accessed, allows for a number of different solutions that may be equally well suited. The similarities of these two profiles indicate that the majority of the induced U 5f moment is present at the interface region, but particularly at the U-Fe interface, where the largest amount of alloying is found. An oscillatory component of the U moment is also present in both profiles, either due to an RKKY-type interaction, as a consequence of the complicated alloy structure. The difficulty in accurately modeling the profile of the U polarisation seems to be a product of the complicated bilayer structure, the variation in U density across the multilayer interfaces, and the relationship between the U moment at different points in the multilayer.

These calculations are extremely computationally intensive and since the structure and asymmetry are similarly well modelled with both the alloy and totally sliced representations, it is more expedient to use the alloy model to simulate the X-ray resonant magnetic reflectivity for samples with thicker U layers.

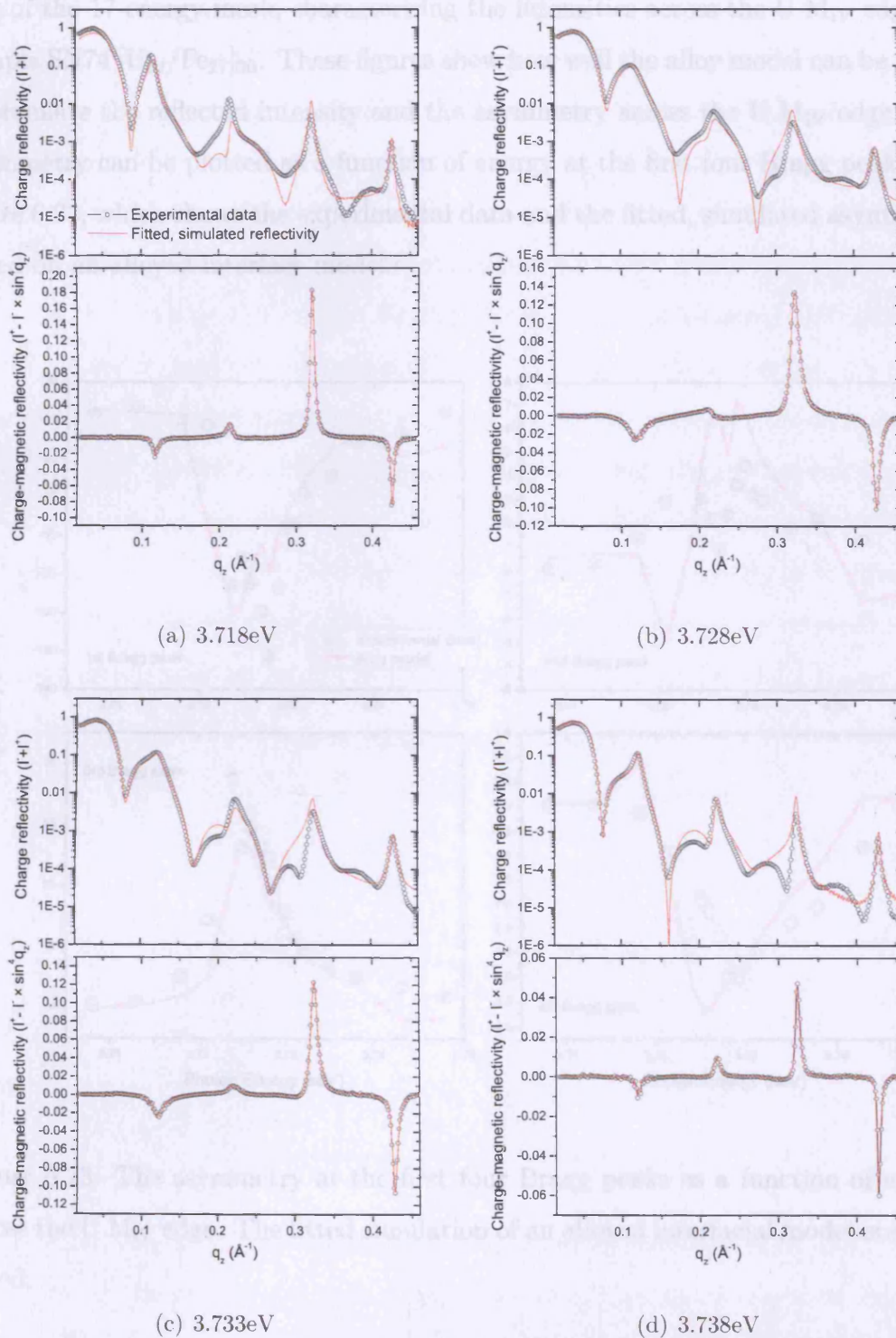
6.4.3 Results - SN74  $[U_{32}/Fe_{27}]_{30}$ 

Figure 6.22: Four example energies of the 17-energy mesh describing the X-ray resonant charge reflectivity (upper panels) and the asymmetry (lower panels).

Figure 6.22 shows the resonant charge reflectivity (upper panels) and magnetic asymmetry (lower panels) at the first four Bragg peaks at four energies, representative of the 17-energy mesh, characterising the intensities across the U  $M_{IV}$  edge for sample SN74  $[U_{32}/Fe_{27}]_{30}$ . These figures show how well the alloy model can be fitted to simulate the reflected intensity and the asymmetry across the U  $M_{IV}$  edge. The asymmetry can be plotted as a function of energy at the first four Bragg peaks, see figure 6.23, which shows the experimental data and the fitted, simulated asymmetry based on an alloyed interface model.

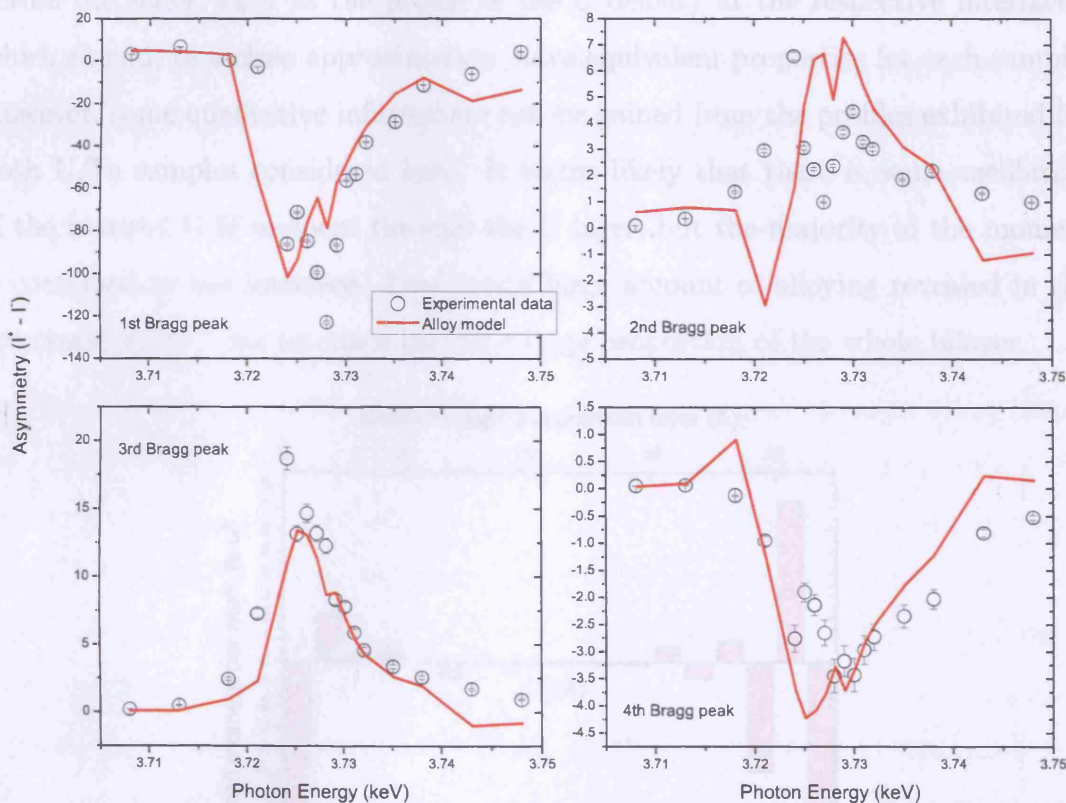


Figure 6.23: The asymmetry at the first four Bragg peaks as a function of energy across the U  $M_{IV}$  edge. The fitted simulation of an alloyed interfacial model is shown in red.

In this instance the uranium component of the multilayer consisted of a central U layer, sliced into six and two alloy slices at each of the U-Fe and Fe-U interfaces. The induced U 5f moment (a.u) has been scaled to the respective density of each

layer to give a profile of the U moment per atom as a function of depth through the uranium layer. Slice 1 represents the bottom of the layer. This profile is shown in figure 6.24.

The extremely complex variation of the induced moment, shown in the profile for sample SN74, highlights the fact that the structure is very complicated and difficult to model precisely. In this case it is likely that there are several statistically reasonable fits to the asymmetry data that would provide fairly different pictures of the polarisation profile. Work is currently underway to simultaneously characterise the structure of a series of samples, allowing for certain consistencies to be controlled across the series, such as the profile of the U density at the respective interfaces, which should, to a close approximation, have equivalent properties for each sample. However, some qualitative information can be gained from the profiles exhibited for both U/Fe samples considered here. It seems likely that there is some oscillation of the induced U 5f moment through the U layer, but the majority of the moment is contained at the interface. Due to the large amount of alloying revealed in the structural model, this interface can be a large proportion of the whole bilayer.

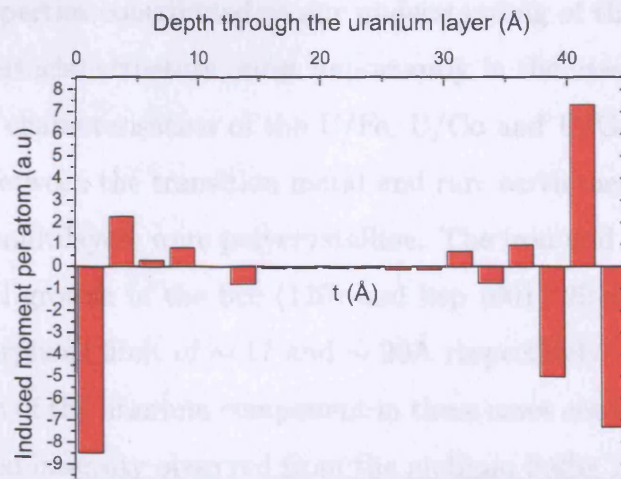


Figure 6.24: The profile of the induced U 5f moment determined from the fitted simulation of the asymmetry data, modelling the structure with alloyed interface regions.

# Chapter 7

## Conclusions

The following discussion will attempt to make some conclusions regarding the structure and magnetism of the three series of uranium multilayers considered within the scope of this work in terms of the bulk properties and the electronic, 5f-3d and 5f-4f interactions.

The structure was investigated using a combination of X-ray reflectivity and X-ray diffraction, however other techniques that were primarily employed to reveal the magnetic properties contributed to our understanding of the more complicated nature of the interfacial structure, most importantly in the case of U/Fe and U/Co multilayers. The characterisation of the U/Fe, U/Co and U/Gd systems showed a strong contrast between the transition metal and rare earth metal multilayers. The U/Fe and U/Co multilayers were polycrystalline. The iron and cobalt layers exhibited a preferential growth in the bcc (110) and hcp (001) directions and indicated a crystalline-amorphous limit of  $\sim 17$  and  $\sim 20\text{\AA}$  respectively. Any preferred crystalline orientation of the uranium component in these cases could not be deciphered, since the diffracted intensity observed from the niobium buffer resulted in fringes at the most likely (closest packed) ortho-rhombic  $\alpha - \text{U}$  reflections. A broad increase in the intensity in this region was observed however, when the uranium layer thickness was increased, indicating the presence of some polycrystalline  $\alpha - \text{U}$ .

The X-ray diffraction spectra of the U/Gd series of samples exhibited much greater relative intensities and displayed a combination of diffracted components from crystalline U and Gd, consistent with the model of a nearly coherent super-

lattice structure. The gadolinium was present in an hcp crystal structure with a preferred orientation along the 001 direction. This resulted in the growth of an unusual uranium crystal structure, suggestive of an hcp phase not found in the bulk, but observed in the U/W system [39]. The X-ray diffracted intensities persisted for U/Gd samples that consisted of very thin U and Gd layers,  $< 10\text{\AA}$ , such that no real crystalline limit could be detected, in sharp contrast to the situation observed in U/Fe and U/Co systems. Future measurements are planned to investigate the in-plane structure of the U/Gd multilayers.

The X-ray reflectivity spectra in the case for all samples could be well fit to relatively simple bilayer structures, highlighting the difficulty in using this technique alone, when more complex interfacial regions are described by a host of other experimental techniques. However, the large number of sharp Bragg peaks, which were present for the case of most samples over a relatively large range in  $Q$  ( $\text{\AA}^{-1}$ ), indicated the lack of impurities in these multilayers in the current sputtering system and the relatively high precision reproducibility of the bilayer structure through a multilayer stack.

The bulk magnetisation measurements were taken using a SQUID magnetometer, due to its very high sensitivity, required in our case, where the large diamagnetic signal from the 1mm thick sapphire substrate swamps the ferromagnetic response. Measurements were made of the absolute and relative ( $\mu_B/\text{atom}$ ) saturation magnetic moment (ferromagnetic) for all three multilayer systems. The U/Fe and U/Co series, indicated a magnetic dead layer of  $\sim 13\text{\AA}$  and  $\sim 15\text{\AA}$  respectively, consistent with the idea of a non-ideal growth and alloyed interfacial region, and consistent with results already published on the U/Fe system [19]. The U/Gd system in comparison, displayed a negligible magnetic dead layer ( $< 5\text{\AA}$ ), but had a saturation moment considerably reduced from the bulk value of  $7.63\mu_B/\text{Gd}$  that could not be explained in terms of an alloy interface region and amorphous-crystalline growth mechanism. The saturation moment tended towards a value of  $\sim 4.5\mu_B/\text{Gd}$  for the case of U/Gd multilayers with thick Gd layers, which could be a consequence of the strain produced by the crystalline U component seen by the nature of the decrease in saturation moment as the U layer is increased. The more idealised growth of

the U/Gd system and the more easily accessible Curie temperature lead to a more in-depth study of the bulk magnetic properties.

The coercive field showed a clear dependence on the gadolinium layer thickness, where thicker Gd layers resulted in larger coercive fields for samples with a constant U layer thickness. This dependence can be attributed to an increase in the domain size. However, the variation of the coercive field with the uranium layer thickness shows a more complicated dependence, where it seems that two compensating effects result in a minimum of the coercive field for a U thickness of  $\sim 20\text{\AA}$ . This could again be due to strain effects, leading to an increase in pinning and an additional energy required to rotate the gadolinium moments for thick U layers, but for the case of thin U layers the increase in U layer thickness could act to improve the crystalline growth of the gadolinium and reduce interfacial defects, resulting in a decrease in coercive field as  $t_U$  increases.

The Curie temperature was determined by temperature dependent magnetisation measurements on a range of U/Gd samples. The observed trend showed a power law dependence of  $T_C$  upon the gadolinium layer thickness, which resulted from the well-known finite-size scaling effect for thin ferromagnetic films [75], modelled as a 3D Ising-type ferromagnet. The pre-factor and exponent were consistent with values previously observed for gadolinium thin films [75], but for the case of very thin Gd layers and sample SN124  $[\text{U}_{10.6}/\text{Gd}_{24.8}]_{20}$ , there was a departure from the power law dependence. When the Gd layers become very thin,  $< 20\text{\AA}$ , there is a tendency towards 2D magnetic behaviour, resulting in a Curie temperature higher than expected, considering a 3D Ising model. The sample grown at higher temperature showed an elevated Curie temperature compared to its structural counterpart, grown at room temperature; an observation made in previous studies of Gd thin films [75].

Bulk magnetisation measurements were also used to investigate the anisotropy. A competing effect was revealed between the volume and surface contributions, resulting in a possible cross over from Gd moments aligned parallel to the plane of the film to a perpendicular magnetic anisotropy, aligning the Gd moments out of the plane of the film. This transition takes place at a gadolinium layer thickness of

$\sim 10\text{\AA}$ , but this value can be increased if the U layer thickness is increased.

Polarised neutron reflectivity measurements were carried out on selected samples from U/Fe, U/Co and U/Gd systems. For the case of actinide/transition metals the sample structures were modelled, by separating the ferromagnetic layers into components of bulk magnetic moment and reduced magnetic moment, which were necessary to well replicate the experimental reflectivity curves for spin up and spin down channels, and consequently the asymmetry ratio. This same method of modelling the ferromagnetic layers did not reproduce the neutron reflectivity spectra for the case of U/Gd multilayers. The closest simulations to the experimental data were produced using a simple bilayer structure, consistent with the X-ray diffraction measurements, describing a less diffuse, interfacial region. The average saturation magnetic moments were consistent with those found using SQUID magnetometry.

In order to probe the 5f-3d and 5f-4f electronic interactions, fundamental to our understanding of the observed magnetic properties of actinide multilayers, the XMCD and XRMR techniques were employed at the U M edges.

By investigating the X-ray absorption spectra and measuring the XMCD of a selected number of samples from each multilayer system, it was possible to extract values for the spin and orbital moments of the induced U 5f magnetism and make a comparative intra and intersystem analysis. A comparison of the magnitudes of the total induced magnetic moment across a series of samples was used to infer a profile of the U polarisation for the case of U/Fe and U/Gd samples. These profiles were based on the assumption that the interfaces were sharp, i.e. no alloying, and that the effect at each interface was equivalent, i.e. that the profile would be symmetric. The total moment for each sample was calculated both with and without the inclusion of the dipole operator term,  $\langle T_z \rangle$ . It is not certain whether the  $\langle T_z \rangle$  term should be accounted for or not, since the 5f bands are not entirely atomic-like nor entirely delocalised and it is even more unclear as to how the behaviour of these bands, interacting with those of the Fe 3d states, Co 3d states or the Gd 4f states (or Gd conduction bands) affects the  $\langle T_z \rangle$  operator. DFT calculations carried out on the U/Fe multilayer system [2], although in an idealised model, revealed that the majority of the induced magnetic moment would be found at the interfaces and

that this moment would be aligned antiparallel to that of the iron. The closest representation to this result is the profile produced, neglecting the  $\langle T_z \rangle$  term, which acts to describe the 5f states as highly delocalised.

The variation in the magnitude of the induced U 5f moment can be understood by considering the hybridisation of the 5f-3d states in U/Fe and U/Co multilayers, a comparison previously made in the respective binary compounds. The U 5f and Fe 3d states overlap in energy by a considerable portion, whereas the U 5f and Co 3d are separated in energy, so that the expected degree of hybridisation is much greater in the U/Fe system than the U/Co system. This can be seen by the considerably larger induced magnetic moment observed in the former than that seen in the latter. For the case of the U/Gd series of samples, the 4f states are far below the Fermi energy and the hybridisation is likely to occur between the U 5f states and the 5d and 6s Gd conduction bands, which carry a small orbital moment. The resultant induced U moment is much smaller in the U/Gd system than that for U/Fe samples. Further measurements are planned on the U/Ni system in order to provide a further comparison across the transition metal series, both in terms of the bulk properties and the electronic interactions, investigated by X-ray resonant techniques.

It was only possible within the current experimental limitations, to measure a detectable asymmetry in a scattering geometry for U/Fe samples. SN71 [U<sub>9</sub>/Fe<sub>34</sub>]<sub>30</sub> and SN74 [U<sub>32</sub>/Fe<sub>27</sub>]<sub>30</sub> were investigated, using X-ray resonant magnetic reflectivity as a means of probing the induced U polarisation as a function of depth through the uranium layers. These measurements were highly sensitive to the structure of the multilayers in terms of the asymmetry detected at the Bragg peak positions for the first four Bragg peaks. A much more complicated alloyed interface region was revealed, as a further, more detailed description of what had already been described by other techniques. The resultant profile of the induced U 5f magnetic moment was considerably more complicated than the one proposed from comparison of the total moment values calculated by XMCD. This was viewed as a consequence of the less than ideal structure, far departed from the assumptions proposed to create the profile from XMCD measurements. Due to the difficulty in precisely determining the structure when presented with such a vast amount of parameter space and the further

difficulties in identifying the magnetic structure as a function of depth through the multilayer, investigations are currently underway to simulate the X-ray resonant magnetic reflectivity for a series of samples simultaneously, in order to consistently identify the interfacial structure, which should have a similar average make-up for each sample. Further measurements are also underway to improve the experimental technique so that the much smaller U 5f moment induced in the U/Gd system can be detected. This would present a potentially, much easier sample structure and therefore a more easily and more reliably extracted profile.

To summarise, the combination of X-ray scattering, bulk magnetisation, neutron scattering and X-ray resonant techniques have provided a highly detailed description of U/Fe, U/Co and U/Gd multilayers in terms of their structural, magnetic and electronic properties. U/transition metal multilayers exhibit polycrystalline Fe and Co layers, oriented bcc (110) and hcp (001) respectively, with poorly crystalline  $\alpha$ -U layers in between. The crystal structures of the layers in the U/Gd system are far more well-defined; diffraction spectra suggest a near coherent, layer by layer growth of hcp Gd orientated in the 001 direction, grown on an exotic hcp phase of uranium, oriented 001. The magnetisation of the transition metal layers can be described by a three component system, describing a crystalline component with bulk moment, an amorphous layer with a reduced moment value and a non-magnetic region, most likely present in an alloy environment. The crystalline gadolinium layers in the U/Gd system displayed a constant value of  $\sim 4.3\mu_B/\text{Gd}$ , reduced from the bulk value by about 40%. Anisotropy measurements of these samples indicated that the moments might be oriented out of the plane of the film if the gadolinium layer thicknesses were less than  $10\text{\AA}$ . A Gd layer thickness dependent study of the Gd Curie temperature exhibited a finite-size scaling relationship. Induced U 5f magnetic moments have been detected for all multilayer systems with varying degrees of polarisation, dependent on the nature and extent of the electronic hybridisation in each case. U(5f)-Fe(3d) hybridisation resulted in induced U moments with values as large as  $0.1\mu_B/\text{U}$ , which were located mainly at the interface region. No such polarisation was observed in the U/Co system; a likely consequence of the larger separation in energy of the U 5f and Co 3d bands. The U/Gd system revealed

an oscillatory, induced polarisation of the U 5f electrons, resulting in U magnetic moment values of up to  $0.01\mu_B/U$ .

Future work is planned to further investigate the U/transition metal series of multilayers, by a study of the U/Ni system. Measurements are also planned to investigate the X-ray magnetic reflectivity of U/Gd multilayers in order to discern the profile of the Gd moment within the gadolinium layers. A Gd layer thickness dependent XMCD study and a characterisation of the in-plane U and Gd structures in U/Gd multilayers are planned. The surface effects of epitaxial thin films of  $\alpha$  - U and of the exotic hcp U structure are to be studied, using resonant X-rays and a program of measurements on multilayers, including uranium compounds is to be started.

## 7.1 Articles - Planned and Published

*Magnetism of uranium/iron multilayers: II. Magnetic properties*, A. M. Beesley, S. W. Zochowski, M. F. Thomas, A. D. F. Herring, S. Langridge, S. D. Brown, R. C. C. Ward, M. R. Wells, R. Springell, W. G. Stirling and G. H. Lander, *J. Phys.: Condens. Matter*, **16** (2004), 8507.

*Polarised neutron reflectivity from U/Fe, U/Gd multilayers*, R. Springell, S. W. Zochowski, S. Langridge, M. F. Thomas, F. Wilhelm, A. Rogalev, S. D. Brown, W. G. Stirling, G. H. Lander, R. C. C. Ward and M. R. Wells, *Physica B*, **385-386** (2006), 173.

*X-ray magnetic circular dichroism study of uranium/iron multilayers*, F. Wilhelm, R. Springell, N. Jaouen, A. Rogalev, A. M. Beesley, S. D. Brown, M. F. Thomas, S. W. Zochowski, S. Langridge, R. C. C. Ward, M. R. Wells, W. G. Stirling and G. H. Lander, *Phys. Rev. B*, **76** (2007), 024425.

*A study of uranium-based multilayers: I. Fabrication and structural characterisation*, R. Springell, S. W. Zochowski, R. C. C. Ward, M. R. Wells, S. D. Brown, L. Bouchenoire, F. Wilhelm, S. Langridge, W. G. Stirling and G. H. Lander, submitted to *J. Phys.: Condens. Matter*.

*A study of uranium-based multilayers: II. Magnetic properties*, R. Springell, S. W. Zochowski, R. C. C. Ward, M. R. Wells, S. D. Brown, L. Bouchenoire, F. Wilhelm, S. Langridge, W. G. Stirling and G. H. Lander, submitted to *J. Phys.: Condens. Matter*.

# Bibliography

- [1] J. A. Thornton. *J. Vac. Sci. Technol.*, 15(2):171, 1978.
- [2] A. Laref, E. Şaşıoğlu, and L. M. Sandratskii. *J. Phys. Condens.: Matter*, 18:4177, 2006.
- [3] chemistry. periodic table. [www.webelements.com](http://www.webelements.com), 2006.
- [4] S. Langridge. <http://www.rl.ac.uk/largescale/>.
- [5] B. Scholtz, R. A. Brand, and W. Keune. *Phys. Rev. B*, 50:2537, 1994.
- [6] M. N. Baibich, J.M. Broto, A. Fert, F. Nguyen Van Dau, F. Petroff, P. Eitenne, G. Creuzet, A. Friederich, and J. Chazelas. *Phys. Rev. Lett.*, 61(21):2472, 1988.
- [7] S. S. P. Parkin, N. More, and K. P. Roche. *Phys. Rev. Lett.*, 64(19):2304, 1990.
- [8] O. Rader, C. Carbone, W. Clemens, E. Vescovo, S. Blügel, W. Eberhardt, and W. Gudat. *Phys. Rev. B*, 45(23):13823, 1992.
- [9] L. Cheng, Z. Altounian, D. H. Ryan, J. O. Ström-Olsen, M. Sutton, and Z. Tun. *Phys. Rev. B*, 69:144403–1, 2004.
- [10] M. Arend, M. Finazzi, O. Schutte, M. Münzenberg, A. M. Diaz, F. Baudelet, Ch. Giorgetti, E. Dartyge, P. Schaaf, J. P. Kappler, G. Krill, and W. Felsch. *Phys. Rev. B*, 57:2174, 1998.
- [11] N. Jauoen, J. M. Tonnerre, D. Raoux, E. Bontempi, L. Ortega, M. Münzenberg, W. Felsch, A. Rogalev, H. A. Dürr, E. Dudzik, G. Van der Laan, H. Maruyama, and M. Suzuki. *Phys. Rev. B*, 66(134420), 2002.

- [12] G. S. Case, M. F. Thomas, C. A. Lucas, D. Mannix, P. Boni, S. Tixier, and S. Langridge. *J. Phys.: Condens. Matter.*, 13:9699, 2001.
- [13] G. H. Lander, M. S. S. Brooks, B. Lebech, P. J. Brown, O. Vogt, and K. Mat-tenberger. *Appl. Phys. Lett.*, 57:989, 1990.
- [14] P. P. Freitas, T. S. Plaskett, J. M. Moreira, and V. S. Amaral. *J. Appl. Phys.*, 64:5453, 1988.
- [15] P. Fumagalli, T. S. Plaskett, D. Weller, T. R. McGuire, and R. J. Gambino. *Phy. Rev. Lett.*, 70:230, 1993.
- [16] D. Mannix, W. G. Stirling, D. G. Bucknall, P. W. Haycock, S. D. Brown, G. H. Lander, and T. S. Plaskett. *Physica B*, 234:470, 1997.
- [17] N. Kernavanois, D. Mannix, P. Dalmas de Réotier, J. P. Sanchez, A. Yaouanc, A. Rogalev, G. H. Lander, and W. G. Stirling. *Phys. Rev. B*, 69:54405, 2004.
- [18] A M Beesley, M F Thomas, A D F Herring, R C C Ward, M R Wells, S Lan-gridge, S D Brown, S W Zochowski, L Bouchenoire, W G Stirling, and G H Lander. *J. Phys.: Condens. Matter*, 16:8491, 2004.
- [19] A M Beesley, S W Zochowski, M F Thomas, A D F Herring, S Langridge, S D Brown, R C C Ward, M R Wells, R Springell, W G Stirling, and G H Lander. *J. Phys.: Condens. Matter*, 16:8507, 2004.
- [20] M. A. Rosa, M. Diego, E. Alves, N. P. Barradas, M. Godinho, M. Almeida, and A. P. Gonçalves. *phys. stat. sol. (a)*, 196(1):153, 2003.
- [21] R. Springell, S. W. Zochowski, S. Langridge, M. F. Thomas, S. D. Brown, W. G. Stirling, G. H. Lander, R. C. C. Ward, and M. R. Wells. *Physica B*, 2006.
- [22] S. D. Brown, A. Beesley, A. Herring, D. Mannix, M. F. Thomas, P. Thomp-son, L. Bouchenoire, S. Langridge, G. H. Lander, W. G. Stirling, A. Mirone, R. C. C. Ward, M. R. Wells, and S. W. Zochowski. *J. Appl. Phys.*, 93:6519, 2003.

- [23] F. Wilhelm, N. Jaouen, A. Rogalev, W. G. Stirling, R. Springell, S. Zochowski, A. M. Beesley, S. D. Brown, M. F. Thomas, G. H. Lander, S. Langridge, R. C. C. Ward, and M. R. Wells. submitted to *Phys. Rev. B*, 2006.
- [24] S. D. Brown. to be submitted.
- [25] D. Weller, S. F. Alvarado, W. Gudat, K. Schroder, and M. Campagna. *Phys. Rev. Lett.*, 54:1555, 1985.
- [26] T. Morishita, Y. Togami, and K. Tsushima. *J. Phys. Soc. Japan*, 54:37, 1985.
- [27] P. Pankowski, L. T. Baczewski, T. Story, A. Wawro, K. Mergia, and S. Messoloras. *phys. stat. sol. (c)*, 1(2):405, 2004.
- [28] K. Mergia, L. T. Baczewski, S. Messoloras, S. Hamada, T. Shinjo, H. Gamari-Seale, and J. Hauschild. *Appl. Phys. A*, 74:1520, 2002.
- [29] L. T. Baczewski, R. Kalinowski, and A. Wawro. *J. Magn. Magn. Mater.*, 177:1305, 1998.
- [30] R. P. Erickson and D. L. Mills. *Phys. Rev. B*, 44:11825, 1991.
- [31] J. Kwo, M. Hong, F. J. Di Salvo, J. V. Wazczak, and C. F. Majkrzak. *Phys. Rev. B*, 35:7295, 1987.
- [32] J. A. Borchers, J. A. Dura, J. Unguris, D. Tulchinsky, M. H. Kelley C. F., Majkrzak, S. Y. Hsu, R. Loloee, W. P. Pratt, and J. Bass. *Phys. Rev. Lett.*, 82:2796, 1999.
- [33] C. Herring. *Magnetism*, volume 4. 1966.
- [34] E. C. Stoner. *Phil. Mag.*, 15:1080, 1933.
- [35] J. C. Slater. *Phys. Rev.*, 49:537, 1936.
- [36] L. F. Mattheiss. *Phys. Rev.*, 134A:970, 1964.
- [37] L. M. Roth, H. J. Zeiger, and T. A. Kaplan. *Phys. Rev.*, 149:519, 1966.
- [38] H. E. Nigh, S. Levgold, and F. H. Spedding. *Phys. Rev.*, 132:1902, 1963.

- [39] L. Berbil-Bautista, Torben Hänke, Matthias Getzlaff, Roland Wiesendanger, Ingo Opahle, Klaus Koepernik, and Manuel Richter. *Phys. Rev. B*, 70:113401, 2004.
- [40] S. L. Molodtsov, J. Boysen, M. Richter, P. Segovia, C. Laubschat, S. A. Gorovikov, A. M. Ionov, G. V. Prudnikova, and V. K. Adamchuk. *Phys. Rev. B*, 57:13241, 1998.
- [41] A. J. Freeman and D. D. Koelling. *The Actinides: Electron Structure and Related Properties*. 1974.
- [42] M. Hansen, R. P. Elliott, and F. A. Shunk. *Constitution of Binary Alloys*. 1958.
- [43] L. Paolasini, G. H. Lander, S. M. Shapiro, R. Caciuffo, B. Lebeck, L.-P. Regnault, B. Roessli, and J-M. Fournier. *Phys. Rev. B*, 54(10):7222, 1996.
- [44] L. Severin, L. Nordström, M. S. S. Brooks, and B. Johansson. *Phys. Rev. B*, 44(17):9392, 1991.
- [45] P. A. B. Toombs. *J. Phys. D*, 1:662, 1968.
- [46] J. Comas and C. A. Carosella. *J. Electrochem. Soc.*, 115:974, 1968.
- [47] Charles Hard Townes. *Phys. Rev.*, 65(11):319, 1944.
- [48] O. Hellwig, G. Song, H. W. Becker, A. Birkner, and H. Zabel. *Mat.-wiss. u. Werkstofftech.*, 31:856, 2000.
- [49] A. Beesley. *Structural and Magnetic Studies on sputtered Uranium/Iron Multilayers*. PhD thesis, University of Liverpool, 2005.
- [50] G. L. Squires. *Introduction to the Theory of Thermal Neutron Scattering*. 1978.
- [51] S. W. Lovesey and S. P. Collins. *X-ray Scattering and Absorption by Magnetic Materials*. 1996.

- [52] Jens Als-Nielsen and Des McMorrow. *Elements of Modern X-ray Physics*. 2001.
- [53] L. G. Parratt. *Phys. Rev.*, 95(2):359, 1954.
- [54] L. Nérot and P. Croce. *Revue Phys. Appl.*, 15:761, 1980.
- [55] S. K. Sinha, E. B. Sirota, S. Garoff, and H. B. Stanley. *Phys. Rev. B*, 38:2297, 1988.
- [56] K. Stoev and K. Sakurai. *The Rigaku Journal*, 14(2):22, 1997.
- [57] P. Croce. *J. Optics(Paris)*, 8:127, 1977.
- [58] P. Croce and L. Nérot. *J. Appl. Cryst.*, 7:125, 1973.
- [59] L. Nérot and P. Croce. *J. Appl. Cryst.*, 8:304, 1975.
- [60] A. L. Patterson. *Phys. Rev.*, 56:978, 1939.
- [61] Ivan K. Schuller. *Phys. Rev. Letts.*, 44(24):1597, 1980.
- [62] Eric E. Fullerton, Ivan K. Schuller, H. Vanderstraeten, and Y. Bruynseraede. *Phys. Rev. B*, 45(16):9292, 1992.
- [63] B. M. Clemens and J. G. Gay. *Phys. Rev. B*, 35(17):9337, 1987.
- [64] W. Sevenhans, M. Gijs, Y. Bruynseraede, H. Homma, and Ivan K. Schuller. *Phys. Rev. B*, 34(8):5955, 1986.
- [65] L. D. Landau and E. M. Lifschitz. *Physik. Z. Sowjetunion*, 8:153, 1935.
- [66] M. T. Johnson, P. J. H. Bloeman, F. J. A. den Broeder, and J. J. de Vries. *Rep. Prog. Phys.*, 59:1409, 1996.
- [67] J. V. Harkins and P. E. Donovan. *J. Phys.: Condens. Matter*, 8(685), 1996.
- [68] H. J. G. Draaisma, W. J. M. de Jonge, and F. J. A. den Broeder. *J. Magn. Magn. Mater.*, 351:351, 1987.

- [69] M. F. Thomas, J. Bland, G. S. Case, J. A. Hutchings, and O. Nikolov. *Hyperfine Interactions*, 126:377, 2000.
- [70] M. F. Thomas, G. S. Case, J. Bland, A. D. F. Herring, W. G. Stirling, S. Tixier, P. Boni, R. C. C. Ward, M. R. Wells, and S. Langridge. *Hyperfine Interactions*, 141:471, 2002.
- [71] F. Huang, M. T. Kief, G. J. Mankey, and R. F. Willis. *Phys. Rev. B*, 49:3962, 1994.
- [72] C. M. Schneider. *Phys. Rev. Lett.*, 64:1059, 1990.
- [73] Z. Q. Qiu, J. Pearson, and S. D. Bader. *Phys. Rev. Lett.*, 70:1006, 1993.
- [74] J. S. Jiang, D. Davidovic, D. H. Reich, and C. L. Chien. *Phys. Rev. Lett.*, 59:2596, 1995.
- [75] M. Farle, K. Baberschke, and U. Stetter. *Phys. Rev. B*, 47:11571, 1993.
- [76] Y. Li, C. Polaczyk, and D. Riegel. *Surface Science*, 402:386, 1998.
- [77] P. Pouloupoulos, A. Scherz, F. Wilhelm, H. Wende, and K. Baberschke. *Phys. Status Solidi A*, 189:293, 2002.
- [78] G. Schütz, W. Wagner, W. Wilhelm, P. Kienie, R. Zeller, R. Frahm, and G. Materlik. *Phys. Rev. Lett.*, 58:737, 1987.
- [79] D. Y. Smith. *Phys. Rev. B*, 13:5303, 1976.
- [80] B. T. Thole, Paulo Carra, F. Sette, and G. van der Laan. *Phys. Rev. Lett.*, 70:1943, 1992.
- [81] Paulo Carra, B. T. Thole, Massimo Alterelli, and Xindong Wang. *Phys. Rev. Lett.*, 70:694, 1993.
- [82] C. T. Chen, Y. U. Idzerda, H.-J. Lin, N. V. Smith, G. Meigs, E. Chaban, G. H. Ho, E. Pellegrin, and F. Sette. *Phys. Rev. Lett.*, 75:152, 1995.
- [83] Gerrit van der Laan and B. T. Thole. *Phys. Rev. B*, 53:14458, 1996.

- [84] José Goulon, Andrei Rogalev, Christophe Gauthier, Chantal Goulon-Ginet, Stéphane Paste, Riccardo Signorato, Claus Neumann, Laurence Varga, and Cécile Malgrange. *J. Synchrotron Rad.*, 5:232, 1998.
- [85] F. M. de Groot, M. A. Arrio, Ph. Sainctavit, Ch. Cartier, and C. T. Chen. *Solid State Commun.*, 92:991, 1994.
- [86] Michael van Veenendaal, J. B. Goedkoop, and B. T. Thole. *Phys. Rev. Lett.*, 77:1508, 1996.
- [87] J. Goulon. *J. de Physique*, 43:539, 1982.
- [88] J. Goulon, C. Goulon-Ginet, R. Cortes, and J. M. Dubois. *J. Phys.*, 43:539, 1982.
- [89] L. Tröger, D. Arvanitis, K. Baberschke, H. Michaelis, U. Grimm, and E. Zschech. *Phys. Rev. B*, 46:3283, 1992.
- [90] P. Pfalzer, J.-P. Urbach, M. Klemm, S. Horn, M. L. denBoer, A. I. Frenkel, and J. P. Kirkland. *Phys. Rev. B*, 60:9335, 1999.
- [91] M. L. Fdez-Gubieda, A. Garcia-Arribas, J. M. Barandiarán, R. López Antón, I. Orue, P. Gorria, S. Pizzini, and A. Fontaine. *Phys. Rev. B*, 62:5746, 2000.
- [92] H. J. Gotsis and P. Strange. *J. Phys.: Condens. Matter*, 6:1409, 1994.
- [93] J.-I. Igarashi and K. Hirai. *Phys. Rev. B*, 50:17820, 1994.
- [94] P. Dalmas de Réotier, A. Yaouanc, G. van der Laan, N. Kernavanois, J.-P. Sanchez, J. L. Smith, A. Hiess, A. Huxley, and A. Rogalev. *Phys. Rev. B*, 60:10606, 1999.
- [95] V. N. Antonov, B. N. Harmon, and A. N. Yaresko. *Phys. Rev. B*, 68:214424, 2003.
- [96] A. N. Yaresko, V. N. Antonov, and B. N. Harmon. *Phys. Rev. B*, 68:214426, 2003.

- [97] M. Finazzi, P. Saintavit, A.-M. Dias, J.-P. Kappler, G. Krill, J.-P. Sanchez, P. Dalmas de Réotier, A. Yaouanc, A. Rogalev, and J. Goulon. *Phys. Rev. B*, 55:3010, 1997.
- [98] A. Bombardi, N. Kernavanois, P. Dalmas de Réotier, G. H. Lander, J. P. Sanchez, A. Yaouanc, P. Burlet, E. Lelièvre-Berna, A. Rogalev, O. Vogt, and K. Mattenberger. *Eur. Phys. J. B*, 21:547, 2001.
- [99] T. Shishidou, T. Oguchi, and T. Jo. *Phys. Rev. B*, 59:6813, 1999.
- [100] M. Komelj and N. Stojic. *Phys. Rev. B*, 71:052410, 2005.
- [101] J. Stöhr and H. König. *Phys. Rev. Lett.*, 75:3748, 1995.
- [102] N. Stojic, J. W. Davenport, K. Komelj, and J. Glimm. *Phys. Rev. B*, 68:094407, 2003.
- [103] Y. Choi, D. Haskel, R. E. Camley, D. R. Lee, J. C. Lang, G. Srajer, J. S. Jiang, and S. D. Bader. *Phys. Rev. B*, 70:134420, 2004.
- [104] M. Blume. *J. Appl. Phys.*, 57:3615, 1985.
- [105] Z. Xu, Y. Liu, P. D. Johnson, and B. S. Itchkawitz. *Phys. Rev. B*, 52:15393, 1995.
- [106] M. Gell-Mann and M. L. Goldberger. *Physical Review*, 96:1433, 1954.
- [107] P. M. Platzman and N. Tzoar. *Phys. Rev. B*, 2:3536, 1970.
- [108] F. de Bergevin and M. Brunel. *Phys. Lett.*, 39A:141, 1972.
- [109] F. de Bergevin and M. Brunel. *Acta Cryst. A*, 37:314, 1981.
- [110] J. H. Hannon, G. T. Trammell, M. Blume, and D. Gibbs. *Phys. Rev. Lett.*, 61:1245, 1988.
- [111] N. Ishimatsu, H. Hashizume, S. Hamada, N. Hosoito, C. S. Nelson, C. T. Venkataraman, G. Srajer, and J. C. Lang. *Phys. Rev. B*, 60:9596, 1999.
- [112] R. de L. Kronig. *J. Opt. Soc. Am.*, 12:547, 1926.

- 
- [113] S. D. Brown, L. Bouchenoire, D. Bowyer, J. Kervin, D. Laundry, M. J. Longfield, D. Mannix, D. F. Paul, A. Stunault, P. Thompson, M. J. Cooper, C. A. Lucas, and W. G. Stirling. *J. Synchrotron Rad.*, 8:1172, 2001.